Energy & Environmental Science

rsc.li/ees
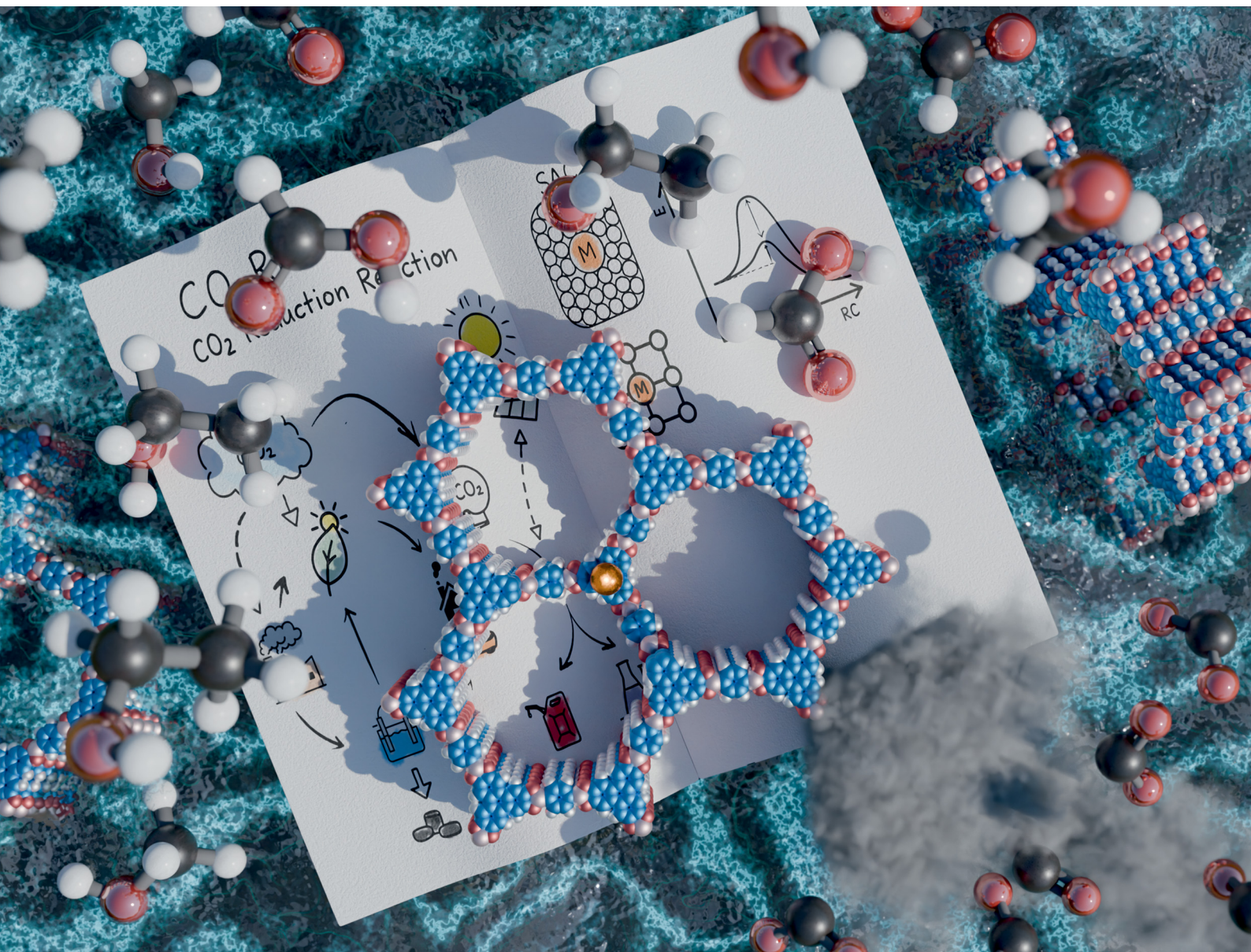
REVIEW ARTICLE

Mani Balamurugan, Aristides Bakandritsos, Sada Venkateswarlu,
Rajenahally V. Jagadeesh, Radek Zboril et al.
Covalent organic and metal organic frameworks based
single atom catalysts for valorisation of CO_2 to value
added chemicals

REVIEW

Check for updates

Covalent organic and metal organic frameworks based single atom catalysts for valorisation of CO₂ to value added chemicals

Sowjanya Vallem, [ID] [a] Malayil Gopalan Sibi, [b] Rahul Patil, [b] Vishakha Goyal, [bi] A. Giridhar Babu, [c] EA. Lohith, [d] K. Keerthi, [d] Muhammad Umer, [e] N. V. V. Jyothi, [d] Matthias Vandichel, [ID] [e] Daniel Ioan Stroe, [ID] [a] Subhasmita Ray, [f] Mani Balamurugan, [ID] *[gb] Aristides Bakandritsos, [ID] *[bh] Sada Venkateswarlu, [ID] *[b] Rajenahally V. Jagadeesh [ID] *[bi] and Radek Zboril [ID] *[bh]

Amidst escalating global concerns over rising atmospheric CO₂ levels, the capture and effective utilization of C_1 and C_{2+} sources are crucial not only for advancing a sustainable society but also for economically viable chemical synthesis. CO₂ valorisation as a chemical feedstock has garnered significant attention, driving the development of diverse catalytic systems and reaction pathways. Among them, single-atom catalysts (SACs) have emerged as a transformative class of materials owing to their maximized atom efficiency, well-defined active sites, and tunable electronic structures, enabling high catalytic selectivity and activity. When hosted on covalent-organic frameworks (COFs) and metal–organic frameworks (MOFs), SACs benefit from the structural regularity, high surface area, and chemical modularity of these porous crystalline scaffolds, further enhancing their catalytic performance and stability. This review provides an in-depth discussion of COF and MOF derived SACs for CO₂ valorisation through electrochemical, photochemical, and thermochemical approaches. We have explored the key factors that influence the performance of the CO₂ reduction reaction (CO₂RR) to enhance both selectivity and efficiency. In addition to catalyst preparation and synthetic applications, we provide an in-depth analysis of the mechanistic aspects and theoretical simulations of the COF and MOF SACs based CO₂ utilization. We explore the role of machine learning models in advancing SACs based CO₂ valorisation. We also identify key challenges including SAC agglomeration, mechanistic ambiguity, selectivity control and limited long term operational stability, while discussing future perspectives (such as electronic structure tuning, multi atom site design, and machine learning-assisted catalyst discovery) in this field of broad scientific, technological and societal interest.

Broader context

Addressing the urgent global challenge of reducing atmospheric CO₂ levels and mitigating climate change is an utmost priority. CO₂ is also increasingly recognized as an abundant and renewable carbon feedstock that can be valorized into value-added chemicals and fuels. Efficient and selective conversion of CO₂, requires the development of advanced catalytic systems. Among these, single-atom catalysts (SACs) have emerged as highly promising candidates due to their maximal atom utilization and exceptional tunability in activity, selectivity, stability, and reusability. The rational design of SACs relies on the appropriate

[a] *Department of Energy, Aalborg University, Aalborg, 9220, Denmark*

[b] *Nanotechnology Centre, Centre for Energy and Environmental Technologies, VSB-Technical University of Ostrava, 17. listopadu 2172/15, 708 00, Ostrava-Poruba, Czech Republic. E-mail: balubdu@gmail.com, a.bakandritsos@upol.cz, venkisada67@gmail.com, jagadeesh.rajenahally@catalysis.de, radek.zboril@upol.cz*

[c] *Department of Basic Sciences, SR University, Warangal 506371, Telangana, India*

[d] *Department of Chemistry, Sri Venkateswara University, Tirupati 517502, Andhra Pradesh, India*

[e] *School of Chemical Sciences and Chemical Engineering, Bernal Institute, University of Limerick, Limerick V94 T9PX, Republic of Ireland*

[f] *Department of Condensed Matter Physics, Faculty of Mathematics and Physics, Charles University, Ke Karlovu 3, Prague 12116, Czech Republic*

[g] *SOFT Foundry Institute, Seoul National University (SNU), Seoul 08826, Republic of Korea*

[h] *Regional Centre of Advanced Technologies and Materials, Czech Advanced Technology and Research Institute, Palacky University, Slechtitelu 27, 77900 Olomouc, Czech Republic*

[i] *Leibniz-Institut fur Katalyse e.V., Albert-Einstein-Str. 29a, Rostock, D-18059, Germany*

9632 | *Energy Environ. Sci.*, 2025, **18**, 9632–9712

This journal is © The Royal Society of Chemistry 2025

choice and integration of precursors and supports. In this regard, covalent organic frameworks (COFs) and metal–organic frameworks (MOFs) are particularly attractive as both precursor materials and supporting architectures. These porous crystalline materials offer high surface areas, well-defined pore structures, and the capacity to anchor metal species at the atomic scale—features essential for optimal catalytic performance. SACs derived from COFs and MOFs exhibit great promise for the thermochemical, photocatalytic, and electrocatalytic reduction of CO_2 into valuable C_1 and C_{2+} products. Moreover, the integration of density functional theory (DFT) and machine learning (ML) approaches can provide mechanistic insights and accelerate the discovery of efficient catalysts.

1. Introduction

The increasing reliance on fossil fuels is raising environmental concerns, particularly due to the greenhouse effect, with CO_2 emissions rising by over 2 ppm annually, posing a significant environmental threat.[1–3] To address this global climate challenge and mitigate atmospheric CO_2 levels, the Paris Agreement was signed in December 2015 under the United Nations Framework Convention on Climate Change (UNFCCC).[4] CO_2 emissions vary across countries, with the highest contributors illustrated in Fig. 1a and b.[5] As fossil fuel consumption continues to drive the rise in CO_2 emissions, innovative solutions for CO_2 conversion are of paramount importance.[6] Simultaneously, CO_2 is considered a promising renewable carbon source and an abundant feedstock for the production of value-added chemicals and fuels such as CO, CH_4, HCOOH, CH_3OH, C_2H_5OH, and C_2H_4, which have garnered significant attention.[7–11] The conversion of CO_2 into value-added products not only benefits national economies but also addresses environmental concerns. To efficiently and selectively convert CO_2, the development and applicability of advanced catalysts are crucial. Ideally, such catalytic systems should be based on heterogeneous materials due to their inherited advantages, including high stability and ease of recycling.

Recent advancements in electrochemical conversion, photochemical catalytic reduction, and thermocatalysis have shown promise in converting CO_2 into various chemicals and fuels.[10–13] Each method operates under specific reaction conditions, with heterogenous catalysts playing a significant role in the CO_2 reduction reaction (CO_2RR), facilitating the production of C_1 and C_{2+} hydrocarbons.[14–17] In thermocatalysis, CO_2 hydrogenation requires significant energy to break its strong C=O bonds, necessitating high temperatures (200 °C to 500 °C) and pressure (10 to 100 bar) for CO_2 valorisation. To enhance reaction rates and selectivity, researchers have developed low-energy barrier nanoparticle catalysts, particularly those based on noble metals.[18,19] The electrochemical CO_2RR initially utilized amalgamated metal compounds. Over time, metallic catalysts (Mo, Ru, Cu) and semiconductor nanoparticles (e.g., p-InS, n-/p-Ga–As) were developed for CO_2 to methanol conversion, typically occurring at the cathode of an electrochemical cell with the appropriate electrolytes.[20–23] However, a major challenge in CO_2RR is the competing hydrogen evolution reaction, which reduces the efficiency and product purity. Another promising approach for CO_2 conversion into fine chemicals and renewable fuels is photochemical catalysis, which harnesses solar energy with zero emissions. In photocatalysis, the surface charge state of the catalyst is crucial for ensuring efficient CO_2 conversion. Researchers have developed various materials including Lanthanides, MXenes, MoS_2, and noble metals (Ru, Rh, Pt) as well as bimetallic and core–shell-based Schottky heterojunctions, where co-catalysts play a key role in accelerating charge transfer and reducing overpotential.[24–29] However, challenges such as efficiency, selectivity, and long-term stability remain major bottlenecks in nanoparticle-based photochemical CO_2RR.[30] To address these limitations across all conversion methods, researchers have recently developed a unique class of metal catalysts known as single-atom catalysts (SACs).[31] Metal single atom (SA) based catalysts are highly desirable because these frontier catalytic materials (SACs) exhibit exceptional atomic efficiency, tunable activity, selectivity, stability, reusability, and quantum size effects.[32–38] Moreover, these advanced materials bridge the gap between homogeneous and heterogeneous catalysis, making them highly preferable for challenging synthetic reactions.[39–42] The design of potential SACs crucially depends on the choice of precursors, substrate supports, and reaction conditions. Among these, COF and MOF serve as excellent precursors and supports for the preparation of desired SAs.[43–47] The timeline of development on COF and MOF based SACs, along with the number of publications on CO_2 conversion, is shown in Fig. 2a and b.[48–51]

Notably, COF and MOF based or derived catalysts offer exceptional specific surface area, unique morphology, mesoporous characteristics, and atomic dispersion of metal species, which are key parameters for SACs to function effectively.[52–59] Compared to traditional nanoparticle-based catalysts, SACs derived from MOFs, which feature unique active sites and adaptable topologies, are emerging as promising materials for CO_2 valorisation.[60–63] Recently, MOF-derived/anchored SACs with specific site coordination arrangements have been designed for CO_2 conversion into targeted products by tailoring MOF precursors and fabrication methods. Additionally, COFs possess huge porosity, and multiple heteroatom functional groups, making them an ideal substrate for SACs. The bottom-up synthesis of COFs using various building blocks allows for the customization of skeleton structures, pore sizes, and topological arrangements.[64,65]

Several reviews have been published on CO_2 reduction reactions,[66–69] primarily focusing on MOF or COF based SACs for electrochemical reduction of CO_2. However, in this work we attempt to meet the urgent need for a comprehensive review CO_2 valorisation using MOF and COF derived SACs through miscellaneous methods, such as thermochemical, photochemical, and electrochemical approaches (Scheme 1). In this review, we provide an in-depth analysis of this topic, covering not only the design and applications of MOF and COF SACs for CO_2 valorisation, but also spectroscopic analyses (ex situ/in situ/operando), density functional theory (DFT) mechanistic studies, and machine learning (ML) models aspects. Additionally, we
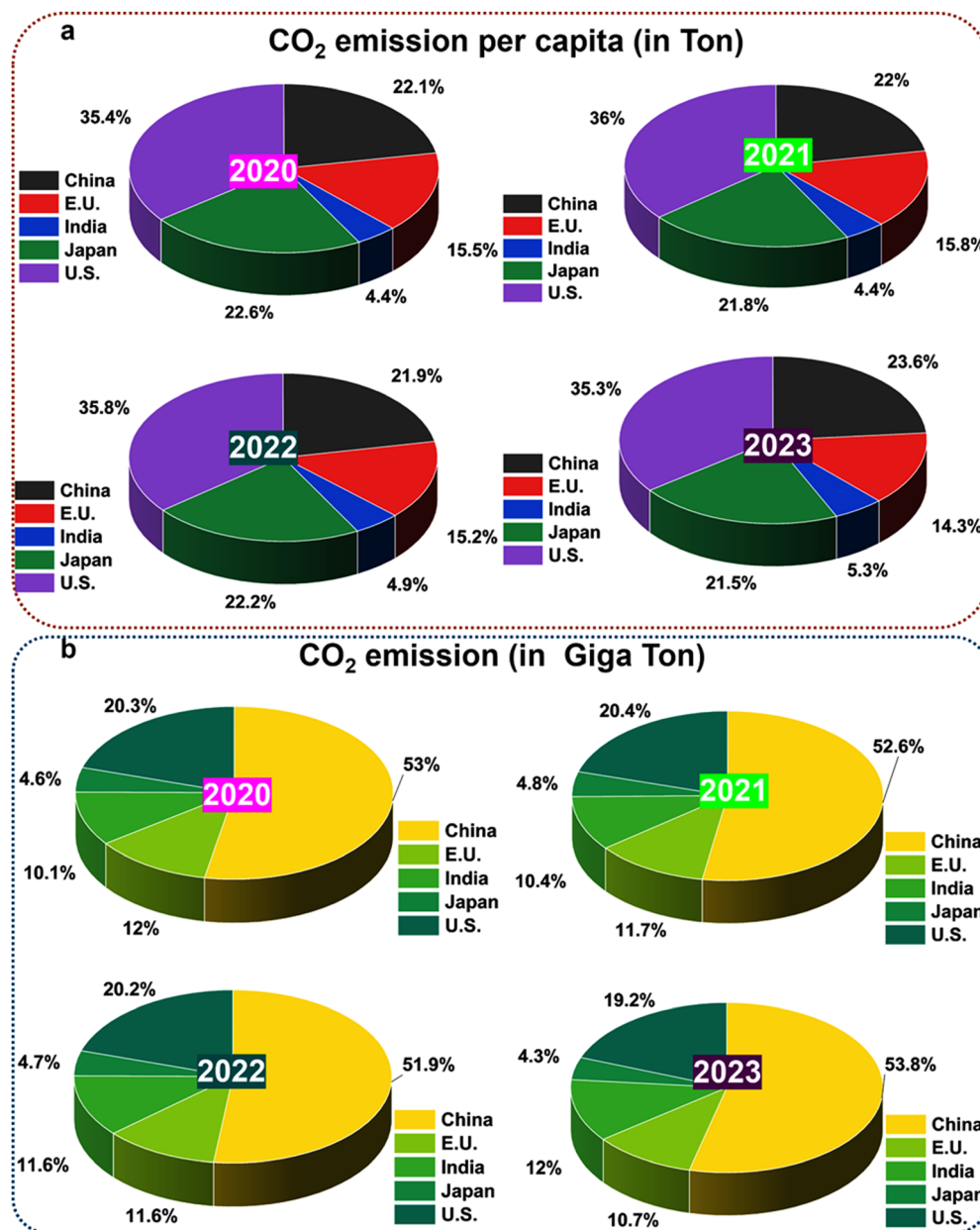
Fig. 1 (a) and (b) Pie chart represents globally, each country produces different levels of CO_2 emissions, and the top contributions from 2020 to 2023 (CO_2 emission in 2023, International Energy Agency).[5]

discuss the limitations and future perspectives on SACs and CO_2 utilization.

2. Synthetic strategies and characterization of COF and MOF-based SACs

The synthesis approaches for MOFs and COFs have been extensively reported in the literature.[70–74] In this chapter, we focus specifically on the synthetic strategies for COF and MOF-based SACs tailored for CO_2RR, along with a discussion of a few adaptable methods initially developed for other catalytic mechanisms but potentially applicable to CO_2RR.

2.1. Synthetic strategies

The synthesis of COF and MOF based SACs requires carefully designed strategies to achieve atomic dispersion, structural stability, and high catalytic efficiency. These methodologies fall into three principal categories: (i) high temperature pyrolytic transformations that exploit framework-derived heteroatom coordination; (ii) pre-synthetic coordination embedding of metal nodes into reticular backbones; and (iii) post-synthetic routes that enable spatial confinement and ligand-mediated
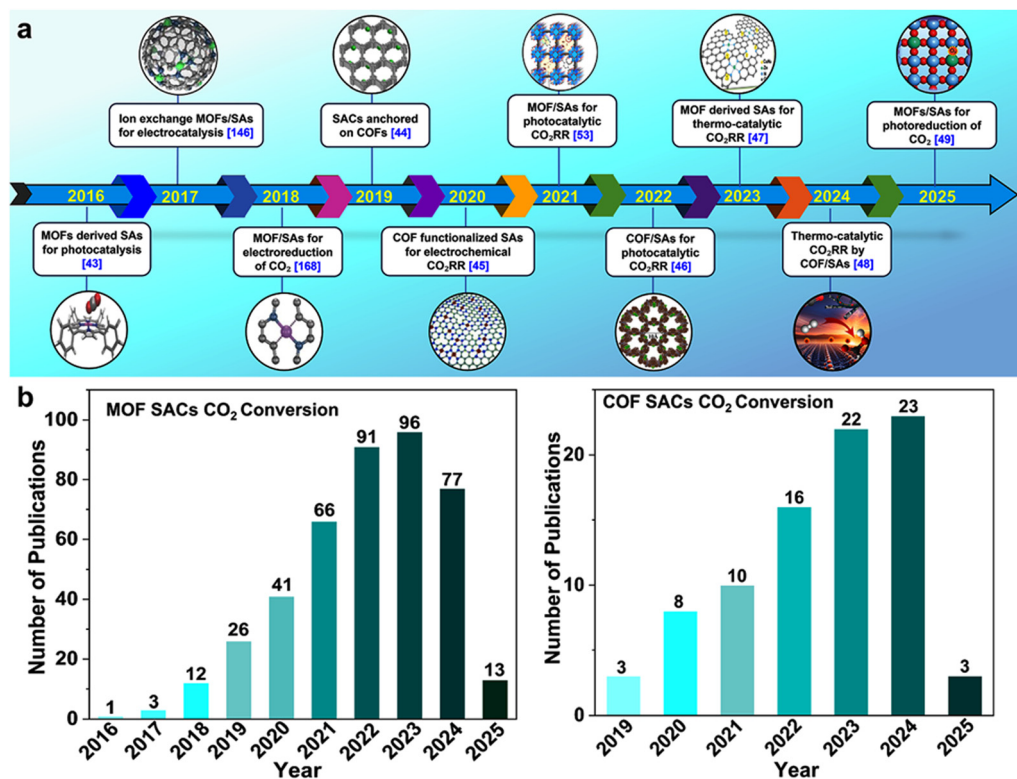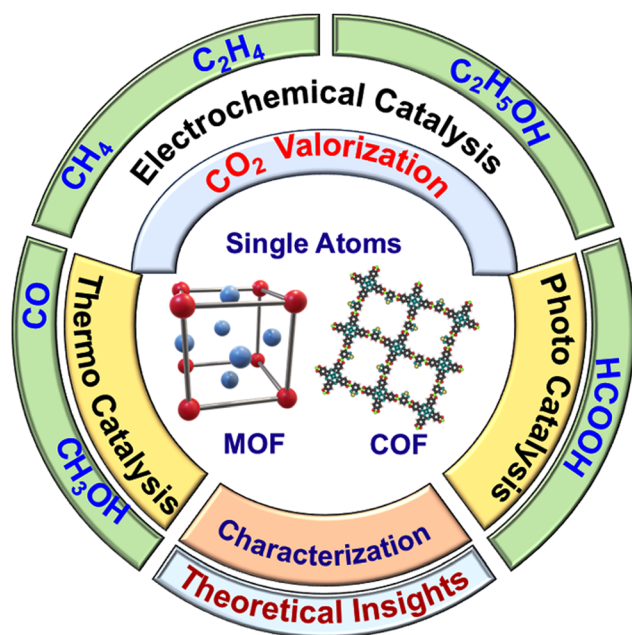
9634 | Energy Environ. Sci., 2025, 18, 9632–9712

This journal is © The Royal Society of Chemistry 2025

Fig. 2 (a) Timeline showing the significant milestones of MOF/COF−SACs in valorisation of CO_2 till date. (b) Number publications on MOF/COF−SACs in valorisation of CO_2 (from web of science).

Scheme 1 Schematic overall representation of COF and MOF single atom catalysts for CO_2 valorisation, along with their characterization and theoretical studies.

stabilization of SACs. Each approach exhibits trade-offs in atomic precision, scalability, and defect tolerance, while utilizing a diverse range of processes such as impregnation, ion

exchange, electrodeposition, and photochemical or chemical reduction. Furthermore, atomic engineering strategies, including SA, dual atom (DA), and multi atom (MA) configurations, are integrated into these synthesis methods. Atomic engineering plays a pivotal role in regulating nucleation, defect formation, and coordination environments, ultimately influencing the structure and functionality of single, dual, and multi atom catalysts.

Optimizing synthesis routes and atomic configuration is vital for enhancing the catalytic activity of SACs in CO_2 conversion.[75,76] Synthesis methods regulate atomic dispersion, coordination environments, and electronic structures, while atomic engineering strategies such as defect creation, coordination tuning, and ligand interactions further refine catalytic performance.[70,77] These factors collectively influence reaction pathways and product selectivity, allowing precise control over catalyst efficiency in CO_2 conversion.

Tailoring synthesis strategies is essential for optimizing SACs for targeted CO_2 valorisation pathways, including electrocatalytic, photocatalytic, and thermocatalysis transformations. The integration of precise synthesis and atomic engineering enables fine tuning of active sites, electronic states, and metal–support interactions, which directly influence reaction kinetics and selectivity. For instance, defect rich MOF derived SACs enhance CO_2 adsorption and activation, while ligand-modified COFs provide tunable coordination environments that steer product selectivity.[78,79] The rational design of SACs through an integrated approach of controlled synthesis and atomic engineering plays a pivotal role

This journal is © The Royal Society of Chemistry 2025

Energy Environ. Sci., 2025, **18**, 9632–9712 | **9635**

in improving catalytic efficiency, stability, and economic feasibility in CO_2 valorisation technologies. To achieve these characteristics, researchers have explored diverse synthesis strategies. This section primarily covers, pyrolysis, pre-synthetic metalation, and post-synthetic metalation which are mostly used for CO_2RR catalyst design.

2.2. Pyrolytic methods

Pyrolytic strategies are among the most widely employed techniques to fabricate SACs from MOFs and COFs due to their ability to simultaneously induce framework carbonization, heteroatom doping, and atomic metal anchoring. These high-temperature treatments commonly facilitate the evolution of metal N_x (and other heteroatom) coordination motifs within thermally transformed carbon skeletons, often mimicking enzymatic active sites. Pyrolysis induces a topological transformation where ligand field stabilization by heteroatoms and energy minimization pathways during carbonization can favour single-atom coordination over nanoparticle aggregation.

2.2.1. COFs. An effective approach to improve the catalytic performance of COF based SACs for CO_2 reduction is to employ COFs as precursor for synthesizing carbon materials through pyrolysis. Due to their two-dimensional carbon rich frameworks and inherent heteroatom contents, COFs act as excellent templates for producing heteroatom doped carbons with tailored electronic structures and catalytically active sites.[80,81] Additionally, COFs that contain metal coordination functionalities, like pyridine and porphyrin units support the formation of metal bound heteroatom doped carbons with periodic structures and uniformly distributed metal sites.[82] The controlled pyrolysis process facilitates the transformation of these well-defined molecular architectures into highly porous and conductive carbon matrices with atomically dispersed metal centers, ensuring optimal catalytic activity and stability.

2.2.1.1. Direct pyrolysis method. In this approach, the COF itself acts as the precursor and is directly converted into a heteroatom-incorporated carbon material with well dispersed SA sites. COFs with metal coordination sites (*e.g.*, porphyrins, imines, pyridines) are directly pyrolyzed in an inert atmosphere to generate SACs. During this process, organic linkers decompose, forming a conductive carbon structure, while metal centers are stabilized within the carbon matrix. For instance, a study reported the synthesis of a Ni SAC using a Ni $(NO_3)_2 \cdot 6H_2O$ and triazole COF as the nitrogen and carbon precursor (Fig. 3a).[80] The COF was subjected to pyrolysis under an inert atmosphere, resulting in the atomically dispersed Ni SAs within N-doped carbon framework. The resulting material delivered a substantial CO_2RR, achieving over 90% FE for CO invention at -0.8 V versus RHE, and maintained stability during extended operation. The strategy of using COFs as precursors not only ensures uniform dispersion of catalytic metal centers but also contributes to improved electrical conductivity, structural integrity, and electronic modulation, making COF-derived SACs highly effective for CO_2 reduction applications.
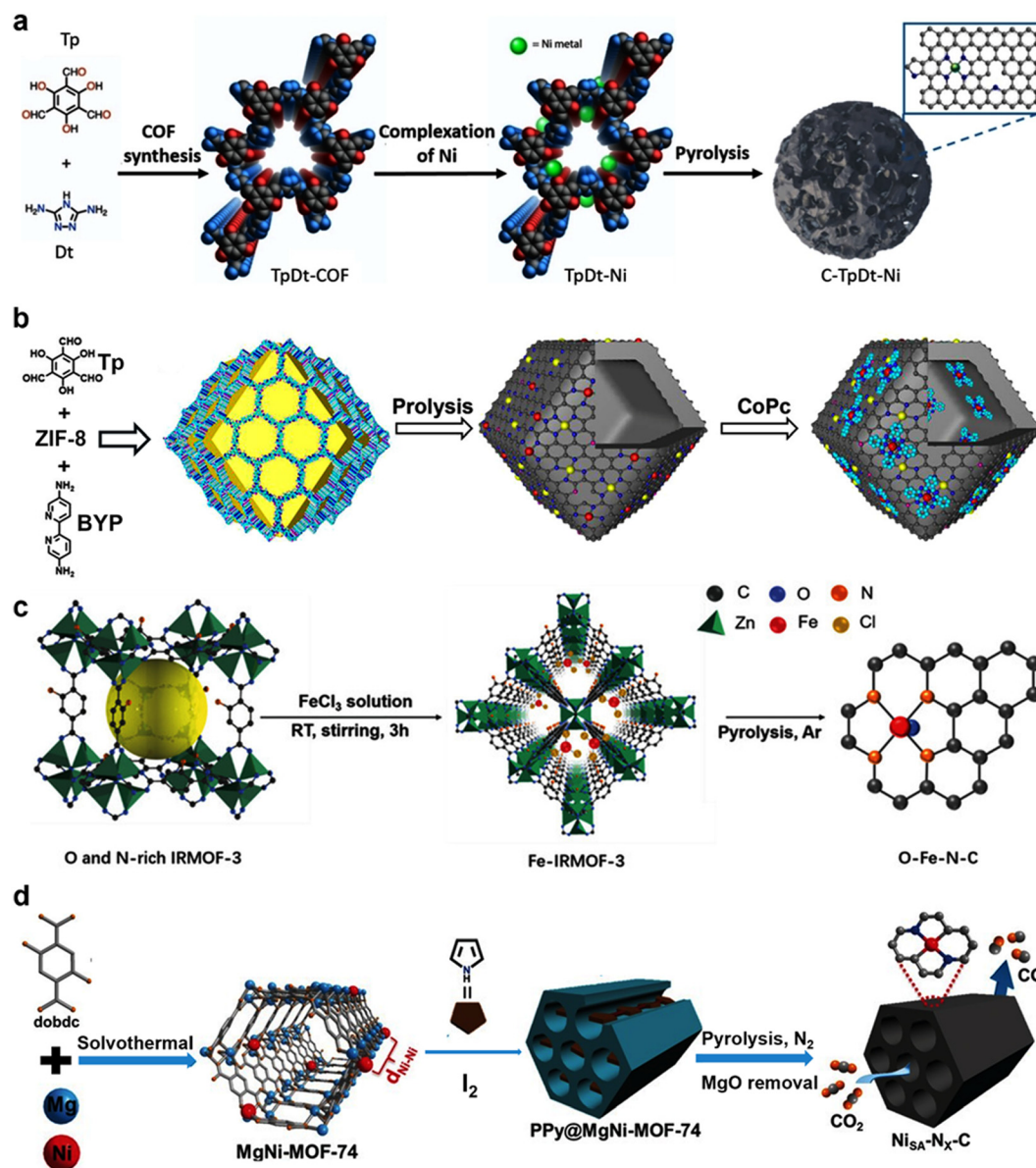
2.2.1.2. Sacrificial template pyrolysis. This strategy introduces an additional layer of structural control. It leverages the decomposition of ligands to generate porosity while stabilizing metal atoms. A COF is combined with a removable template (such as silica, MOFs, or polymers) and subjected to pyrolysis. The template is then etched/removed away, yielding a highly porous carbon framework with SACs. This sophisticated technique ensures precise control over SAC dispersion by utilizing a sacrificial template which is eliminated during pyrolysis, resulting in a finely tuned porous architecture. A notable example of this method for CO_2RR is the synthesis of a core–shell hybrid catalyst integrating a COF with ZIF-8, which upon pyrolysis forms a dual atom catalyst (Fig. 3b).[83] In this strategy, CoN_4O and Zn–N_4 sites (2.47 wt% and 11.05 wt%, respectively) are embedded within a hollow carbon matrix, ensuring a high accessible atomic catalytic center. This design enables the catalyst to achieve an impressive faradaic efficiency (FE) of 92.6% for CO at -0.8 V *vs.* RHE and a turnover frequency (TOF) of 1370.24 h^{-1} at -1.0 V. Furthermore, the designed SACs demonstrate exceptional durability, maintaining activity and selectivity over 30 hours of continuous operation. Theoretical calculations reveal that COF originated Co–N_4–O serves as the primary active site for CO_2RR, while Zn sites benefit from synergistic interactions, collectively enhancing activity and selectivity.

2.2.2. MOFs. MOFs can serve as effective templates for transforming low-nuclearity clusters into atomically dispersed SACs upon pyrolysis, enabling efficient CO_2RR to value-added products.[84] This approach leverages the well-defined microporous structure of MOFs to confine and stabilize metal SACs, mitigating aggregation and ensuring atomic dispersion. Upon pyrolysis, the resulting SACs exhibit enhanced catalytic activity and selectivity by facilitating multi-site synergism, which strengthens C–C coupling and directs CO_2 reduction toward desirable products.[84]

2.2.2.1. Direct pyrolysis. In this approach, MOFs are subjected to thermal treatment in an inert (N_2, Ar) or reducing (H_2) atmosphere, leading to carbonization of the organic ligands while metal sites remain atomically dispersed. Tailoring the organic components of MOFs allows for the controlled integration of heteroatoms (including oxygen, sulfur and phosphorous) through pyrolysis. Through strategic pyrolysis, the introduction of heteroatoms such as oxygen, sulfur, and phosphorus can be achieved by tailoring the organic ligands within MOFs. In this approach, a nitrogen and oxygen-rich isoreticular MOF (IRMOF-3) was employed as a precursor to engineering axial oxygen coordination to Fe–N_4 sites (Fig. 3c).[85] This O–Fe–N–C structure showed impressive CO_2RR activity, delivering 95% of FE for CO at -0.50 V *vs.* RHE and maintaining stability over 30 hours. The incorporation of oxygen in the Fe–N_4 center not only enhances CO desorption but also suppresses the competing hydrogen evolution reaction (HER), leading to improved selectivity. This work underscores the potential of direct pyrolytic treatment of heteroatom enriched MOFs as tunable precursors for designing high performance SACs tailored for CO_2 valorisation.

9636 | *Energy Environ. Sci.*, 2025, **18**, 9632–9712

This journal is © The Royal Society of Chemistry 2025

Fig. 3 Schematic illustration of SAC synthesis strategies: (a) direct pyrolysis of COFs. Reproduced from ref. 80 with permission from Wiley (CC-BY 4.0), copyright 2022. (b) Sacrificial template-assisted pyrolysis of COFs. Reproduced from ref. 83 with permission from Wiley (CC-BY 4.0), copyright 2023. (c) Direct pyrolysis of MOFs. Reproduced from ref. 85 with permission from Wiley (CC-BY 4.0), copyright 2022. (d) Sacrificial template-assisted pyrolysis of MOFs for CO_2RR. Reproduced from ref. 89 with permission from Wiley, copyright 2020.

2.2.2.2. Sacrificial and confined pyrolysis. MOFs act as both a template and a metal precursor, undergoing thermal decomposition to form atomically dispersed metal species on a porous carbon network.[86] The controlled decomposition allows for defect-rich carbon matrices that enhance catalytic activity. This strategy capitalizes on the selective decomposition of MOFs in combination with sacrificial templates to fabricate atomically dispersed metal sites within a porous carbon matrix.[87] The MOF precursor is mixed with a removable template, typically a polymeric material or metal hydroxides, which is then pyrolyzed under inert conditions.[88] During pyrolysis, the template undergoes decomposition, leaving behind a highly porous carbon structure embedded with well dispersed metal atoms. This technique offers fine control over the size and dispersion of the metal centers, critical for optimizing catalytic performance. A noteworthy example of this method for CO_2RR involves the preparation of Ni SACs with distinct $Ni–N_x–C$ (x = 2, 3, 4) coordination embedded in nitrogen-doped graphitic carbon. In this method, a magnesium oxide (MgO) template decomposes under pyrolysis, followed by acid etching treatment. The magnesium oxide provides a structural scaffold for the carbon framework, while Mg^{2+} facilitates the special isolation of nickel centers, promoting the formation of $Ni–N_x–C$ coordination. This method ensures a high density of uniformly distributed SAs and significantly enhances key electrocatalytic parameters, such as increased electrochemical surface area, optimized electronic structure, and improved mass transport.

This journal is © The Royal Society of Chemistry 2025

Energy Environ. Sci., 2025, **18**, 9632–9712 | **9637**

The resultant $Ni–N_x–C$ metal sites while preserving the MOF derived framework (Fig. 3d).[89] This structure illustrated a notable FE of over 97% for CO production at -0.76 V *vs.* RHE, alongside a high current density of 52.7 mA cm^{-2} and an impressive TOF of 9097 h^{-1}. Additionally, it exhibited exceptional durability, maintaining stable catalytic activity over 40 hours of continuous operation, underscoring its potential for efficient CO_2RR applications.

Whereas as, confined pyrolysis methods employ nanoconfinement to limit atomic migration and aggregation of metal atoms, thereby stabilizing atomically dispersed SACs. Confined pyrolysis is also a strategy to regulate the structural transformation of MOFs into porous carbon materials while preserving their framework integrity and optimizing catalytic properties. Unlike conventional pyrolysis, which often leads to collapse or shrinkage, confined pyrolysis employs hard templates such as silica-based or polymeric materials to maintain structural integrity, prevent metal nanoparticle agglomeration, and facilitate the formation of a robust porous network.[90] A key example is the synthesis of Zn–N–HOPCPs, where ZIF-8 single crystals are embedded within a SiO_2 template before pyrolysis, yielding a 3D-ordered macroporous carbon structure (Fig. 4a).[91] This hierarchical architecture enhances molecular diffusion, maximizes active site exposure, and significantly improves CO_2 conversion efficiency, particularly in cycloaddition with epoxides. Notably, the Zn–N–HOPCP catalyst, synthesized *via* confined pyrolysis, demonstrated outstanding performance in CO_2 photoconversion to cyclic carbonates under mild conditions. Owing to its broad light absorption spectrum (230–800 nm), this catalyst achieved an impressive 95% catalytic yield at room temperature and low pressure when coupled with TBAB as a co-catalyst. The high surface area (1128 m^2 g^{-1}) and well dispersed single Zn sites played a crucial role in enhancing CO_2 activation. Consequently, Zn–N–HOPCPs exhibited superior activity and stability, underscoring the effectiveness of confined pyrolysis in producing highly efficient catalysts for CO_2 utilization in value-added chemical synthesis.

Recently, MOF-derived dual atom catalysts (DACs) have demonstrated enhanced catalytic efficiency due to synergistic contacts between homo or hetero metal sites. Expanding on this concept, pyrolysis-derived multi-atom catalysts introduce an additional level of tunability by incorporating a third metal atom, which strengthens electronic interactions and optimizes intermediate adsorption and reaction kinetics. A notable example of this approach is the synthesis of Fe–Co–Ni@NC trimetallic catalysts from MOF precursors (Fig. 4b).[92] This strategy ensures atomic-level dispersion of Fe, Co, and Ni on a porous carbon framework without requiring acid treatment. The synthesis of Fe–Co–Ni TACs anchored on hollow carbon structures follows a systematic multi-step approach to achieve atomic dispersion and enhanced catalytic performance. Initially, $Fe(acac)_3$ is incorporated *in situ* during the self-assembly of ZIF-8, leveraging its molecular compatibility to be efficiently confined within the MOF cages. The precursor-loaded MOF undergoes carbonization, forming an Fe–N-doped porous carbon (Fe@NC) structure. The Fe–NC nanoparticles are then dispersed in a Tris buffer solution

and coated with polydopamine through dopamine self-polymerization. The polydopamine layer, rich in hydroxyl and nitrogen functional groups, facilitates the coordination of Co and Ni cations *via* covalent bonding or electrostatic attraction. Subsequent annealing at 900 °C under a nitrogen atmosphere results in the formation of Fe–Co–Ni@NC, where atomically dispersed Fe, Co, and Ni sites are stabilized within a hierarchically porous carbon framework, optimizing catalytic activity for ORR/OER. This process effectively prevents metal aggregation during pyrolysis, ensuring homogeneous atomic dispersion. The resulting Fe–Co–Ni@NC structure provides well-defined $Fe–N_4$, $Co–N_4$, and $Ni–N_4$ coordination sites, leading to superior electrocatalytic performance in ORR and OER. The synergy among the three metal centers augments the adsorption and activation of key intermediates, significantly enhancing catalytic efficiency compared to SACs and DACs. Although this system was designed for ORR/OER, its underlying synthesis strategy, and electronic tuning principles are highly relevant for CO_2RR catalyst development. Given the pivotal role of nickel and its heteroatomic coordination in modulating CO_2RR activity and selectivity, similar MOF derived pyrolysis strategies could enable the rational design of high-performance multi-atom catalysts for CO_2RR.[93–95] Future studies could explore tailored trimetallic configurations to further enhance C–C coupling, CO_2 activation, and long-term catalytic stability.

Although pyrolysis-derived SACs enhance conductivity and stability by forming confined sites such as M–N–C, $M–N_4$, and $M–N_4$–O in carbon frameworks, alternative synthesis strategies enable atomic-scale metal incorporation while preserving the porous structure integrity of COFs and MOFs. Among these, pre-synthetic metalation integrates metal centers directly into the framework during assembly, ensuring precise atomic coordination and uniform dispersion. As discussed in the following sections, this approach provides significant advantages in maintaining framework stability and tailoring the metal coordination environment.

2.3. Non-pyrolytic methods

Non-pyrolytic approaches offer superior control over metal site coordination and the local environment compared to high-temperature pyrolysis methods. These methods avoid harsh conditions, thereby preserving the desired metal ligand coordination geometries that are critical for achieving high catalytic selectivity.

2.3.1. Pre-synthetic metalation

2.3.1.1. COFs. Pre-synthetic metalation is a strategic approach in the design of SACs within COFs, where metal centers are directly incorporated into the framework during polymerization. This method ensures precise atomic dispersion, strong metal–ligand coordination, and enhanced catalytic stability, making it a highly effective route for electrocatalytic applications such as CO_2RR.

A notable example of this approach is the synthesis of CoPc-DSDS-COF and CoPc-DNDS-COF, where Co-hexadecafluorophthalocyanine (CoPc) serves as the metal node and organic linkers such as 1,2,4,5-benzenetetrathiol (DSDS) or 2,5-diaminobenzene-1,4-dithiol (DNDS) create an extended conductive network (Fig. 5a).[96]

9638 | *Energy Environ. Sci.*, 2025, **18**, 9632–9712

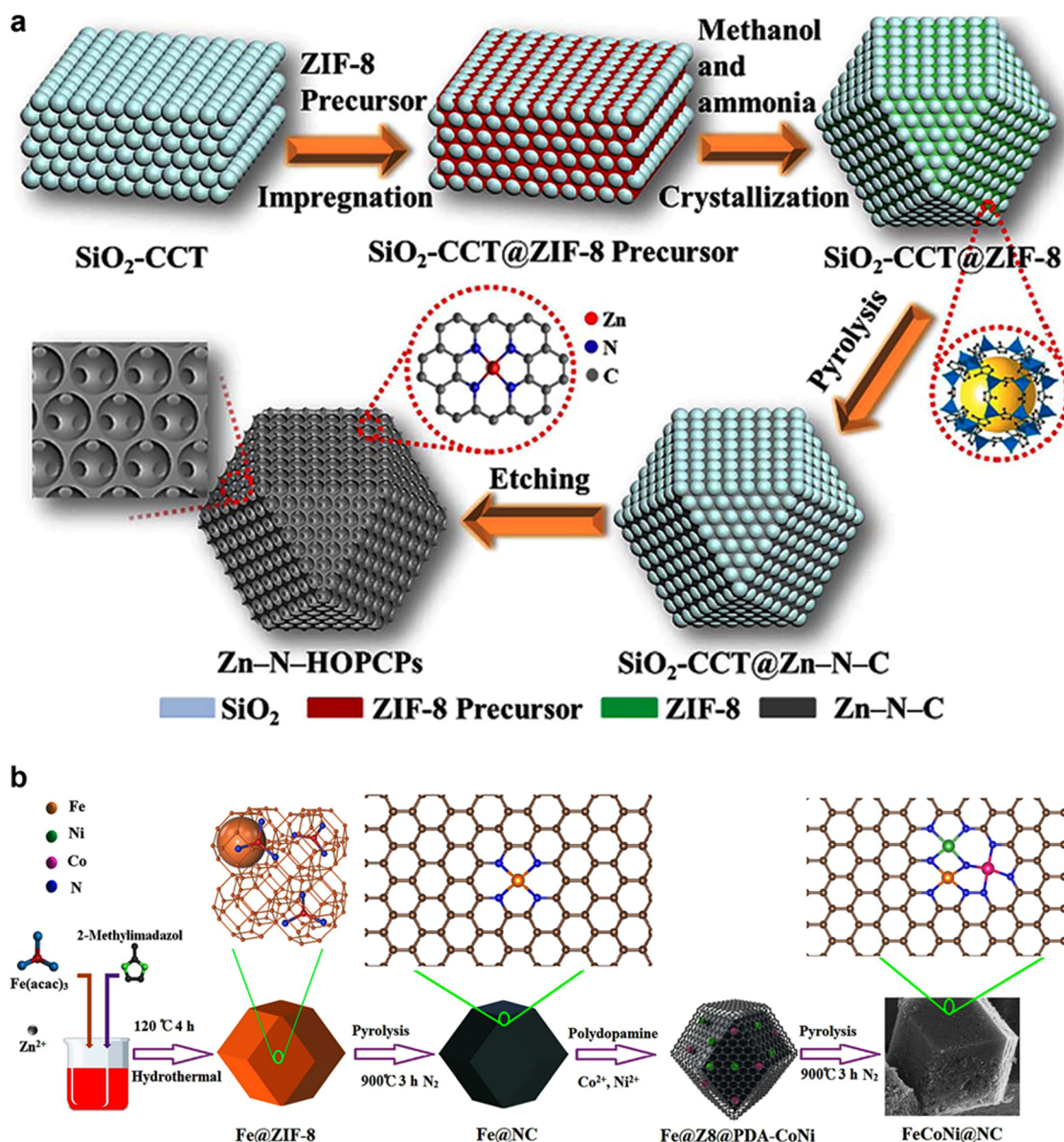This journal is © The Royal Society of Chemistry 2025

Fig. 4 Representative examples of (a) the confinement pyrolysis approach for MOF derived SACs, highlighting the controlled conversion of MOFs into atomically dispersed catalysts. Reproduced from ref. 91 with permission from Elsevier, copyright 2020. (b) Multi atomic sites derived from MOF *via* pyrolysis. Reproduced from ref. 92 with permission from Elsevier, copyright 2024.

By integrating metallophthalocyanines as an intrinsic part of the COF backbone, the resulting materials exhibit a well-defined atomic Co–N$_4$ coordination environment without requiring post-synthetic modifications or high-temperature pyrolysis. This controlled metalation ensures that the Co centers are uniformly distributed throughout the framework, preventing aggregation and maximizing active site exposure. The pre-synthetic incorporation of CoPc into the COF structure enhanced its electrical conductivity and charge transport, which is crucial for efficient electrocatalysis. The electronic band structure of these COFs enabled favourable charge transfer and optimal binding of CO$_2$ reduction intermediates, ultimately improving catalytic activity and selectivity. Experimentally, CoPc-DNDS-COF demonstrates superior CO$_2$-to-CH$_4$ conversion, whereas CoPc-DSDS-COF shows

selective CO production, highlighting the tunability of these materials based on linker modifications. This pre-synthetic metalation approach thus offers significant advantages over post-synthetic methods by preserving framework integrity, ensuring precise metal coordination, and enabling systematic structure–property optimization for CO$_2$RR.

2.3.1.2. MOFs. Pre-synthetic incorporation of SACs into MOFs ensures uniform atomic dispersion and strong coordination with linkers or metal nodes, preventing aggregation while optimizing catalytic activity for CO$_2$RR. Unlike post-synthetic modifications, this approach integrates metal precursors directly into the MOF structure during synthesis, enabling precise control over coordination environments and electronic properties.
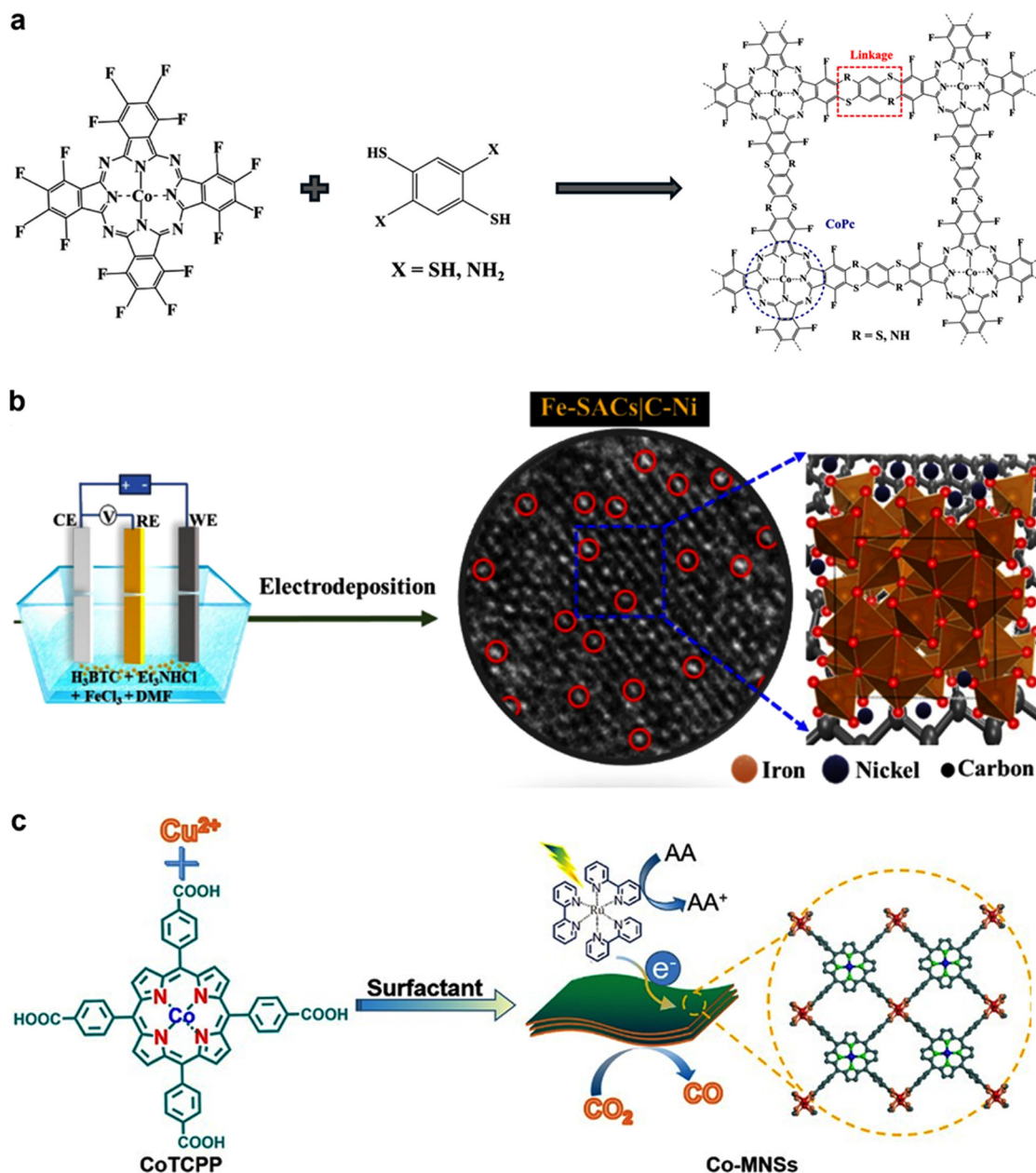
Fig. 5 Schematic of SAC synthesis strategies: (a) post-synthetic metallization for COF based SACs. Reproduced from ref. 96 with permission from American Chemical Society, copyright 2025. (b) Pre-synthetic electrodeposition for MOF based SACs. Reproduced from ref. 97 with permission from Royal Society of Chemistry, copyright 2024. (c) Surfactant-assisted MOF synthesis for atomic dispersion. Reproduced from ref. 98 with permission from Springer, copyright 2023.

One such method involves electrodeposition assisted MOF growth, where Fe SAs are deposited onto carbon-modified nickel nanosheets (C–Ni NS) through an electrochemical process (Fig. 5b).[97] In this approach, Fe^{3+} ions are reduced to Fe^{2+} in the presence of benzenetricarboxylate (BTC^{3-}), facilitating MOF formation directly on the electrode surface. This *in situ* coordination prevents metal clustering while enhancing metal–support interactions, leading to stable and efficient catalytic sites for HER and OER. This strategy has the potential to be a suitable approach for designing MOF SACs for CO_2RR. Another effective strategy employs surfactant-assisted SA incorporation, as demonstrated in the synthesis of ultrathin Co-MOF nanosheets (Fig. 5c).[98] In this example, polyvinylpyrrolidone acted as a structure-directing agent, selectively capping specific crystal planes and restricting growth in the lateral direction, resulting in well-defined two-dimensional MOF nanosheets with well-dispersed Co–N_4 SACs. This tailored morphology enhances the density of accessible catalytic sites while improving charge separation and CO_2 adsorption, resulting in a photocatalytic CO_2 to CO conversion rate of 7041 μmol g^{-1} h^{-1} with 86%

9640 | *Energy Environ. Sci.*, 2025, **18**, 9632–9712

This journal is © The Royal Society of Chemistry 2025

selectivity. The precise control over atomic dispersion and electronic structure achieved through these pre-synthetic methodologies drives the development of highly efficient and durable MOF-based SACs for electrochemical and photocatalytic CO_2 reduction.

2.3.2. Post-synthetic metalation

2.3.2.1. COFs. In the post-synthetic metalation approach, a well-defined COF is first synthesized, providing a porous and stable scaffold, and the metal species are subsequently introduced *via* methods such as impregnation, ion exchange, or electrochemical deposition. This method ensures precise control over metal loading while preserving the COF structural integrity. An example of this strategy is demonstrated in the synthesis and post-metalation of a nitrogen rich COF. The COF was constructed using 2,3,6,7,10,11-triphenylenehexamine and hexaketocyclohexane as precursors, forming a highly crystalline, layered conjugated structure (Fig. 6a).[99] Once the COF was successfully synthesized, Pt SAs were incorporated post-synthetically through an electrochemical deposition process in an acidic medium. This process enabled confinement of the Pt atoms within the nitrogen rich carbon framework, ensuring atomic-level dispersion. This post-metalation strategy significantly improved catalytic activity by optimizing electron transfer at the $Pt–N_2$ coordination sites. Additionally, the extended 2D conjugation of the COF enhanced charge transport, resulting in ultra-low overpotentials and high mass activity for the HER across different electrolytes. By leveraging post-synthetic metalation, this approach demonstrates the flexibility of COFs as tuneable platforms for SACs, where atomic-level control over metal anchoring can be achieved without disrupting the pre-formed framework. Beyond HER, post-synthetic metalation offers promising opportunities for tailoring COF–SACs for CO_2RR. For instance, host–guest post-modification strategies can be utilized to introduce CO_2RR-active metals such as Cu, Ni, and Fe onto pre-synthesized COFs. Functionalized COFs with nitrogen or oxygen rich moieties can serve as anchoring sites for these metals, facilitating uniform atomic dispersion while maintaining high stability under electrochemical conditions. Further, locking and post-metalation can modulate COF hydrophobicity/hydrophilicity, thereby tuning the local microenvironment for improved CO_2 adsorption and activation.[79]

2.3.2.2. MOFs. Post-synthetic modifications offer an effective route to introduce SACs into MOFs while preserving their porous framework. Unlike direct incorporation during MOF synthesis, post-synthetic methods enable precise control over atomic dispersion and electronic interactions, ultimately influencing the catalytic performance for CO_2RR. Various strategies have been employed to stabilize SAs within MOFs, including ligand coordination, defect engineering, metal node substitution, and pore confinement mechanisms.[100–103] These approaches prevent metal aggregation, optimize active site interactions, and maintain MOF structural integrity, thereby improving charge transfer and selectivity. By tailoring metal–supported coordination interactions and spatial confinement,
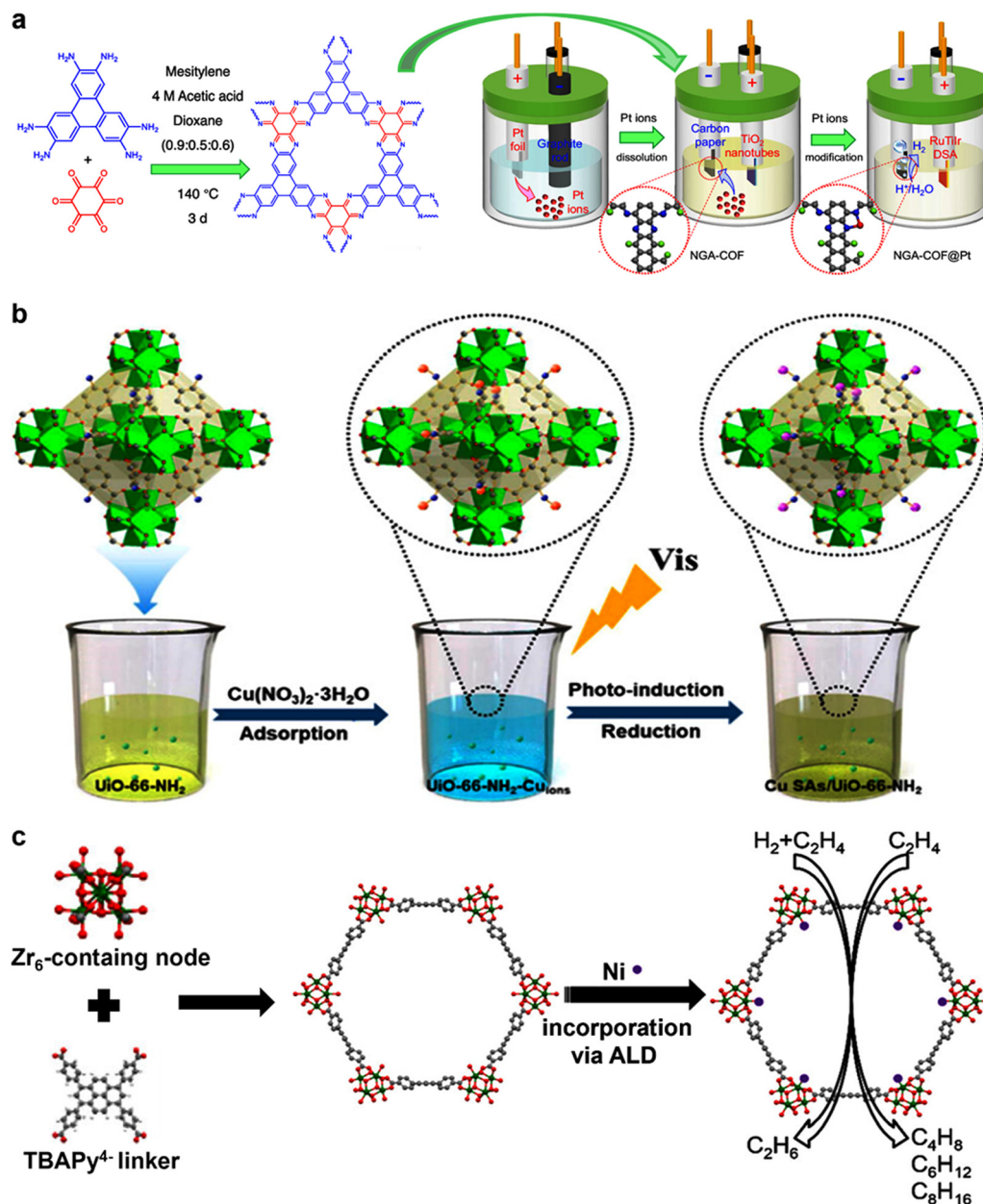
these strategies enable the development of highly efficient and durable catalysts.

Among these strategies, photo-assisted methods offer a distinct advantage by enabling mild and controlled synthesis conditions while maintaining the porous framework of MOFs. A representative example is the photoinduction method used to construct Cu SAs on UiO-66-NH_2, a MOF recognized for its superior CO_2 adsorption capacity (Fig. 6b).[104] In this approach, copper nitrate pentahydrate is introduced into a suspension of pre-synthesized UiO-66-NH_2, where the –NH_2 groups serve as coordination sites, capturing Cu precursors and ensuring their spatial confinement at the atomic level. Unlike conventional high-temperature pyrolysis methods that risk framework degradation and metal aggregation, visible-light irradiation is employed to anchor and stabilize Cu SAs, preserving the MOF structure while facilitating strong Cu–N coordination within the framework. This mild and controllable synthetic approach ensures better atomic dispersion, thereby optimizing the electronic environment of Cu SACs. The photoinduced interaction between Cu and N leads to a two-coordinate planar geometry, effectively stabilizing the Cu SAs. Moreover, this process modulates the electronic properties of the material, reducing the bandgap and enhancing charge separation efficiency, which is beneficial for CO_2RR. The optimized Cu SAs/UiO-66-NH_2 catalyst exhibits improved CO_2 activation, endorsing the formation of COOH* intermediates and selectively converting CO_2 into ethanol and methanol.

The photoinduction method provides a precise and energy-efficient approach for SAC fabrication by employing post-synthetic metalation combined with ligand-assisted stabilization. Its ability to maintain structural integrity while optimizing active sites makes it a promising strategy for developing high-performance MOF-SACs for CO_2RR. This approach exemplifies how tailored post-synthetic methodologies expand the design possibilities of MOF based catalysts, paving the roadmap for more efficient and sustainable CO_2 valorisation technologies.

2.3.2.3. Other methods. Atomic layer deposition (ALD) and chemical vapor deposition (CVD) facilitate precise control over the formation of SACs by enabling atomic-scale deposition and uniform dispersion of metal atoms onto various supports. ALD, known for its unique ability to deposit noble metals and metal oxides, ensures precise control over film uniformity and morphology, rendering it well-suited for large aspect ratio and porous architectures.[105] ALD involves sequential precursor adsorption, reaction, and purging steps, allowing fine-tuning of metal atom loading and dispersion. Despite its advantages, ALD requires specialized equipment and incurs high operative costs, limiting its widespread adoption. On the other hand, CVD enables the deposition of SACs through vapor-phase reactions at elevated temperatures, facilitating strong metal–support interactions and uniform dispersion. CVD is extensively applied in catalyst design for chemical transformations and energy applications due to its capability to tailor SAC properties at the atomic level.[106] While ALD- and CVD-derived SACs have been successfully employed in various catalytic processes, their direct application in COF and MOF based SACs for CO_2RR remains

This journal is © The Royal Society of Chemistry 2025

Energy Environ. Sci., 2025, **18**, 9632–9712 | **9641**

Fig. 6 Schematic representation of (a) the post-synthesis incorporation of SACs into COFs through electrodeposition. Reproduced from ref. 99 with permission from Nature, copyright 2024. (b) The post-synthesis SAC reduction on MOF through photo irradiation. Reproduced from ref. 104 with permission from American Chemical Society, copyright 2020. (c) Illustrative example to show SACs implantation on post-synthesis MOF using ALD. Reproduced from ref. 109 with permission from American Chemical Society, copyright 2016.

largely unexplored (Fig. 6c).[107–109] However, given their proven efficacy in fabricating highly stable and active SACs, these techniques hold significant potential for designing next-generation MOF and COF based SACs tailored for CO_2RR.

A facile gas-migration strategy has been developed to transform bulk metals directly into single atoms on a support, offering great potential for large scale production of single-atom catalysts (SACs).[110] In this approach, copper foam and ZIF-8 precursors are placed separately in a porcelain tube furnace. The ZIF-8 is pyrolyzed at 900 °C under an inert argon atmosphere, while ammonia gas is simultaneously introduced

through the system *via* the copper foil. Under these conditions, the strong Lewis acid base interactions between Cu atoms and NH_3 molecules lead to the formation of volatile $Cu(NH_3)_x$ species, which are ejected from the copper foam. These volatile Cu species are subsequently trapped by the defect-rich nitrogen moieties in the carbon support, forming atomically dispersed Cu single atoms on N-doped carbon (Cu-SA/N–C). This gas migration strategy has also been successfully applied to graphene oxide materials possessing abundant defect sites. The key principle of this method lies in the role of ammonia as a carrier gas that extracts Cu atoms from the bulk metal and

9642 | *Energy Environ. Sci.*, 2025, **18**, 9632–9712

This journal is © The Royal Society of Chemistry 2025

facilitates their chelation with nitrogen sites on the porous carbon. These nitrogen sites are generated *in situ* by the volatilization of Zn from ZIF-8 at high temperatures, leaving behind anchoring nodes for single-atom coordination. This innovative strategy opens new avenues for producing SACs directly from bulk metals, significantly advancing the scalability and industrial applicability of single-atom catalysts. Furthermore, the design methods, associated challenges, and future prospects of SACs are summarized in Table 1.

Building upon the discussion of synthesis methods, the strategic design of SACs and dual-atom catalysts (DACs) has significantly advanced CO_2RR by optimizing active site utilization and enhancing selectivity.[111–113] However, further improvements in catalytic performance require moving beyond a single variety of isolated metal centers. Multi-atom catalysts offer an advanced approach by incorporating atomically dispersed multimetallic sites or well-defined clusters, fostering synergistic interactions that can modulate electronic structures and reaction kinetics.[114] A carefully selected combination of SACs can effectively address the inherent limitations of individual catalysts. For example, Co and Fe-based SACs exhibit strong CO binding, which hampers CO desorption, whereas Ni-based SACs facilitate CO release but encounter high energy barriers for COOH formation.[75,115,116] To mitigate these challenges, DA and MA catalysts have been explored, leveraging cooperative effects between metal centers to enhance catalytic activity and efficiency. Although direct reports on multi-atom catalysts for CO_2RR remain scarce, studies in other catalytic transformations suggest that controlled nucleation and confinement strategies, such as those employed in MOFs and COFs, could be adapted for their rational design in CO_2RR.[93,117] Integrating insights from SACs and DACs, future research could strategically engineer multi-metallic atomic active centers within porous frameworks to achieve optimal stability, electronic properties, and reactivity, further advancing the prospects of electrochemical CO_2 conversion.

3. Characterization techniques

Characterization techniques are essential for the structural identification and detailed understanding of SACs, as these materials possess unique atomic-scale features that differ significantly from conventional catalysts.[118] Recent advances in electron microscopy, spectroscopy, and *in situ*/*operando* methods have provided deeper insights into the structure and behavior of SACs during catalytic processes.[119] These techniques help chemists analyze not only the atomic configuration but also the electronic properties, coordination environments, and dynamic interactions of SAs in catalytic systems.[120] SACs based on MOFs and COFs require precise characterization due to their atomic-scale dispersion and complex electronic structures. Various advanced *ex situ* and *in situ* techniques have been employed to analyze the structural, electronic, and catalytic properties of these materials, ensuring a comprehensive understanding of their CO_2RR performance.[121]

3.1. *Ex situ* techniques

Ex situ characterization techniques are crucial for gaining insight into the structural and electronic properties of MOF and COF-based SACs before and after catalytic reactions. Electron microscopic techniques such as high-resolution transmission electron microscopy (HRTEM) and aberration-corrected scanning transmission electron microscopy (AC-STEM) provide direct imaging of single metal atoms embedded in MOF and COF derived supports.[122] While HRTEM is widely used to

Table 1 SAC design methods, challenges and the future prospects

Method	Challenges	Future prospects
Direct pyrolysis	Metal aggregation at high temperatures	Improved precursor design with atom-trapping ligands
	Limited atomic control	Use of additives to prevent sintering
	Poor dispersion at high loadings	
Sacrificial and confined pyrolysis	Complex synthesis of templates	Scalable low-cost MOF/COF alternatives
	Scalability limited by precursor cost	Dual-template or hard–soft template combinations. Combination with 2D materials for enhanced exposure
	Multi-step fabrication. Restricted diffusion of reactants during catalysis	
Pre-synthetic metalation	Low thermal stability of frameworks	Introduction of new and potential linker and MOF/COF design for enhanced thermal and chemical robustness
	Limited to compatible metal–ligand systems	Controlled dual-metal SACs
Post-synthetic metalation	Weak coordination may lead to leaching	Creating suitable coordination environment of the metal centre with heteroatoms (for example N or P)
	Incomplete metal incorporation	Application in liquid-phase catalysis
ALD (vapor phase)	High cost and low throughput	Integration with batch ALD systems
	Requires specialized equipment	High-value device-level SAC design (*e.g.*, sensors, fuel cells)
	Not easily scalable	
CVD (vapor phase)	Metal aggregation at high temperature	Tunable gas-phase synthesis for batch-scale SACs
	Complex precursor control	Strong metal–support interaction engineering
	Limited substrate versatility	
Molten salt pyrolysis	Post-synthesis salt removal	Green salt systems (eutectics)
	Corrosive environment	High-throughput and template-free SAC synthesis
	Limited support compatibility	
Gas Migration strategy	Reactor design complexity	Scalable production using bulk metals
	Control over metal migration path and trapping	Broader application to various defect-engineered supports
	Ammonia safety concerns	

This journal is © The Royal Society of Chemistry 2025

Energy Environ. Sci., 2025, **18**, 9632–9712 | 9643

visualize morphology and atomic dispersion, AC-STEM with high-angle annular dark-field (HAADF) imaging enables atomic level resolution, offering a more precise identification of isolated SAs. The identification of SACs relies on the bright contrast features observed in HAADF-STEM images, which effectively distinguish them from the surrounding atoms of the support. This technique provides direct evidence for the presence of isolated metal atoms, confirming their dispersion without aggregation into clusters or nanoparticles.[123] Additionally, AC-HAADF-STEM intensity profiles offer valuable insights into the spatial distribution of these single atoms on the support matrix, further validating their uniform dispersion (Fig. 7a). However, distinguishing metal single atoms from other elements is challenging unless there is a significant difference in their atomic numbers. For example, NiIn SACs on MOF derived nitrogen-doped carbon

(NDC), AC-STEM imaging may struggle to differentiate Ni atoms from In (Fig. 7b).[124] To overcome this, the simplest approach is to apply electron energy lose spectroscopy (EELS) mapping assists in confirming the spatial distribution of SACs, ensuring their uniform dispersion (Fig. 7c and d). While HAADF-STEM imaging and EELS spectroscopy offer direct insights into SACs, their operation under high-energy electron beams can lead to structural degradation and unintended migration of metal atoms. To mitigate these challenges and ensure accurate characterization, experiments are often conducted at lower voltages and temperatures. In this context, low-temperature scanning tunneling microscopy (LT-STM) emerges as a more suitable technique for probing single atoms, as it allows for precise imaging without inducing structural alterations. As a representative example, LT-STM was employed to investigate Fe–N$_4$ centers embedded in a carbon
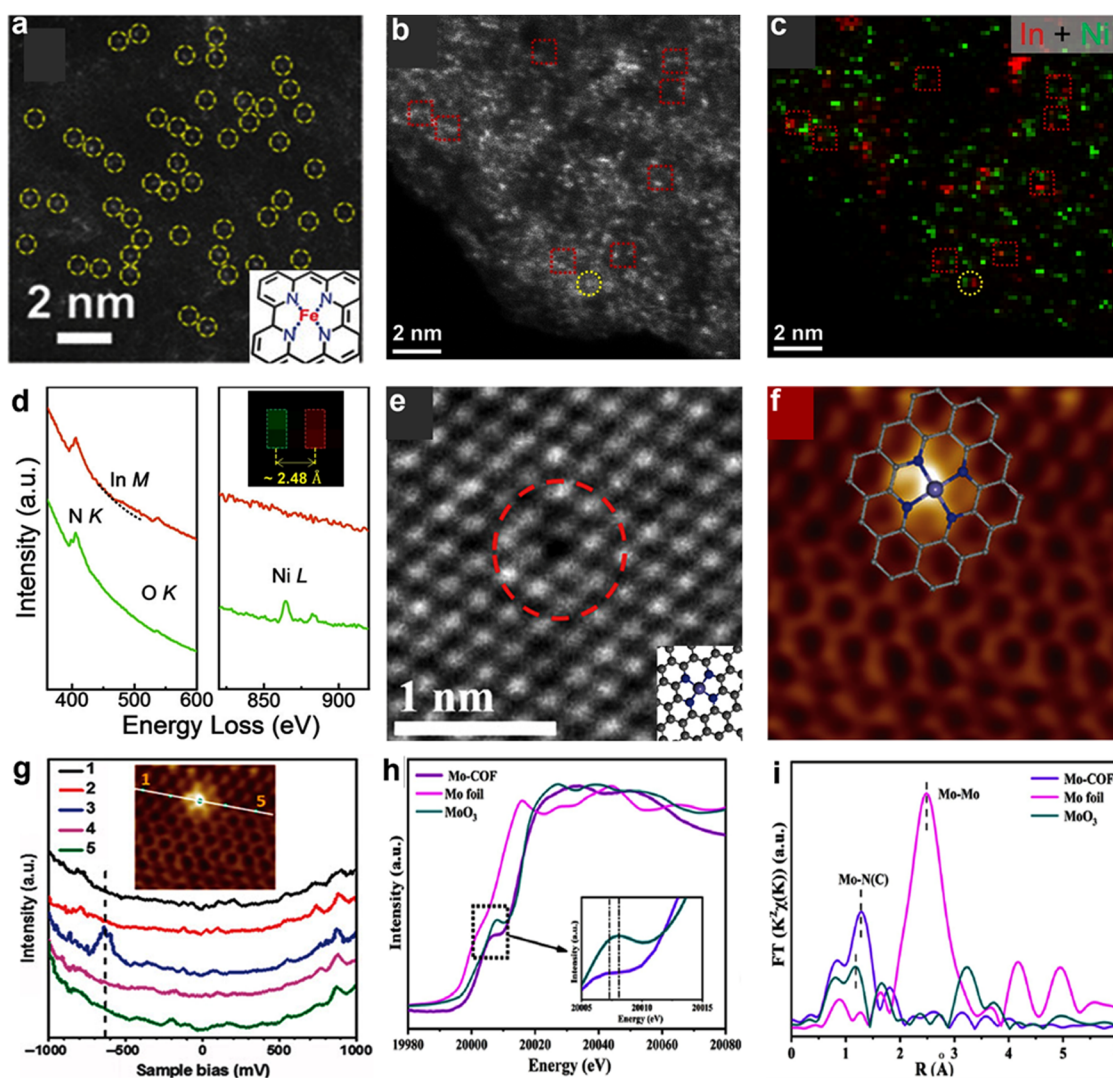

Fig. 7 (a) Identification of SACs using AC-STEM (inset: schematic of SAC structure). (b) HAADF image of dual atom catalysts, (c) EELS mapping distinguishing Ni and In atoms, (d) corresponding EELS spectra. Reproduced from ref. 124 with permission from Wiley, copyright 2023. (e) HRTEM image of Fe–N$_4$ site (inset: schematic of Fe–N$_4$), (f) LT-STM image of Fe–N$_4$, (g) dI/dV spectra along with line section shown in the inset. Reproduced from ref. 125 with permission from Science (CC-BY 4.0), copyright 2015. (h) EXAFS spectrum of Mo-COF, and (i) Fourier-transformed Mo K-edge EXAFS of Mo-COF compared to Mo foil and MoO$_3$. Reproduced from ref. 128 with permission from Elsevier, copyright 2021.

9644 | *Energy Environ. Sci.*, 2025, **18**, 9632–9712

This journal is © The Royal Society of Chemistry 2025

matrix, providing atomic-resolution imaging of the local environment (Fig. 7e–g).[125] The Fe center appeared as a bright spot, with adjacent carbon and nitrogen atoms exhibiting enhanced apparent height, indicating localized electronic enrichment caused by Fe incorporation. Furthermore, STM simulations corroborated the experimental images, confirming that the Fe–N$_4$ center modifies the density of states of nearby atoms, highlighting the power of LT-STM in resolving atomic structures and electronic properties of single-atom sites.

Spectroscopic techniques play a vital role in understanding the electronic structure and chemical interactions of SACs. X-ray photoelectron spectroscopy is commonly used to analyze surface chemical states and elemental composition.[126] However, for SACs, X-ray absorption spectroscopy (XAS) has emerged as a more powerful tool due to its ability to probe both the electronic configuration and local coordination environment at subatomic resolution. This makes XAS particularly advantageous in unraveling the structural and chemical identity of isolated metal sites, even in complex matrices like MOFs, COFs, or carbon supports. XAS, comprising XANES and extended EXAFS, provides subatomic resolution of electronic configurations. While XANES helps in identifying oxidation states and coordination geometries, EXAFS gives details on bond distances and coordination numbers.[127] For instance, in Mo-COF, XAS provided clear evidence confirming the atomic dispersion of Mo sites (Fig. 7h and i).[128] The Mo K-edge XANES spectrum showed that the absorption edge of Mo–COF closely matched MoO$_3$, indicating a +6 oxidation state (Fig. 7h). A slight shift in the pre-edge region indicated Mo coordination with nitrogen, rather than oxygen. Further, FT-EXAFS as shown in Fig. 7i revealed a primary peak at ~1.28 Å (Mo–N/Mo–C bond), with no detectable Mo–Mo peak, directly confirming isolated Mo atoms without clustering. Wavelet transform (WT) analysis supported this finding, showing a scattering signal at ~5.15 Å^{-1} (Mo–N/Mo–C), unlike Mo foil (Mo–Mo) or MoO$_3$ (Mo–O). This combined spectral evidence underscores the strength of XAS in identifying and characterizing SACs in COFs.

3.2. *In situ* characterization techniques

In situ characterization techniques are indispensable for elucidating the real-time structural, electronic, and chemical evolution of SACs based on MOFs and COFs during CO$_2$RR.[129] Traditional *ex situ* techniques only capture static snapshots before or after the reaction, leaving critical transient processes such as intermediate formation, active site restructuring, and dynamic coordination changes largely unexplored. In contrast, *in situ* tools bridge this gap, offering unprecedented mechanistic insights into how SACs dynamically adapt under realistic electrochemical conditions.[130]

3.2.1. *In situ* TEM. *In situ* transmission electron microscopy (TEM) has proven to be a reliable approach to directly monitor the dynamic evolution of SACs during synthesis, offering real-time insights into atomic rearrangements and dispersion processes under precisely controlled conditions. This technique is particularly valuable for MOF- and COF-derived SACs, where *in situ* environmental TEM (ETEM) enables the visualization of the
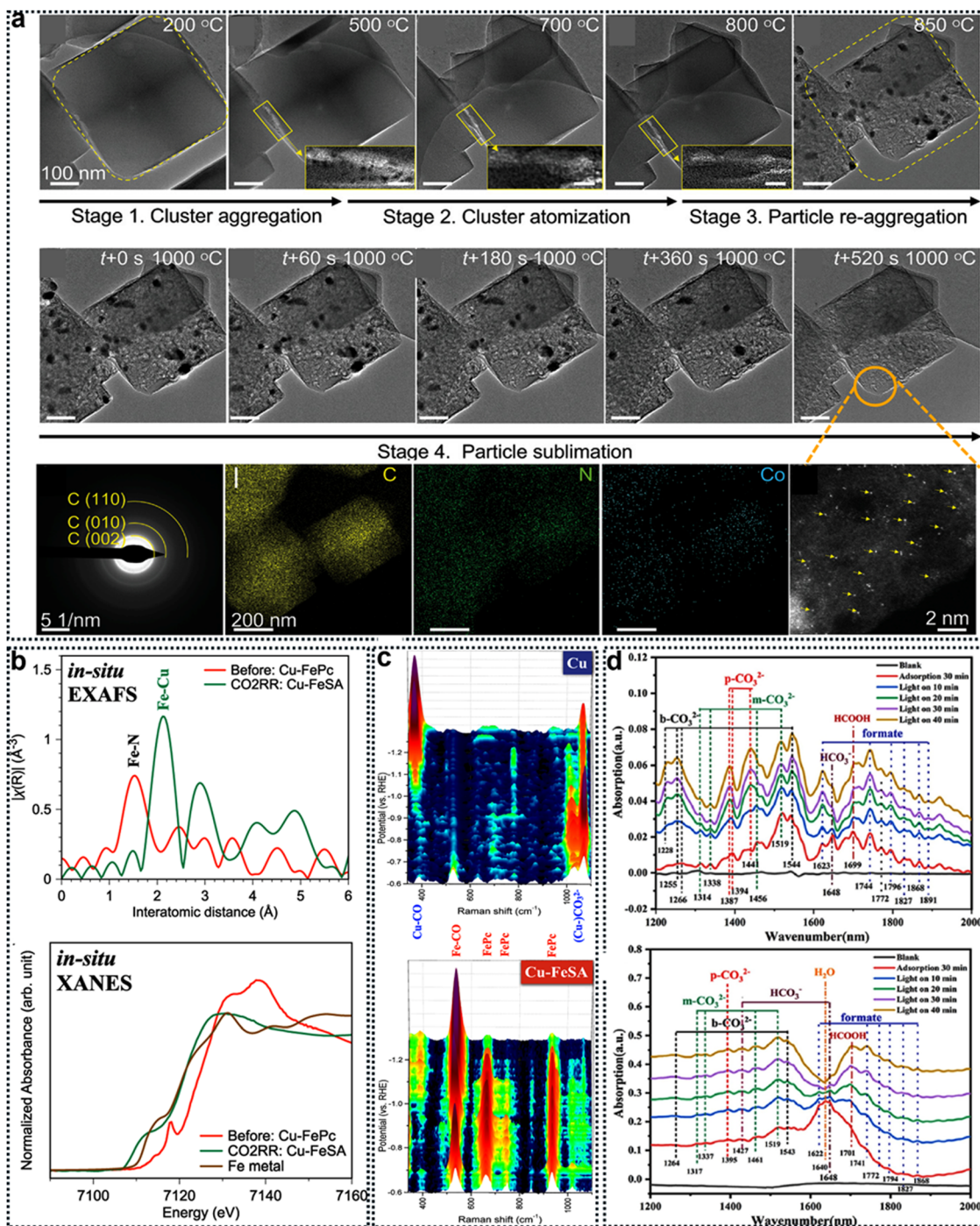
transformation from nanoparticles to isolated single atoms.[131] Such observations reveal key processes, including temperature-induced sintering and atomization, occurring simultaneously. For example, during the thermal conversion of Co nanoparticles supported on ZIF derived carbon, *in situ* TEM captured the gradual particle growth followed by rapid atomization at elevated temperatures as illustrated in Fig. 8a along with the corresponding EDS analysis.[132] These real-time insights not only clarify the underlying mechanisms governing SAC formation but also provide essential guidance for optimizing synthesis parameters to achieve uniform atomic dispersion.

3.2.2. *In situ* X-ray absorption spectroscopy. *In situ* XAS, including XANES and EXAFS, enables real-time tracking of oxidation states, coordination numbers, and bond distances, offering atomic-level resolution of dynamic structural changes.[133] To elucidate the structural and electronic transformations occurring in COF–SACs during CO$_2$RR, *in situ* XAS provides invaluable insights into atomic coordination environments and the oxidation state evolution of active sites under electrochemical conditions. For instance, when a negative bias was applied to a Fe-phthalocyanine (FePc)-modified COF system during CO$_2$RR, *in situ* Fe K-edge XAS revealed the progressive cleavage of Fe–N bonds, indicating the dissociation of Fe from its phthalocyanine ligand (Fig. 8b).[134] Simultaneously, a new Fe–Cu coordination environment was detected, signifying the *in situ* restructuring of FePc into Cu–Fe SA sites (Cu–Fe SA) supported on the COF-derived carbon matrix. EXAFS fitting confirmed the appearance of Fe–Cu metallic bonding with reduced coordination intensity compared to bulk Fe metal, reflecting the atomically dispersed nature of Fe within the copper framework. This structural evolution was accompanied by a shift in the Fe oxidation state, transitioning from a cationic Fe center in FePc to a metallic Fe state upon electroreduction. The dynamic coordination evolution captured by XAS demonstrated that the phthalocyanine ligand detaches from the surface as the Fe atom relocates into the Cu matrix, stabilizing Fe single atoms and preventing agglomeration. Such *in situ* structural reconstruction not only reveals how the local atomic environment evolves under operating conditions but also highlights the role of the COF host in preserving isolated active sites, which is essential for maintaining selectivity and stability during CO$_2$RR.

3.2.3. *In situ* Raman spectroscopy. Complementing the atomic-scale structural insights from XAS, *in situ* Raman spectroscopy further probes the chemical evolution of surface species, intermediate adsorption, and molecular transformations occurring during CO$_2$RR at COF–SAC interfaces.[135] Tracking the Raman spectra of the Cu–FePc precursor film under electrochemical polarization uncovered the gradual disappearance of vibrational signatures associated with the phthalocyanine ligand, particularly in the range of 660–935 cm^{-1}, indicating detachment of the macrocyclic ring as the potential shifts toward more negative values (Fig. 8c).[134] Concurrently, new peaks emerged, corresponding to the adsorption of *CO intermediates on both Fe and Cu sites, with Fe-bound *CO (Fe–CO stretch) exhibiting notably stronger intensity compared to Cu-bound *CO. This selective capture of CO intermediates at Fe sites highlights the preferential CO$_2$ activation and *CO

This journal is © The Royal Society of Chemistry 2025

Energy Environ. Sci., 2025, **18**, 9632–9712 | **9645**

Fig. 8 (a) *In situ* TEM images illustrating temperature and time-dependent molecular transformations during the formation of MOF-derived SACs. Reproduced from ref. 132 with permission from Wiley, copyright 2022. (b) *In situ* XAS analysis of Cu–Fe SACs under operando conditions during CO_2RR. (c) *In situ* Raman spectroscopy revealing the mechanistic evolution of the SAC environment during CO_2RR. Reproduced from ref. 134 with permission from Nature (CC-BY 4.0), copyright 2022. (d) *In situ* FT-IR spectroscopy demonstrating the real-time mechanistic interplay within the SAC environment during CO_2RR. Reproduced from ref. 128 with permission from Elsevier, copyright 2021.

stabilization at the newly formed Cu–Fe SA sites. Moreover, the evolution of surface-bound carbonates and formate species was tracked, providing direct evidence for the stepwise conversion of CO_2 at atomically dispersed Fe centers. Notably, the observed shift in the C≡O stretching vibration from Cu to Fe sites as the

reaction progressed demonstrated how the local atomic coordination dynamically governs the adsorption preference and intermediate transfer pathways. By correlating these spectral changes with applied potential and reaction time, *in situ* Raman not only captured the dynamic reconstruction of the catalyst

9646 | *Energy Environ. Sci.*, 2025, **18**, 9632–9712

This journal is © The Royal Society of Chemistry 2025

surface but also revealed the active participation of isolated Fe sites in driving CO_2 activation and selective intermediate conversion. Together, the combined insights from *in situ* XAS and Raman spectroscopy provide a realistic picture of how structural reconstruction, coordination evolution, and surface intermediate chemistry collectively dictate the catalytic performance of COF derived SACs in CO_2RR.

3.2.4. *In situ* Fourier-transform infrared spectroscopy. *In situ* FTIR has emerged as a powerful technique to uncover intermediate species and reaction pathways during CO_2 reduction on SACs, offering molecular-level insights under working conditions. By continuously flowing CO_2-saturated electrolytes across the electrode surface and monitoring the real-time evolution of surface species, this technique provides direct evidence of intermediate adsorption, transformation, and desorption.[136] For instance, in a recent study investigating atomically dispersed Mo sites embedded in COF, *in situ* FTIR revealed the sequential formation of carbonate species upon CO_2 adsorption, including monodentate (m-CO_3^{2-}) and bidentate carbonate (b-CO_3^{2-}), each exhibiting characteristic peaks in the region of 1200–1600 cm^{-1}.[128] As shown in Fig. 8d, the potential shifted toward more negative values, these species gradually evolved into format (HCOO*) and carboxyl (COOH*) intermediates, which were detected through their distinct vibrational signatures above 1600 cm^{-1}. Notably, the intensity and stability of the COOH* peak were found to directly depend on the local coordination environment of the Mo site, indicating that the SA center actively stabilizes this intermediate, a critical step for selective CO production. Additionally, time-resolved FTIR tracking under dynamic potential sweep conditions demonstrated that COOH* intermediates persisted longer at Fe sites compared to pristine carbon, underscoring the unique catalytic role of the atomic metal site in modulating intermediate binding strength. Beyond carbonates and carboxyl species, *in situ* FTIR also captured emerging peaks between 2800–3000 cm^{-1}, attributed to C–H stretching vibrations, signalling the onset of C_1 or C_2 hydrocarbon formation when protonation pathways became favourable. Such real-time spectroscopic monitoring enables a direct correlation between applied potential, surface species evolution, and product selectivity, providing crucial mechanistic insights into how SACs modulate CO_2 activation, intermediate stabilization, and product formation pathways. This comprehensive understanding helps rationally tune the electronic structure and coordination environment of SACs to enhance CO_2RR efficiency and selectively drive multi-carbon formation.

A combination of *ex situ* and *in situ* techniques is essential for characterizing MOF and COF derived SACs for CO_2RR applications. Electron microscopy techniques provide atomic-level structural insights, while spectroscopic methods reveal electronic and chemical properties.[137] *In situ* techniques further enhance understanding by tracking dynamic changes during catalytic reactions, offering valuable insights for designing efficient CO_2RR catalysts.[138] Future studies should focus on integrating multiple characterization techniques to leverage their complementarities and to achieve a more comprehensive understanding of SAC functionalities.[139]

4. Applications of COF and MOF-based/derived SACs for catalytic valorisation of CO_2

4.1. Factors influencing CO_2 conversion on MOF and COF based/derived SACs

The conversion of CO_2 into valuable chemicals and fuels is a crucial strategy for mitigating climate change and reaching carbon neutrality. Among the various types, SACs show promising activity and selectivity.[140–143] Although various carbon and nitrogen sources have been used as platforms for preparing the SACs, MOFs and COFs have emerged as promising platforms due to their high surface area, tunable porosity, and well-defined active sites. Thus, MOF-based SACs present a highly promising avenue for CO_2RR, bridging the gap between molecular catalysts and heterogeneous electrocatalysts with unprecedented control overactive site architecture. Nevertheless, CO_2 conversion efficiency on these SACs is governed by a range of multifaceted factors. In the following section, we assess the critical parameters that dictate the catalytic performance of MOF and COF-derived SACs for CO_2 transformation.

Initially, MOFs were used to produce highly conductive N-doped carbon materials through high-temperature annealing, as MOF-derived carbon exhibits greater efficiency than the original MOF under harsh conditions. This approach also helps mitigate disadvantages related to stability and reactivity in such an environment.[144] However, the presence of metal ions is more important for enhancing the catalytic rate. Since MOFs contain abundant N-ligands, they transform into N-doped carbon during pyrolysis, where the N-ligands act as an anchor, stabilizing metal atoms *via* metal–N coordination bonds. This stabilization leads to the formation of desired active sites for synthesizing various MOF derived SACs.[144,145] The CO_2 conversion efficiency of MOF and COF derived SACs depends on various intrinsic factors, such as the modulation of the active sites and morphology as well as extrinsic properties, including metal coordination environments, electronic structures, porosity, and reaction conditions.[146]

CO_2 conversion by MOF derived SACs can be achieved through various methods, including thermochemical, electrochemical, photochemical, and other approaches, each with unique advantages and challenges. Thermochemical CO_2 reduction involves high-temperature catalytic processes, such as the hydrogenation of CO_2 to methanol or hydrocarbons *via* Fischer–Tropsch synthesis. This method often requires metal-based catalysts like Cu, Fe, or Ru to drive the reaction efficiently. Electrochemical CO_2 reduction (eCO_2R) utilizes renewable electricity and electrocatalysts to convert CO_2 into valuable products such as carbon monoxide, formate, and hydrocarbons. Catalysts for eCO_2R range from molecular complexes to nanostructured metals and single-atom catalysts.[147] Photochemical CO_2 reduction, on the other hand, mimics natural photosynthesis by using semiconductor photocatalysts (*e.g.*, TiO_2, perovskites, and MOF) to capture solar energy and drive CO_2 conversion into chemicals like methane or methanol and so on. Each of these methods presents distinct challenges-thermochemical methods

require high energy input, electrochemical approaches face selectivity and stability issues, photochemical systems suffer from low quantum efficiency, and biochemical strategies require careful control of biological activity. Future advancements in catalyst design, reactor engineering, and process integration are essential to improve efficiency and scalability for industrial CO_2 utilization.

4.2. Electrocatalytic reduction of CO_2: fundamentals and mechanisms

Electrocatalytic CO_2 reduction reaction (eCO$_2$RR) is an effective strategy for reducing carbon emissions, while simultaneously generating chemicals and fuels. This process involves converting CO_2 into reduced C_1–C_n carbon products using renewable electricity, typically in aqueous or non-aqueous electrolytes.[147] The efficiency and selectivity of eCO$_2$RR largely depend on the choice of catalysts, which can range from homogeneous to heterogeneous materials, including transition metal catalysts, SACs, hybrid catalysts, and MOFs. Additionally, the integration of *operando* spectroscopy and computational modeling has provided deeper insights into reaction mechanisms, enabling the rational design of improved electrocatalysts. Furthermore, coupling eCO$_2$R with renewable hydrogen sources or co-electrolysis with other sustainable materials could enhance both sustainability and economic feasibility. Despite these advancements, challenges such as high overpotentials, the competing hydrogen evolution reactions, and limited catalyst durability must be addressed for large-scale applications. The development of innovative catalytic materials, electrolyte engineering, and system-level optimization are crucial steps toward realizing the industrial implementation of eCO$_2$R as a sustainable carbon utilization technology.

The eCO$_2$RR is a complex multi-step process that involves the activation of CO_2 and its subsequent conversion into various C_1 products such as CO, formate, methane, and methanol, as well as C_2 products such as ethylene, ethanol, and acetic acid (Fig. 9).[147–153] The reaction occurs at the electrode–electrolyte interface, where CO_2 molecules are adsorbed onto the catalyst surface and undergo electron transfer, protonation, and bond rearrangements. The efficiency and selectivity of CO_2RR depend on several factors, comprising the choice of catalyst, applied potential, electrolyte composition, and reaction conditions. The mechanism generally begins with the activation of CO_2, which is thermodynamically stable and requires an initial electron transfer to generate the $CO_2^{\bullet-}$ radical anion. This intermediate can follow different pathways depending on the catalyst and reaction conditions. For instance, on transition metal catalysts like gold (Au) and silver (Ag), $CO_2^{\bullet-}$ can be protonated to form adsorbed CO as a key intermediate. Depending on the intermediate binding energy, CO either desorbs from the catalyst surface, undergoes further reduction if the active sites have a sufficient binding affinity, or poisons the catalyst due to excessively strong binding. The electrochemical reduction of CO_2 on single-atom catalysts happens through several proton-coupled electron transfer steps. Like on Au or Ag, the CO_2 molecule attaches to the single metal atom, forming a bent M–CO$_2$H

intermediate that is stabilized by metal–carbon interaction. This activation step is needed for further reduction. With continuous electron and proton transfers, CO or other products are formed. The selectivity of SACs depends on how strongly the intermediates (especially *COOH and *CO) bind and on the metal atom's coordination environment. For example, Cu-based catalysts, which have intermediate binding affinity for CO, facilitate further proton-electron transfer steps, leading to C–C coupling and the formation of hydrocarbons for example ethylene and ethanol. The unique ability of Cu to stabilize CO and promote its dimerization is critical for the formation of C_{2+} products. Another important reaction pathway is the direct protonation of $CO_2^{\bullet-}$ to formate, which is favoured in metals like Sn, Pb, and Bi. These catalysts stabilize the HCOO* intermediate, preventing its further reduction to CO or hydrocarbons. Similarly, the intermediate binding affinity of CO without dimerization leads to further reduced C_1 products such as methane and methanol, which are typically dictated by the catalytic active site. Competing side reactions, particularly the hydrogen evolution reaction (HER), often reduce the efficiency of CO_2RR. Suppressing HER is vital for improving the FE toward CO_2 reduction products. Strategies such as electrolyte engineering, catalyst surface modification, and pH optimization help enhance CO_2RR selectivity by tuning the reaction environment. Understanding the mechanistic pathways of CO_2RR is essential for developing next-generation catalysts that can drive the reaction with higher efficiency, selectivity, and durability, paving the way for the sustainable usage of CO_2 as a feedstock for fuels and chemicals. In the following sections, the synthetic methodology used to design various coordination structures and the effect of local structure on CO_2RR will be discussed.

4.2.1. Factors affecting the performance of SAC.
The effectiveness of SACs in CO_2RR arises from a synergistic optimization of metal choice, atomic structure, electronic tuning, support engineering, intermediate binding, reaction conditions, and stability strategies. Careful control of these parameters is essential to achieve high activity, selectivity, and durability for practical CO_2 conversion. The type of metal atom (*e.g.*, Ni, Fe, Co, Cu) directly affects the adsorption and activation of CO_2 as well as the binding strength of key intermediates. For example, Ni and Fe SACs are highly selective for CO, whereas Cu SACs can facilitate further reduction to hydrocarbons or multi-carbon products due to their unique *CO binding energy. Likewise, the number and type of coordinating atoms (N, O, S, or P) influence its electronic environment and reactivity. Classic M–N$_4$ structures favour CO production, while mixed coordination environments (*e.g.*, M–N$_3$S, M–N$_2$O$_2$) allow fine-tuning of activity and selectivity by altering electron density and local geometry around the active site. Moreover, the d-band center and overall charge distribution of the single-atom site govern how strongly it binds CO_2 and intermediates. Optimal electronic properties help achieve the right balance between activation of CO_2 and easy desorption of products like CO. The catalyst support also plays a crucial role in stabilizing the single metal atom and enabling efficient charge transfer. Carbon-based supports (*e.g.*, N doped carbon) with or without defect sites enhance the
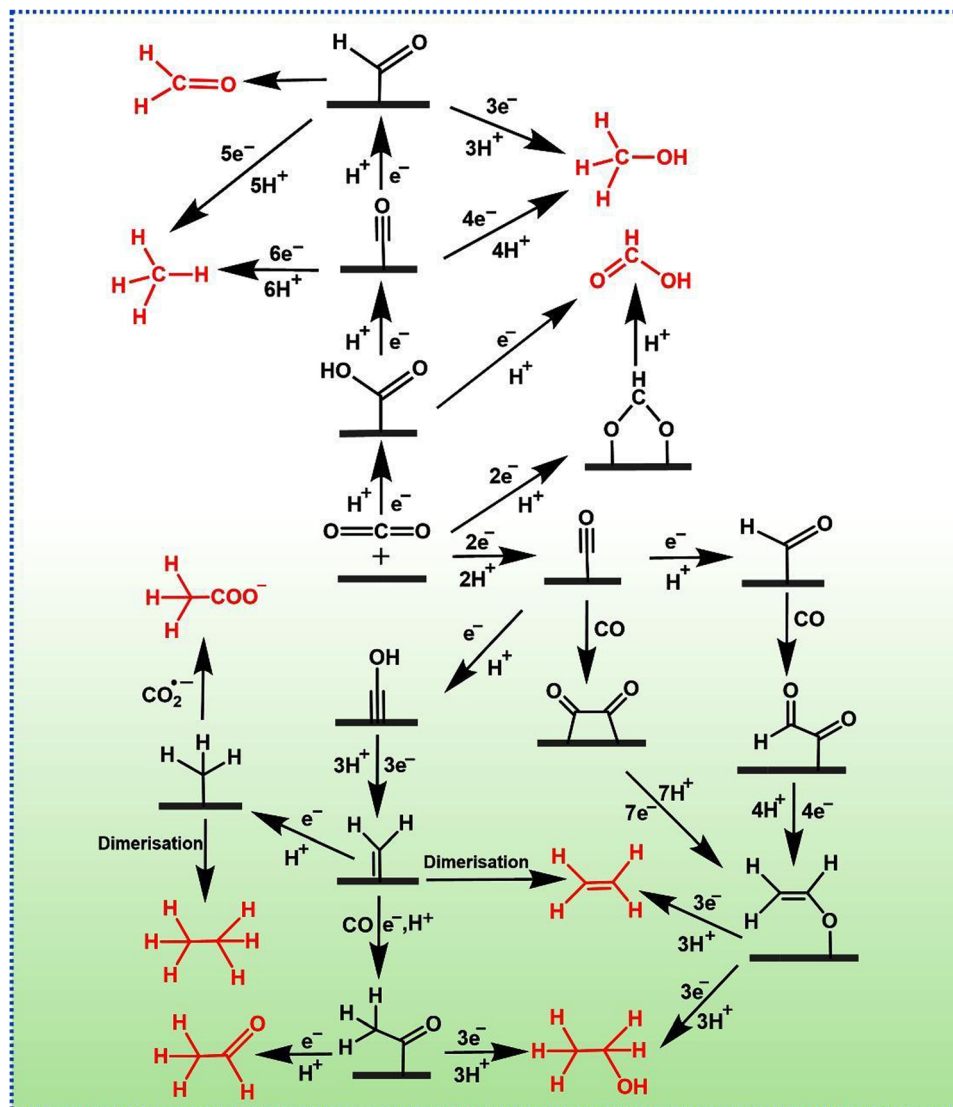
9648 | *Energy Environ. Sci.*, 2025, **18**, 9632–9712

This journal is © The Royal Society of Chemistry 2025

Fig. 9 General mechanism and strategy for C_1 products: (a) General mechanism for CO_2RR to C_1 products. (b) General mechanism for CO_2RR to C_2 products.

interaction between CO_2 and the active metal center. The adsorption strength of intermediates, especially *COOH and *CO, is critical for controlling both reaction rates and selectivity. A strong binding to *COOH aids CO_2 activation, but the *CO intermediate must bind moderately so that it can either desorb as CO or undergo further reduction. The electrolyte composition, pH, applied potential, and the presence of co-ions or additives can all affect the energy landscape of the CO_2RR pathway. For instance, alkali metal cations (K^+, Cs^+) can stabilize charged intermediates, while pH influences proton availability for proton-coupled electron transfer steps. The ability of SACs to maintain atomically dispersed active sites during reaction is essential. Agglomeration of single atoms into nanoparticles can drastically alter selectivity and reduce performance. Strong metal–support interactions and proper coordination design help enhance stability under operational conditions. The following section mainly discusses the role of ligands in modulating the activity and selectivity of the SACs.

4.2.2. Modulation of the active site. In SACs, the nature of the metal center and its coordination environment play a pivotal role in determining electronic properties, catalytic activity, and stability. These factors influence activation barriers, charge distribution, and electron transfer efficiency, all of which directly impact CO_2 reduction performance. Focusing solely on the metal content provides an incomplete understanding of SAC behavior; instead, a comprehensive analysis must consider the local coordination environment to accurately interpret catalytic activity, selectivity, and durability. The ligand environment surrounding the metal center strongly affects its electronic structure, thereby modulating CO_2 activation and reactivity. Coordination numbers directly influence charge distribution and electron transfer, shaping the reaction pathway toward specific products such as CO, hydrocarbons, or oxygenates. The strength of metal–ligand interactions is also crucial, as robust coordination bonds prevent metal leaching and catalyst deactivation under electrochemical conditions.

This journal is © The Royal Society of Chemistry 2025

Energy Environ. Sci., 2025, **18**, 9632–9712 | **9649**

By precisely tuning the electronic and geometric structure of the active site, catalytic performance can be optimized. Ligand field engineering modifies the d-band electronic states, affecting CO_2 adsorption and activation pathways, while the introduction of heteroatoms near the metal site can regulate charge density, enhancing selectivity and reaction rates. Additionally, the dynamic restructuring of metal sites under reaction conditions can generate more active and resilient catalytic centers. Synergistic interactions between metal atoms and organic linkers further improve stability and prevent catalyst degradation. The coordination environment defines the immediate atomic arrangement surrounding each metal atom, specifying which atoms (e.g., nitrogen, carbon, oxygen, sulfur) are directly bonded to the metal and their spatial arrangement. This structure dictates the formation of different SAC active sites, such as $M-N_4$, $M-N_2O_2$, or $M-N_3S$, each exhibiting distinct catalytic properties. In the following sections, the key factors influencing CO_2RR performance will be discussed, along with how synthetic strategies enable structural tunability to achieve high selectivity and efficiency (Table 2).

4.2.3. Nitrogen coordinated SACs. SACs have emerged as a promising platform for CO_2 conversion due to their atomically dispersed active sites, which maximize catalytic efficiency and selectivity. However, their practical application is often hindered by metal aggregation and instability under operational conditions. To address these challenges, precise heteroatom doping plays a crucial role in modulating both the electronic and geometric structures of SACs, optimizing catalytic pathways for enhanced CO_2 electroreduction. Compared to conventional bulk-incorporated Ni–N catalysts, a surface-confined approach significantly improves the accessibility, stability, and reusability of single-atom active sites, making them more viable for scalable applications. A notable example is the synthesis of Ni SACs using a MOF template. This process involves confining nickel ions within the MOF porous network, followed by pyrolysis to generate a nitrogen-doped carbon (NDC) structure with atomically dispersed Ni sites. The resulting catalyst exhibits a highly porous architecture, ensuring optimal interaction with reactants and enhanced stability of active sites. This Ni SAC demonstrates superior electrocatalytic performance, achieving a FE of 71.9% for CO (as denoted in eqn (1)) production at -0.9 V vs. RHE, outperforming conventional nickel nanoparticle catalysts (Fig. 10a–c). The precise atomic dispersion of Ni, coupled with nitrogen coordination, enhances CO_2 activation while minimizing side reactions such as hydrogen evolution. These advancements highlight the potential of MOF-derived SACs as a scalable and efficient solution for sustainable CO_2 electroreduction.[154]

$$CO_2 + 2H^+ + 2e^- \rightarrow CO + H_2O \quad -0.117 \text{ V vs. RHE} \quad (1)$$
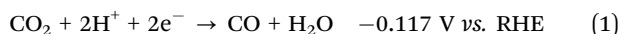
Designing isolated and uniformly coordinated SACs remains a significant challenge, as high-temperature synthesis often leads to atom aggregation. To overcome this, Yifan Ye et al. exploited a surface functionalization strategy to synthesize $Fe-N_4$ electrocatalysts using zeolitic imidazolate framework-8 (ZIF-8) and ammonium ferric citrate (AFC). By selectively confining Fe–N sites on the surface of MOF-derived carbon structures, this approach ensures a high density of accessible active sites simultaneously preventing metal aggregation, resulting in superior catalytic activity. The synthesized C-AFC@ZIF-8 catalyst demonstrates exceptional electrochemical performance, achieving a CO FE of 93.0% at -0.43 V vs. RHE, significantly outperforming conventional Fe–N–C catalysts. Spectroscopic analyses confirm that the Fe centers predominantly adopt a porphyrinic $Fe-N_4$ coordination environment, which optimally modulates electronic properties and enhances *COOH intermediate stabilization. Furthermore, DFT calculations illustrate that the $Fe-N_4-OH$ coordination effectively tunes charge distribution, improving CO_2 binding affinity and catalytic efficiency.[155] Likewise, Tran Ngoc Huan et al. used phenanthroline and iron salts with ZIF-8 as a source to make Fe–N–C materials for CO_2 electroreduction to CO. By tuning the FeN_4-to-Fe nanoparticle ratio, they controlled the CO/H_2 product ratio for syngas production, which is vital for tailoring the gas mixture for various downstream applications. By controlling the ratio of catalytically active $Fe-N_4$ sites to less selective Fe nanoparticles, the materials enriched with $Fe-N_4$ sites exhibited high FE for CO exceeding 90% at a relatively low overpotential of -0.6 V vs. RHE with a current density of 4.5 mA cm^{-2}.[156]

Yang et al. present a novel strategy for creating surface-enriched nickel single-atom catalysts (SAs) using thermal atomization of Ni NPs supported on NDC supports (SE–Ni SAS@PNC). This top-down approach facilitates high atom utilization on the catalyst surface. Through the annealing, the strong interaction between Ni nanoparticles and the N-doped carbon support causes the Ni nanoparticles to decompose, leading to the stabilization of atomically dispersed Ni atoms on the carbon surface. The progressive decomposition of Ni NPs ultimately results in their atomization. The SE–Ni SAS@PNC catalyst exhibits high FE over 90% in the potential range -0.6 to -1.0 V and at -0.9 V, the partial current density reaches to 16.42 mA cm^{-2}.[157] Unlike the physically absorbed iron in the pores of ZIF, the mixed metallic MOFs (ZIF-8) stabilize Fe dispersion in precursors through covalent bonding between Fe ions and 2-methylimidazole, where Fe ions are in the nodes. During annealing to produce M–N–C catalysts, Zn acts as a spacer, dispersing Fe to prevent the formation of metallic clusters. Using this strategy, Pan and co-workers achieved a high CO FE of 93% using single atomic $Fe-N_4$ catalysts. Using DFT studies, they found that edge-hosted $M-N_{2+2}-C_8$ moieties bridging two adjacent armchair-like graphitic layers act as better catalysts than that of usually proposed bulk-hosted $M-N_4-C_{10}$ site implanted within a graphitic layer (Fig. 10d).[158] Similarly, the precise control over the local atomic structure of Cu active sites was tested, specifically, by creating edge-hosted $Cu-N_4$ sites within micropores between graphitic layers ($Cu-N_4C_8$) compared to bulk-hosted $Cu-N_4$ sites ($Cu-N_4C_{10}$). The researchers synthesized Cu–N–C catalysts with varying Cu precursor amounts to precisely control the density of $Cu-N_4$ sites and tune their local atomic arrangement and overall electronic structure (Fig. 10e–h). The edge-hosted $Cu-N_4C_8$ shows higher surface area and enhanced active sites that exhibited 96% FE_{co} at -0.8 V vs. RHE with a current density of -8.97 mA cm^{-2}. Whereas bulk-hosted $Cu-N_4C_{10}$ lacked the distinct micropore

9650 | Energy Environ. Sci., 2025, **18**, 9632–9712

This journal is © The Royal Society of Chemistry 2025

Table 2 The key factors influencing CO_2 reduction reaction (CO_2RR) performance to achieve high selectivity and efficiency

Electrocatalyst	Electrolyte	Potential (V)	Product	FE (%)	Ref.
M–N$_4$ SAC					
Ni SAs/N–C	0.5 M KHCO$_3$	−0.89	CO	71.9	145
C-AFC©ZIF-8 (Fe–N)	1.0 M KHCO$_3$	−0.43	CO	93	146
Fe–N–C	0.5 M NaHCO$_3$	−0.6	CO	90	147
SE-Ni SAs@PNC	0.5 M KHCO$_3$	−0.7 to 1.2	CO	90	148
Fe–N$_{2+2}$–C$_8$	0.5 M KHCO$_3$	−0.58	CO	93	149
Cu–N$_4$C$_8$	0.1 M KHCO$_3$	−0.8	CO	96	150
Co–N$_4$	0.1 M KHCO$_3$	−0.8	CO	82	152
Ni SAs/NCNTs	0.5 M KHCO$_3$	−0.9	CO	97	153
Ni–N–C	0.5 M KHCO$_3$	−0.8	CO	96.8	153
Ni–N–C	0.5 M KHCO$_3$	−0.66 to −0.96	CO	100	154
Fe–N$_4$	0.1 M KHCO$_3$	−0.8	CO	90	155
Cu–N$_4$–C/1100	0.1 M KHCO$_3$	−0.9	CO	98	156
Fe–N–C900	0.1 M KHCO$_3$	−1.2 V (V Ag/AgCl)	CO	86.8	157
Fe–N–C-1000	0.5 M KHCO$_3$	−0.9	CO	100	158
Ni–N/C@900	0.1 M KHCO$_3$	−0.76	CO	90	159
M–Ni–N–C-2/CNTs	0.1 M KHCO$_3$	−0.7	CO	98	160
Pyrrolic *vs.* Pyridinic					
Ni SAC-1000	0.5 M KHCO$_3$	−0.8	CO	98.2	161
Cu-SA/NPC	0.1 M KHCO$_3$	−0.36	CH$_3$COCH$_3$	36.7	162
Fe^{3+}–N–C	0.5 M KHCO$_3$	−0.2	CO	>80	163
Ni–N$_3$–C	0.5 M KHCO$_3$	−0.75	CO	99.37	164
Ni–N$_{Pyrrolic}$–C	0.5 M KHCO$_3$	−0.85 V	CO	92	165
Low-coordinate SACs					
C–Zn$_1$Ni$_4$ ZIF-8	1 M KHCO$_3$	−0.83	CO	98	166
Co–N$_2$	0.5 M KHCO$_3$	−0.68	CO	94	167
Cu–N–C-900	0.1 M KHCO$_3$	−1.6	CH$_4$	38.6	168
NiSA–N$_2$–C	0.5 M KHCO$_3$	−0.8	CO	98	82
Ni–N$_3$–C	0.5 M KHCO$_3$	−0.65	CO	95.6	169
MS-L-Ni–NC (Ni–N$_3$–C)	0.5 M KHCO$_3$	−0.8	CO	98.7	170
Fe/Ni–N–C	0.5 M KHCO$_3$	−0.677	CO	92.9	171
Ni–NC–NS (Ni–N$_2$–C)	0.5 M KHCO$_3$	−1.0	CO	86	172
Ni–N$_3$/NC	0.1 M KHCO$_3$	−1.3	CO	94.6	173
Axially coordinated SACs					
Fe-SA/ZIF (Fe–N5)	0.1 M KHCO$_3$	−0.7	CO	98	174
Ni–N$_4$–O/C	0.5 M KHCO$_3$	−0.9	CO	100	175
Carbon coordinated SACs					
Co–N$_2$–C$_3$	0.1 M KHCO$_3$	−0.8	CO	92	176
Co–C$_2$N$_2$	0.1 M KHCO$_3$	−0.8	CO		177
Ni–N$_1$–C$_3$	0.5 M KHCO$_3$	−0.9	CO	97	178
Oxygen coordinated SACs					
Fe$_1$N$_2$O$_2$/NC	0.1 M KHCO$_3$	−0.5	CO	99.7	179
FeN$_2$O$_2$/NC	0.5 M KHCO$_3$	−0.7	CO	95.5	180
Sulphur coordinated SACs					
Co–S$_1$N$_3$	0.5 M KHCO$_3$	−0.5	CO	98	181
MnN$_3$S$_1$	0.5 M KHCO$_3$	−0.45	CO	70	182
Ni–NSC	0.5 M KHCO$_3$	−1.035	CO	98	183
Phosphorous coordinated SACs					
Ni-SA/CN-P	0.5 M KHCO$_3$	−0.8	CO	96.9	184
Ni–P$_1$N$_3$	0.5 M KHCO$_3$	−0.75	CO	98	185
Halogen coordinated SACs					
Ni$_1$–N–C (Cl)	0.5 M KHCO$_3$	−0.7	CO	94.7	187
NiN$_4$Cl–ClNC	0.5 M KHCO$_3$	−0.7	CO	98.7	188
Ni–NBr–C	0.5 M KHCO$_3$	−0.7	CO	97	189
FeN$_4$Cl/NC	0.5 M KHCO$_3$	−0.6	CO	90.5	190
P-block metal SACs					
In$^{\delta+}$–N$_4$	0.5 M KHCO$_3$	−0.95	HCOOH	96	191
In–N–C	0.5 M KHCO$_3$	−0.99	HCOOH	80	192
InA/NC	0.5 M KHCO$_3$	−2.1 *vs.* Ag/Ag$^+$	CO	97.2	193
In-SAC-1000	0.5 M KHCO$_3$	−0.6	CO	97	194
Bi SAs/NC	0.1 M NaHCO$_3$	−0.5	CO	97	195
Al–NC	0.1 M KHCO$_3$	−0.65	CO	98.76	196
SnN$_3$O$_1$	0.1 M KHCO$_3$	−0.7	CO	94	197
Hetero-metal SACs					
NiCu-SACs/N–C	0.5 M KHCO$_3$	−0.6	CO	92.2	198
Co$_{0.5}$Ni$_{0.5}$–N–C	0.5 M KHCO$_3$	−0.5 to −1.1	CO	50 ± 5	199
Ni–Al NC	0.1 M KHCO$_3$	−0.8	CO	98	200
Cu–In–NC	0.1 M KHCO$_3$	−0.7	CO	96	201
Ni/Fe–N–C	0.5 M KHCO$_3$	−0.7	CO	98	202
NiN$_3$©CoN$_3$–NC	0.1 M KHCO$_3$	−1.1	CO	97.7	203

Table 2 (continued)

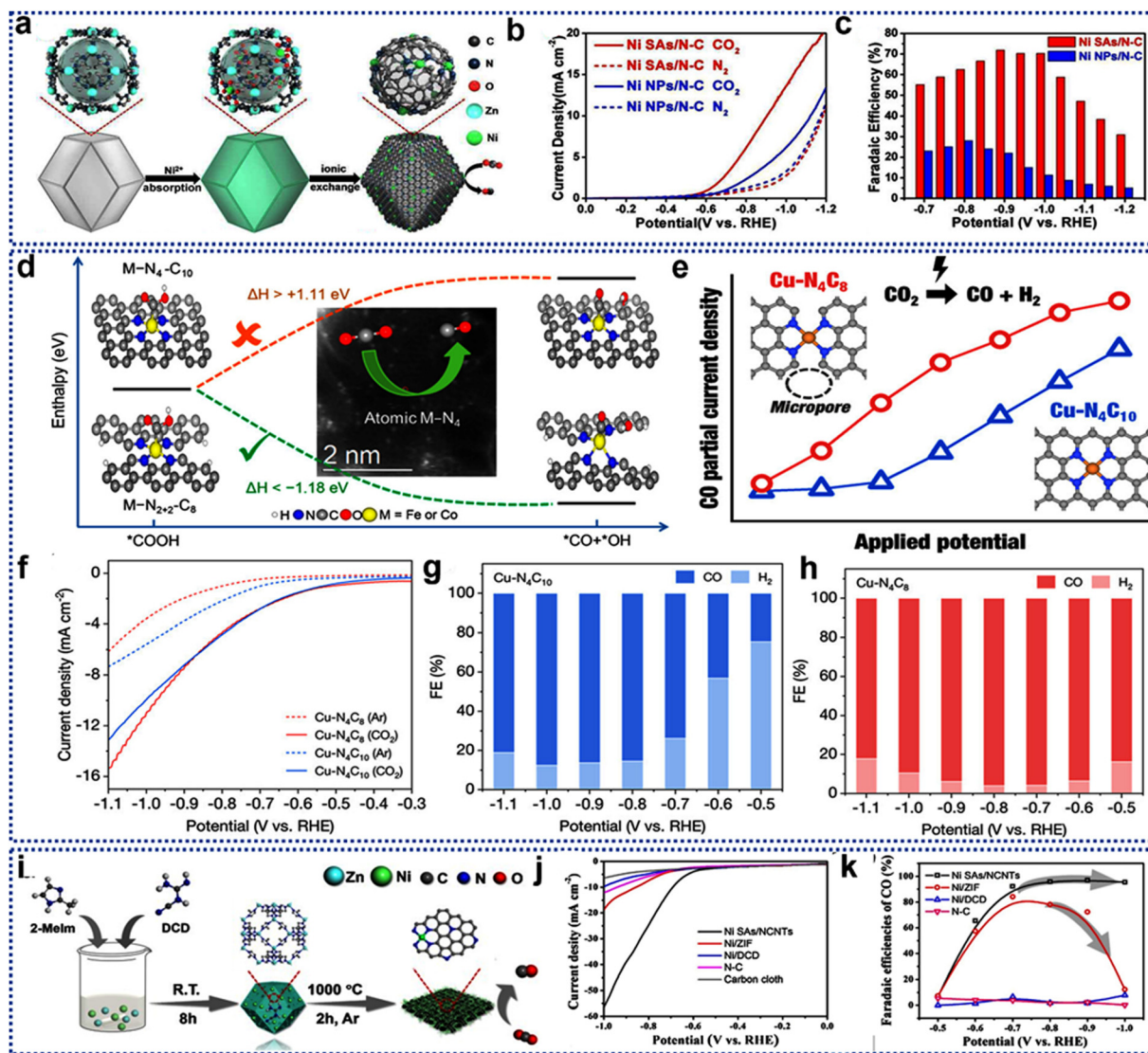| Electrocatalyst	Electrolyte	Potential (V)	Product	FE (%)	Ref.
Ni/Cu–N$_6$–C	0.5 M KHCO$_3$	−0.6	CO	97.7	204
Ni–N$_3$/Cu–N$_3$	0.5 M KHCO$_3$	−1.1	CO	99.1	205
Cu–Fe–N$_6$–C	0.1 M KHCO$_3$	−0.7	CO	98	206
Fe/Cu–N–C	0.1 M KHCO$_3$	−0.8	CO	99.2	207
O–Ni$_2$–N$_6$	1.0 M KHCO$_3$	−1.25	CO	94.3	208
Fe$_2$–N$_6$–C–O	0.5 M KHCO$_3$	−0.8	CO	95.85	209
Fe$_2$N$_6$	0.1 M KHCO$_3$	−0.6	CO	96	210
CuNi-DSA/CNFs	0.1 M KHCO$_3$	−0.98	CO	99.6	211
InNi DS/NC (O–In–N$_6$–Ni)	0.5 M KHCO$_3$	−0.7	CO	96.7	115
Fe$_1$–Ni$_1$–N–C	0.5 M KHCO$_3$	−0.5	CO	96.2	212
Others					
Ni–NPIC4	0.5 M KHCO$_3$	−0.65	CO	95.1	213
Ni$_1$−N−C-50	0.5 M KHCO$_3$	−0.7	CO	96	214
Ni$_x$−N–C	0.5 M KHCO$_3$	−0.7	CO	80	215
Ni$_{Mn}$–N–C	0.5 M KHCO$_3$	−0.72	CO	98.5	216
FeSAs/CNF-900	0.5 M KHCO$_3$	−0.47	CO	86.9	217
CHK-cOCTA	0.1 M KHCO$_3$	−1.5	CH$_4$	54.8	218
Ni/HH	0.5 M KHCO$_3$	−0.77	CO	97.9	219
Ni–NG–acid	0.5 M KHCO$_3$	−0.9	CO	97	220
mesoNC–Fe	0.1 M KHCO$_3$	−0.73	CO	85	221
Ni/NCTs	0.5 M KHCO$_3$	−0.8	CO	100	223
Ni–NC$_3$@Cu$_2$O	1.0 M KOH	−1.2	C$_2$H$_4$ C$_2$H$_5$OH CH$_3$COOH	60	224
Ni SACs–Cu NPs	1.0 M KOH	−0.7	C$_2$H$_4$ C$_2$H$_5$OH CH$_3$COOH	80	225
P-NiSA/PCFM	0.5 M KHCO$_3$	−0.7	CO	96	226
CuSAs/TCNFs	0.1 M KHCO$_3$	−0.9	CH$_3$OH	44	227
Ni–PCNFs	0.1 M KHCO$_3$	−1.5	CO	98.6	228
Zn-SA/CNCl-1000	1.0 M KOH	−0.93	CO	97	229
Ni/Zn-6	0.1 M KHCO$_3$	−1.0	CO	94	230

structure and performed far more poorly with a significantly narrower potential range and lower FE$_{co}$. DFT calculations demonstrate that the unique micropore structure of the Cu–N$_4$C$_8$ catalysts modifies the Cu atoms d-orbital energy levels, shifting the d-band center upwards in the adsorbed *COOH intermediate. This modification decreases electron occupancy in the *COOH antibonding states, lowering the free-energy barrier for *COOH formation and reducing the activation energy, which accounts for increased reaction kinetics and rate enhancements. This correlates well with superior experimentally observed reaction performance characteristics for these edge-hosted materials compared to related materials exhibiting alternative Ni coordination.[159]

Similarly, by controlling the pyrolysis temperature of a zinc–cobalt bimetallic MOF, the researchers synthesized Co SAs with either four-coordinated Co with nitrogens (Co$_1$–N$_4$) or a mixture of nitrogens and carbons (Co$_1$–N$_{4−x}$C$_x$) on a nitrogen-doped porous carbon (NDPC) support. However, the Co$_1$–N$_4$ catalyst exhibited superior performance (FE; 82%) with a current density of −15.8 mA cm$^{−2}$ for CO production at −1.0 V vs. RHE. Mechanistic studies revealed that higher catalytic activity was attributed to the enhanced binding strength of CO$_2$ and facilitated CO$_2$ activation at the Co$_1$–N$_4$ active site.[160] Although, the synthesis of Ni-SAC from ZIF is promising, scaling up is difficult due to the lower yield. To enhance the hetero atom doping and metal doping, additional nitrogen sources are required. For instance, Peilong Lu et al. utilized a facile method for the

synthesis of single atomic nickel anchored N-doped carbon nanotubes (Ni SAs/NCNTs) by simply pyrolyzing the mixture of dicyandiamide and 2-methylimidazole with Zn/Ni salts (Fig. 10i–k). The Ni SAs/NCNTs exhibited high Ni loading as high as 6.63 wt% and achieved high FE >95% for CO from −0.7 to −1.0 V, with a peak FE of 97% at −0.9 V at an appreciable current density of 41.5 mA cm$^{−2}$.[161] To identify the intrinsic properties of SACs in eCO$_2$R, several catalysts were synthesized using a similar protocol. However, creating catalysts with very similar microenvironment and support effects is challenging. The uniform catalyst structure allows for a direct comparison of different single-atom metals. This was verified by constructing isostructural multivariate metal–organic frameworks (MTV-MOFs) incorporating different metal porphyrin linkers (Fe, Co, Ni, Cu). The metal-porphyrin units acted as precursors, and ZrO$_2$ acted as a template. The Ni$_1$–N–C displayed exceptional CO$_2$ reduction selectivity, up to 96.8% FE for CO, significantly exceeding those of Fe, Co, and Cu analogues.[162] Similarly, precise control over atomic environment of the single-atom metal site is always intriguing. Wang et al. report a systematic examination into the function of single atomic metal catalysts (Fe, Co, Ni) dispersed on NDC (M–N–C) catalysts. To achieve a metal-pyridine N (M–N$_x$) coordination structure, MOFs were used as precursors and double-stage pyrolysis was employed to create these catalysts. The first step involves the generation of C-ZIF by pyrolysis of ZIF-8 at 1000 °C followed by metalation, and the second pyrolysis step enhanced the generation of pyridine-like coordination with

9652 | Energy Environ. Sci., 2025, 18, 9632–9712

This journal is © The Royal Society of Chemistry 2025

Fig. 10 (a) Pictorial representation of the formation of Ni SAs/N–C. (b) LSV of different Ni SAs. (c) Potential dependant CO FEs by Ni SAs/N–C. Reproduced from ref. 154 with permission from American Chemical Society, copyright 2017. (d) Free energy profile of M–N$_4$–C$_{10}$ and M–N$_{2+2}$–C$_8$ sites towards CO formation. Reproduced from ref. 158 with permission from American Chemical Society, copyright 2018. (e) CO partial current density as a function of Cu–N$_4$C$_8$ and Cu–N$_4$C$_{10}$ catalysts. (f) LSV curves of Cu–N$_4$C$_8$ and Cu–N$_4$C$_{10}$ catalysts. (g) and (h) FE of CO and H$_2$ vs. applied potentials for (g) Cu–N$_4$C$_8$ and (h) Cu–N$_4$C$_{10}$ catalysts. Reproduced from ref. 159 with permission from Wiley (CC-BY 4.0), copyright 2024. (i) Scheme of the formation of Ni SAs/NCNTs. (j) LSV curves of Ni SAs/NCNTs. (k) Potential dependant CO FE by Ni SAs/NCNTs. Reproduced from ref. 161 with permission from Elsevier, copyright 2019.

Ni-center. The selectivity for CO production followed the trend Ni > Co > Fe, while the activity towards CO production followed a different order: Co > Ni > Fe. The Ni–N–C catalyst exhibits outstanding selectivity with high FE close to 100%, for CO from −0.66 to −0.96 V.[163]

Likewise, the engineering of Fe–N$_4$ active sites with controlled Fe–N bond lengths within a MOF-derived carbon matrix, offers precise control over the electronic and geometric environment of the catalytic centers. In this work, the catalytic performance was tuned by both intrinsic and extrinsic factors, and by systematically tuning the particle size, the Fe loading and Fe–N bond structures were tuned. The optimal Fe–N$_4$ catalyst shows a CO FE exceeding 90% across a broad potential

range, with a peak current density of 25 mA cm^{-2} at −0.8 V vs. RHE. Interestingly, spectroscopic analysis and DFT calculations validated the importance of Fe–N bond contraction in optimizing *COOH binding energies, reducing the energy barrier for CO$_2$ reduction while maintaining high selectivity. This work not only provides fundamental insights into structure–activity relationships but also offers a rational design strategy for scalable and efficient CO$_2$ electroreduction catalysts.[164] Effects of annealing temperature on the stabilization of single atoms have been extensively explored in many previous studies, as higher annealing temperature enhances the graphitization of the carbon matrix. In this context, the authors achieve this by precise control of the catalyst's coordination environment to

successfully synthesize atomically dispersed Cu–N$_x$ (x = 3, 3.3, 3.8, 4) moieties anchored on a three-dimensional porous carbon support. The optimized Cu–N$_4$ catalyst (Cu–N$_4$–C/1100) displays significantly enhanced catalytic performance for CO$_2$RR, achieving FE > 90% for CO over a broad potential window (−0.6 V to −1.1 V $vs.$ RHE) and a maximum of 98% FE at −0.9 V. This surpasses the CO selectivity of most of the previously reported copper-based single-atom catalysts. DFT calculations suggested the crucial role of the *COOH intermediate and its efficient interaction with the edge-hosted Cu–N$_4$ sites in facilitating the desorption of *CO.[165] Similarly, a series of Fe–N–C catalysts were synthesized via direct pyrolysis of iron metal organic framework (Fe-BTT) with high nitrogen content at 800, 900, and 1000 °C, followed by acid treatment. Among them, Fe–N–C900 catalyst showed exceptional electrochemical performance for CO$_2$ reduction to CO, achieving a FE of 86.8% at −1.2 V $vs.$ Ag/AgCl, with an overpotential of 496 mV and a current density of 1.26 mA cm^{-2}. Advanced characterization techniques revealed a uniform cubic morphology and consistently distribution of pyridinic nitrogen and porphyrin-like Fe–N$_x$, which were significantly exposed after acid leaching. The Fe–N–C900 catalyst's superior performance was attributed to its high specific surface area, and mesoporous structure.[166] In the same way, Xie $et\ al.$ developed various metal nitrogen carbon (M–N–C) catalysts, where M represents Fe, Ni, Mn, Co, or Cu derived from MOFs for the electrochemical reduction of CO$_2$ to CO. However, the Fe–N–C catalyst exhibited the best CO$_2$RR catalytic performance, achieving nearly 100% FE for CO at −0.9 V $vs.$ RHE even more than that of the Ni–N–C catalyst. Moreover, the Fe–N–C electrocatalyst annealed at 1000 °C displayed the highest catalytic activity and CO selectivity.[167]

High-temperature annealing processes always led to the agglomeration of metal ions to generate metal nanoparticles. MOFs are promising precursors due to their well-defined structures and ability to isolate metal centers. However, annealing the nitrogen-free MOF due to the absence of anchoring hetero atom usually ends up with metal nanoparticle decorated carbon. To overcome this issue spacers are used to separate the metal ions. The researchers synthesized Ni–N–C catalysts by the pyrolysis of bimetallic Ni/Mg-MOF-74 where Mg^{2+} acts as spacers and urea as a nitrogen source. The Ni–N–C@900 °C catalyst exhibited 90% FE for CO with a current density of 4.2 mA cm^{-2} at −0.76V $vs.$ RHE. In contrast, the Mg-free Ni-MOF-74 mainly produced Ni nanoparticles resulting in decreased selectivity toward CO production.[168] The sustainable and scalable strategy for producing efficient Ni–N–C catalysts for eCO$_2$R using an environmentally friendly aqueous synthesis approach is demanding. Most of the current methods often use harmful organic solvents and produce catalysts with low metal loading and primarily microporous structures, hindering efficient mass transport. To overcome this issue, Yixin Zhang $et\ al.$ used a surfactant-modified strategy to synthesize Ni–N–C catalysts from MOFs. Specifically, they used acetyltrimethylammonium bromide (CTAB) in an aqueous solution to modify the ZIF-8 MOF, facilitating better Ni^{2+} ion adsorption and creating mesopores in the resulting material. The ideal catalyst (M–Ni–N–C-2/ CNTs) showed high catalytic activity (j_{CO}; −19.8 mA cm^{-2}) and

selectivity for CO with a FE of 98% at −0.7 V $vs.$ RHE at −1.0 V $vs.$ RHE. Moreover, it was suggested that the pyrrolic nitrogen coordinated Ni–N$_x$ sites contribute significantly to the enhanced performance of the catalyst.[169]

4.2.3.1. Effect of pyridinic vs. pyrrolic nitrogen coordination. The role of pyridinic or pyrrolic nitrogen coordination with single metal atoms is often discussed in CO$_2$ reduction reactions. To understand the importance of the nature of nitrogen atoms, the researchers synthesized a pyrrolic N-stabilized nickel SAC using Ni-ZIF-8 as a precursor (Fig. 11a–c). By carefully controlling the pyrolysis temperature, they obtained catalysts with varying ratios of pyrrolic N to pyridinic N and differing coordination numbers of Ni in Ni–N$_x$ active sites (Ni SAC-800 and Ni SAC-1000). Higher pyrolysis temperature (Ni SAC-1000) led to an increased pyrrolic N/pyridinic N ratio and lower Ni–N$_x$ coordination numbers, significantly improving CO$_2$RR performance. Ni SAC-1000 showed high FE for CO (98.24%) at −0.8 V $vs.$ RHE compared to Ni SAC-800 (40.76%). DFT calculations showed that a higher pyrrolic N content and lower Ni–N$_x$ coordination in Ni SAC-1000 decreased the energy barrier for CO desorption, thereby improving activity and selectivity.[170] Similarly, the effect of pyridinic or pyrrolic nitrogen in catalytic activity and selectivity was explored on single atomic copper catalysts in CO$_2$RR. The researchers demonstrate a single copper atom, precisely anchored to four pyrrolic nitrogen atoms within a NDPC support (Cu–SA/NPC), achieves a remarkable FE of up to 36.7% for acetone (as denoted in eqn (2)) production compared to the Cu–SA/NPC$_{Ar}$ (Cu–pyridinic–N$_4$ site). This significantly surpasses the performance of previously reported catalysts for CO$_2$ reduction to acetone. DFT calculations reveal the underlying mechanism, confirming the crucial role of the specific Cu–pyrrolic–N$_4$ coordination environment in facilitating CO$_2$ activation and C–C coupling, key steps in multi-carbon product formation (Fig. 11g and h).[171] The control of a metal's oxidation state and its interaction with the support can lead to the creation of highly effective metal catalysts for CO$_2$ reduction. However, the strong electronic coupling to the conductive carbon support is crucial for stabilizing the metal center in a higher oxidation state. In this context, Jun Gu $et\ al.$ developed atomically dispersed Fe^{3+} sites as electrocatalysts for CO$_2$ reduction to CO, synthesized through the pyrolysis of Fe-doped zinc imidazolate framework (ZIF-8). The Fe^{3+}–N–C catalyst displays CO$_2$ reduction with low overpotential (80 mV) and better partial current density of 94 mA cm^{-2}. Spectroscopic characterization reveals that the Fe^{3+} sites are stabilized by pyrrolic nitrogen atoms within the NDC matrix. The superior activity of Fe^{3+} sites was attributed to facile CO$_2$ adsorption and CO desorption compared to conventional Fe^{2+} sites.[172]

$$3CO_2 + 16H^+ + 16e^- \rightarrow CH_3COCH_3 + 5H_2O \quad -0.31\ V\ vs.\ RHE \tag{2}$$
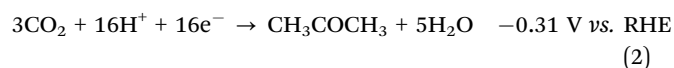
The optimal catalytic performance can be achieved when the nickel atoms (Ni) are predominantly coordinated with three nitrogen (N) atoms, forming Ni–N$_3$ sites, where these nitrogen atoms are predominantly of the pyrrolic type. This is demonstrated using

a Ni-doped ZIF-8 precursor, showing how carefully selected synthesis conditions yield this specific coordination and maximize the generation of active sites with this coordination type. DFT calculations are pivotal to establishing the critical role of this Ni–N$_3$ configuration. They show that the Ni–N$_3$ configuration where Ni is specifically bound to pyrrolic N sites has the most favourable energy profile for the catalytic reaction steps. Importantly, this contrasts with other potential structures (Ni coordinated to pyridinic N atoms), underscoring that precise control over coordination is critical to catalyst effectiveness. The optimized Ni–N$_3$–C catalyst (predominantly utilizing Ni–N$_3$ active sites coordinated with pyrrolic nitrogen) exhibits exceptional performance: 99.37% FE for CO at −0.75 V vs. RHE and a remarkably high TOF of 3498 h^{-1} at this voltage, ranking among the highest CO$_2$RR activities reported (Fig. 11i–k). The improved electrocatalytic activity stems from both: (1) the intrinsic superior kinetics of the pyrrolic Ni–N$_3$ sites (as elucidated by DFT calculations for the energetics of *COOH and CO binding & desorption) which are energetically favourable towards *COOH formation (a key intermediate in CO$_2$ reduction), and (2) the unique electronic structure arising from this unique coordination and influenced by the abundance of pyrrolic nitrogen.[173] The strategic modification in the local bonding environments near the catalytic center alters the reaction kinetics. To verify this phenomenon, the researchers synthesized two distinct Ni–N–C catalysts: Ni–N$_{Pyrrolic}$–C (pyrrole-type ligand) and Ni–N$_{Pyridinic}$–C (pyridinic-type ligand). The Ni–N$_{Pyrrolic}$–C shows extremely high CO partial current density (60 mA cm^{-2} at −1.0 V vs. RHE), demonstrating impressive electrocatalytic CO$_2$ reduction capability across multiple current densities and a FE above 90% across a broad range (−0.6 to −1.0 V). DFT predicted that the electron-donating nature of pyrrole ligands in Ni–N$_{Pyrrolic}$–C decreases the electron cloud density on the neighboring nitrogen atoms thereby causing strong electron depletion around the Ni atoms thus further promoting enhanced interaction, reduced overpotentials, and thus increased reaction kinetics and rate (Fig. 11d–f).[174]

4.2.4. Vacancy engineering. The deliberate creation of structural defects such as metal, carbon, or nitrogen vacancies has emerged as a powerful strategy to optimize the performance of SACs. In SACs derived from MOF and COF, vacancies play a crucial role in modifying the local coordination environment, electronic properties, and adsorption behavior of key intermediates during the CO$_2$RR. Fon instance, in MOF- or COF-derived SACs, creating N or C vacancies around the metal atom can lower its coordination number (e.g., from M–N$_4$ to M–N$_3$ or M–N$_2$). This asymmetric coordination increases the density of unpaired d-electrons, improving the adsorption and activation of CO$_2$ and intermediates like *COOH. Vacancies adjust the charge density around the single metal atom. For example, N vacancies in M–N$_4$ moieties increase the electron density on the metal, improving the *COOH formation step and lowering overpotentials. The presence of vacancies often introduces localized unsaturated sites with stronger binding to the oxygen atoms of CO$_2$, leading to more efficient activation (bending of linear CO$_2$ into an acti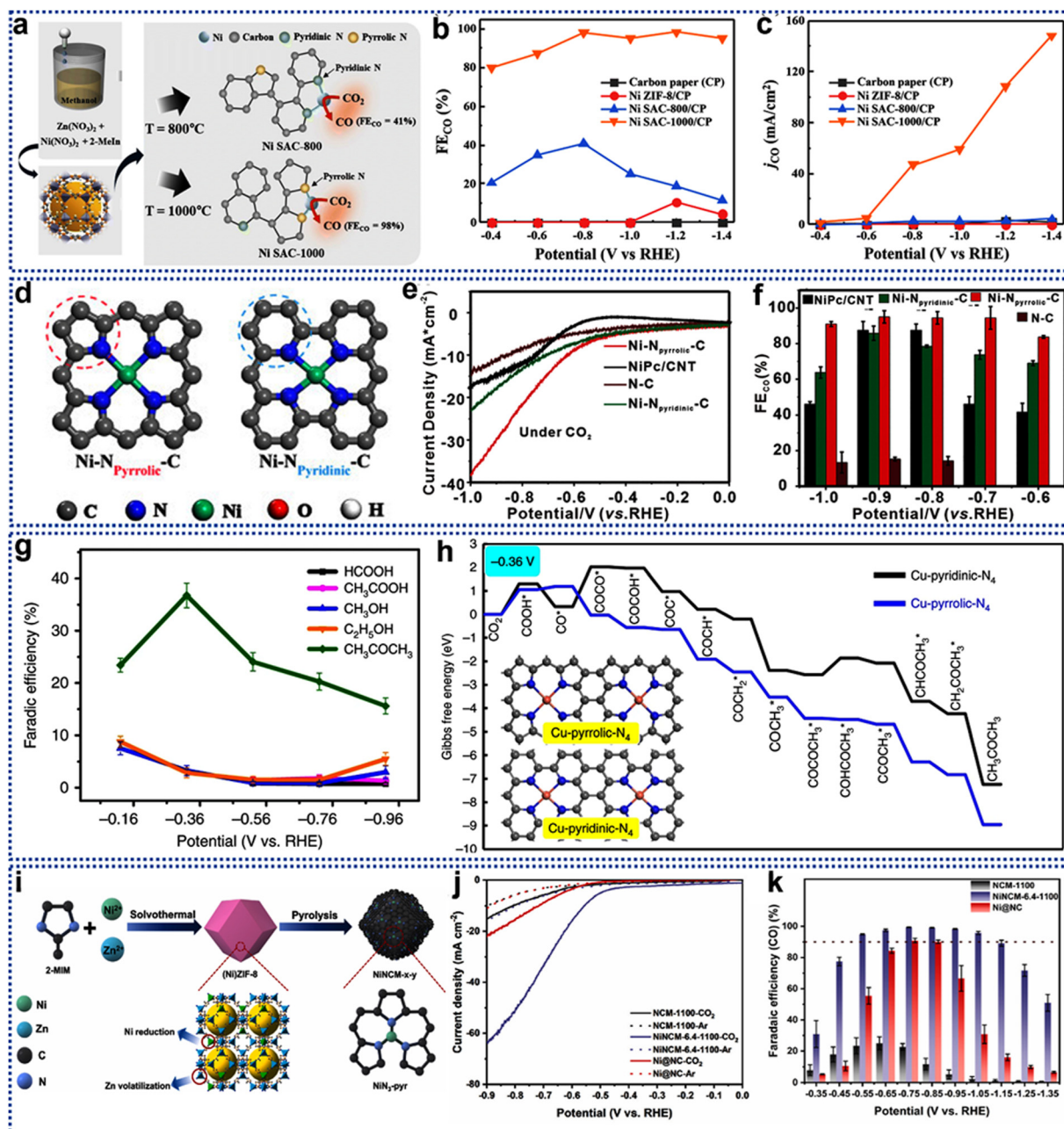vated structure). Defects in MOF or COF derived carbon matrices act as anchoring sites, preventing migration and aggregation of single atoms under reaction conditions. Vacancies influence the binding of intermediates (*COOH, *CO) and can promote pathways toward either CO formation (e.g., Ni–N$_3$ sites) or multi-carbon products (e.g., Cu-based defective SACs). For instance, Cu SACs with adjacent carbon vacancies can stabilize *CO intermediates, favouring C–C coupling.

Annealing temperature always plays a pivotal role in achieving a new coordination motif. Prolonged annealing conditions can enhance the evaporation of the Zn as well as nitrogen and it may create defect sites in the carbon matrix. By employing the self-sacrificial template method, the researchers achieved a high Ni loading of 5.44 wt% while maintaining atomic Ni dispersion. The bimetallic ZIF precursor yielded the C–Zn$_1$Ni$_4$ ZIF-8 catalyst under controlled pyrolysis conditions and exhibited remarkable CO$_2$RR performance high CO FE of 98% at −1.0 V vs. RHE. DFT calculations suggest that enhanced activity stems from the unique electronic properties of the coordinatively unsaturated atomically dispersed Ni–N$_2$V$_2$ structural motif as the most favourable active site (Fig. 12a–c).[175] Similarly, high-temperature annealing processes were considered as a strategy to make less nitrogen-coordinated SACs at high-temperature enhance carbon coordination along with nitrogen ligands. By carefully managing the pyrolysis temperature during catalyst synthesis, the researchers selectively prepared Co catalysts featuring two-coordinate (Co–N$_2$), three-coordinate (Co–N$_3$), and four-coordinate (Co–N$_4$) Cobalt centers. The results reveal that the Co–N$_2$ catalyst achieves superior CO$_2$RR performance compared to Co–N$_3$ and Co–N$_4$. The Co–N$_2$ exhibited a remarkable CO FE of 94% at an overpotential of 520 mV along with a current density of 18.1 mA cm^{-2} (vs. RHE). The enhanced activity and selectivity are attributed to the lower coordination number in Co–N$_2$, which facilitates the activation of CO$_2$ to form the CO$_2^{\bullet-}$ intermediate, a key step in CO$_2$RR.[176]

Copper is mostly acting as a better catalyst for C$_2$-product selectivity, and it was already established that nearby cooper center is crucial for C–C coupling in most catalysts. However, controlling the proximity of active sites in single-atom copper catalysts is always challenging. The author successfully controlled the distance between neighboring Cu–N$_x$ sites and the metal loading by controlling the annealing temperature, which demonstrated the ability to control the selectivity towards methane or ethylene. At lower copper concentrations (<2.4 mol%), the Cu–N$_x$ sites are sufficiently far apart to favour the formation of methane (CH$_4$), a C$_1$ product, as the dominant CO$_2$ reduction pathway. At higher concentrations (4.9 mol%), the proximity of the copper sites enables C–C coupling to form ethylene (C$_2$H$_4$), a C$_2$ product. This illustrates a critical relationship between catalyst structure (Cu site density) and the selectivity of the CO$_2$RR. DFT calculations supported that the isolated Cu–N$_4$ and the isolated Cu–N$_2$ sites predominantly yield CH$_4$ while two proximate Cu–N$_2$ sites allow two CO intermediates to bind facilitating C–C coupling towards C$_2$H$_4$ formation.[177] Precise control over the coordination environment of SACs is crucial for optimizing catalytic activity and selectivity, yet is difficult to achieve. Existing methods

This journal is © The Royal Society of Chemistry 2025

Energy Environ. Sci., 2025, **18**, 9632–9712 | **9655**

Fig. 11 (a) Schematic diagram of the formation of Ni SAC-1000. (b) CO FE of Ni SAC-1000. Potential dependent CO current density for Ni SAs/N−C. Reproduced from ref. 170 with permission from Royal Society of Chemistry (CC-BY 4.0), copyright 2024. (d) DFT optimized structure of Ni−$N_{pyrrolic}$−C and Ni−$N_{pyridinc}$−C. (e) LSV curves of Ni−$N_{pyrrolic}$−C and Ni−$N_{pyridinc}$−C. (f) CO FE of Ni−$N_{pyrrolic}$−C and Ni−$N_{pyridinc}$−C. Reproduced from ref. 174 with permission from Elsevier, copyright 2023. (g) FE of CO_2 reduction products of Cu−pyrrolic−N_4 catalyst. (h) Free energy diagram of acetone formation for Cu−pyrrolic−N_4 and Cu−pyridinic−N_4. Reproduced from ref. 171 with permission from Nature (CC-BY 4.0), copyright 2020. (i) Scheme of the formation of NiNCM$_{x−y}$. (j) LSV curves of NiNCM$_{x−y}$. (k) Potential $vs.$ FE of CO for NiNCM$_{x−y}$. Reproduced from ref. 173 with permission from Elsevier, copyright 2023.

often rely on MOFs containing abundant nitrogen, limiting their generalizability. The researchers developed a "host–guest cooperative protection" approach. This involves the synthesis of a bimetallic MgNi-MOF-74 which acts as a host. Pyrrole monomers were then introduced into the MOF channels and polymerized *in situ*, acting as guest. The Mg^{2+} ions present in the host spatially separate the Ni^{2+} ions within the MOF structure, preventing Ni atom clustering during pyrolysis. Likewise, polypyrrole acts as

both a nitrogen source (for stabilizing Ni) and a protective agent preventing aggregation. By controlling the pyrolysis temperature, three catalysts NiSA–N_4–C, NiSA–N_3–C, and NiSA–N_2–C with differing Ni–N coordination numbers (4, 3, and 2 respectively) were successfully synthesized. Among them, NiSA–N_2–C displayed significantly better catalytic activity with 98% FE for CO at −0.8 V (*vs.* RHE). DFT study proved that NiSA–N_2–C favoured COOH* intermediate formation (rate-determining step), explaining

9656 | *Energy Environ. Sci.*, 2025, **18**, 9632–9712

This journal is © The Royal Society of Chemistry 2025

the catalyst's high activity.[89] Existing methods often lack precise control over the coordination number of the central atom. Therefore, post-synthetic metal substitution (PSMS) was employed as a strategy to achieve precise control over the coordination number. The researchers employed a two-step strategy, which involves the synthesis of zinc-based metal–organic framework (ZIF-8) and pyrolysis to generate a NDC material (Zn–N$_3$–C) followed by etching and Ni substitution resulting in a new catalyst (Ni–N$_3$–C). Ni–N$_3$–C exhibited higher FE for CO production (up to 95.6%) compared to Ni–N$_4$–C and the undoped N-doped carbon material (N–C) (Fig. 12d–f).[178] The crucial innovation lies in utilizing a 2D bimetallic ZIF precursor and a molten salt method, which prevents the typical aggregation and structural collapse observed in high-temperature pyrolysis of such materials. This leads to a unique catalyst with a high surface area and density of well-defined, highly active Ni sites, ultimately resulting in superior catalytic performance. The molten salt method is pivotal in avoiding the typical structural degradation during pyrolysis that commonly occurs with zeolite-based precursors. By using molten NaCl/KCl, they create an ionic liquid medium during pyrolysis that encapsulates and stabilizes the precursor nanosheets preventing agglomeration and structural collapse and yielding ultrathin layered nanosheets after pyrolysis and acid-washing treatment.

The exceptional properties translate into outstanding electrocatalytic performance in the CO$_2$RR. The MS–L–Ni–NC demonstrates high CO FE (FE$_{co}$) of >95.9% over a broad potential window, achieving an ideal FE$_{co}$ of 98.7% at −0.8 V vs. RHE (reversible hydrogen electrode), substantially outperforming catalysts prepared via alternative methods (MS–Ni–NC, D–L–Ni–NC). The superior results are corroborated by unusually large partial current densities (20.6 mA cm^{-2} at −1.0 V vs. RHE). DFT calculations provide compelling mechanistic support for the observed activity and selectivity. The analysis confirms that the coordinated unsaturated pyridine Ni–N$_2$ sites are responsible for high activity because the calculations of Gibbs free energy differences predict these are favourable for the formation of *COOH (a reaction intermediate) and CO desorption, both key steps in the CO$_2$RR reaction.[179]

Traditional pyrolysis of MOF precursors at elevated temperature often results in the formation of inactive metal nanoparticles due to the aggregation of metallic atoms. This research cleverly avoids this using a molten salt (NaCl/KCl) bath during pyrolysis of the layered Fe/Ni-ZIF-8 structure that avoids agglomeration due to preventing nanoparticle collapse or shrinkage. This preserves the precursor's 2D layered morphology, preventing the loss of active sites. It presents a strategy to create highly efficient and durable bimetallic Fe/Ni–N–C catalysts for eCO$_2$R by using a combination of Fe/Ni–ZIF-8 as the precursor, and pyrolysis in an ionic-liquid molten salt bath. The key innovation is the use of a 2D layered precursor which avoids agglomeration and enables the controlled generation of well-exposed and highly active sites. The subsequent Fe/Ni–N–C catalyst achieves a remarkable CO FE (FE$_{co}$) of 92.9% and TOF of 10.77 × 10^3 h^{-1} in a typical H-cell configuration. It further demonstrates the synergistic effects of Fe and Ni in promoting superior charge transfer, making this novel material robust and stable.[180] Utilizing a crystallographically

engineered MOF nanosheet as a support material for atomically dispersed nickel (Ni) single atoms, where controlled vacancy formation maximizes the density of unsaturated NiN$_2$–V$_2$ sites and is directly responsible for enhanced activity. The catalyst, Ni–NC–NS, was synthesized via solvent-controlled growth of 2D MOF nanosheets (ZIF-8–NS), followed by nickel incorporation and a carefully controlled pyrolysis at 950 °C. This process removes Zn from the structure, precisely generating Ni–NC–NS in nanosheet morphology while preventing unwanted Ni particle formation and/or aggregation. The Ni–NC–NS catalyst exhibited almost 100% FE for CO (FE$_{co}$) from −0.7 to −1.0 V versus RHE (Fig. 12g–i). The NiN$_2$–V$_2$ sites exhibit a significantly lower energy barrier for *COOH intermediate formation compared to materials containing different numbers of atomic sites.[181] SACs, especially those with low-coordination configurations, present a potential solution because of their unique electronic structures and maximized atom utilization. A coordinately unsaturated Ni–N$_3$ single-atom electrocatalyst supported on a MOF-derived N-doped carbon (NC) support was prepared. The MOF was used to generate an N–C framework with abundant exposed N sites, followed by the introduction of Ni atoms to generate an atomically precise, low-coordination structure, creating active Ni–N$_3$ sites within a carbon support matrix. The Ni–N$_3$/NC catalyst exhibited highly efficient CO$_2$-to-CO conversion with a FE of 94.6% at a current density of 100 mA cm^{-2}.[182]

4.2.5. Axial coordination effects. An atomic-level understanding of SACs is essential for developing more efficient electrocatalysts for CO$_2$RR. Like natural systems, axial coordination tunes the catalytic activity of many catalysts. Cheng et al. present the synthesis of an atomically dispersed Fe–N$_5$ catalyst derived from zeolitic imidazole framework-8 (ZIF-8) and ferrocene, denoted Fe–SA/ZIF, for CO$_2$RR. The Fe–SA/ZIF exhibited high activity and selectivity for CO, with a FE of 98% at −0.7 V vs. RHE. DFT calculations revealed the enhanced activity originates from the out-of-plane coordinated pyridinic N-ligand in the Fe–N$_5$ site, which reduces CO adsorption energy (Fig. 13a–c).[183] The axial coordination strategy is commonly found in biological systems, where it regulates the reactivity of the metal center. As the eCO$_2$R is thermodynamically unfavourable and kinetically sluggish, the slow reaction kinetics of the initial electronation step significantly hampers the efficiency of CO$_2$ conversion. Existing catalysts often show low selectivity due to competing hydrogen evolution reactions. The researchers successfully demonstrated the incorporation of one axial oxygen atom within a carbon matrix (Ni–N$_4$–O/C) to the atomically dispersed Ni–N$_4$ motif. This axial oxygen atom influenced the dynamic activation of adsorbed reaction intermediates and the resulting Ni–N$_4$–O/C electrocatalyst shows nearly 100% FE for CO at −0.9 V vs. RHE (Fig. 13d–g).[184]

4.2.6. Carbon coordination effects. Manipulating coordination environments through careful design can significantly enhance electrocatalytic CO$_2$RR to CO. Carbon coordination affects the electronic structure of the single metal atom. In M–N$_x$–C$_y$ catalysts, for example, the specific configuration (x, y) affects the metal's d-band center and electron density, which subsequently influence CO$_2$RR reactivity, intermediate adsorption/desorption,
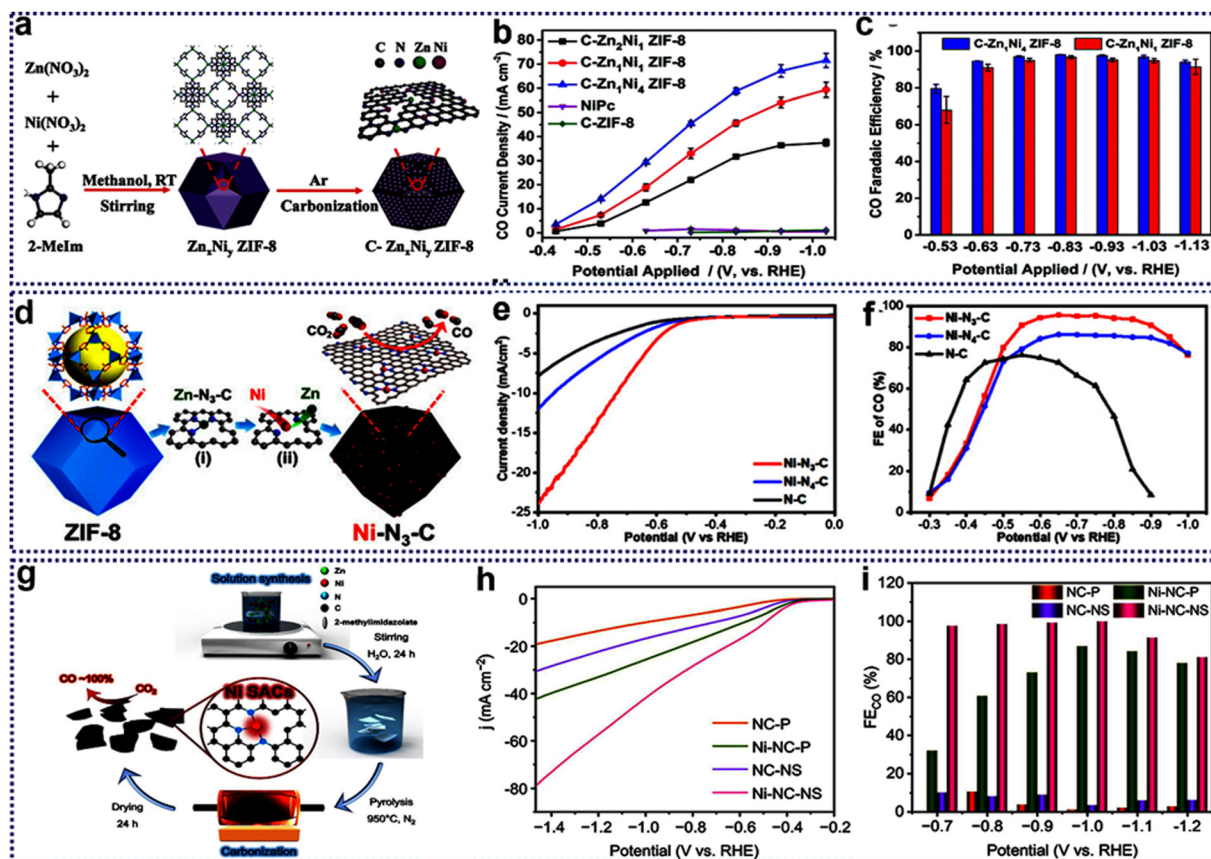
Fig. 12 (a) Graphical representation of the synthesis of C−Zn$_x$Ni$_y$ ZIF-8. (b) CO partial current density of C−Zn$_x$Ni$_y$ ZIF-8. (c) Applied potential dependence of CO FE of C−Zn$_x$Ni$_y$ ZIF-8. Reproduced from ref. 175 with permission from Royal Society of Chemistry, copyright 2018. (d) Fabrication of low-coordination single-atom Ni electrocatalysts Ni−N$_3$−C. (e) LSV curves of Ni−N$_3$−C. (f) FE of CO for Ni−N$_3$−C. Reproduced from ref. 178 with permission from Wiley, copyright 2021. (g) Schematic of the synthesis method and proposed vacancy-manipulated Ni−N$_x$ active site architecture of Ni−NC−NS. (h) LSV curves of Ni−NC−NS. (i) FE of CO Ni−NC−NS. Reproduced from ref. 181 with permission from Wiley (CC-BY 4.0), copyright 2024.

and overall catalytic activity and selectivity. The effect of annealing temperature in controlling the coordination motif was further verified by Huiyuan Cheng et al. By controlling the annealing temperature (from 1000 to 1200 °C), various structural motifs, such as Co−N$_4$C$_1$, Co−N$_3$C$_2$, and Co−N$_2$C$_3$ were synthesized from Co incorporated ZIF. The EXAFS data is well fitted with the Co−N$_3$C$_2$ configuration. Also, it was highlighted that Co−N$_2$C$_3$ SAC exhibits the best CO$_2$RR activity, achieving a CO FE of 92% at −0.8 V vs. RHE, with a CO partial current density of 8.3 mA cm^{-2}. These superior results were attributed to the increased Co–C coordination in Co−N$_2$C$_3$, which leads to electron enrichment of the Cobalt centers, promoting CO$_2$ activation and facilitating CO formation (Fig. 14d–f).[185] During the annealing process of ZIF-M mixtures, Zn typically vaporizes, allowing incorporation of the target metal atoms. To maximize the efficiency of Co-incorporation, the core–shell nanostructure is rationally designed to prevent loss during high-temperature pyrolysis and synthesized from core–shell ZnO@Zn/Co–ZIF precursor using ZnO nanoparticle and 2-methylimidazole and cobalt salts. The synthesized CoSA–HNC catalyst exhibits a 3D hollow structure and sponge-like thin shell with a hierarchical porous system on carbon with a C$_O$−N$_2$C$_2$ coordination motif, which maximizes active site exposure and facilitates the transport of electrons. Through EXAFS

fitting it was suggested that approximately 84.7% of Co species were present as single atoms with Co–C$_2$N$_2$ configuration in the Co NP–SNC.

However, the C$_O$−N$_2$C$_2$ demonstrates poor CO FE of 35% at 1.0 V but 100% FE for syngas (Fig. 14g–i).[186] Single–atom catalysts (SACs) have shown promise, with low-coordinated structures (e.g., M–N$_x$–C$_y$ where $x < 4$) offering potentially superior activity compared to the more common and often less active M–N$_4$ configurations. A novel Ni SACs (Ni–N$_1$–C$_3$) was synthesized via an in situ method involving the pyrolysis of a nickel-impregnated metal–organic framework (MET-6) precursor, followed by an acid washing step (Fig. 14a–c). The optimized Ni–N$_1$–C$_3$ catalyst demonstrated a high CO FE of 97% at −0.9 V vs. RHE. DFT calculations revealed that the unique electronic structure of Ni–N1–C$_3$ featuring a low coordination number, coupled with an upward-shifted d-band center and rich charge density on Ni sites, resulted in favourable *COOH adsorption and decreased energy barrier for *COOH formation. The results demonstrate a feasible pathway to efficiently reduce CO$_2$ by tuning electronic structures through control of coordination and catalyst support.[187]

4.2.7. Oxygen coordination effects. Oxygen coordination is a powerful tool for influencing the activity and selectivity of SACs, but it is crucial to appreciate its complexity. Oxygen
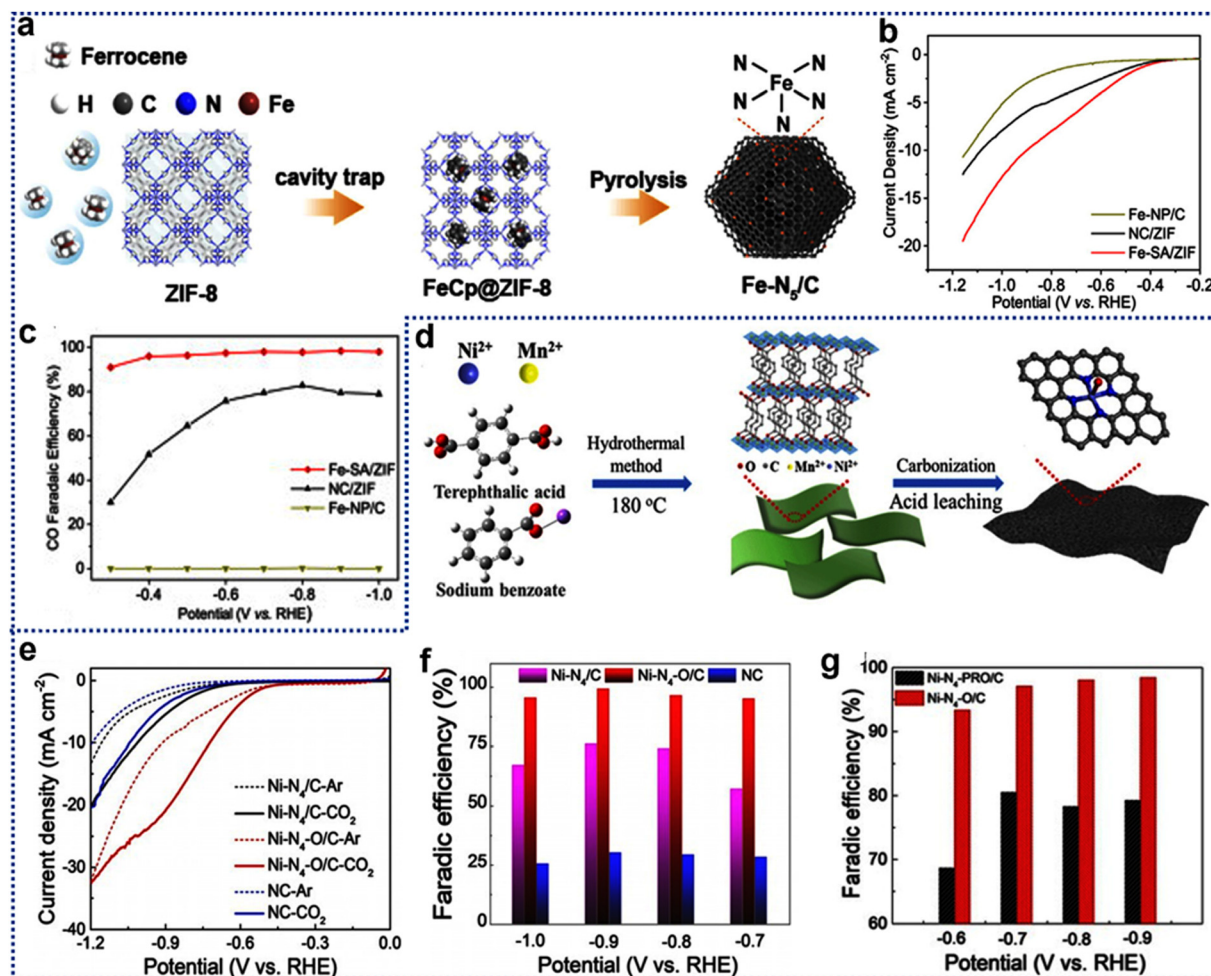
9658 | Energy Environ. Sci., 2025, 18, 9632–9712

This journal is © The Royal Society of Chemistry 2025

Fig. 13 (a) Synthetic scheme of Fe−SA/ZIF preparation. (b) Polarization curve of Fe−SA/ZIF with various materials. (c) FE of CO for Fe−SA/ZIF. Reproduced from ref. 183 with permission from Elsevier, copyright 2021. (d) Demonstration of the synthesis process of Ni−N$_4$−O/C. (e) LSV of Ni−N$_4$−O/C. (f) FEs of CO at various potentials for Ni−N$_4$−O/C. (g) The differences in CO FEs of Ni−N$_4$−PRO/C and Ni−N$_4$−O/C. Reproduced from ref. 184 with permission from Wiley, copyright 2021.

coordination alters the metal atoms' electronic structure. The electronegativity of oxygen leads to changes in the d-band center, charge density, and electronic state. The specific oxygen coordination motif profoundly impacts local charge distribution within the catalytic centers. This also directly alters the electronic configurations of the active sites, significantly influencing catalytic reactivity. Traditional SACs usually contain a rich nitrogen environment. However, tuning the local coordination environment is a key to tune the CO_2 absorption and activation of key intermediates. In 2022, Zhao *et al.*, successfully created a uniform, atomically precise Fe sites with $Fe_1N_2O_2$/NC coordination motif for CO_2RR using nitrogen-assisted pyrolysis of oxygen-rich MOF-74 as precursors (Fig. 15a–c). Each Fe central atom was coordinated with two oxygen and two nitrogen atoms and anchored on N-doped carbon. Interestingly, $Fe_1N_2O_2$/NC exhibited high CO selectivity and FE above 95% from −0.4 to −0.8 V, reaching 99.7% at −0.5 V. Simulations showed the N and O ratio around Fe was vital for regulating CO_2-to-CO conversion. N_2O_2-coordinated Fe sites exhibited a lower free energy change for COOH* formation and CO desorption, boosting reaction kinetics

and catalytic activity.[188] The change of coordination environment of SACs is always beneficial due to the alteration of intermediate binding energy with the metal center. For instance, the researcher synthesized FeN_2O_2/NC catalyst using a facile, scalable method based on ZIF-8. Initially, ZIF-8 with its characteristic rhombic dodecahedral morphology is prepared through high-temperature calcination removing Zn and creating a NDPC support with various surface defects that are conducive to high transition-metal atom utilization efficiency. Subsequent calcination in the presence of $FeCl_2$ (and post-treatment in HCl) results in atomically dispersed FeN_2O_2 sites (Fig. 15d–f). FeN_2O_2/NC exhibits exceptionally high selectivity FE > 80% from −0.7 to 1.0 V reaching a maximum FE_{co} of 95.5% at −0.7 V *vs.* RHE. The enhanced performance is ascribed to a significantly lower energy barrier for *COOH formation (a key intermediate) compared to related catalysts which lack well-defined FeN_2O_2 sites. Additionally, the Fe sites themselves are less effective at facilitating hydrogen evolution thereby avoiding substantial product impurities from H_2 formation during CO_2 reduction tests.[189]
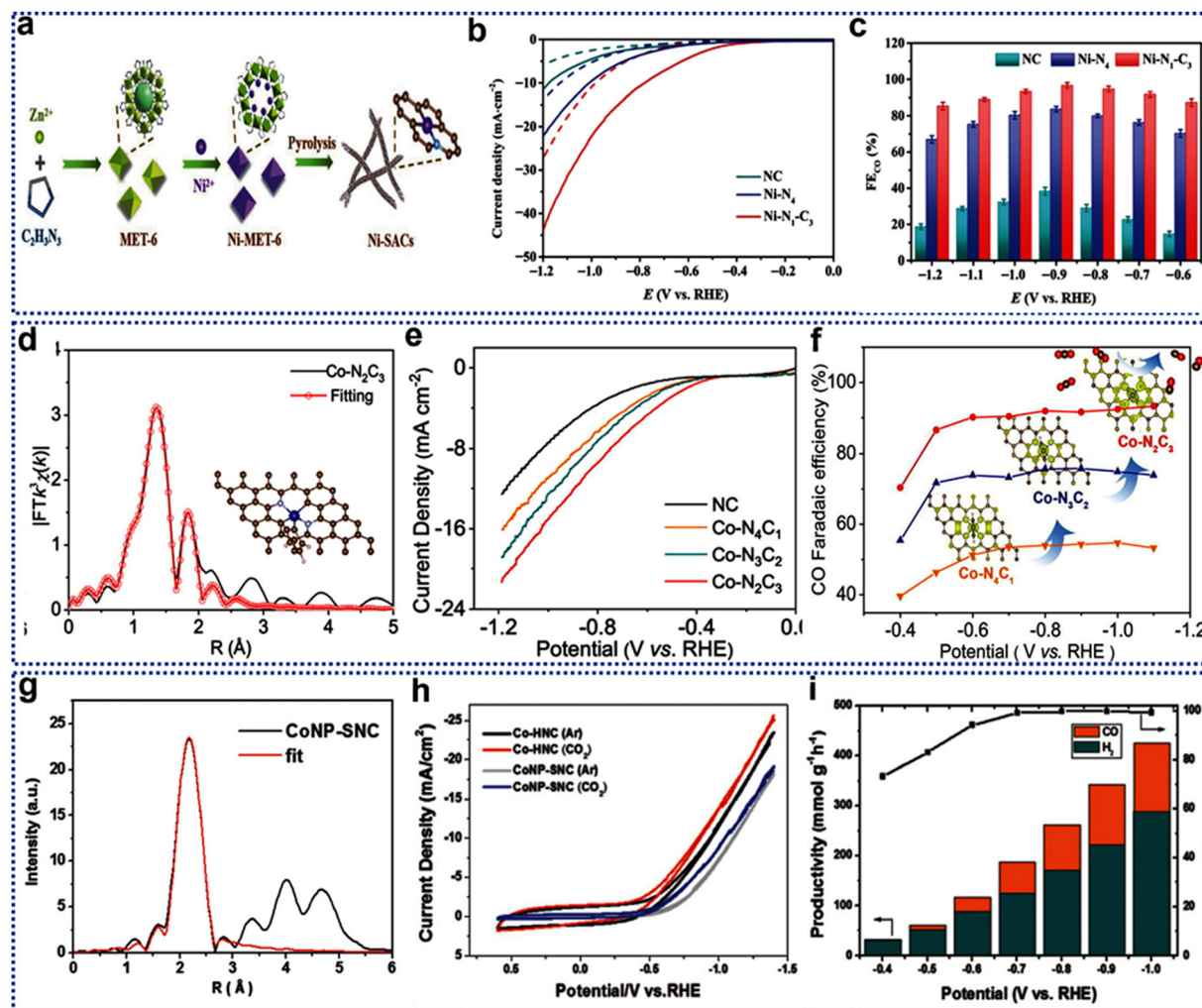
This journal is © The Royal Society of Chemistry 2025

Energy Environ. Sci., 2025, **18**, 9632–9712 | **9659**

Fig. 14 (a) Graphic demonstration of Ni–SAC preparation. (b) and (c) LSV curve and FE of CO for Ni N_1–C_3. Reproduced from ref. 187 with permission from Springer, copyright 2023. (d) EXAFS fitting curves of Co–N_2C_3 at R space with proposed model inserted. (e) Polarization curves of Co–$N_{5-x}C_x$ and NC. (f) FE_{CO} for Co–$N_{5-x}C_x$. Reproduced from ref. 185 with permission from Elsevier, copyright 2022. (g) EXAFS fitting of Co NP–SNC at R space. (h) Polarization curves of Co–HNC and Co NP–SNC. (i) Dependence of productivity and FE of Co–HNC on the applied potential. Reproduced from ref. 186 with permission from Wiley, copyright 2018.

4.2.8. Sulphur coordination effects. Sulphur (S) coordination in SACs is emerging as a potent strategy for enhancing catalytic activity and selectivity but requires careful consideration. The combination of S and N offers unique synergistic activity effects that need precise control to optimize and thereby further enhance catalytic capabilities. S lower electronegativity relative to nitrogen results in modified d-band filling and charge distribution compared to purely nitrogen-coordinated SACs. The modification of local electron configuration changes overall catalytic performance parameters like activity, selectivity, and even stability. Like carbon coordination, the researchers used a thermal replacement strategy (from 800 to 1100 °C), systematically replacing coordinated N with S they synthesized Co–S_xN_{4-x} SACs (where x = 0, 1, 2, 3) by controlling pyrolysis of the Co-doped ZIF-8 nanoparticles (Fig. 16a–d). They found that Co–S_1N_3 exhibited the best CO_2RR performance with a high CO FE of 98 ± 1.8% and a high TOF of 4564 h^{-1} at a low overpotential of just 410 mV ($vs.$ RHE). This enhanced performance of Co–S_1N_3 was ascribed to the precisely

balanced binding ability of key CO_2RR intermediates (COOH* and CO*) achieved by the tuned local coordination environment. This work establishes an effective approach for manipulating SAC structure to improve catalytic activity and selectivity.[190] Hui-Ying Tan et $al.$ developed effective electrocatalysts for the electrochemical reduction of CO_2 (eCO_2RR) by employing MOF-templated synthesis of atomically dispersed manganese (Mn) catalysts. Interestingly, S incorporation into a MOF-derived Mn-based SAC (MnSA/SNC) demonstrates a significant improvement in catalytic performance than that of non-sulfurized counterpart (MnSA/NC). X-ray absorption spectroscopy (XAS) and electrochemical analysis have shown that the MnN_3S_1 coordination environment plays a crucial role in stabilizing key reaction intermediates, particularly *COOH, through potential S–O interactions (Fig. 16e–g). This S modification not only improves catalytic selectivity, achieving a peak efficiency of ∼70% at −0.45 V $versus$ RHE. The insights gained from this work provide a strong foundation for future advancements in MOF-derived catalysts for sustainable CO_2
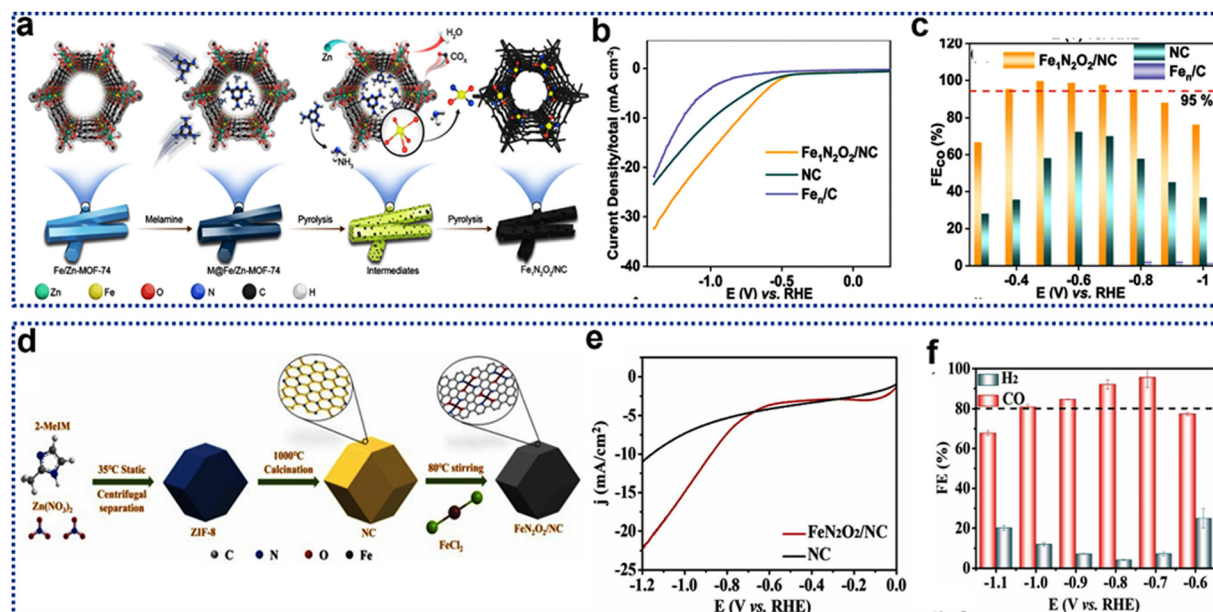
Fig. 15 (a) Graphically presentation of the synthesis of $Fe_1N_2O_2/NC$. (b) LSV curves of $Fe_1N_2O_2/NC$, Fe_n/C, and NC catalysts. (c) CO partial current densities $Fe_1N_2O_2/NC$. Reproduced from ref. 188 with permission from Royal Society of Chemistry, copyright 2022. (d) Synthesis illustration of FeN_2O_2/NC. (e) Polarization curves of FeN_2O_2/NC. (f) CO partial current densities of FeN_2O_2/NC. Reproduced from ref. 189 with permission from Elsevier, copyright 2025.
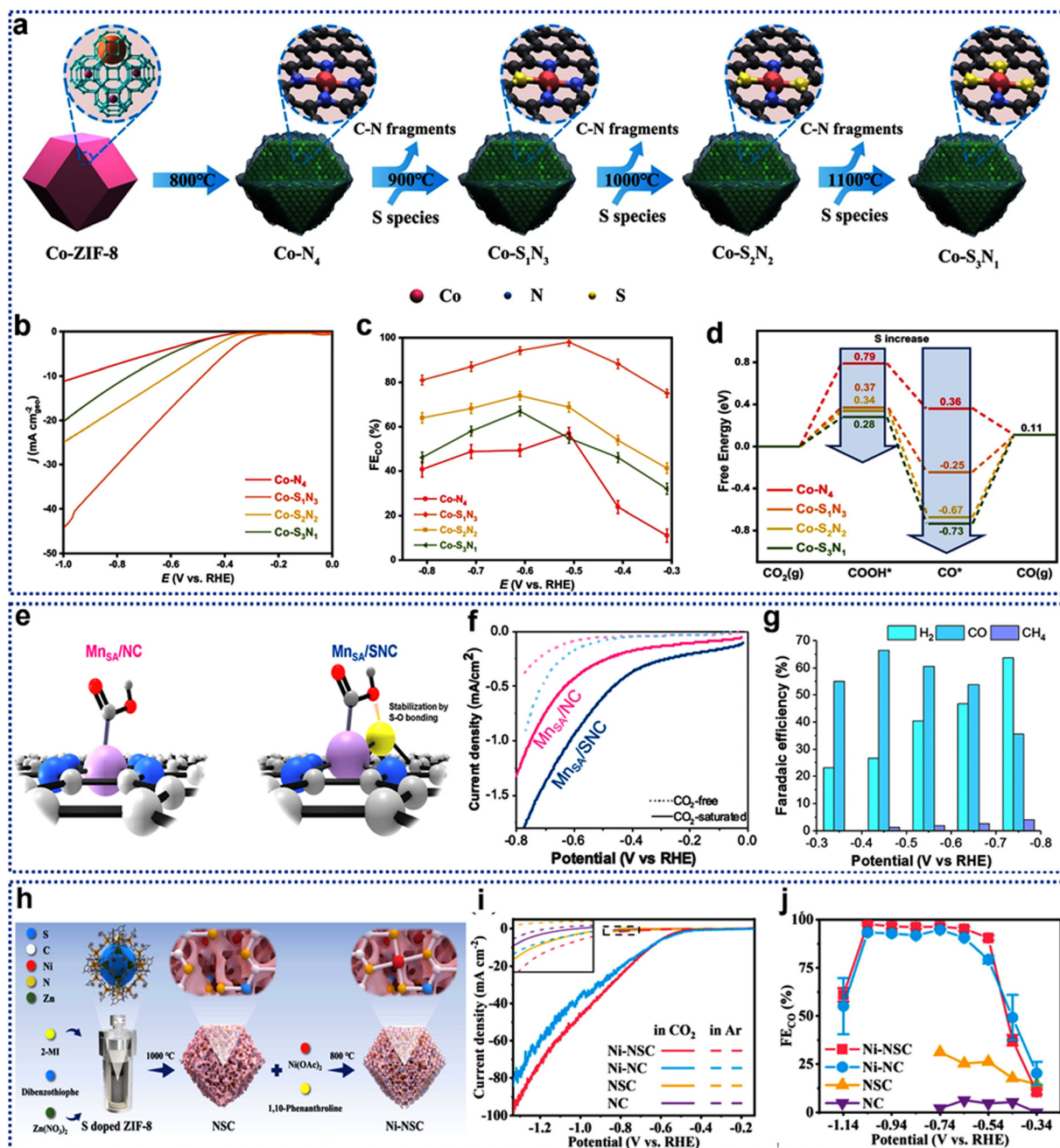
conversion, contributing to the development of carbon-neutral energy technologies.[191] Not only does the coordinated S atom enhance the CO_2RR, but the S atom near the $Ni-N_4$ site also electronically tune the catalytic activity. For instance, the Ni–N–S SAC is synthesized with the S atom strategically incorporated in the second coordination shell around the central Ni atom, directly interacting with the N sites in the NDC material. This interaction creates high levels of activity by modifying the local electronic structure and the distribution of these sites around the Ni metal centers (Fig. 16h–j). Ni–N–S demonstrates an exceptionally high CO FE ($FE_{co} \sim 98\%$ at 425 mV). DFT calculations revealed that incorporating these S atoms in the second shell boosts CO_2 reduction to CO by enhancing charge transfer rates and stabilizing the crucial *H intermediate at N–S active sites and substantially enhancing activity compared to materials synthesized without sulfur. The presence of S is particularly effective in lowering the free energy of the key *H proton-coupling step.[192]

4.2.9. Phosphorous coordination effects. Phosphorus (P) coordination provides a powerful tool to control the electronic structure and catalytic properties of SACs. Alteration in the electronic structure around the single-metal site through specific phosphorus-based bonding often results in a significant enhancement or tuning of catalytic performance. Precisely controlling the coordination environment of each active site *via* heteroatom doping is essential for optimizing catalytic properties in a predictable manner. P atoms have a larger atomic radius than N. This size difference creates structural defects in the carbon matrix, increasing the number of unsaturated carbon atoms, which alters the electronic structure and potentially facilitate easier activation of the CO_2 molecule.

The phosphorus doped Ni–SA/CN–P catalyst exhibit 91.8% of CO FE at −1.1 V and the CO current density in the flow cell reached to 91.2 mA cm^{-2}, which is better than that of the sample Ni–SA/CN without phosphorous dopant. The introduced P atoms adjust the electronic environment around Ni (Fig. 17a–c). XPS and DFT analysis showed that the P dopants reduce the energy required to form the crucial *COOH intermediate (a key step in the CO_2RR process), likely through modification of the d-band energy levels of the nickel active sites, causing shifts in charge distribution, thereby reducing the energetic barrier to the CO_2RR process.[193] While metal–nitrogen (M–N_x) sites in N-doped carbon materials are promising, introducing other heteroatoms, like phosphorus (P), can further tune the electronic structure and enhance catalytic performance. Nickel single-site catalysts (SSCs) with dual-coordinated phosphorus and nitrogen (Ni–P_xN_y, x = 1,2; y = 3,2) atoms were synthesized *via* an *in situ* phosphorization method using a 2-methylimidazole and triphenylphosphine (PPh$_3$) containing precursor (Fig. 17d–f). Ni–P_1N_3 exhibited significantly superior CO_2RR activity than Ni–N_4. Specifically, Ni–P_1N_3 showed a CO FE in the range of 85.0%–98.0% over a wide potential range (−0.65 to −0.95 V *vs.* RHE) with a CO current density reaching 14.30 mA cm^{-2}. DFT calculations showed that the asymmetric Ni–P_1N_3 structure was more energetically favourable for CO_2 intermediate (COOH*) adsorption/desorption compared with the Ni–N_4 configuration. These enhanced binding properties resulted in accelerated reaction kinetics, higher CO selectivity, and enhanced catalytic performance. This work provides an effective strategy for creating highly active and selective SSCs and demonstrates how controlling the coordination environment by utilizing multiple heteroatoms is crucial for maximizing CO_2RR efficiency and targeting specific reaction products.[194]

This journal is © The Royal Society of Chemistry 2025

Energy Environ. Sci., 2025, **18**, 9632–9712 | **9661**

Fig. 16 (a) Synthetic scheme of Co−S$_x$N$_{4−x}$ SACs. (b) Polarization curves of Co−S$_x$N$_{4−x}$ SACs. (c) FE of CO for Co−S$_x$N$_{4−x}$ SACs. (d) Intermediate free energy changes for for CO$_2$RR to CO on the Co−S$_x$N$_{4−x}$ SACs. Reproduced from ref. 190 with permission from Nature (CC-BY 4.0), copyright 2025. (e) Graphical drawing of the preparations of Mn$_{SA}$/SNC. (f) LSV profiles of the Mn$_{SA}$/NC and Mn$_{SA}$/SNC. (g) CO$_2$RR FE at various applied potentials of the Mn$_{SA}$/SNC. Reproduced from ref. 191 with permission from American Chemical Society, copyright 2021. (h) Synthetic scheme of Ni−NSC. (i) LSV curves of Ni-NSC. (j) FE$_{CO}$ at various applied potentials for Ni−NSC. Reproduced from ref. 192 with permission from Elsevier, copyright 2024.

4.2.10. Boron coordination effects. The M-N$_4$ structures coordination motif was commonly observed in many cases and their symmetrical electronic density limits catalytic activity. Therefore, to improve efficiency, the creation of an asymmetric coordination structure is inevitable. Like the S, O, or other heteroatom-coordinated SAC. Boron coordination offers a unique and powerful strategy for tuning the catalytic behavior of SAs. Boron can be incorporated during the synthesis of carbon-based

materials. This may result in altered electronic properties. However, methods often suffer from difficulty in controlling of exact positioning of specific active B sites which frequently limits control and can often decrease efficiency. The researchers synthesized a novel single-atom nickel catalyst (Ni–SACs@BNC) featuring an asymmetric Ni–N$_3$–B coordination using a boron-doped nitrogen-rich carbon substrate. The synthesis involved using a MOF as a template, introducing phenylboronic acid (PBA) as a
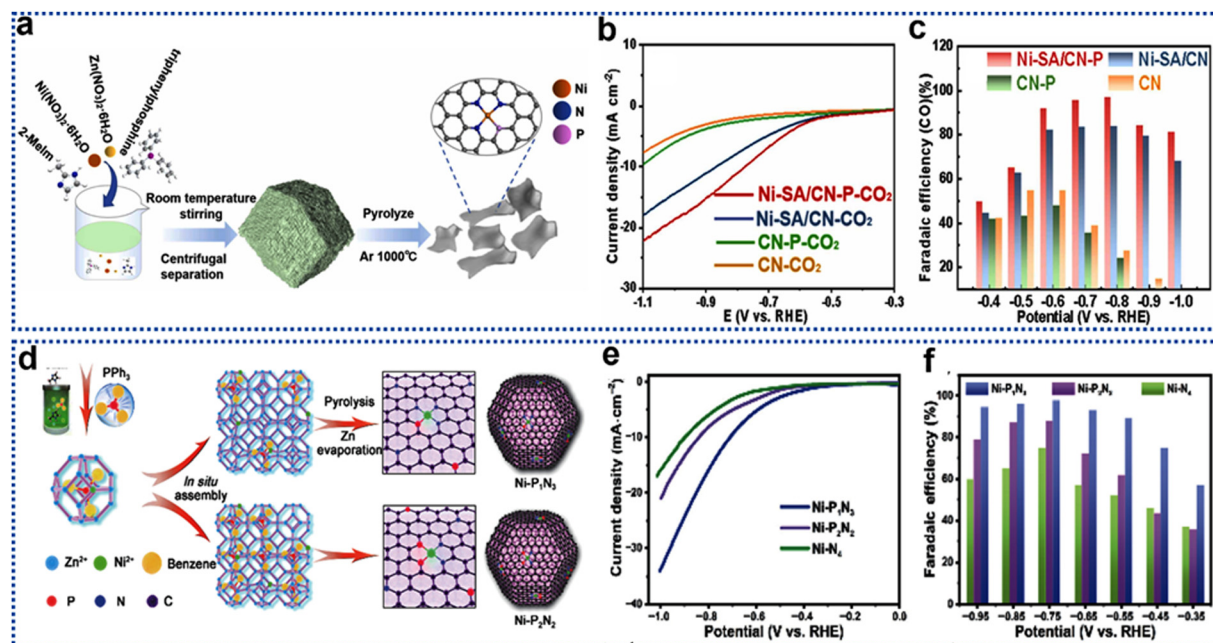
9662 | Energy Environ. Sci., 2025, 18, 9632–9712

This journal is © The Royal Society of Chemistry 2025

Fig. 17 (a) Synthetic scheme of Ni–SA/CN–P. (b) LSV curves of Ni–SA/CN–P. (c) Potentialdependent CO FE for Ni–SA/CN–P. Reproduced from ref. 193 with permission from Elsevier, copyright 2024. (d) Synthetic scheme of Ni–P_xN_y. (e) LSV graph of Ni–P_xN_y. (f) CO FE of the Ni-P_xN_y at different potentials. Reproduced from ref. 194 with permission from Springer, copyright 2023.

boron source, and subsequent incorporation of nickel chloride. Photocatalytic experiments demonstrated significantly higher CO_2 reduction activity for Ni–SACs@BNC compared to Ni–SACs@NC under visible light, particularly in terms of CO production rate and selectivity. PL spectroscopy, transient-state surface photovoltage spectroscopy, and time-resolved PL decay analysis revealed that Ni–SACs@BNC exhibited better charge separation and electron trapping. DFT calculations further substantiated the improved activity by revealing a lower energy barrier for the rate-determining step of CO_2 reduction and explaining the impact of asymmetric charge distribution in optimizing CO_2 binding and activation on Ni–SACs@BNC compared to the symmetric Ni–SACs@NC.[195]

4.2.11. Halogen coordination effects. Halogen coordination in single-atom catalysts (SACs) is a relatively nascent but rapidly expanding field of research. Halogens (F, Cl, Br, I) possess unique electronic and steric properties that, when incorporated into a SACs coordination sphere, can significantly alter its catalytic behavior compared to more commonly studied nitrogen or oxygen coordination. This modulation of electronic structure leads to potential enhancements in activity, selectivity, and, importantly, catalyst stability and durability for diverse applications. Precise tuning of SAC coordination, particularly in the axial position (out of the plane of the primary ligand), is a significant challenge. The researchers employed a post-metal halide modification (PMHM) strategy, which involves the synthesis of N–C from a metal–organic framework (ZIF-8) followed by post-metal halide decoration (Fig. 18a–c). Different nickel halides using NiX_2 were introduced to selectively attach to the support. This process ensured control over the number and kind of axial ligands while minimizing undesirable Ni aggregation.

The Ni_1–N–C (Cl) catalyst (with the most electronegative chlorine atom axially coordinating the nickel), exhibited the best performance with FE for CO reaching ~95%. DFT calculations supported that the axially coordinated chlorine atom facilitates *COOH intermediate formation, thus lowering the activation energy and boosting the overall reaction rate.[196] SACs, particularly M–N–C structures (M = transition metal), have emerged as a cost-effective alternative. However, the stability of Ni based SACs remains a challenge due to issues such as Ni leaching and structural degradation over extended periods of electrolysis. This study focuses on improving the stability and activity of Ni-based SACs *via* Cl-doping to create highly stable and efficient catalysts for CO_2RR. Cl- and N-doped porous carbon nanosheets with atomically dispersed NiN_4Cl active sites (NiN_4Cl–CINC) were synthesized using a molten-salt-assisted pyrolysis strategy. A Ni-doped Zn-based ZIF (Ni/Zn–ZIF) nanosheet was employed as the precursor, mixed with NaCl/KCl salts, and then heated under an Ar atmosphere (Fig. 18d–f). The NiN_4Cl–CINC with atomically dispersed NiN_4Cl active sites exhibit 98% FE for CO. DFT calculations also suggested improved stability resulting from the electronic effects induced by both Ni–Cl and C–Cl bond formation. DFT simulations indicated lower free energy barriers for COOH* formation on NiN_4Cl–CINC. This study demonstrates a highly effective strategy for creating stable and active Ni-based SACs for CO_2RR by incorporating Cl doping into the carbon support to form atomically dispersed NiN_4Cl active sites.[197]

To address the challenges in CO_2 electroreduction a high-performance membrane electrode assembly (MEA) was designed using a novel single atom catalyst. An asymmetrically coordinated Ni single-atom catalyst, Ni–NBr–C, featuring axial Br coordination at NiN_4Br sites anchored onto hollow Br/N co-doped carbon

This journal is © The Royal Society of Chemistry 2025

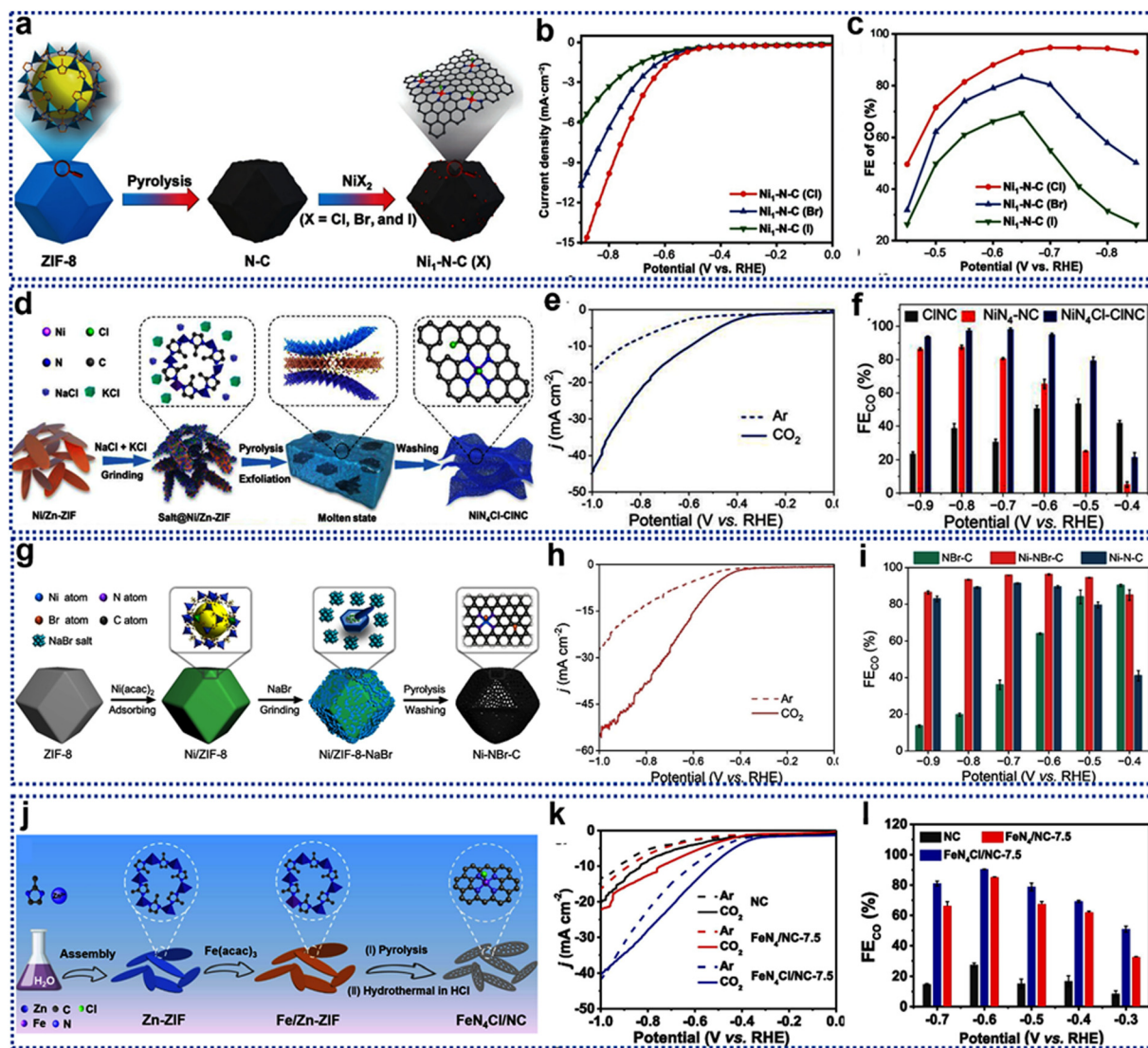*Energy Environ. Sci.,* 2025, **18**, 9632–9712 | **9663**

Fig. 18 (a) Synthetic scheme of the Ni−N−C(X). (b) LSV curves of Ni−N−C(X). (c) CO faradaic efficiencies of Ni−N−C(X). Reproduced from ref. 196 with permission from Springer, copyright 2022. (d) Schematic diagram to produce NiN$_4$Cl−ClNC. (e) LSV curves of NiN$_4$Cl−ClNC. (f) CO faradaic efficiencies of NiN$_4$Cl−ClNC. Reproduced from ref. 197 with permission from Wiley (CC-BY 4.0), copyright 2023. (g) Schematic diagram of the synthetic route of Ni−NBr−C. (h) LSV curves of Ni−NBr−C. (i) FE$_{co}$ of Ni−NBr−C. Reproduced from ref. 198 with permission from Wiley, copyright 2025. (j) Pictorial demonstration of the synthesis of FeN$_4$Cl/NC. (k) LSV curves of various FeN$_4$Cl/NC. (l) Potential dependent CO FE of FeN$_4$Cl/NC-7.5. Reproduced from ref. 199 with permission from Elsevier, copyright 2022.

nanocages, was synthesized using a NaBr-assisted confined-pyrolysis strategy (Fig. 18g–i). The Ni–NBr–C catalyst demonstrates superior performance in an MEA device, achieving a CO FE exceeding 97% over a current density range of 50–350 mA cm^{-2}. This work strongly suggests this catalyst has significant potential for industrial-scale CO$_2$ electroreduction applications.[198] Introducing axial atoms into M–N–C SACs is proposed as a general strategy for designing advanced catalysts for various electrochemical applications. Thus, iron–nitrogen–carbon single-atom catalysts (Fe–N–C SACs), often exhibiting relatively low selectivity and activity due to strong CO* binding on Fe sites, were modified by introducing an axial chlorine (Cl) atom to create FeN$_4$Cl/NC. This was achieved by pyrolyzing Fe-loaded 2D ZIF nanosheets followed by low-temperature incubation in HCl (Fig. 18j–l). X-ray

absorption spectroscopy (XAS) confirmed the FeN$_4$Cl structure with axial Cl coordination at 2.26 Å and four N at 2.02 Å. The resulting catalyst demonstrates a CO FE of 90.5%, and high current density (10.8 mA cm^{-2}) at a low overpotential of 490 mV. The enhanced performance was attributed to the Cl-induced modulation of Fe electronic structure facilitating CO* desorption and inhibiting H* adsorption, as predicted and supported by DFT calculations.[199]

4.2.12. P-block metal SACs. The design of SACs has revolutionized electrocatalytic CO$_2$RR due to their high atomic utilization, tunable coordination environments, and well defined active sites. While transition-metal SACs (e.g., Fe, Co, Ni, Cu) have been widely studied, P-block metals (e.g., Sn, Bi, Pb, In) have gained attention due to their unique electronic configurations, oxophilicity, and

9664 | Energy Environ. Sci., 2025, 18, 9632–9712

This journal is © The Royal Society of Chemistry 2025

ability to stabilize intermediates like *OCHO, which are critical for formate or CO production. Unlike transition metals, P-block metals typically exhibit s-p hybrid orbitals and weaker binding with *CO, which favours formate ($HCOO^−$) or HCOOH formation rather than CO or hydrocarbons. As SACs, these metals can be anchored on nitrogen-doped carbon ($M-N_x$), MOFs and COFs support to tune selectivity, activity, and stability.

Most of the SACs described in the literature are based on d-block metals due to their diverse oxidation states, and readily tunable electronic properties. Similarly, in recent years p-block elements as single atoms enable precise control over the electronic and geometric structure of the active site, maximizing atom utilization efficiency and potentially leading to improved selectivity and activity. However, challenges exist because p-block SACs often exhibit lower stability compared to their d-block counterparts due to their weaker metal–ligand interactions. Furthermore, controlling the coordination environment and oxidation state of the isolated p-block atom presents a significant synthetic challenge. The In-SAs/NC catalyst was synthesized via a facile two-step method. First, indium(III) acetylacetonate [$In(acac)_3$] was encapsulated within a ZIF-8 matrix. Subsequently, pyrolysis of the $In(acac)_3$@ZIF-8 precursor under an inert atmosphere resulted to the formation of an In-SAs/NC catalyst. The In-SAs/NC catalyst demonstrated a high FE of 96% for formate at −0.65 V vs. RHE, with a current density of 8.87 mA cm$^{−2}$.[200] The single atomic In catalyst (In–N–C) was prepared by pyrolyzing In-doped ZIF-8 at 900 °C in an N_2 atmosphere. The increasing ratio of In:Zn in In–N–C is because of the evaporation of Zn ions during pyrolysis, whereas In mostly remains in the catalyst. The In–N–C acts as an effective catalyst for CO_2 to formic acid/formate in aqueous media with a FE of ∼80% at −0.99 V relative to RHE. The atomic In (Indium) has strong electronic interaction with neighboring nitrogen atoms on the carbon skeleton, enabling efficient conversion of CO_2 to formate. DFT calculations suggested that the low energy barrier for the *OCHO intermediate formation improved the CO_2 conversion to format.[201]

While indium exhibits format selectivity, exploiting local coordination environment design principles of single atom catalyst, possibly switches the dominant reaction pathway from formate production to CO generation. The researchers synthesized, InA/NC catalyst via pyrolysis of an indium-BTC metal–organic framework (MOF) and dicyandiamide (DCD). By the controlled pyrolysis (temperature ranges from 700–1000 °C) successful dispersion and coordination of indium at an atomic level was achieved. The InA/NC catalyst pyrolyzed at 1000 °C, demonstrates remarkable selectivity towards CO production in a mixed ionic liquid/acetonitrile (MeCN) electrolyte, in stark contrast to typical In-based catalysts that favour format production. The FE for CO reaches 97.2%, with a total current density of 39.4 mA cm$^{−2}$.[202] Similarly, to achieve the selectivity shift, the researchers synthesized In-SAs/NC catalysts using a two-step method involving the encapsulation of $In(acac)_3$ within a MOF (MIL-68) derived from 1,4-benzenedicarboxylic acid, and pyrolysis at controlled temperatures (800 °C and 1000 °C, yielding In-SAs-800 and In-SAs-1000). In-SAs-1000 (prepared at 1000 °C), exhibited an exceptionally high FE for CO (up to 97%

at −0.6 V vs. RHE), compared to In-SAs-800 which favoured formate (Fig. 19a–c). The selectivity shift was directly correlated with nitrogen content, which is controlled by pyrolysis temperature. DFT calculations suggest that In–N_4 centers favour formate production, while, as nitrogen content decreased while increasing the pyrolysis temperature, neighbouring carbon atoms emerge as the catalytic centers responsible for preferential CO production.[203]

Erhuan Zhang et al. used similar approach in synthesis of Bi–N_4 SACs by combined pyrolysis of Bi-MOF and dicyandiamide. By in situ environmental transmission electron microscopy (ETEM) the author confirmed the initial Bi nanoparticle formation followed by atomization, facilitated by the ammonia (NH_3) released from the decomposition of dicyanamide during pyrolysis. Characterization confirms the presence of Bi SAs coordinated with four nitrogen atoms (Bi–N_4) within the porous carbon support (Fig. 19d–f). The Bi SAs/NC catalyst exhibits higher activity for CO_2RR to carbon monoxide (CO) compared to bismuth clusters or nanoparticles (Bi NPs/NC, Bi Cs/NC) attaining a high FE of 97% at a very low overpotential of 0.39 V vs. RHE.[204] Likewise, being one of the most abundant elements in Earth's crust, the researchers synthesize a SAC with atomically dispersed aluminium (Al) atoms coordinated with four nitrogen atoms (Al–N_4) on a NDC support. The Al–NC catalyst synthesized using complex-assisted pyrolysis strategy (Fig. 19g–i). A NDC support was first synthesized by pyrolyzing the ZIF-8 followed by the $Al(phen)_3$ complex was successfully adsorbed onto the NC–($Al(phen)_3$@NC) and pyrolyzed again. The Al–N_4 site cleverly manages the kinetic barrier problem found with other, simpler, traditional single-atom transition-metal catalysts. The Al–NC catalyst exhibits high FE for CO of 98.76% at −0.65 V vs. RHE and dramatically surpassing the performance of other traditional single atom nickel (Ni–NC) and iron (Fe–NC) catalysts. DFT calculations confirm the comparatively lower energy barrier for *COOH formation and *CO desorption when compared to those using alternative single atom transition metal-based catalysts studied.[205] The synthetic control over both atomic-level catalyst site configurations and their influence on regulating and tuning reaction pathway energies to maximize yield towards different products is promising. The SACs with Sn–N_4 configuration is known for its poor CO selectivity because it predominantly generates formic acid (as denoted in eqn (3)) and hydrogen (H_2). To overcome this issue, the researchers synthesized SnN_3O_1 motif supported on a N-doped carbon matrix (NC) by a gas transport strategy. NC was obtained by simple pyrolysis of ZIF-8 precursor and used as substrate and SnO_2 powder was used as the Sn and O sources. During annealing, volatile Sn species, from the evaporation of SnO_2, transferred to the surface of NC and were coordinated by heteroatoms, forming the Sn–NOC electrocatalyst (Fig. 19j–l). Especially, the loading level of Sn atoms in Sn–NOC catalysts can be controlled by adjusting the pyrolysis temperature from 950 to 1050 °C. The Sn–NOC annealed at 1000 °C catalyst exhibits a maximum FE of 94% at −0.7 versus RHE with a CO partial current density of 13.9 mA cm$^{−2}$. DFT calculations support the finding that the unique SnN_3O_1 atomic arrangement reduces the activation energy barriers for *COOH

This journal is © The Royal Society of Chemistry 2025

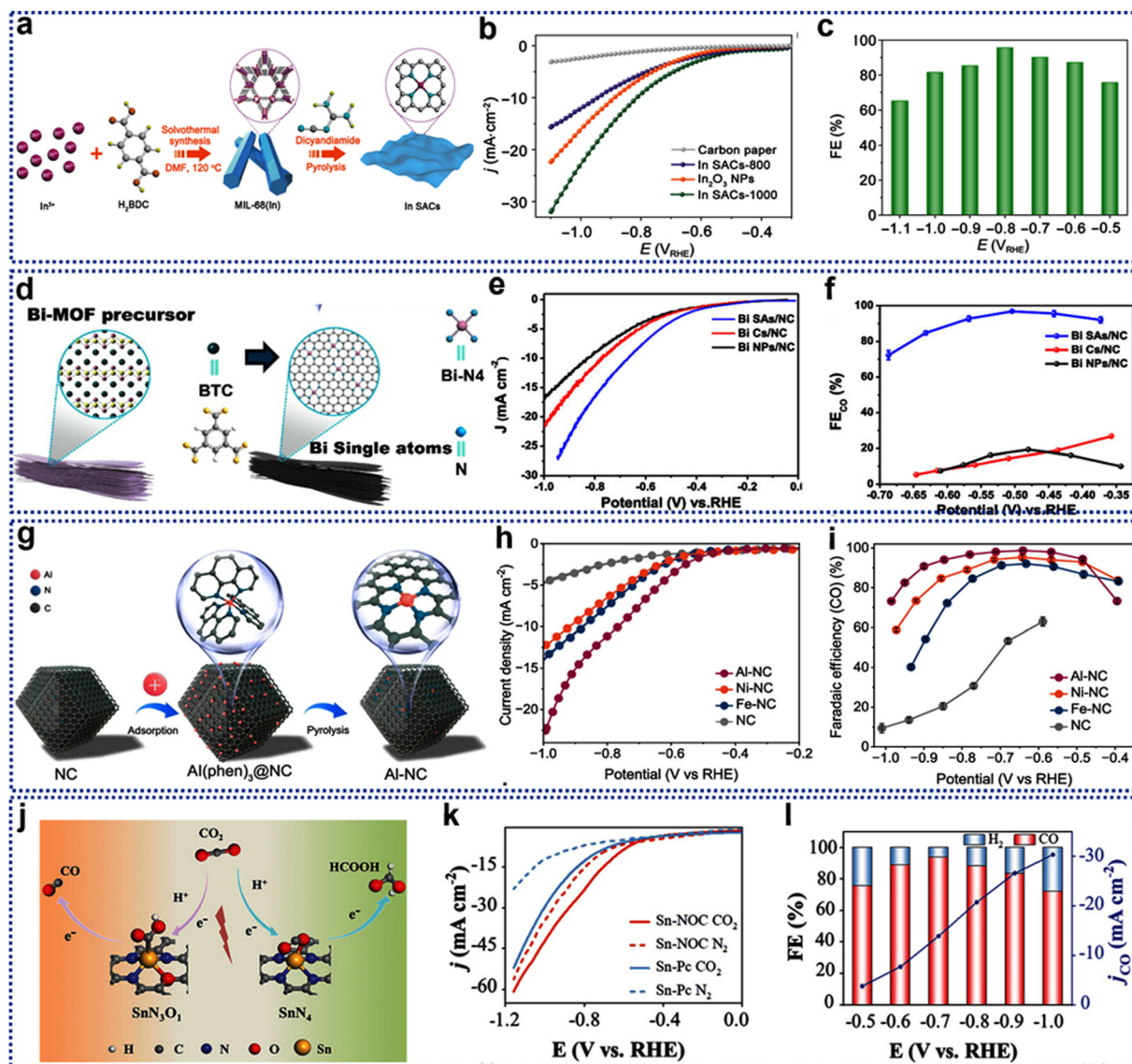Energy Environ. Sci., 2025, **18**, 9632–9712 | 9665

Fig. 19 (a) Synthetic scheme of InSAC. (b) LSV curves of InSAC. (c) FE_{CO} of InSAC at various potentials. Reproduced from ref. 203 with permission from Springer, copyright 2022. (d) Representation of the conversion from Bi-MOF to single Bi atoms. (e) LSV curves of Bi SAs/NC. (f) FE_{CO} of Bi SAs/NC at various potentials. Reproduced from ref. 204 with permission from American Chemical Society, copyright 2019. (g) Schematic demonstration of Al–NC. (h) LSV curves of Al–NC synthesis. (i), FE_{CO} for Al–NC at various potentials. Reproduced from ref. 205 with permission from American Chemical Society, copyright 2024. (j) Schematic representation of activity difference between Sn–N$_4$ $vs.$ SnN$_3$O. (k) Polarisation curves of Sn–NOC and Sn–Pc. (l) FE of CO and H$_2$ catalyzed by Sn–NOC at various potentials. Reproduced from ref. 206 with permission from Wiley (CC-BY 4.0), copyright 2021.

formation, while significantly increasing the activation barrier for the competing HCOO intermediate formation.[206]

$$CO_2 + 2H^+ + 2e^- \rightarrow HCOOH \quad -0.25 \text{ V } vs. \text{ RHE} \quad (3)$$

4.2.13. Hetero-metal doping and dual atomic sites. The strategic design of atomically dispersed diatomic active sites can be leveraged through dynamic structural rearrangements within carbon supports. This approach allows fine-tuning the electronic and geometric environment of catalytic sites, leading to boosted activity, selectivity, and stability in various electrochemical reactions. By precisely controlling the coordination environment and electronic interactions between the two active

metal centers, researchers can optimize reaction pathways, lower energy barriers, and improve overall catalytic efficiency. In this section, recent studies have demonstrated that dynamic rearrangements within the carbon matrix can facilitate the stabilization of reactive intermediates and create co-operative between adjacent metal atoms, significantly outperforming conventional SACs. Moreover, this strategy enables the engineering of defect sites, heteroatom doping, and charge redistribution, further optimizing the catalyst's performance in CO$_2$RR. The ability to fine-tune these interactions at the atomic level opens new frontiers in designing next-generation electrocatalysts with unprecedented efficiency and durability. For instance, the NiCu–SACs/N–C catalyst was synthesized through

a hydrothermal method followed by pyrolysis of a NiCu–ZIF precursor. NiCu–SACs/N–C catalysts achieve unprecedentedly high FE for ethanol generation (92.2% at −0.6 V *vs.* RHE), far exceeding that of catalysts using similar metals but without the dual site design and using just isolated single atoms (Fig. 20a–c). Enormously low onset potential of −0.4 V *vs.* RHE also confirms exceptional catalytic performance which substantially exceeds all previously reported results related to CO$_2$RR-producing multi-carbon materials in literature. DFT-based energetics show how Ni–N$_3$ facilitates the production of *CO, which reacts with itself

during the multi-step CO$_2$RR reaction and is subsequently transformed into ethanol products at neighboring Cu sites.[207] The dual atom catalyst (DAC) decorated on a hierarchical carbon matrix offers a promising strategy by creating locally optimized high-pH reaction environments that control the electronic and geometric properties within these catalytic systems, achieving exceptional efficiency in complex CO$_2$ electroreduction. The researchers used DFT calculations to predict that the CoN$_4$ moiety is responsible for H$_2$ generation whereas NiN$_4$ sites efficiently generate CO during CO$_2$ reduction reactions. Based
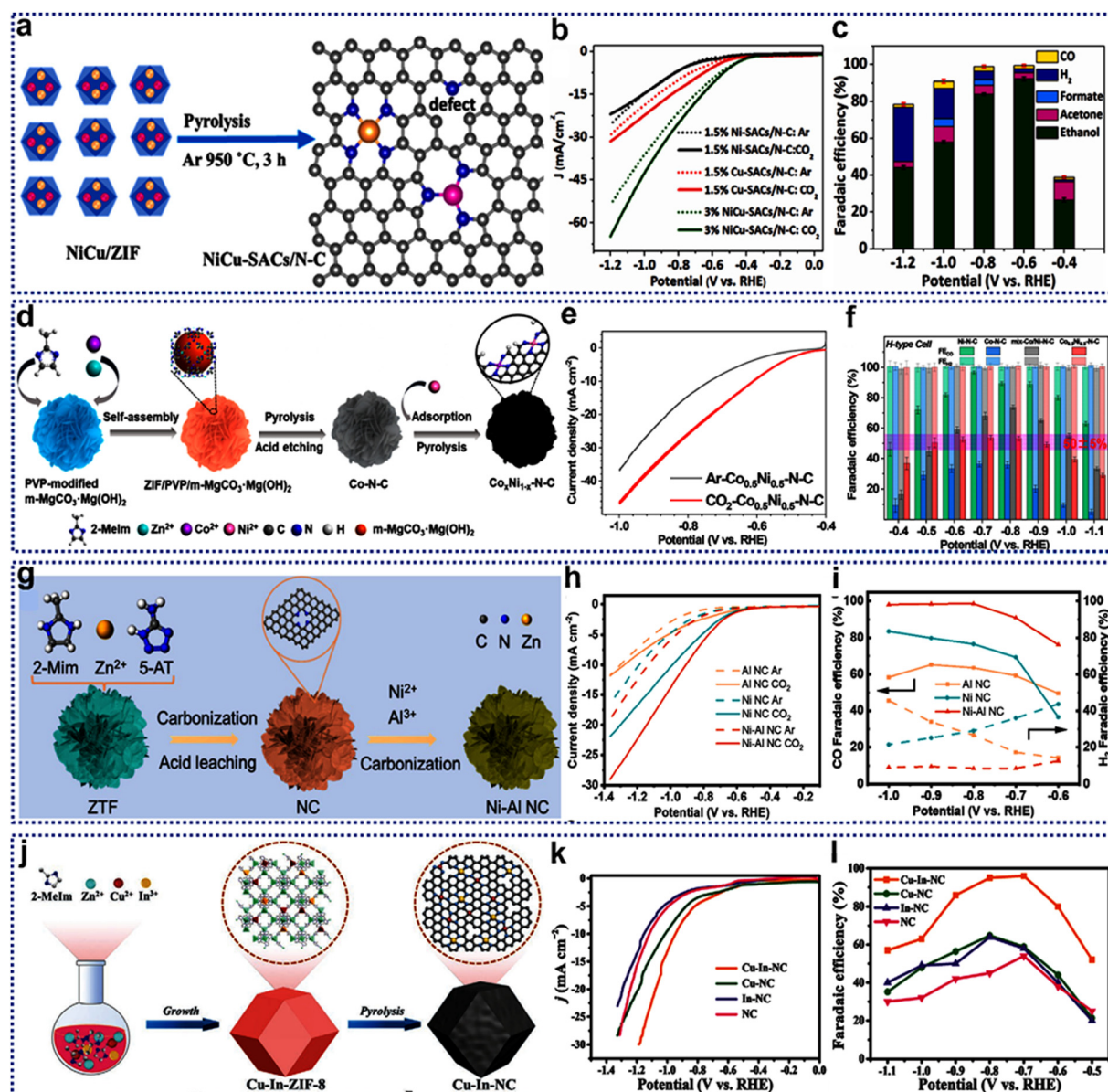
Fig. 20 (a) Synthetic scheme of NiCu–SACs/N–C catalyst. (b) Comparative LSV of different NiCu–SACs/N–C catalyst. (c) FE of CO for NiCu–SACs/N–C at various potentials. Reproduced from ref. 207 with permission from Elsevier, copyright 2024. (d) Pictorial representation of the synthesis of Co$_x$Ni$_{1−x}$–N–C. (e) LSV curve of Co$_{0.5}$Ni$_{0.5}$–N–C. (f) FE of CO for Co$_{0.5}$Ni$_{0.5}$–N–C at various potentials. Reproduced from ref. 208 with permission from American Chemical Society, copyright 2023. (g) Schematic demonstration of the synthesis of Ni–Al NC catalyst. (h) LSVs of different Ni–Al NC. (i) FE of CO for Ni–Al NC at various applied potentials. Reproduced from ref. 209 with permission from Royal Society of Chemistry, copyright 2024. (j) Pictorial representation of the synthesis of Cu–In–NC. (k) LSV curve of Cu–In–NC. (l) FE of CO for Cu–In–NC at various potentials. Reproduced from ref. 210 with permission from Wiley, copyright 2022.

on this they synthesized the hierarchical DSAC (Co$_{0.5}$Ni$_{0.5}$–N–C) by employing a basic magnesium carbonate (m-MgCO$_3$·Mg(OH)$_2$) as a template system along with the addition of polyvinylpyrrolidone (PVP), 2-methylimidazole (2-Melm), and a mixture of Zn, Co, and Ni salts that produced an extremely stable, cost-effective system exhibiting good atomic homogeneity in these complex catalyst system (Fig. 20d–f). A locally high-pH microenvironment formed by the reaction of CO$_2$ and H$_2$O at this optimized Ni/Co material combination is largely responsible for improving both selectivity and efficiency which is absent in the mixed Co–N–C and Ni–N–C catalyst samples.[208] The introduction of aluminium (Al) into the Ni–N$_4$–C, which promotes p–d orbital hybridization with Ni, possibly enhanced catalytic activity and stability. To achieve this, the researchers synthesized Ni-Al NC catalyst using zeolitic tetrazolate framework (ZTF) precursor created using zinc acetate, (2-mim), and 5-aminotetrazole (5-AT) and followed by carbonization at 900 °C under Argon. After acid washing and treatment with additional Al^{3+} and Ni^{2+} solutions then heat treated again to get the final catalysts. Ni–Al NC catalyst exhibits high CO FE exceeding 90% at −0.7 to −1.0 V vs. RHE, and a highest of 98% at −0.8 V (Fig. 20g–i).[209] The use of main-group metals as a regulators in dual atom catalysts offers a novel strategy for creating effective catalysts for industrial–scale CO$_2$ conversion. Cu–In–NC was synthesized through pyrolysis of a Cu–In-co-doped ZIF-8 MOF under an argon atmosphere leading to isolated, uniformly distributed single atoms as well as showing distinct porosity. The Cu–In–NC shows a high FE of 96% for CO at −0.7 V vs. RHE (Fig. 20j–l). This surpasses the performance of its monometallic counterparts. DFT calculations suggest that the incorporation of HER sluggish In atoms acts as an electronic modifier, influencing the electron density and local structure of the Cu sites to effectively decreasing the energy barrier of the rate-determining step in CO$_2$RR.[210]

The incorporation of dissimilar metal centers close to the catalytically active site correspondingly induces the electronic modulation of the catalysts, which leads to altering the intermediate binding energy and the intrinsic catalytic activity and stability as well. The researchers introduced diatomic Ni–Fe sites anchored on nitrogen doped carbon. This catalyst demonstrates superior performance compared to its single-atom counterparts. The Ni/Fe–N–C catalyst was synthesized via pyrolysis of a Fe-doped Ni–ZIF-8 precursor following an ion-exchange strategy. The Ni/Fe–N–C catalyst displays high CO FE >90% over a broad potential window (−0.5 to −0.9 V vs. RHE), reaching 98% at −0.7 V vs. RHE. It maintains exceptional selectivity (>99%) for over 30 hours of continuous operation (Fig. 21a–c). DFT calculations indicate that the Ni–Fe pair acts synergistically, lowering the reaction energy barriers associated with *COOH formation and CO desorption resulting in greatly improved activity compared to monometallic Ni and Fe centers.[211] Coupling hetero-nuclear transition metal atoms with well-controlled synthesis methods, promotes the formation of well-defined active sites, thereby maximizing the surface areas conducive to high mass transfer and minimizing the undesired competing reactions. The researchers synthesized the NiN$_3$@CoN$_3$–NC catalyst via a multistep process involving the preparation of Zn/Co/Ni–zeolite imidazolate frameworks (ZIFs), followed by

pyrolysis. This approach effectively creates isolated and well-defined Ni and Co dual-atom active sites. The coupled Ni–Co dual-atom catalyst displays significantly enhanced CO$_2$ reduction activity than that of its single-atom equivalents (Ni SACs and Co SACs). The NiN$_3$©CoN$_3$–NC shows FE towards CO formation (FE$_{co}$ > 90% in the potential window from −0.6 V to −1.1 V) reaching a maximum FE$_{co}$ of 97.7% at −0.7 V with a partial current density of 14 mA cm^{-2} at −1.1 V vs. RHE (Fig. 21d–f).[212] Similarly, a copper atom was introduced near to nickel site and the Ni/Cu–N–C was synthesized via a host–guest approach using a Cu–phenanthroline complex within a NiZn–ZIF-8 precursor. The Ni/Cu–N–C catalyst exhibits a record-high TOF of 20 695 h^{-1} at −0.6 V vs. RHE and FE of 97.7% for CO. The incorporation of Cu near the Ni center leads to an upward shift of Ni 3d band energy, favourably influencing the interaction between Ni and the *COOH intermediate. This reduces the activation energy for the rate-determining step (*COOH formation). Operando XAS supports this, showing a reversible shift in the Ni oxidation state during catalysis indicating charge transfer processes (Fig. 21g-i).[213] Similarly, Ni–Cu dual atom sites supported on hollow NDC were developed and demonstrated remarkable performance than that of single-metal catalysts and previously reported dual-atom catalysts. The atomically dispersed Ni–Cu catalyst exhibits near FE of 100% CO across all pH conditions, with CO partial current densities of 190 ± 11 mA cm^{-2} (acidic), 225 ± 10 mA cm^{-2} (neutral), and 489 ± 14 mA cm^{-2} (alkaline). DFT calculations suggest that Cu pushes the Ni d-band center toward the Fermi level. This modulates the binding energy of the COOH* intermediate and accelerates its formation, thereby contributing toward increased and overall, significantly boosting catalytic conversion to CO, while further reducing those reaction energies (Fig. 21j–l).[214]

Controlled structural modification with a synergistic relationship of single atom sites significantly impacts efficiency, stability, and selectivity. For instance, researchers developed Cu and Fe diatomic sites and demonstrated the synergistic relationship between them in CO$_2$RR compared to monometallic Cu–N–C and Fe–N–C catalysts. Cu–Fe–N$_6$–C was synthesized via pyrolysis of a PcCu–Fe–ZIF-8 precursor. The Cu–Fe–N$_6$–C catalyst exhibits a high FE of 98% at −0.7 V vs. RHE, maintaining 98% of its initial FE after 10 hours of continuous electrolysis.

The superior activity is ascribed to the cooperative catalytic effect of the Cu and Fe sites, where the Cu–Fe diatomic structure enhances the adsorption of CO$_2$ and lowers the activation energy barrier for CO$_2$ reduction to CO. This directly promotes efficient catalytic processes and produces high yield of desired products toward maximization of efficiency (Fig. 22a–c).[215] Precisely controlled Fe–Cu diatomic sites within a nitrogen-rich carbon matrix optimized to enhance CO$_2$ reduction efficiency. Fe/Cu–N–C was synthesized through a MOF-assisted approach by incorporating Fe and Cu precursors into a ZIF-8 framework. Careful control of precursor placement, using Fe(acac)$_3$ within the ZIF-8 cavities and Cu directly coordinated to the N atoms within the structure minimized aggregation, generating an optimal N$_4$Fe–CuN$_3$ diatomic structure. The Fe/Cu–N–C catalyst demonstrates a high CO FE (>95% over a broad potential window of −0.4 to −1.1 V vs.

9668 | Energy Environ. Sci., 2025, **18**, 9632–9712

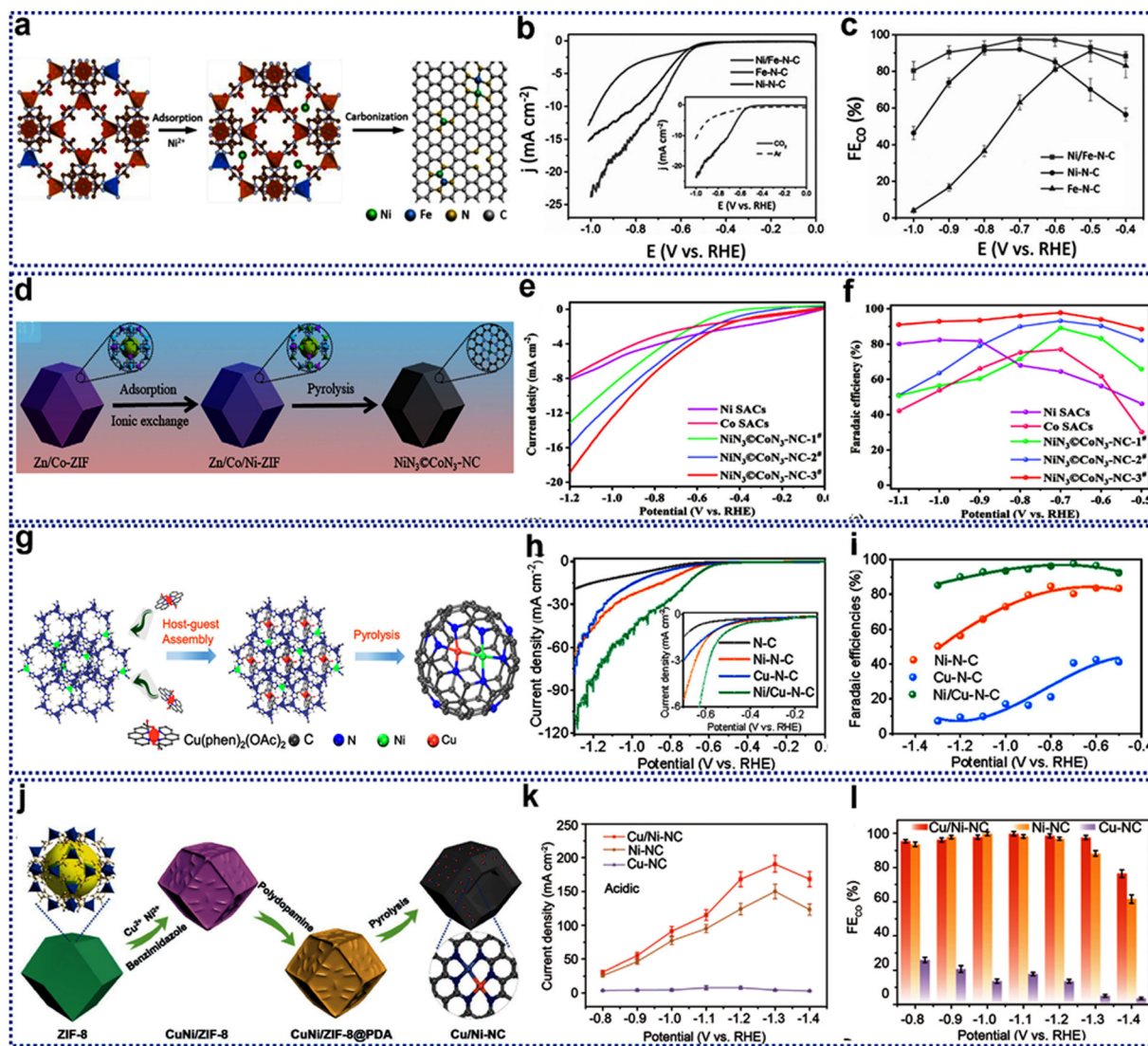This journal is © The Royal Society of Chemistry 2025

Fig. 21 (a) Schematic of Ni/Fe−N−C synthesis. (b) Linear sweep voltammograms (LSVs) of Ni/Fe−N−C catalysts. (c) CO faradaic efficiency (FE) for Ni/Fe−N−C at various potentials. Reproduced from ref. 211 with permission from Wiley, copyright 2019. (d) Schematic of NiN₃@CON₃−NC synthesis. (e) LSV of NiN₃@CON₃−NC catalyst. (f) CO FE for NiN₃@CON₃−NC at various potentials. Reproduced from ref. 212 with permission from Elsevier, copyright 2023. (g) Schematic of Ni/Cu−N−C synthesis. (h) LSVs of Ni/Cu−N−C catalysts. (i) CO FE for Ni/Cu−N−C at various potentials. Reproduced from ref. 213 with permission from American Chemical Society, copyright 2022. (j) Schematic of Cu/Ni−NC synthesis. (k) LSV of Cu/Ni−NC catalyst. (l) CO FE for Cu/Ni−NC at various potentials. Reproduced from ref. 214 with permission from Wiley, copyright 2023.

RHE, reaching 99.2% at −0.8 V *vs.* RHE), high TOF (5047 h^{-1} at −1.1 V *vs.* RHE), and low overpotential (50 mV), significantly surpassing most reported single-atom catalysts. DFT calculations suggest a cooperative effect between the Fe and Cu atoms, accelerating charge transfer and adjusting the d-band center, thus decreasing the activation energy barriers for *COOH formation and *CO desorption (Fig. 22d–f).[216] The influence of precisely controlled metal–metal interactions is a crucial need for improved performance and selectivity for CO₂ electroreduction. To illustrate, the Ni₂(dppm)₂Cl₃ cluster was subsequently incorporated into a ZIF-8-derived NDC matrix and pyrolysis in an Ar atmosphere produced the Ni₂/NC catalyst. This approach yielded a uniform catalyst featuring two Ni₁–N₄ moieties sharing two nitrogen atoms. The Ni₂/NC demonstrates a CO FE of 94.3% at a current density of

150 mA cm^{-2}, along with high stability. *Operando* synchrotron X-ray absorption fine structure (XAFS) and FTIR spectroscopy revealed a dynamically changing structure, including oxygen-bridge formation at negative potentials resulting in a stabilized and unusually highly active O–Ni₂–N₆ structure (Fig. 23a–c). The dynamically evolving site facilitates CO₂RR efficiency under operating electrochemical conditions. The proposed reaction mechanism suggests that this specific, oxygen-bridged Ni₂–N₆ site structure strongly influences the kinetic rate-limiting step of *COOH formation.[217] Similarly, it was anticipated that the incorporation of another iron can tune the electronic structure *via* orbital coupling and possibly enhance the activity and selectivity. The common limitation of single Fe–N–C catalysts is strong CO binding, which limits the activity and leads to high overpotentials.
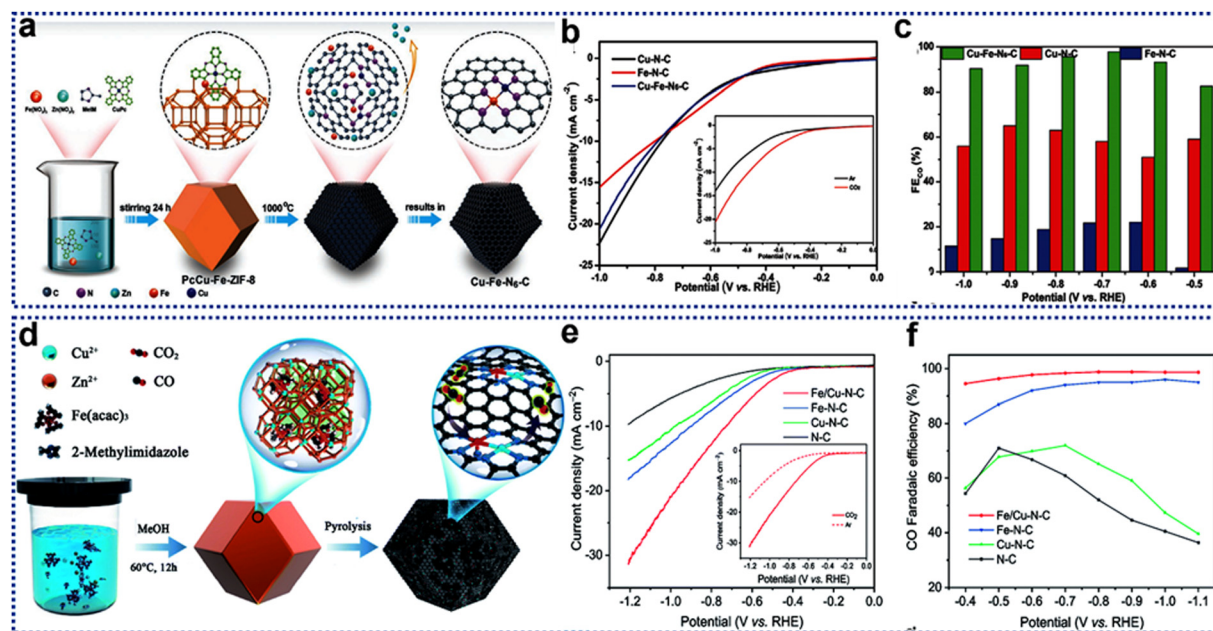
Fig. 22 (a) Schematic illustration of Cu–Fe–N$_6$–C synthesis. (b) Linear sweep voltammogram (LSV) of Cu–Fe–N$_6$–C. (c) CO faradaic efficiency (FE) for Cu–Fe–N$_6$–C at various potentials. Reproduced from ref. 215 with permission from Wiley, copyright 2021. (d) Schematic illustration of Fe/Cu–N–C synthesis. (e) LSVs of Fe/Cu–N–C catalysts. (f) CO FE for Fe/Cu–N–C at various potentials. Reproduced from ref. 216 with permission from Royal Society of Chemistry, copyright 2021.

To validate, a series of electrocatalysts (Fe$_1$–N$_4$–C and Fe$_2$–N$_6$–C) with well-defined Fe single-atom and dual-atom sites were synthesized using a template-assisted approach by pyrolyzing at Ar/H$_2$ atmospheres to control site structures. The Fe$_2$–N$_6$–C dual-atom catalyst exhibits a significantly higher TOF of 26 637 h^{-1} and improved durability compared to the Fe$_1$–N$_4$–C SACs. The FE for CO production exceeds 80% over a wide potential range. Detailed experimental and theoretical analysis reveal that the orbital coupling between the two Fe atoms in the Fe$_2$–N$_6$–C catalyst reduces the energy gap between antibonding and bonding states in CO adsorption, thus promoting CO$_2$RR activity and facilitating CO desorption (Fig. 23d–f).[218] Likewise, precisely constructed homonuclear Fe$_2$N$_6$ diatomic sites anchored on NDPC were synthesized *via* pyrolysis of a Fe$_2$(CO)$_9$-containing ZIF-8 precursor. The Fe$_2$N$_6$ diatomic catalyst exhibits high CO FE of up to 96% at −0.6 V *vs.* RHE and a remarkably low Tafel slope of 60 mV dec^{-1}. This surpasses the performance of single atom FeN$_4$ catalysts which suffer from typically slow kinetics associated with sluggish CO desorption steps. DFT calculations show a significantly lower energy barrier for CO$_2$ activation and CO desorption on Fe$_2$N$_6$ compared to FeN$_4$ sites.[219]

Tuning the coordination motif always influences the CO$_2$RR by exploiting the interatomic electronegativity offset within a dual atom catalyst (DAC). For instance, CuNi–DSA/CNF DSA catalyst, featuring atomically dispersed Cu and Ni sites supported on PVP electrospun carbon nanofibers were synthesized and compared the performance to monometallic counterparts. DFT calculations reveal that the electronegativity difference between Cu and Ni subtly modulates the electronic structure of the active sites. This was experimentally verified and observed

high CO FE of 99.6% across a broad potential window (−0.78 to −1.18 V *vs.* RHE), a high TOF of 2870 h^{-1}, and exceptional long-term stability. The findings establish the interatomic electronegativity offset as a powerful design principle for highly selective and efficient CO$_2$RR electrocatalysts, offering valuable insights into catalyst design for sustainable energy conversion.[220] Similarly, the rational designing of O-bridged bimetallic sites significantly enhances the performance of single-site catalysts for CO$_2$ reduction. This approach provides key mechanistic insights and offers potential routes for high efficiency. For instance, an oxygen-bridged indium-nickel (In–O–Ni) dual-SACs supported on nitrogen doped carbon (InNi DS/NC) was successfully synthesized and In and Ni atoms decorated in a unique proximal arrangement, featuring an axial oxygen atom bridging the In and Ni centers (Fig. 23g–i). The oxygen bridge (In–O–Ni unit) was suggested as the crucial one to the catalyst's performance. The catalyst InNi DS/NC exhibits FE for CO production of >90% across a broad potential range (−0.5 to −0.8 V *vs.* RHE), reaching a maximum of 96.7% at −0.7 V *vs.* RHE with a high j_{CO} of 317.2 mA cm^{-2} at −1.0 V *vs.* RHE (in a flow cell). DFT calculations disclose that the electronic modification arising from the In–O–Ni DSA optimizes the adsorption energy of *COOH intermediate, by lowering the activation energy barrier for CO production. This effect is further enhanced by a reduction in the *COOH formation energy and enhanced CO desorption relative to their monometallic analogues.[124]

The importance of neighboring single-atom interactions in electrocatalysis, offering a new design strategy for multi-metal SACs. Most SACs are designed with isolated metal centers, neglecting possible long-range interactions between neighboring single atoms that could modulate catalytic performance. Inspired by metalloenzymes, where adjacent metal sites
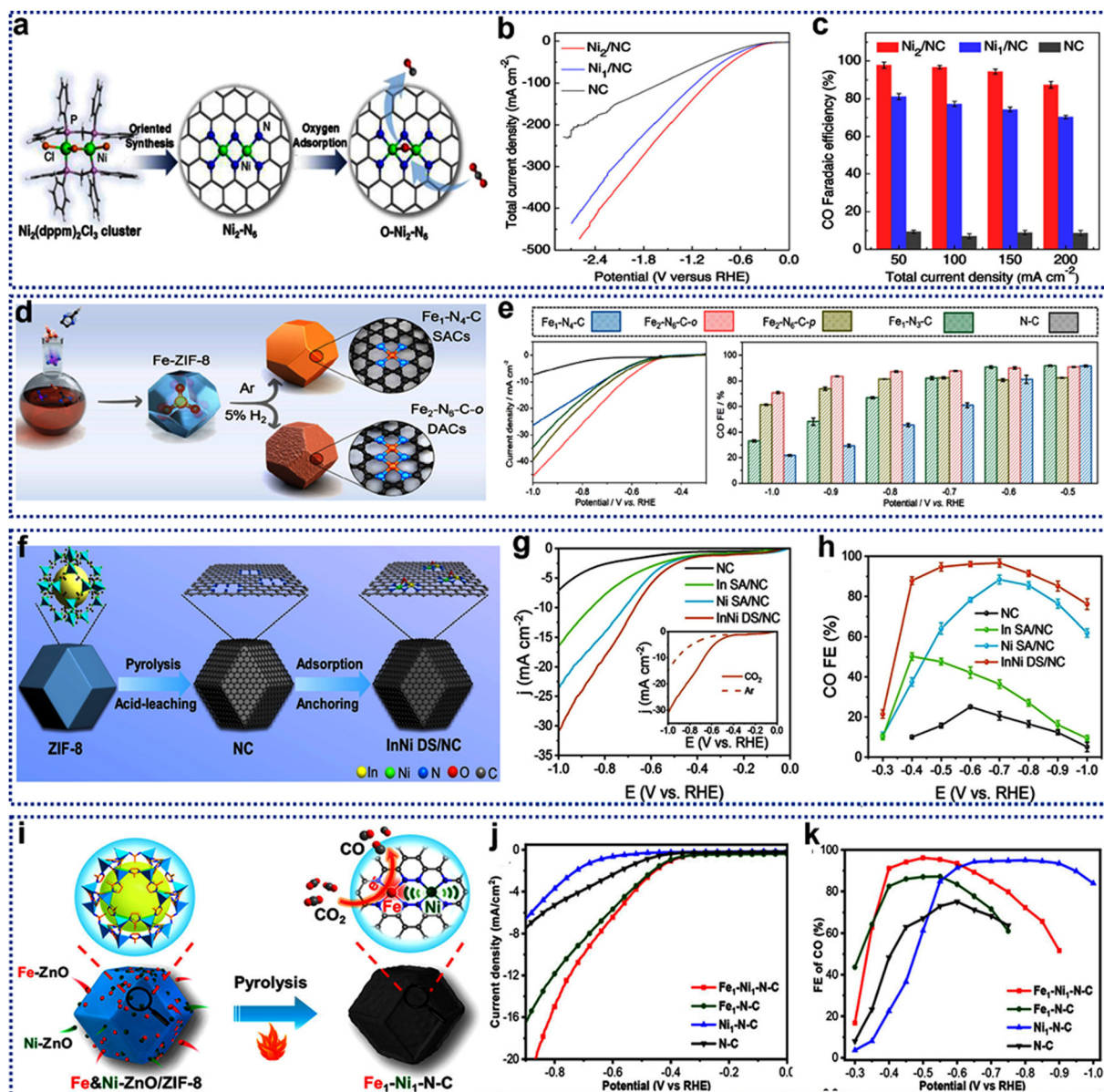
9670 | *Energy Environ. Sci.*, 2025, **18**, 9632–9712

This journal is © The Royal Society of Chemistry 2025

Fig. 23 (a) Schematic of Ni_2/NC synthesis. (b) LSVs of different Ni_2/NC catalysts. (c) CO FE for Ni_2/NC at various potentials. Reproduced from ref. 217 with permission from American Chemical Society, copyright 2021. (d) Pictorial representation of the synthesis of $Fe_2–N_6–C–O$. (e) LSV curve and FE of CO for $Fe_2–N_6–C–O$ at various potentials. Reproduced from ref. 218 with permission from American Chemical Society, copyright 2022. (f) Pictorial representation of the synthesis of InNi DS/NC. (g) LSV curve of InNi DS/NC catalyst. (h) CO FE for InNi DS/NC at various potentials. Reproduced from ref. 124 with permission from Wiley, copyright 2023. (i) Schematic of $Fe_1–Ni_1–N–C$ synthesis. (j) LSVs of different $Fe_1–Ni_1–N–C$ catalyst. (k) FE of CO for $Fe_1–Ni_1–N–C$ at various potentials. Reproduced from ref. 221 with permission from American Chemical Society, copyright 2021.

cooperate in substrate activation, this study by Jiao et al. explores the non-bonding interactions between Fe and Ni single atoms in a NDC ($Fe_1–Ni_1–N–C$) catalyst for CO_2 electro-reduction. $Fe_1–Ni_1–N–C$ was synthesized through a Zn-assisted atomization strategy, using the direct annealing of MOFs incorporating Fe and Ni-doped ZnO NPs (Fig. 23j–l). The $Fe_1–Ni_1–N–C$ catalyst demonstrated a remarkably high CO FE of 96.2% at −0.5 V, significantly outperforming $Fe_1–N–C$ and $Ni_1–N–C$ catalysts composed of isolated Fe or Ni single atoms. The superior activity of $Fe_1–Ni_1–N–C$ is attributed to a synergistic non-bonding interaction between the adjacent Fe and Ni single-atom pairs. DFT

calculations reveal that this interaction significantly activates the Fe atoms to promote the formation of the COOH* intermediate.[221]

4.2.14. Morphology, porosity, and support effects. The hierarchical porosity of MOFs and COFs influences CO_2 diffusion and accessibility to active sites. Micropores facilitate high CO_2 uptake, while mesopores enhance mass transport and reaction kinetics. The rational design of pore size and connectivity improves selectivity toward specific CO_2 reduction products. The interaction between the single-atom site and carrier the support material (e.g., carbon, metal oxides) affects electron transfer efficiency. Graphene based carrier supports enhance

conductivity and stabilizes the metal center, preventing aggregation. Efficient charge transfer between the single-atom site and the conductive network is critical for catalytic performance. Integration with conductive materials (*e.g.*, carbon nanotubes, and graphene) improves charge mobility. Proton-coupled electron transfer (PCET) dynamics govern selectivity toward CO, CH_4, or multi-carbon products. SACs suffer from metal leaching and aggregation under operational conditions. Robust MOF and COF frameworks prevent metal migration and enhance long-term stability. Post-synthetic modifications and defect engineering improve SAC resilience.

Tuning the morphology of the precursor is considered one of the most effective synthetic strategies for developing highly efficient and selective electrocatalysts. For instance, interconnected Ni–N-doped porous carbon (NiNPIC) materials were synthesized using Zn–Ni bimetallic MOFs *via* a simple and rapid ultrasonic-assisted synthesis method. The approach enabled precise control over the amount of Ni incorporated into the final catalyst. The NiNPIC catalysts demonstrated a high CO FE of 95.1% with CO current density of 10.2 mA cm^{-2}.[222] Traditional methods for synthesizing carbon-based SACs using electric heating are time-consuming, energy-intensive, and require inert gas protection. These methods also suffer from the potential aggregation of single atoms during the extended heating period. The researchers used a microwave-assisted rapid pyrolysis method to overcome the drawbacks of conventional electric heating. They used a Ni-doped ZIF (Ni–ZIF-8) as a precursor, and the $ZnCl_2$/KCl mixture acted as a microwave absorber, dramatically reducing pyrolysis time to just 3 minutes while ensuring complete carbonization without needing inert gas protection. The KCl concentration influenced the catalyst's morphology, composition, and electrocatalytic performance. The optimized Ni_1-N-C catalyst (Ni_1–N–C–50, produced using a 50 : 1 KCl/$ZnCl_2$ ratio) displayed exceptional activity and selectivity for CO_2 electroreduction with high FE for CO (up to 96%).[223] The catalysts with high micropores and mesopores generated during pyrolysis enhance CO_2 adsorption, and mass transport and prevent bubble formation in the electrolyte, both improving overall performance. The researchers designed a hierarchical nanoporous Ni–N–C catalyst obtained from a porphyrin-based zirconium MOF (PCN-222) synthesized from TCPPNi [TCPP = meso-tetra(4-carboxyphenyl)porphyrin] and $ZrOCl_2$ (Fig. 24a and b). The Ni_{20}–N–C catalyst delivered high FE for ($\sim$99%) at −0.6 V *vs.* RHE and partial current densities for CO in 2 M $KHCO_3$ (200 mA cm^{-2} at −0.30 V *vs.* RHE, highlighting the enhancement enabled by the improved mass transfer.[224] The principles of differing diffusion rates are leveraged in targeted ways to modify the structure and improve performance in SACs. The Kirkendall effect is employed indirectly during the synthesis process by introducing a sacrificial template material. During high-temperature pyrolysis, the more mobile elements diffuse out, creating voids, porosity and potentially unique architectures within the solid framework and the less mobile element is left behind. The resultant material will have tailored porosity and offer improved catalyst dispersion that simultaneously influences reactant diffusion and mass transport. The researchers synthesized a multicomponent catalyst, NiMn–N–C,

by introducing a trace amount of Mn into a Ni–N–C catalyst precursor derived from a MOF (Fig. 24f–h). The addition of Mn, even in trace amounts, triggers the Kirkendall effect during the pyrolysis step of catalyst synthesis and causes significant alterations in the catalyst's morphology and changes in surface chemical composition. The optimized NiMn–N–C catalyst exhibits a high CO FE of over 90% across a significant range of applied potentials, outperforming simpler, standard non-Mn catalysts.[225] Although MOFs can be employed as an excellent precursor for the synthesis of SACs, most of the active sites are buried inside the carbon matrix, which hinders the accessibility of active sites. To overcome this issue, Xi Chen *et al.* introduced large mesopores into the nano frames to increase the availability of single-atom sites and also boost mass and charge transports. The mesoporous carbon nano frames embedded with atomically dispersed catalyst FeSAs/CNF-900 from Fe-doped MOFs demonstrated remarkable performance and exhibited a high CO FE of 86.9% at −0.47 V *vs.* RHE and a CO partial current density of 3.7 mA cm^{-2}. Also, it was confirmed that the Fe centers predominantly exist in a porphyrinic Fe–N_4 coordination environment, which optimally modulates electronic properties and enhances *COOH intermediate stabilization (Fig. 24c–e).[226] Precise morphological control of MOF is crucial, offering potential avenues for the highly targeted design and fabrication of efficient electrocatalysts for CO_2RR. For instance, by tuning the MOF precursor morphology (controlled through the addition of different salts during synthesis), the relationship between the morphology and composition of a multicomponent copper-based nanoreactor catalyst was explored by Wanfeng Xiong *et al*. Through the pyrolysis of MOF precursors with different structures (cuboctahedron, cube, truncated octahedron, and octahedron), the researchers synthesized copper-based nanoreactors with varied structures and compositions and evaluated their performance in electrocatalytic CO_2 reduction. Characterization reveals that CHK–COCTA possesses a unique combination of Cu–N_4 single-atom sites, Cu_2O nanoparticles, and metallic copper (Cu). These multiple components act synergistically as tandem catalytic sites. It was proposed that CO_2 is initially converted to CO at the Cu–N_4 sites, and subsequently, CO is converted to deep reduction products as denoted in eqn 4 and 5 (primarily CH_4, and lesser amounts of C_2H_4) at the Cu_2O/Cu sites.[227]

$$CO_2 + 8H^+ + 8e^- \rightarrow CH_4 + 2H_2O \quad 0.17 \text{ V } vs. \text{ RHE} \quad (4)$$

$$2CO_2 + 12H^+ + 12e^- \rightarrow C_2H_4 + 4H_2O \quad 0.08 \text{ V } vs. \text{ RHE} \quad (5)$$
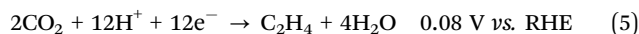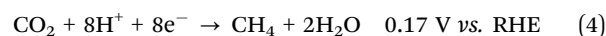
Improving both the number and availability of active sites is crucial for better catalytic performance. The hierarchical hollow structure facilitates increased active site accessibility, faster reaction kinetics, and high selectivity and stability. The researchers synthesized a series of Ni SACs with different morphologies (hierarchical hollow, nanosheets, nanorods, and solid cubes) by carefully controlling the solvent mixture during MOF precursor synthesis (Fig. 24i–k). This enabled them to compare the effect of morphology on catalyst activity while maintaining the chemical composition consistently. The Ni SAC with an urchin-like hierarchical hollow structure (Ni/HH) showed superior performance

9672 | *Energy Environ. Sci.*, 2025, **18**, 9632–9712

This journal is © The Royal Society of Chemistry 2025
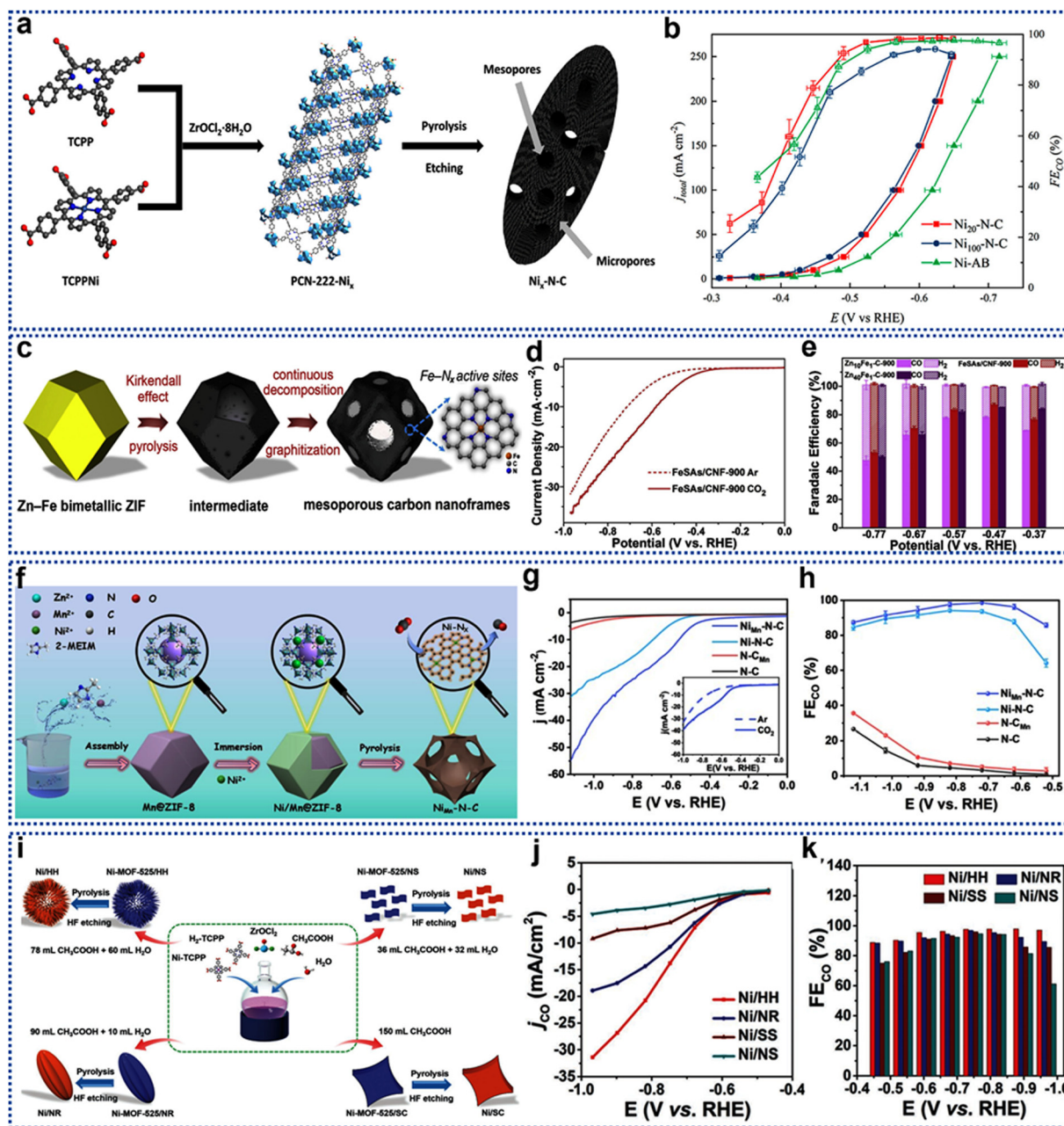
Fig. 24 (a) Illustration of Ni_x–N–C catalyst fabrication. (b) Total current density and CO faradaic efficiency (FE) vs. potential for Ni_{20}–N–C, Ni_{100}–N–C, and Ni–AB catalysts. Reproduced from ref. 224 with permission from American Chemical Society, copyright 2020. (c) Schematic illustration of FeSAs/CNF-900 formation. (d) Linear sweep voltammograms (LSVs) of FeSAs/CNF-900. (e) CO partial current densities for Zn_xFe_y–C–T catalysts at various potentials. Reproduced from ref. 226 with permission from Elsevier, copyright 2020. (f) Schematic illustration of NiMn–N–C synthesis. (g) LSVs of NiMn–N–C. (h) CO FEs of NiMn–N–C. Reproduced from ref. 225 with permission from Royal Society of Chemistry, copyright 2025. (i) Preparation of Ni SACs with urchin-like hierarchical architecture (Ni/HH), nanosheets (Ni/NS), nanorods (Ni/NR), and solid cubes (Ni/SC). (j) CO partial current densities (j_{CO}) of Ni SACs. (k) CO FEs of Ni SACs. Reproduced from ref. 228 with permission from Wiley, copyright 2023.

for the selective electroreduction of CO_2 to CO with higher FE for CO (up to 98%) compared to other Ni SAC morphologies, such as nanosheets, nanorods, and solid cubes. *In situ* attenuated total reflection surface-enhanced infrared (ATR-SEIRAS) spectroscopy revealed that Ni/HH facilitated the formation of the *COOH intermediate, leading to faster reaction kinetics. The overall superior performance was attributed to the higher accessibility of active sites within the porous structure, which collectively

contributed to enhanced catalytic activity.[228] Creating highly active and selective CO_2RR electrocatalysts remains a significant challenge. The paper investigates the use of an amino-functionalized MOF as a precursor to generate a unique electrocatalyst with improved performance. An amino-functionalized nickel-based MOF (NH_2–Ni-MOF) was synthesized and subsequently used as a precursor to derive a novel Ni SAC embedded in multilayer nitrogen-doped graphene (Ni–NG–acid). Control

samples, including a similar MOF without amino groups (Ni-MOF) leading to a catalyst (Ni NPs@NG–acid), were synthesized for comparison. The Ni–NG–acid catalyst demonstrated excellent performance for CO_2RR to CO, exhibiting FE over 90% within a wide potential window (-0.6 to -1.2 V $vs.$ RHE), with a maximum efficiency of 97% at -0.79 V $vs.$ RHE. A high CO partial current density (27.2 mA cm^{-2}) was also observed. The annealing temperature optimization tests demonstrated the effect of various temperatures on the structural and compositional properties of the catalysts with optimal performance occurring at around $1000\ ^\circ$C.[229]

4.2.15. SAC-based on core–shell tandem. The construction of SACs from MOFs using oxide-mediated core–shell strategies represent one of the most fascinating approaches. By coating MOF precursors with oxide layers such as SiO_2, ZnO, and Cu_2O, metal aggregation during high-temperature pyrolysis can be effectively suppressed, enabling the stabilization of isolated single atoms within a porous carbon matrix. Beyond physical confinement, these oxide shells modulate the coordination environment, introduce structural defects, and tailor the

porosity of the final material. The mesoporous structure ensures increased exposure of active sites, leading to superior electrocatalytic stability and reusability over prolonged operation. In such context, Xiaohui Sun $et\ al.$ developed a mesoporous NDC (mesoNC-Fe) catalyst containing atomically dispersed iron sites for electrocatalytic CO_2 reduction (eCO$_2$RR). The MOF synthesis involves a SiO_2 assisted templating strategy to effectively prevent Fe nanoparticle aggregation while maintaining a high surface area and porosity (Fig. 25a–c). Using spectroscopic characterizations, the existence of a porphyrinic Fe-N$_4$ coordination environment was confirmed. The catalyst exhibits exceptional activity and selectivity, achieving a FE of $\sim$85% for CO at -0.73 V $vs.$ RHE, and the CO partial current density (j_{CO}) reached 3.7 mA cm^{-2}. In particular, the mesoNC–Fe demonstrates a shift in optimal CO production to lower overpotentials compared to conventional Fe–N–C catalysts by reducing energy input for efficient CO_2 valorisation.[230] Like SiO_2, a polystyrene (PS) sphere can be used as a template to grow a Zn-based metal–organic framework (ZIF-8) shell, creating a core–shell structure (PS@ZIF-8). Removing the PS core via solvent treatment and
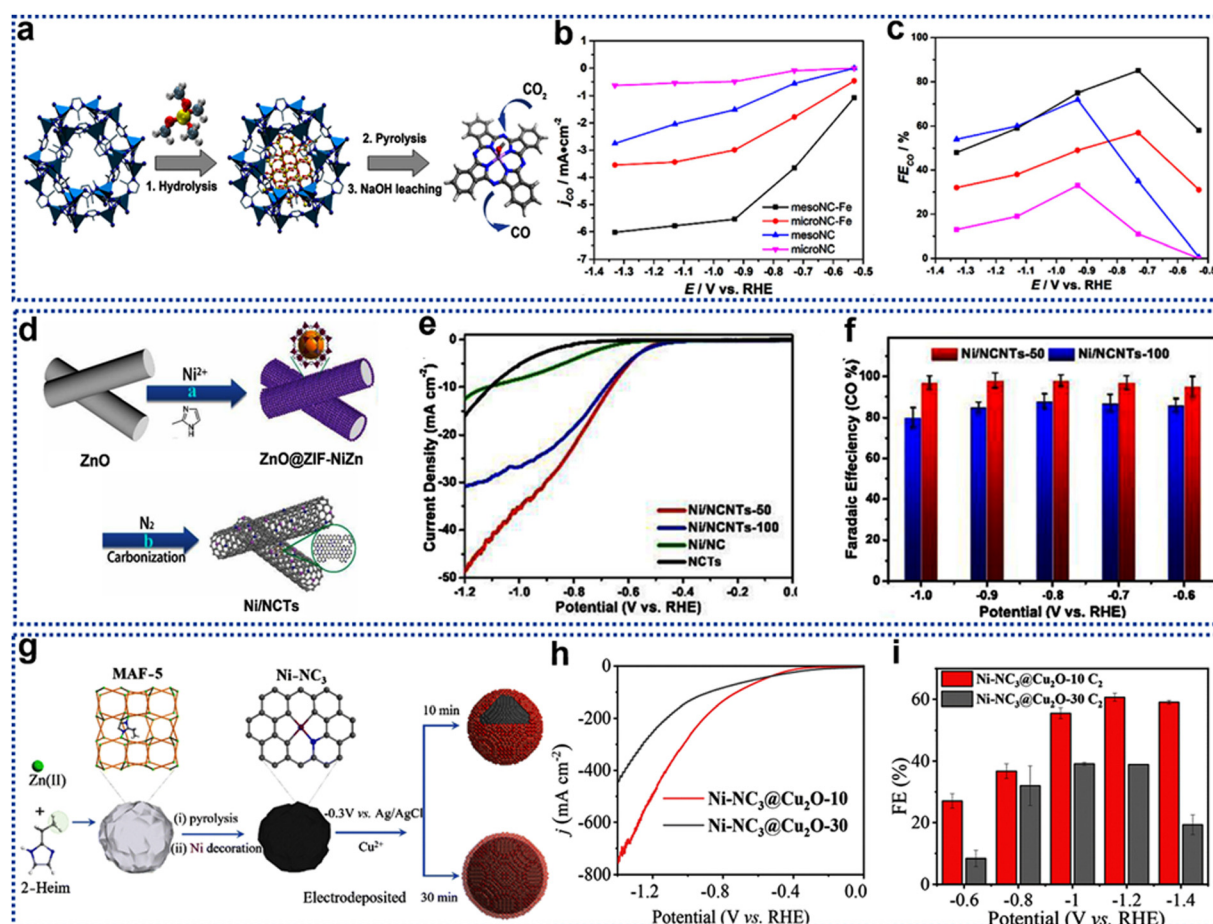
Fig. 25 (a) Schematic of mesoNC-Fe synthesis from ZIF-8-Fe@SiO$_2$. (b) CO partial current density for mesoNC–Fe. (c) CO faradaic efficiency (FE) for mesoNC–Fe at various potentials. Reproduced from ref. 230 with permission from Elsevier, copyright 2019. (d) Schematic of ZnO@ZIF-NiZn core–shell nanorod synthesis and Ni/NCNT fabrication. (e) Linear sweep voltammograms (LSVs) of Ni/NCNTs. (f) CO FE for Ni/NCNTs at various potentials. Reproduced from ref. 232 with permission from Elsevier, copyright 2020. (g) Schematic of NiNC$_3$@Cu$_2$O fabrication. (h) LSVs of NiNC$_3$@Cu$_2$O. (i) CO FE for NiNC$_3$@Cu$_2$O at various potentials. Reproduced from ref. 233 with permission from Royal Society of Chemistry, copyright 2025.

subsequent controlled pyrolysis of the resulting hollow ZIF-8 shell under a nitrogen atmosphere yields the final hollow porous carbon (HPC) catalyst. Using this method, the researchers synthesized an HPC catalyst containing a very high concentration (11.3 wt%) of atomically dispersed zinc (Zn) and uniformly distributed nitrogen (N) dopants. The resultant HPC-800 catalyst exhibits exceptional catalytic activity towards CO_2 cycloaddition with epoxides at ambient temperatures under light irradiation which enables highly effective conversion to occur at this substantially lower temperature.[231] Likewise, to create a highly effective and robust electrocatalyst for CO_2RR, the slow reaction kinetics and current density to be enhanced. To overcome these issues, a core–shell strategy was used. In detail, the self-sacrificial template method was employed where ZnO nanorods served as the core, while a bimetallic ZIF (ZIF-NiZn) acted as the shell to form the core–shell structure (Fig. 25d–f). Pyrolysis and acid etching of the ZnO core yield leave atomically dispersed Ni species on nitrogen-doped carbon nanotubes (Ni/NCTs). The Ni/NCTs catalyst demonstrated high CO selectivity, achieving nearly 100% FE at −0.6 V to −1.0 V *vs.* RHE. The Ni/NCTs had a hierarchically porous structure with numerous nanotubes, contributing to enhanced mass transport and greater accessibility of the active sites.[232]

The strategic combination and engineering of distinct catalytic centers can significantly enhance CO_2RR performance, enabling the production of highly valuable multi-carbon products. The researchers synthesized a Ni–NC_3@Cu_2O core–shell nanoreactor where single-atom Ni–NC_3 is partially or fully encapsulated by electrodeposited Cu_2O. Ni–NC_3 was synthesized through the carbonization of a metal-azolate framework (MAF), followed by the deposition of a Cu_2O nanoparticle shell using a simple, controllable electrochemical deposition process (Fig. 25g–i). Ni–NC_3@Cu_2O-10 catalyst exhibited an impressively high FE for C_2 products, achieving a FE for ethanol of 55.5% at −1.0 V *vs.* RHE and reaching as high as 60.6% under a slightly stronger driving force (−1.4 V *vs.* RHE), surpassing many previous reports. The Ni–NC_3 core component provides CO intermediates which then undergo further reaction over Cu_2O where C–C coupling takes place.[233] The successful creation of a novel tandem catalytic system demonstrates exceptionally high efficiency and an impressive degree of control over product selectivity to maximize specific outputs. The author synthesized a tandem catalyst by incorporating Ni SAs into ZIF-8 through an ion exchange method, resulting in a highly uniform distribution of single-atom nickel active centers throughout the carbon matrix. Subsequently, Cu NPs and Ni@ZIF-8 materials were physically mixed and subjected to pyrolysis at 900 °C under an inert Ar atmosphere, followed by acid-washing. This process produced a high density of catalytic centers within this advanced composite material. The catalyst, Ni SACs–Cu NPs, consists of Ni SACs encapsulated within copper nanoparticles (Cu NPs) predominantly exhibiting the (111) crystal facet. This unique design enables efficient and selective CO_2 reduction through cooperative catalysis, where Ni SACs generate CO, which subsequently undergoes C–C coupling reactions on the Cu NPs, leading to the production of acetate (60%) and/or syngas with highly tunable CO/H_2 ratio.[234]

4.2.16. Scale-up and free-standing SACs. The design strategy and direct implementation of the hierarchically structured gas diffusion electrode present a major step toward enabling the large-scale production of CO from atmospheric CO_2. A high-yield, elastic, and free-standing Ni SAC decorated porous carbon membrane (NiSA/PCFM) catalyst was synthesized using an electrospinning technique, followed by controlled thermal treatment using a mixture containing ZIF-8 nanoparticles, nickel nitrate, and polyacrylonitrile (PAN) (Fig. 26a–c). The membranes were then pyrolyzed to produce NiSA/PCFM catalyst. The NiSA/PCFM catalyst exhibited 96% CO FE at −0.7 V RHE. The NiSA/PCFM exhibited industrial-level activity with a partial current density of 308.4 mA cm^{-2} for CO at −1.0 V *vs.* RHE with 88% FE over 120 h.[235] Utilization of a highly porous scaffold with appropriate functionalities and efficient single-atom dispersion maximizes atom utilization efficiency compared to traditional nanoparticle catalysts, where only surface atoms are active. Through such structured designs higher efficiency and selectivity can be achieved, and product selectivity can potentially be tuned due to the limited mass transfer during CO_2RR. The authors used a TCNF structure as a support not merely as a structural component but its porous, interconnected architecture provides several crucial advantages. The abundant, exposed single-atom sites maximize the electrochemically active surface area. A comparison with similar Cu SACs that lack the through-hole architecture demonstrated its clear benefits. The CuSAs/TCNF architecture exhibited a remarkable FE of 44% for methanol (as denoted in eqn (6)) with a high partial current density (−93 mA cm^{-2}). The selectivity for methanol was nearly absolute, outperformed many previously reported CO_2 reduction catalysts (Fig. 26d–f).[236] Most SACs are in powder form, requiring additional steps (*e.g.*, binder coating) for electrode fabrication which complicates the process and can reduce the stability of the electrode. Therefore, developing a self-supported electrode incorporated with single Ni-atom can overcome this limitation. The researchers used electrospinning method to synthesize self-supported porous carbon nanofiber (PCNF) electrode decorated with atomically dispersed Ni catalysts using polyacrylonitrile (PAN), melamine, and Ni-ZIF8 precursor mixtures. The resulting electrospun nanofibers were then subjected to high-temperature treatment in a nitrogen atmosphere to achieve carbonization and form the Ni–PCNF composite electrode. The optimal Ni–PCNF–0.5PMMA catalyst exhibited a CO FE of 98.6% at −1.5 V (*vs.* RHE) in the H-cell and demonstrated remarkably stable high current density ($>$100 mA cm^{-2}) in flow-cell tests. The improved performance was ascribed to the synergistic effects of the porous structure, which facilitated efficient CO_2 and electrolyte mass transport, and the high activity of single Ni atoms.[237]

$$CO_2 + 6H^+ + 6e^- \rightarrow CH_3OH + H_2O \quad -0.39 \text{ V } vs. \text{ NHE} \quad (6)$$
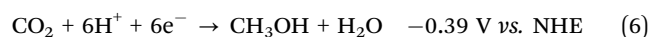
Substrate functionalization in SACs is a versatile approach that significantly influences and optimizes catalytic properties. Understanding how modifications to substrates interact with SACs opens opportunities to design even more advanced catalytic systems. Functionalization alters the substrate's electronic
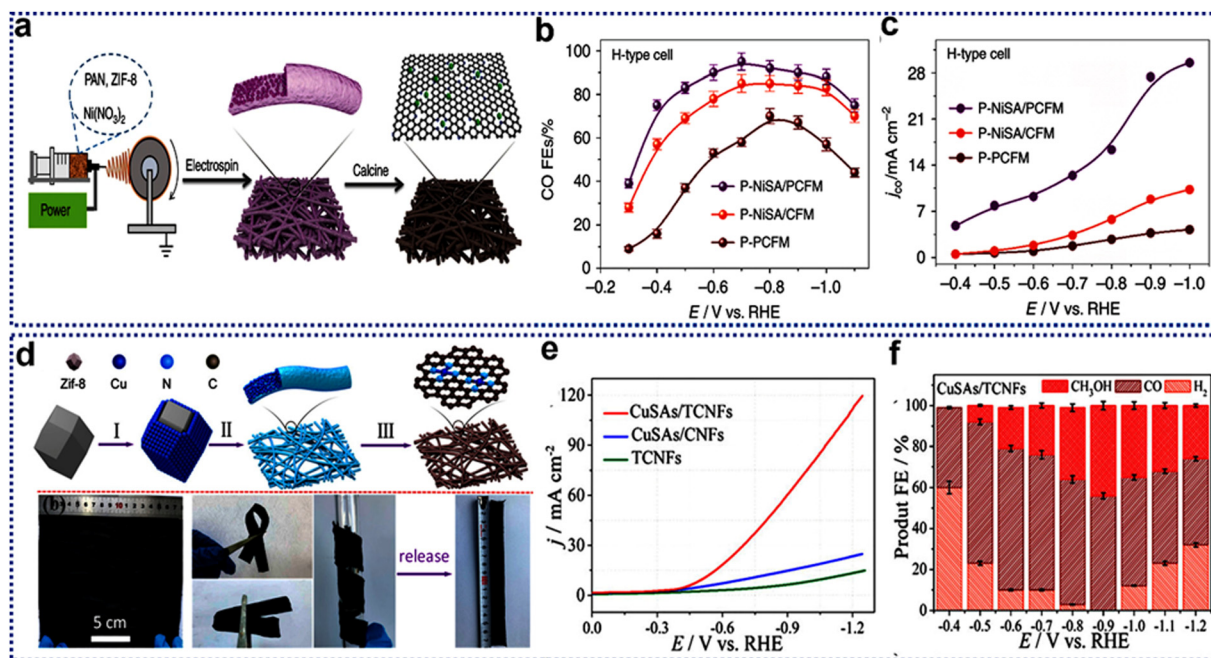
This journal is © The Royal Society of Chemistry 2025

Energy Environ. Sci., 2025, **18**, 9632–9712 | **9675**

Fig. 26 (a) Schematic of NiSA/PCFM catalyst synthesis via electrospinning. (b) CO FE for NiSA/PCFM. (c) Partial current densities for NiSA/PCFM at various potentials. Reproduced from ref. 235 with permission from Nature (CC-BY 4.0), copyright 2020. (d) Synthesis and images of flexible CuSAs/TCNFs membranes. (e) Linear sweep voltammograms (LSVs) of CuSAs/TCNFs membranes. (f) CO FE for CuSAs/TCNFs membranes at various potentials. Reproduced from ref. 236 with permission from American Chemical Society, copyright 2019.

and geometric properties to create a more favourable environment for the atomically dispersed metal, ultimately impacting the catalyst's overall behavior. For instance, Shengjie Wei et al. used a planar chlorination strategy, which modifies the $Zn-N_4$ sites coordination environment, contrasting with previous axial chlorination methods. The adjacent $C-C_1$ bond induces self-reconstruction, transforming traditional, less active planar $Zn-N_4$ sites into more active, lower coordinated, and symmetry-broken $Zn-N_3$ sites. This process modifies the electronic structure of the catalytic sites to promote stronger binding to reaction intermediates. This work demonstrates a ground-breaking method for dramatically improving CO_2RR performance via symmetry breaking at the atomic scale. The optimized Zn–SA/CNCl–1000 catalyst exhibits FE for CO of about 97% and a partial current density of 271.7 mA cm^{-2} at −0.93 V vs. RHE. In situ EXAFS measurements demonstrate the structural changes of the Zn sites during the catalytic process, support the proposed self-reconstruction of the catalytic site via $Zn-N_4$ into $Zn-N_3$ active species during electro reduction reactions. DFT calculations verify the adjacent C–Cl bond in the modified $Zn-N_3$ site facilitates easier protonation of the adjacent nitrogen atom, altering the $Zn-N_4$ site symmetry towards enhanced COOH* adsorption, and lowering the energy barriers for the rate-determining steps to improve CO_2RR to CO conversion selectivity.[238] This research details a highly efficient and selective MOF-derived nickel SACs (NaCl@Ni/Zn-6) for electrolytic bicarbonate conversion to CO. The catalyst's exceptional performance stems from a unique combination of atomically dispersed Ni active sites and abundant mesopores (around 35.4 nm) created by a NaCl-assisted pyrolysis that dramatically improves local reactant-transport

within the catalyst. The catalyst's performance significantly exceeds that of precious metal-based catalysts, highlighting its potential for large-scale applications in CO_2 reduction. The researchers employed a one-step pyrolysis approach to synthesize a Ni SAC starting from a ZIF-8 precursor. Enhanced mass transport results in improved electrocatalytic performance, significantly exceeding precious metal catalysts under comparable test conditions. NaCl@Ni/Zn-6 displays an impressively high FE for CO (FE_{co}) of 67.2% with a current density of 100 mA cm^{-2}.[239] The synthesis of covalent triazine frameworks (CTFs) with high crystallinity is very challenging. Moreover, very rarely was CTF used as a source for the synthesis of SAC. The researchers developed a novel, efficient method for synthesizing crystalline CTFs and subsequently utilized them as a platform for creating SACs for eCO_2R. A solvent- and catalyst-free method yielded crystalline CTFs with a BET surface area of 255 m^2 g^{-1}. By treatment with molten $ZnCl_2$ significantly increased the surface area to 663 m^2 g^{-1} and single-atom $Ni-N_3-C$ sites were successfully generated. Electrochemical CO_2 reduction by $Ni-N_3-C$ sites demonstrated exceptional performance, with a maximum FE for CO production of 97.5% at −0.52 V (vs. RHE) at −1.02 V (vs. RHE).[240]

4.2.17. External factors: electrolyte effects. Electrolyte concentration is a critical design variable in CO_2 reduction, influencing both activity and selectivity through intricate, interconnected pathways. These pathways have a profound impact on reactivity and product selectivity. Specific cations in the electrolyte play a significant role by affecting CO_2 adsorption and reduction while simultaneously modulating HER suppression and reaction energetics. Certain cations enhance CO_2 adsorption and accelerate specific steps in CO_2RR kinetics by altering EDL structure while

selectively suppressing the HER pathway, thereby dramatically improving overall CO_2 reduction performance and maximizing CO selectivity. Electrolyte composition influences ion transport, EDL properties, and product selectivity. pH-dependent modulation of active sites also alters reaction thermodynamics and kinetics.

While the role of cations, particularly K^+, in influencing CO_2RR activity and selectivity is widely acknowledged, their precise mechanistic influence remains debated. Previous studies using Au-based catalysts yielded ambiguous results because the rate-determining step (RDS) in CO_2RR on Au is electron transfer, which is unlikely to be directly impacted by K^+. This research utilizes a highly symmetrical Ni–N_4 structure, largely inert in both CO_2RR and HER, allowing the isolation of K^+ effects and providing a clear platform for investigating K^+ precise mechanistic role

(Fig. 27a–c). In the absence of K^+, the Ni–N_4 catalyst exhibited little to no CO_2RR activity, with HER being the dominant reaction. However, upon adding K^+, the CO_2RR activity increased dramatically. A significant shift in the RDS occurred: from a concerted proton–electron transfer (CPET) in the absence of K^+ to a predominantly independent proton transfer when K^+ is present, lowering the overall reaction barrier and achieving near 100% CO FE at high current densities. *In situ* XANES measurements revealed that K^+ interacts non-covalently with chemisorbed CO_2, changing the bond geometry of CO_2 and its vibrational behaviour. These *in situ* findings directly illustrate how K^+ stabilizes chemisorbed CO_2. Grand canonical potential kinetics (GCP-K) simulations supported the experimental results showing a lower overall energy barrier for the K^+ influenced reaction pathway and a much lower onset potential (-0.524 V) compared
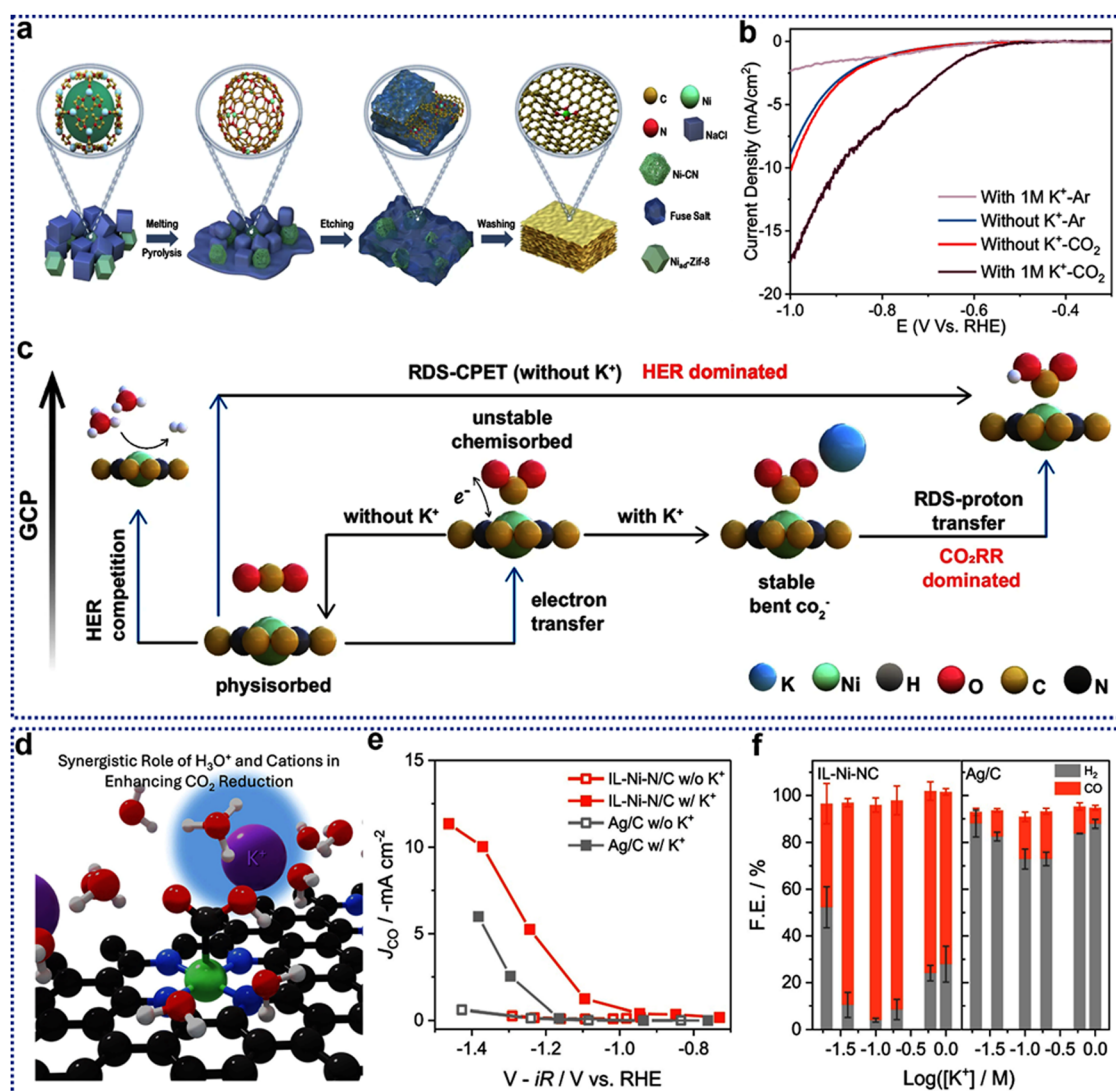
Fig. 27 (a) Schematic of Ni–N_4–HM synthesis. (b) Linear sweep voltammograms of Ni–N_4–HM in electrolytes of pH 3. (c) Proposed CO_2RR mechanism showing the effect of K^+ concentration on energy barriers for CO_2RR and HER. Reproduced from ref. 241 with permission from Nature, copyright 2024. (d) Pictorial representation of K^+ concentration effects in CO_2RR using Ni–N–C catalyst. (e) CO current density of IL–Ni–NC and Ag/C catalysts with and without added K^+. (f) CO faradaic efficiency (FE) for IL–Ni–NC and Ag/C at various potentials. Reproduced from ref. 242 with permission from Elsevier, copyright 2025.

to reported results using other Ni catalysts and far outperforming the HER. This study offers definitive experimental and theoretical evidence that K^+ facilitates the reaction by forming a non-covalent interaction with chemisorbed CO_2, stabilizing the chemisorbed intermediate, lowering the activation energy, and thus achieving highly efficient and selective CO_2 reduction. The findings directly reconcile experimental and theoretical studies on CO_2RR and address long-standing questions concerning the mechanistic role of cations in enhancing electrocatalytic activity.[241] Similarly, the effect of strong concentration on Ni–N–C electrocatalysts for CO_2 reduction in acidic media in strongly acidic conditions was explored. Hyewon Yun *et al.* demonstrated high concentrations of cations (specifically K^+) synergistically enhance the CO_2RR activity of Ni–N–C catalysts in acidic media (Fig. 27d–f). This effect surpasses simple additive contributions, showcasing a true synergistic interaction between the cations and protons. A shift from H_2O to H_3O^+ as the primary proton source accelerates CO_2RR kinetics at strongly acidic pH levels (<2). This is significant because acidic environments inherently favour protonation processes but hinder CO_2 reduction due to enhanced HER competition and low CO_2 solubility. It was demonstrated that leveraging the accelerated H_3O^+ protonation in high CO activity in acidic MEA resulted in nearly 95% FE for over 50 h at -100 mA cm^{-2}. The enhanced activity of IL–Ni–NC under acidic conditions was significantly influenced by efficient control over the transport of protons and cations, resulting in overall superior catalytic performance. The importance of controlled proton delivery and reduced HER were demonstrated. *In situ* ATR-SEIRAS data reveals increased CO adsorption at higher K^+ concentrations, especially at pH 1.7, which confirms the strong influence of cations in improving catalytic kinetics and shows distinctly varied interfacial water behaviour and local pH under different acidic conditions, explaining the role of H_3O^+ in accelerating reaction rates and stability in an acidic MEA under specific conditions. Furthermore, DFT calculations exposed lower free energy barriers for COOH formation under higher K^+ concentrations due to significant H_3O^+ effects and further synergistic effects between cations and protons.[242]

This comprehensive understanding of multifaceted factors will pave the way for the rational design of next-generation catalysts for sustainable CO_2 conversion technologies. In summary, coordination tuning in MOF and COF based catalysts plays a pivotal role in optimizing the eCO_2RR by precisely modulating the electronic structure, local charge distribution, and active site environment. By strategically adjusting metal ligand interactions, heteroatom doping, and substrate functionalization, these porous frameworks enhance catalytic activity, selectivity, and stability while facilitating efficient electron transfer and intermediate stabilization. Such tunability not only deepens the mechanistic understanding of CO_2 electro reduction but also offers a rational design approach for next-generation catalysts, contributing to the development of sustainable carbon-neutral technologies.

4.3. Photocatalytic valorisation of CO_2

Photocatalytic CO_2 reduction offers a promising route to control CO_2 levels in the atmosphere while simultaneously producing valuable chemicals using sunlight as a clean and sustainable energy source. This process mimics natural photosynthesis, harnessing solar energy to convert CO_2 into CO, CH_4, CH_3OH, and HCOOH. However, developing efficient and selective photocatalysts remains a significant challenge. The generally accepted mechanism of photocatalysis involves several key steps, including charge separation, CO_2 activation, and efficient electron transfer for the conversion of CO_2 into valuable products. Each of these steps must be optimized to enable effective catalytic processes. For a photocatalyst to be effective, it must efficiently absorb sunlight across a broad range of wavelengths, facilitate efficient separation of photogenerated electron–hole pairs, and minimize electron–hole recombination (Fig. 28). Various strategies, including bandgap engineering, surface modification, and the use of co-catalysts, have been explored to optimize light absorption and charge separation.[243,244]

Significant progress has been made in photocatalytic CO_2 reduction research, with various semiconductor materials (TiO_2, ZnO, CdS, *etc.*), MOFs, and single-atom catalysts being explored. However, improving the efficiency, selectivity, and long-term durability of these photocatalysts remains a key challenge in the field. Continued efforts in materials design, synthesis, characterization, and mechanistic understanding, along with advanced modeling, are expected to accelerate advancements and pave the way toward

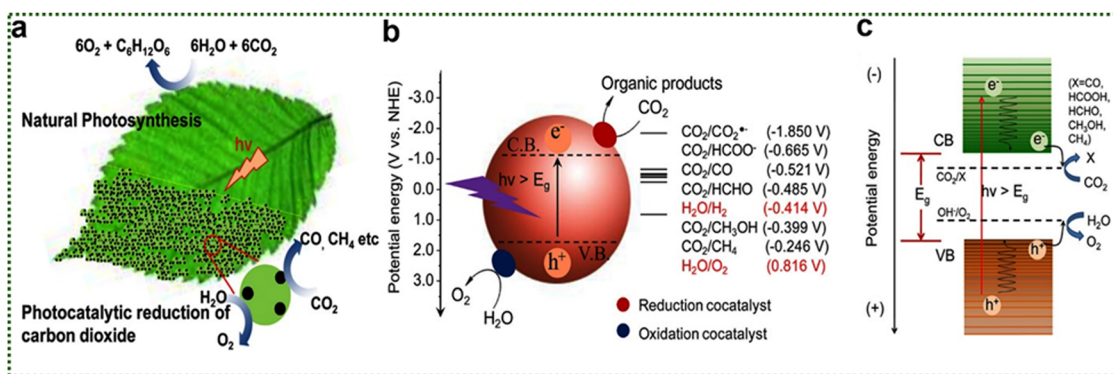**Fig. 28** (a) Schematic of artificial photosynthesis system. (b) Schematic illustration of the reaction mechanism. (c) Relative energy levels involved in semiconductor photocatalytic CO_2 reduction. Reproduced from ref. 243 with permission from American Chemical Society, copyright 2017.

9678 | *Energy Environ. Sci.*, 2025, **18**, 9632–9712

This journal is © The Royal Society of Chemistry 2025

cost-effective, scalable technologies for solar fuel production and carbon mitigation.[245,246] Coordination tuning plays a crucial role in optimizing the photocatalytic CO_2 reduction performance of MOF and COF based catalysts by precisely modulating the electronic structure, charge distribution, and local environment of active sites. By adjusting metal–ligand coordination, heteroatom doping, and linker functionalization, these porous frameworks can

enhance light absorption, facilitate charge separation, and stabilize key reaction intermediates. Such tunability not only improves catalytic efficiency and selectivity but also provides a platform for rational catalyst design aimed at sustainable CO_2 conversion. Several MOF and COF-based materials have been explored as photocatalysts for CO_2RR. For instance, 2,2′-bipyridine-based COF containing single Ni sites (Ni–TpBpy) was investigated as a

Fig. 29 (a) Schematic of CO_2 photocatalytic reduction using Ni–TpBpy. (b) and (c) CO and H_2 evolution by Ni–TpBpy under 1 and 0.1 atm CO_2. (d) CO_2 reduction yields (2 h reaction) using TpBpy with different metal ions. Reproduced from ref. 246 with permission from American Chemical Society, copyright 2019. (d) Synthesis of TPy-COF and BPy-COF for the fabrication of TPy-COF-Co and BPy-COF-Co. (e) Time-resolved generation of Gas (CO and H_2) over TPyCOF-Co. (f) Gas production rates in the CO_2 photoreduction over TPy-COF-Co, BPy-COF-Co, and TBp-COF-Co. Reproduced from ref. 247 with permission from Wiley, copyright 2025. (g) Synthesis of COFs with different N species (COF-Ph, COF-Py, COF-Pz) and their Co-coordinated counterparts (COF-Ph-Co, COF-Py-Co, COF-Pz-Co). (h) Photocatalytic CO_2 reduction activities (3 h) over various catalysts. (i) Time-dependent CO and H_2 evolution during photocatalytic CO_2 reduction by [Ru]-photosensitized COF-Py-Co. Reproduced from ref. 248 with permission from Elsevier, copyright 2025. (j) Pictorial representation of the synthesis of Mo-COF. (k) Photocatalytic evolutions of CO, C_2H_4 and CH_4 by Mo-COF. (l) Time-resolved generation of Gas (CO, C_2H_4, and CH_4) over Mo-COF. Reproduced from ref. 128 with permission from Elsevier, copyright 2021.

This journal is © The Royal Society of Chemistry 2025

Energy Environ. Sci., 2025, 18, 9632–9712 | 9679

photocatalyst for CO_2RR (Fig. 29a–c). Ni–TpBpy efficiently enhanced CO selectivity in aqueous media, achieving a yield of 4057 µmol g^{-1} over a 5-hour reaction with 96% selectivity.[246] Similarly, a CoN_4Cl_2 single site was fabricated by loading Co species into a 2,2′-bipyridine and triazine-containing COF. The TPy-COF-Co displayed a high CO production rate (426 mmol g^{-1} h^{-1}) turnover number (2095) and TOF (1607 h^{-1}). Theoretical calculation suggested the enhanced charge transfer from triazine-based COF framework to CoN_4Cl_2 sites facilitated CO_2 activation by lowering the energy barrier of *COOH generation (Fig. 29d–f).[247] In contrast, tuning the coordination number altered the product distribution significantly. For example, a 2,2′-bipyridine-based COF (TpBpy) with MoN_2 sites (Mo-COF) efficiently catalyzed CO_2 photoreduction to C_2H_4 with a selectivity of 32.92% along with

CH_4. This coordination tuning strategy in other catalytic systems opens new possibilities for photocatalytic CO_2 reduction to higher carbon products (Fig. 29j–l).[128] Similarly, single-atomic COF composed of different types of coordinated nitrogen atoms, such as imine, pyridine, and pyrazine N, were constructed to study their effects on electronic structure and photocatalytic CO_2 reduction. The imine and pyridine N atoms coordinated single-atomic Co COF exhibited a CO evolution rate of 85.5 µmol h^{-1} with 96.4% selectivity in the presence of Ru photosensitizer, outperforming pyrazine N atoms coordinated Co sites (24.3 µmol h^{-1}, 65.5% selectivity) (Fig. 29g–i).[248] Based on the polar coordination microenvironment, an effective Ni-SAs anchored on N, O sites of COF was synthesized using an atomic deposition method, as shown in (Fig. 30a), and
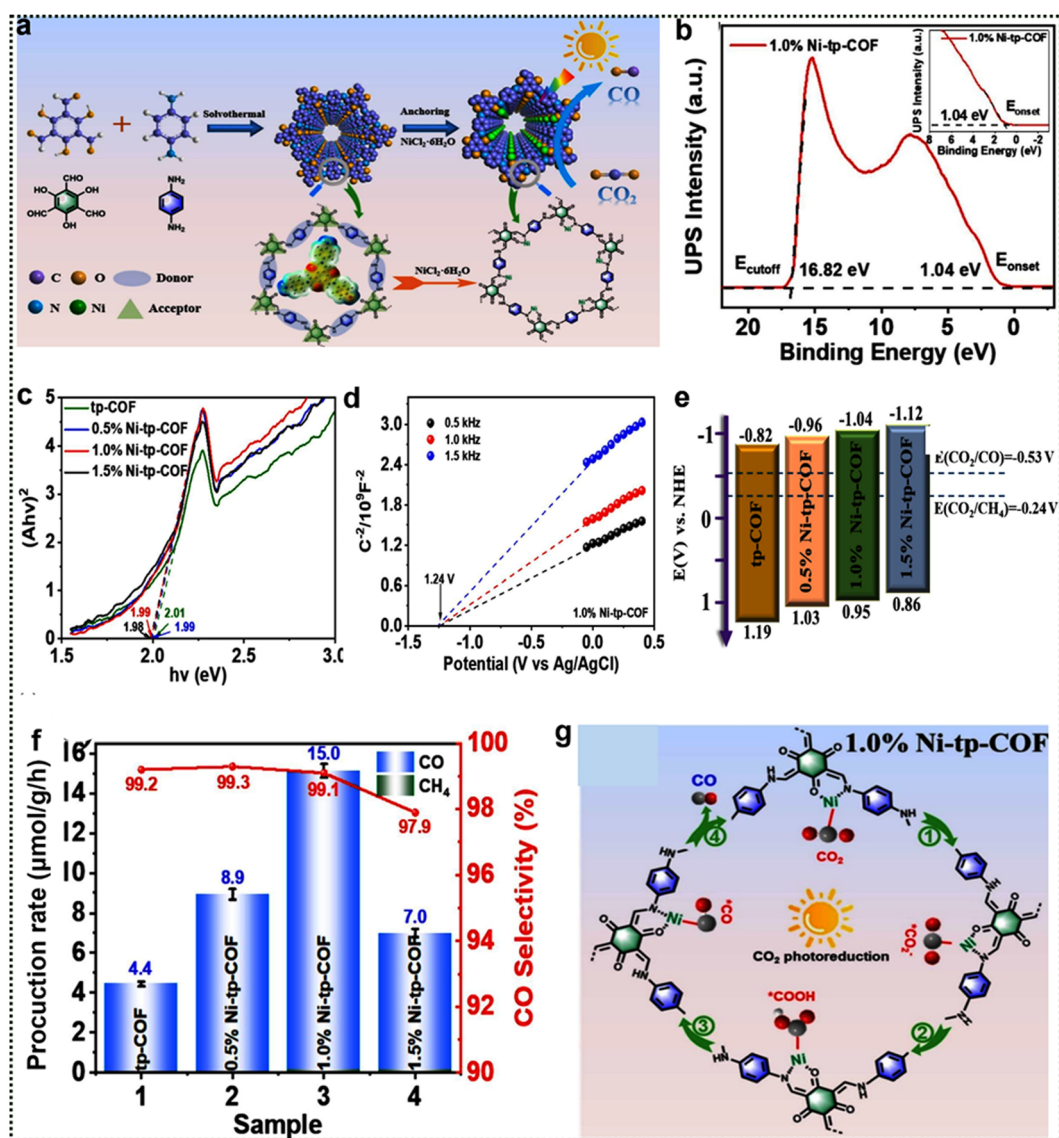
Fig. 30 (a) Schematic presentation of synthesis of Ni anchored COF. (b) UPS spectra of 1.0% Ni-tp-COF. (c) Tauc plots of tp-COF and Ni-tp-COF catalysts. (d) Mott-Schottky plot of 1.0% Ni-tp-COF. (e) Band structures tp-COF and Ni-tp-COF catalysts. (f) Photocatalytic CO_2 reduction, CO production, and the selectivity performance of the photocatalysts. (g) Mechanism of photocatalytic CO_2 reduction using 1.0% Ni-tp-COF under visible light. Reproduced from ref. 249 with permission from Elsevier, copyright 2025.

9680 | Energy Environ. Sci., 2025, 18, 9632–9712

This journal is © The Royal Society of Chemistry 2025

applied for efficient photocatalytic CO_2RR.[249] To understand the band structure of the photocatalyst, ultraviolet photo-electron spectroscopy (UPS) analysis was performed on 1.0% Ni-tp-COF (Fig. 30b). The valence band (VB) value was determined as 1.00 V, calculated from the cutoff energies (E_{cutoff}) of 16.82 eV and onset energies (E_{onset}) of 1.04 eV. The VB potential was calculated using the formula $EVB = 21.22 − (E_{cutoff} − E_{onset})$, resulting in a VB potential of 5.44 eV, which was then referenced to the reversible hydrogen electrode VB potential −4.44 eV. Furthermore, the band gap energy (E_g) for1.0% Ni-tp-COF was found to be 1.99 eV, closely matching that of pristine tp-COF 2.01 eV (Fig. 30c). Moreover, 1.0% Ni-tp-COF catalyst exhibited a positive slope in the Mott-Schottky plots, confirming their n-type semiconductor characteristics (Fig. 30d). For n-type semiconductors, the conduction band (CB) potential can be approximated to the flat band potential. The CB potentials, measured against Ag/AgCl, were found to be −1.02, and −1.24 V, corresponding to −0.82, −1.04 V versus the normal hydrogen electrode (NHE), respectively. Based on these values and the bandgap energies, the valence band (VB) potentials were calculated using the relation $E_{VB} = E_{CB} + E_g$ yielding VB positions of 1.19, 0.95 0.86 V versus NHE (Fig. 30e). Notably, the CB potentials of all samples are more negative than the reduction potential of CO_2 to CO, indicating a strong thermodynamic driving force for the CO_2 reduction reaction (CO_2RR) and demonstrating the excellent reductive capability of these photocatalysts. The 1.0% Ni-tp-COF catalyst produce with a yield of 15.0 $\mu mol\ g^{-1}\ h^{-1}$ and highly selective conversion of CO_2 to CO (>99%) (Fig. 30f). Under visible light irradiation, photogenerated electrons and holes are produced within the photocatalyst. These charge carriers drive the adsorption of CO_2 molecules onto the surface of catalytic active sites, forming adsorbed $*CO_2$ intermediates. Afterward, the $*CO_2$ species undergo a series of reduction steps: a one-electron transfer leads to the formation of *COOH intermediates, followed by a two-electron transfer resulting in the generation of *CO species. Finally, the *CO desorbs from the catalyst surface, leading to the production of CO gas (Fig. 30g). This sequence of adsorption, stepwise reduction, and desorption constitutes the fundamental mechanism underlying the photocatalytic valorisation of CO_2. Beyond the intrinsic catalytic sites in metal nodes and organic linkers, MOFs have also been extensively utilized as hosts for confining or supporting guest catalytic sites, leveraging their high surface area and well-defined porous structures. Additionally, MOFs can act as tailored microenvironments, influencing the catalytic behaviour and reactivity of encapsulated species.

MOF-derived materials, owing to their structural versatility and compositional tunability, have garnered significant attention as electrocatalysts for CO_2 reduction. Notably, heteroatom-doped carbon materials derived from MOFs provide a straightforward and effective strategy for designing high-performance CO_2RR catalysts. A MOF assisted synthetic approach for generating high-performance atomic pair photocatalysts for efficient CO_2 photoreduction to CO is considered highly promising. In particular, the synergistic effects of carefully tailored dual atomic catalytic sites enhance performance by modifying reaction

kinetics while significantly boosting the CO_2RR selectivity. For instance, Co_1Cu_1/NC was synthesized using a MOF-assisted strategy involving the pyrolysis of a ZIF-8 precursor, in which copper nitrate ions were incorporated into the cavities, and cobalt-tetrabenzoporphyrin (CoTBPP) was anchored onto the external surface of ZIF-8. Notably, characterization data divulge the 4N-coordinated metal atom ($N_2–Co–N_2–Cu–N_2$) in Co_1Cu_1/NC (Fig. 31a–c). The Co_1Cu_1/NC photocatalyst, exhibits significantly enhanced CO_2 reduction activity (22.46 $mmol\ g^{-1}$) in conjunction with $[Ru(bpy)_3]^{2+}$ as a photosensitizer, and a CO selectivity of 83.4% after 2 hours of visible-light irradiation. The excellent photocatalytic activity of Co_1Cu_1/NC is attributed to the formation of the *COOH intermediate, facilitated by a mechanism in which CO_2 activation and reduction are enabled through synergistic effects between neighbouring $Co–N_4$ and $Cu–N_4$.[250] Understanding the impact of coordination number in SACs photocatalytic CO_2RR is particularly intriguing, as it can influence the binding affinity of reactive intermediates and active sites at molecular level. For example, a series of Co single atom photocatalysts, $Co_{SA}–N_x/C$, with varying nitrogen coordination numbers, were synthesized, and their CO_2 photoreduction properties were investigated. The $Co_{SA}–N_2/C$ photocatalyst exhibited superior CO_2 photoconversion activity and CO selectivity (82.6%) compared to $Co_{SA}–N_3/C$ and $Co_{SA}–N_4/C$. Additionally, it demonstrated a high CO yield rate of 10 110 $\mu mol\ g^{-1}\ h^{-1}$ with outstanding stability.

The activity enhancement of $CoSA–N_2/C$ photocatalyst was ascribed to increased CO_2 adsorption due to the unoccupied Co 3d electronic orbitals and a reduction in *COOH intermediate energy barrier (Fig. 31d–f). Thus, the regulation of local coordination structure and its effect in the CO_2 photo reduction was emphasized.[251] Similarly, the breaking symmetry of SACs could boost performance and tune selectivity. For instance, Ni–SACs@BNC was synthesized and the Ni–SACs@BNC catalyst exhibited high photocatalytic CO_2 reduction activity and selectivity, achieving a CO evolution rate exceeding that of Ni–SACs@NC and the analogous control catalyst (N–C), reaching as high as 93.2% under optimized reaction conditions for 3 hours under visible light (Fig. 31j–k).[195] Similarly, SAC symmetry was further tuned using an axial coordination strategy. For example, atomically precise $Fe–N_4O$ active sites were generated via a facile, low-temperature (500 °C) top-down strategy, which involved high-temperature pyrolysis (500 °C) under Ar to achieve in situ direct atomization of Fe particles in the presence of NH_4Cl, significantly increasing the C=O content on the catalyst support. A clear positive correlation was found between C=O concentration, catalyst activity, and reaction selectivity. CO_2 photoreduction experiments using a $Ru(bpy)_3Cl_2$ photosensitizer demonstrated remarkably enhanced performance parameters and established both catalyst selectivity and activity. Fe–NO/NC achieved a high TON of 1494 in 1 hour for CO generation with 86.7% selectivity, demonstrating remarkable stability across multiple test cycles with consistently high performance (Fig. 31g–i).[252] The development of photocatalysts with hierarchical pores could alter the mass transport properties and electrical surface characteristics, potentially enhancing the efficiency overall photocatalytic

This journal is © The Royal Society of Chemistry 2025

Energy Environ. Sci., 2025, 18, 9632–9712 | 9681
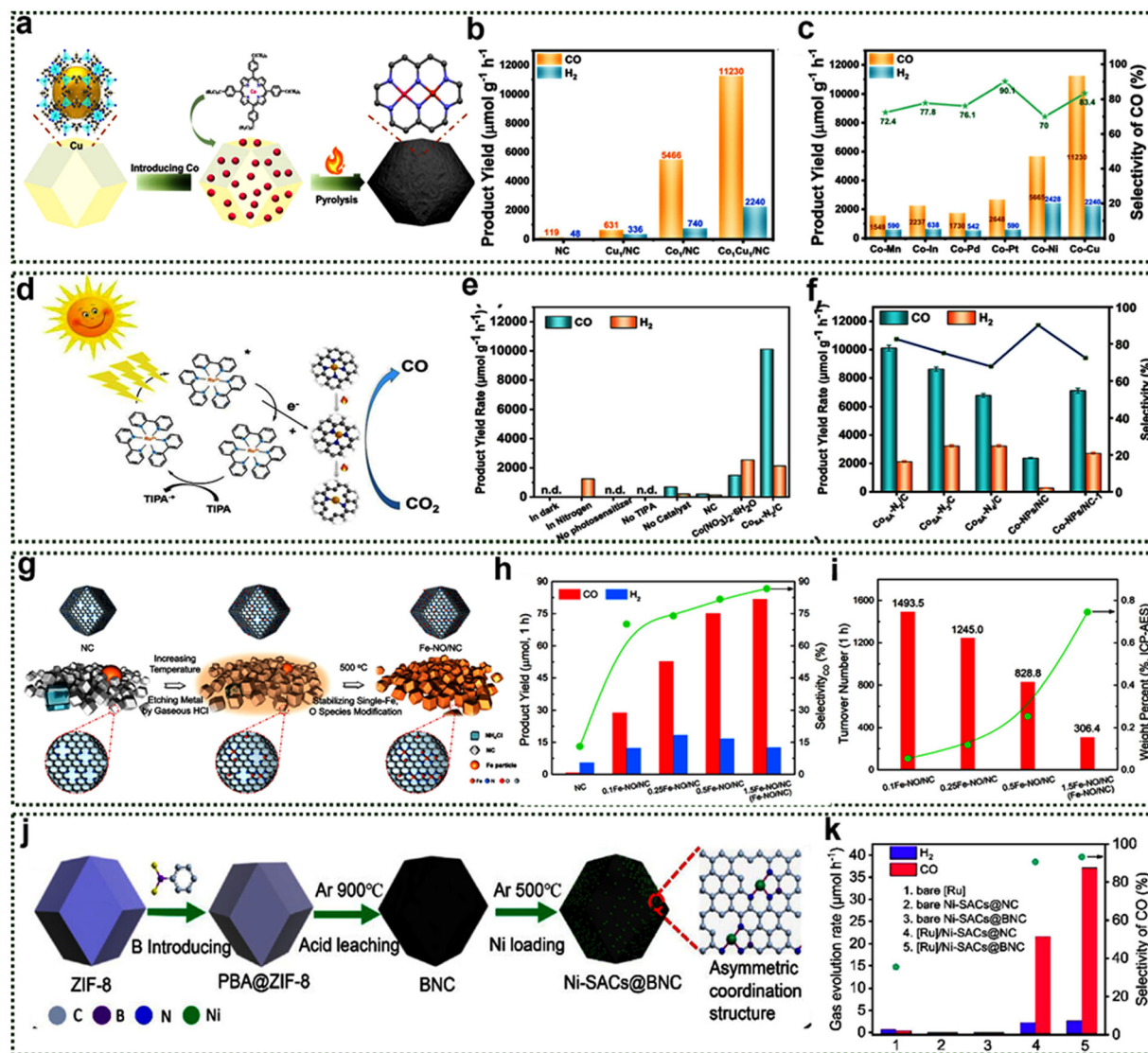
Fig. 31 (a)–(c) Synthesis, CO/H$_2$ yields (2 h visible light irradiation, λ > 420 nm), and CO selectivity of Co$_1$Cu$_1$/NC with varying dual-metal site coordination environments. Reproduced from ref. 250 with permission from American Chemical Society, copyright 2023. (d)–(f) CO$_2$ photoreduction activity (CO/H$_2$ yield rates) for CoSA–N$_x$/C under various conditions, compared to other cobalt catalysts (2 h visible light irradiation). Reproduced from ref. 251 with permission from Elsevier, copyright 2024. (g)–(i) Fe–N–O/NC synthesis, CO$_2$ photoreduction activity with different Fe loadings, and turnover numbers (TONs) (2 h visible light irradiation). Reproduced from ref. 252 with permission from American Chemical Society, copyright 2020. (j) and (k) Ni–SACs@BNC synthesis and photocatalytic CO$_2$R activity (3 h irradiation under varying conditions). Reproduced from ref. 195 with permission from American Chemical Society, copyright 2025.

efficiency. For instance, a hierarchical porous single atomic cobalt photocatalyst containing highly distributed, isolated Co single atoms on micro and mesoporous NDC (0.8-Co–ISAS/MMNC-900) was developed and used as a catalyst for the photoconversion of CO$_2$ to CO. The catalyst exhibited a high CO formation rate (7261 μmol g^{-1} h^{-1}) with 90.1% selectivity. DFT calculation revealed that the porous carbon structure encouraged the development of an exterior local electric field, which enhanced charge separation and enabled the accumulation of photo-excited electrons for effective CO$_2$ adsorption and *COOH intermediate formation. This unique strategy facilitates improved photocatalytic CO$_2$RR *via* multiscale morphology engineering.[253] Moreover, to understand the cooperative effect

between SAs and NPs on the photochemical valorisation of CO$_2$, a simple solvothermal method followed by impregnation was used to design a Co-SAs/Al-bpydc/Ni-NPs catalyst (Fig. 32a).[254] SEM, HAADF–STEM, and elemental mapping images (Fig. 32b–g) clearly illustrated the presence of Co-SAs and Ni-NPs. In this photocatalytic system under visible light ($\lambda \geq$ 420 nm), the enormously dispersed Co SAs effectively adsorb and activate CO$_2$ molecules, while the Ni NPs facilitate protons transfer to Co SAs, leading to a highly selective conversion of CO$_2$ to CO (91%) with a yield of 12.8 mmol g^{-1} h^{-1} (Fig. 32i). The Co-SAs/Al-bpydc/Ni-NPs catalyst exhibits a higher photocurrent response than its counterparts, attributed to the excellent migration photogenerated electron–hole pairs (Fig. 32j). In addition to the experimental results, DFT

9682 | *Energy Environ. Sci.*, 2025, **18**, 9632–9712

This journal is © The Royal Society of Chemistry 2025
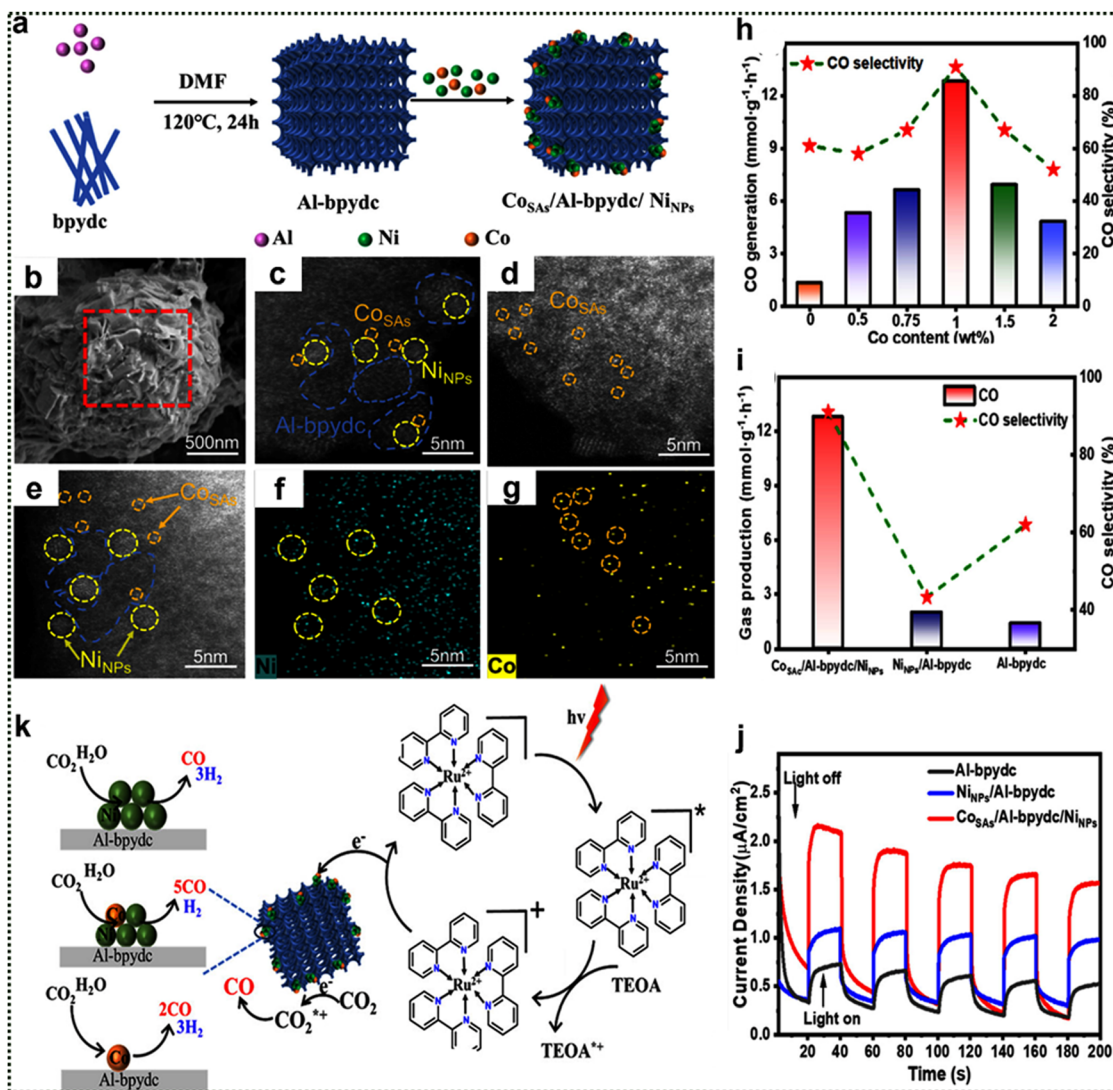
Fig. 32 (a) Synthesis of the Co-SAs/Al-bpydc/Ni-NPs catalyst. (b)–(g) SEM, HAADF STEM, and elemental mapping images of Co-SAs/Al-bpydc/Ni-NPs. (h) CO selectivity as a function of Co SAs loading. (i) CO production rate and selectivity of the Co-SAs/Al-bpydc/Ni-NPs catalyst compared to its counterparts. (j) Photocurrent response of the Co-SAs/Al-bpydc/Ni-NPs catalyst and its counterparts. (k) Schematic representation of Ni-NPs/Al-bypdc, Co-SAs/Al-bpydc/Ni-NPs, and Co-SAs/Al-bypdc photocatalytic CO_2 RR (orange and green spheres Co, Ni). Reproduced from ref. 254 with permission from American Chemical Society, copyright 2024.

calculations revels that the synergistic effect between Co SAs and Ni NPs lowers the energy barrier for CO_2 RR and enhances CO selectivity compared to individual Co SAs and Ni NPs (Fig. 32k), in the presence of a photosensitiser (Ru complex) and sacrificial agent (triethanolamine). In summary, coordination tuning in MOF and COF based catalysts serves as a powerful strategy to enhance the efficiency and selectivity of photocatalytic CO_2 reduction.[255–260] By precisely modulating metal–ligand inter-actions, electronic structures, and surface properties, these materials facilitate optimal charge separation, stabilize key intermediates, and promote desired reaction pathways. The tunability of these frameworks not only advances the funda-mental understanding of photocatalysis but also paves the way for the rational design of next-generation catalysts for sustain-able CO_2 conversion.

4.4. Thermo-catalytic valorisation of CO_2

Thermochemical CO_2 hydrogenation provides a viable strategy for extending the utilization of renewable resources for fuel and chemicals production while mitigating global warming. Beyond their well-established industrial applications, foundations, thermochemical approaches are particularly attractive due to their potential for the direct synthesis of various compounds, especially, those involving intricate C–C couplings, such as carbon monoxide, organic oxygenates, aromatics, carboxylic acids, and hydrocarbons across a broad carbon number range C_1–C_{11+}.[261–265] Conventional metal catalysts have enabled many catalytic processes, but they often require harsh operating temperatures and/or pressures, as well as expensive precious metals and metal oxide supports, which are further associated with low product selectivity. The use of SACs offers a promising

strategy to address these challenges by improving energy efficiency, and atomic utilization. Their unique chemical properties are expected to enhance the selectivity of specific products.[266] Although SACs have shown great potential, maintaining structural flexibility and stabilizing metal centers on the support surface remain crucial for completing the catalytic cycle. Furthermore, the effective conversion of CO_2 requires a catalyst system with multiple active metal sites for CO_2 adsorption and hydrogen dissociation. These active sites are often dispersed on a support, which is very important, and poses a limitation for SACs in thermal CO_2 conversion. However, multi-active site catalysts, such as single-atom decorated highly porous materials derived from MOF or COF have demonstrated superior activity and selectivity in CO_2 reduction. Since water is an undesirable byproduct in thermocatalytic CO_2 conversion, the development of water-stable MOFs is crucial. This can be achieved by incorporating a strong Lewis base linker (*e.g.*, carboxylate-based) and defective metal node sites with strong Lewis acid metal ions (*e.g.*, Zr^{4+}) or saturated four-coordinate Zn (a strong Lewis base). Such an approach would significantly expand the applicability of SACs in thermochemical CO_2 hydrogenation.

Investigating possible synergies between atomic-level active sites during design optimization to enhance specific reaction steps without compromising other catalytic activities presents an exciting avenue for further research in catalytic design. Consequently, Hu *et al.* synthesized an effective catalyst (CuZnN$_x$@C–N) made up of Zn single atoms and Cu clusters stabilized by nitrogen sites on a carbon skeleton using ZIF-8 as the precursor material.[267] The synthesis method is illustrated in Fig. 33a. Upon high-temperature calcination, the MOF structure decomposes, leading to the high dispersion of Zn, which interacts with the N atoms and functions as a single atom site, confirming its atomic dispersion (Fig. 33b). However, the EXAFS spectrum of the CuZnN$_x$@C–N catalyst exhibits a stronger signal intensity at the Cu–N bond position, while the Cu–Cu peak intensity is also pronounced, (Fig. 33c), indicating that the Cu species in the calcined sample exist as nanoparticles comprising Cu^0 and CuN$_x$ sites, which are important for hydrogen dissociation.

Initially, CuO$_x$ nanoparticles were encapsulated in ZIF-8 as guest particles. Upon calcination, Cu atoms underwent redistribution due to their coordination with N atoms at high temperatures. Notably, since pyridinic N and pyrrolic N more effectively anchor SAs than graphitic N due to geometric effects, pyridinic N is the predominant N species in the catalyst, alongside some pyrrolic N and a minor fraction of graphitic N. The M–N$_4$ active site, coordinated by four N atoms, is believed to facilitate electron transport and promote the formation of key intermediates in CO_2 reduction. In this context, the four-coordinated Zn–N$_4$/C and Zn free N$_4$/C structures exhibit stronger adsorption capacities and more active sites for $*CO_2$ than pyridinic N alone (N/C). The N$_4$/C structure, particularly the Zn containing variant, provides numerous adsorption sites for $*COOH$, favouring CO generation. Beyond, serving as anchoring sites, N atoms also induce Lewis basicity in neighbouring C atoms *via* electron pair induction in

pyridinic N, making pyridinic N atoms a significant active site for CO_2 reduction.[268] Concurrently, CuN$_x$ is considered a principal active site for CO_2 hydrogenation, as Cu sites efficiently adsorb and activate H_2 molecules. Fig. 33d indicates the formation of ZIF-8 after the addition of CuO$_x$, with the synthesized ZIF-8 maintains its original hydrophobicity. The study reports that the bifunctional catalyst, incorporating the Zn–N$_4$ structure and the ultrasmall CuN$_x$ clusters, exhibits outstanding catalytic performance in CO_2 hydrogenation, facilitating highly efficient CO generation under atmospheric pressure. Catalytic testing showed that the catalyst calcined at 500 °C exhibited limited activity for CO_2 reduction due to insufficiently coordinated active sites at lower calcination temperatures. However, increasing the calcination temperature enhanced catalytic activity and selectivity Fig. 33e. In particular, the catalyst calcined at 700 °C achieved the highest catalytic activity, approaching the thermodynamic equilibrium conversion rate (49.9%) of CO_2 under the given reaction conditions while maintaining long-term catalyst stability Fig. 33f. Conversely, the catalyst calcined at 800 °C exhibited reduced CO_2 conversion due to a significant decline in specific surface area. Notably, the CO_2 conversion rate of the CuZnN$_x$@C–N catalyst calcined at 700 °C improved substantially at reaction temperatures exceeding 400 °C, approaching the thermodynamic equilibrium conversion rate Fig. 33g. Moreover, the CO selectivity of CuZnN$_x$@C–N remained consistently above 99% across various reaction temperatures Fig. 31h. Additionally, the space-time of CO for all catalysts increased significantly with rising reaction temperature Fig. 33i, attributed to favourable reaction kinetics. These findings establish CuZnN$_x$@C–N as one of the high-performance catalysts reported for CO_2-to-CO thermochemical conversion.

Formic acid is an organic acid recognized as one of the most promising modern fuel sources for low-temperature proton–exchange membrane fuel cells, as well as a renewable hydrogen carrier. The current commercial process, which produces 800 kT (kilo ton) of formic acid annually, involves the use of methanol, toxic carbon monoxide, and corrosive sodium methoxide.[269] Therefore, formic acid produced *via* CO_2 hydrogenation represents an important biodegradable and sustainable feedstock for the future. Due to the high kinetic and thermodynamic stability of CO_2, noble metal-based homogeneous catalysts are typically employed for formic acid synthesis. Recently, Fellenberg *et al.* developed ruthenium (Ru) single-atom sites densely packed on COF for CO_2 hydrogenation into formic acid.[270] They synthesized COF using various organic linkers to tune nitrogen density within the framework, thereby tailoring the Ru single atoms shown in Fig. 34a. Experimental data indicate that, at the same Ru content, the COF chemical composition plays a more significant role in determining the fraction of isolated SA Ru species. COFs enable ruthenium catalysts with extremely high densities of single-atom sites, leading to an improvement in TOF, which contributes significantly to the design of highly active catalysts. The hydrogenation reaction was conducted under relatively mild conditions, at a total pressure of 40 bar and temperatures of 90 °C and 120 °C, with H_2/CO_2 ratios of 1 and 3 in aqueous medium. Among the tested catalysts, 10% ruthenium anchored on a COF synthesized

9684 | *Energy Environ. Sci.*, 2025, **18**, 9632–9712

This journal is © The Royal Society of Chemistry 2025
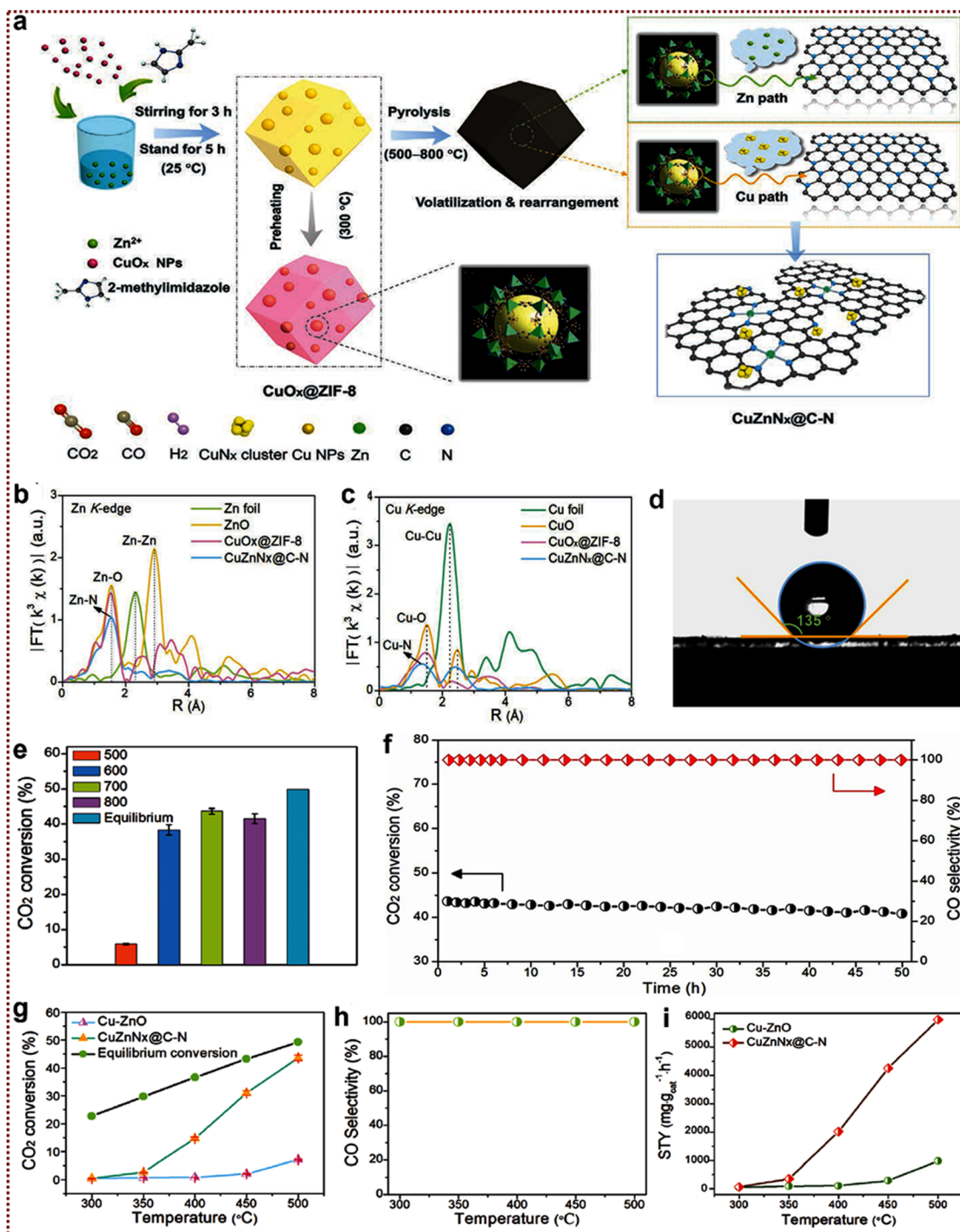
Fig. 33 (a) Schematic representation for the synthesis of CuZnN$_x$@C−N catalyst. (b) EXAFS of CuO$_x$@ZIF-8, CuZnN$_x$@C−N (700 °C), Zn foil and ZnO. (c) EXAFS of CuO$_x$@ZIF-8, CuZnN$_x$@C−N(700 °C), Cu foil and CuO. (d) Hydrophobic angle measurement. (e) Influence of calcination temperature on RWGS performance. (f) The stability test of CuZnN$_x$@C−N catalyst in RWGS reaction. (g)–(i) The catalytic performance of the CuZnN$_x$@C−N catalyst calcined at 700 °C. Reproduced from ref. 267 with permission from Wiley, copyright 2023.

with benzene-1,3,5-tri carboxaldehyde (TFB) and hydrazine (Hz) (Ru10% TFB Hz) exhibited the highest TOF (243 h^{-1}) at both 90 °C and 120 °C. In Ru10% COF TFB o-Tol, the amounts of Ru–N complexes and Ru hydroxide species increased under the reaction conditions, while the concentration of metallic Ru phases decreased. This suggests the redispersion of Ru species and an enhanced interaction between Ru complexes and N species in the COF during the reaction Fig. 34b. Conversely, a progressive increase in metallic ruthenium species was observed in Ru10% TFB-TAB (Fig. 34c and d), indicating the oxidation of Ru SA sites due to the absence of oxygen in the COF framework. This suggests that intrinsic catalytic activity (TOF) is strongly influenced by the
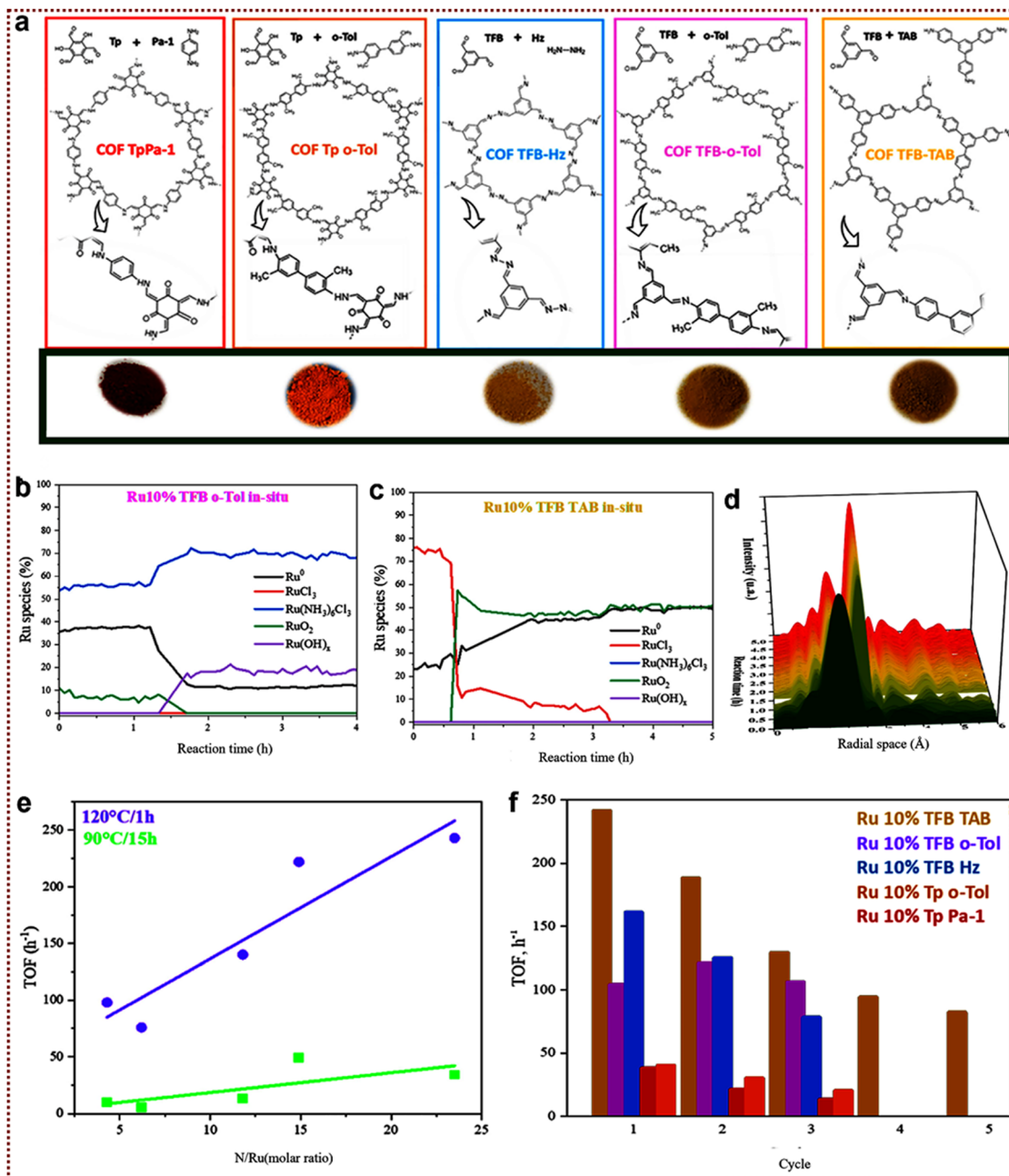
Fig. 34 (a) COF synthesized with various molecular linkers with visual aspects. (b) and (c) Evolution of catalyst phase composition during the CO_2 hydrogenation, Ru10% TFB o-Tol and Ru10% TFB TAB. (d) Evolution of *in situ* XAS spectra during the CO_2 hydrogenation, Ru10% TFB-TAB. (e) TOFs measured on the Ru/COF catalysts at 90 °C and 120 °C as functions of N/Ru experimental molar ratio. (f) Stability of various catalysts. Reproduced from ref. 270 with permission from Elsevier, copyright 2024.

nitrogen content in the catalysts. As the N/Ru ratio increased, overall intrinsic activity also increased Fig. 34e. However, while Ru10% TFB-TAB, and TFB-Hz were initially the most active catalysts, they lost activity in the second and third reaction cycles (Fig. 34f). In contrast, Ru10% TFBo-Tol maintained it's catalytic, which correlated with a decrease in the concentration of Ru SA site activity. The thermocatalytic hydrogenation of CO_2 to alcohols has garnered significant interest, as both methanol and ethanol offer ease of transport and substantial value in chemical synthesis. Traditional CO_2 hydrogenation using metal oxides

requires harsh reaction conditions (>300 °C, 1–5 MPa), leading to excessive energy consumption.[271] Designing, a functionalized material that can simultaneously anchor metal SAs for hydrogen dissociation and enhance CO_2 adsorption is an efficient strategy for thermocatalytic conversion. Recently, Rosado *et al.*, rationally designed and synthesized a functionalized NU-1000 MOF that serves as a platform for the simultaneous coordination stabilization of Cu SAs and CO_2 adsorption, enabling its effective conversion to methanol.[272] By modifying the ligand before the MOF synthesis, NU-1000 was functionalized with primary amino

9686 | *Energy Environ. Sci.*, 2025, **18**, 9632–9712

This journal is © The Royal Society of Chemistry 2025

groups ($-NH_2$), which have a high affinity for CO_2 adsorption, and free thiol functionalities ($-SH$), which exhibit strong interactions with Cu SAs. These functional groups were incorporated into the framework using post-synthetic solvent-assisted ligand incorporation. Under working conditions, the NU-1000-based Cu SACs exhibited a high methanol space-time yield (STY), surpassing that of the industrially important $CuZnO/Al_2O_3$ catalyst. Notably, the catalytic of the MOF-based catalyst increased with temperature, whereas the commercial catalyst showed reduced performance beyond 260 °C due to nanoparticles sintering. Moreover, the MOF catalyst demonstrated significant activity at temperatures as low as 180 °C, achieving an STY of 35 mg MeOH g_{cat}^{-1} h^{-1}, which steadily increased with temperature, reaching 103 mg MeOH g_{cat}^{-1} h^{-1} at 280 °C. This enhancement was attributed to the favoured adsorption of CO_2 at the strategically incorporated $-NH_2$ sites and the high concentration of active copper sites dispersed as individual atoms along the MOF channels. While the thermocatalytic hydrogenation of CO_2 to ethanol and higher alcohols is of great interest, large-scale production remains a significant challenge. Recently, Liu et al. developed a state-of-the-art catalyst for CO_2

hydrogenation to ethanol by precisely depositing single-atom Ir species onto phosphorous cluster islands on In_2O_3 nanosheets. This catalyst achieved an impressive ethanol yield of 3.33 mmol g^{-1} h^{-1} and TOF of 914 h^{-1} under 1.0 MPa (H_2/CO_2 = 3 : 1) at 180 °C.[262] Therefore, catalysts with high surface area and precisely controlled active sites for CO_2 adsorption and molecular hydrogen dissociation are highly attractive. Single-atom decorated MOFs or COFs are promising candidates for thermocatalytic CO_2 reduction in the near future. The top papers published in recent years on electrochemical, photochemical, and thermochemical CO_2 valorisation are summarized in Table 3.

5. Mechanistic understanding of SACs in CO_2 valorisation

A comprehensive understanding of the catalytic mechanism in SACs requires the integration of both experimental and theoretical approaches. While in situ characterization techniques provide real-time insights into dynamic structural and chemical

Table 3 Top publications of CO_2 valorisation used in electrochemical, photoelectrochemical, and thermal processes

Electrocatalyst	Electrolyte	Product	FE (%)	Potential (V)	Turn over frequencies (TOF-h^{-1})	Current density (mA cm^{-1})	Ref.
A–Ni–NSG	0.5 M $KHCO_3$	CO	97%	0.61	14 800	22.0	128
Ni–N–C	0.5 M $KHCO_3$	CO	96.8	−0.80	11 315	27.0	153
Fe^{3+}–N–C	0.5 M $KHCO_3$	CO	>80	−0.20	~1100	94.0	163
C–Zn_1Ni_4 ZIF-8	1 M $KHCO_3$	CO	98	−0.83	10 087	44.1	166
Ni–NBr–C	0.5 M $KHCO_3$	CO	97	−0.70	35 289.7	350	189
InA/NC	0.5 M $KHCO_3$	CO	97.2	−2.10	~40 000	39.4	193
Al–NC	0.1 M $KHCO_3$	CO	98.76	−0.65	12 960	330	196
Ni/Cu–N_6–C	0.5 M $KHCO_3$	CO	97.7	−0.60	20 695	>100	204
Ni–N_3/Cu–N_3	0.5 M $KHCO_3$	CO	99.1	−1.10	22 304	88.0	205
Zn-SA/CNCl-1000	1.0 M KOH	CO	97	−0.93	29 325	271.7	229

Photocatalytic	Condition	Light	Product	Selectivity (%)	TOF or TON	Yield	Ref.
Ni–TpBpy	(Acetonitrile, pure water, triethanolamine)	300 W Xe lamp	CO	96 (5 h)	13.62 (5 h)	4057 µmol g^{-1}	237
Tpy–COF–Co	(Acetonitrile, deionized water, triethanolamine)	300 W Xe lamp	CO	—	(TOF) 1607 h^{-1} and TON 2095	426 mmol g^{-1} h^{-1}	238
Co_1Cu_1/NC	(Acetonitrile, pure water, triisopropanolamine)	300 W Xe lamp	CO	83.40 (2 h)	59	22.46 mmol g^{-1}	241
Co_{SA}–N_x/C	(Acetonitrile, pure water, triisopropanolamine)	300 W Xe lamp	CO	82.60	98 (2 h)	10 110 µmol g^{-1} h^{-1}	242
Fe–NO/NC	(Acetonitrile, deionized water, triethanolamine)	300 W Xe lamp	CO	86.70	1494 (1 h)	81.8 µmol	243
Co-COF	(Acetonitrile, [Ru(bpy)$_3$Cl$_2$]·6H$_2$O, TEOA)	300 W Xe lamp	CO	95.70	(TOF) 111.8 h^{-1}	18 000 µmol g^{-1} h^{-1}	255
Fe SAS@Tr-COF	(Acetonitrile, water, [Ru(bpy)$_3$Cl$_2$]·6H$_2$O, TEOA)	300 W Xe lamp	CO	96.40	2.89	980.3 µmol g^{-1} h^{-1}	46
Cu-SA/CTF	(Triethanolamine, water)	300 W Xe lamp	CH_4	98.31	24.05 (4 h)	32.56 µmol g^{-1} h^{-1}	256
TCM-Bpy-COF-CoAC	(acetonitrile, water, [Ru(bpy)$_3$Cl$_2$]·6H$_2$O, TEOA)	5 W LED (λ = 400–800 nm)	CO	81.80	—	26 650 µmol g^{-1} h^{-1}	257
Pt-SA/CTF-1	(Triethanolamine, water)	300 W Xe lamp	CH_4	76.60	—	—	258
Fe@MIL-OV-300	(Triethylamine, acetonitrile, water)	300 W Xe lamp	CH_3OH	—	(TOF) 16.03 h^{-1}	15.85 mmol g^{-1} at 4 h	259
NiSAs@NPs/TC	(Deionized water, CO_2 gas)	300 WXe lamp	CO, CH_4	—	—	35.60 and 3.41 µmol g^{-1} h^{-1}	260

Thermocatalytic	Condition	Temperature	Product	Selectivity (%)	TOF or TON	Yield	Ref
Co–N–C	Mixed gas ($H_2/CO_2/N_2$)	500 °C	CO	~100	73 h^{-1}	37.5 mol kg^{-1} h^{-1}	246
20% Co–N–C			CH_4	99.3		33.6 mol kg^{-1} h^{-1}	
NU-1000-NH_2/PrS–Cu	CO_2 and $3H_2$	280 °C	CH_3OH	100	—	100 mg MeOH g_{cat}^{-1} h^{-1}	257

changes during catalytic processes, theoretical methods such as DFT offer predictive understanding by modeling atomic interactions, reaction pathways, and energy landscapes before or after experimental validation.[273] This is particularly essential for complex systems such as MOF-derived and COF-based SACs, where diverse atomic environments and multifunctional sites add significant complexity to mechanistic interpretation. To address this challenge, the combination of DFT simulations and machine learning (ML) techniques has emerged as a powerful strategy, enabling the identification of key mechanistic steps, adsorption configurations, and structure-performance correlations with atomic-level precision. Together, these complementary approaches provide a holistic view of SAC functionality, facilitating rational design and optimization for targeted CO_2 valorisation.

5.1. DFT studies

For SACs employed in CO_2 valorisation, DFT studies have played a particularly vital role in understanding the interplay between isolated metal centers and surrounding ligands or carbon supports, which govern the activation of CO_2 and the selectivity toward desired products. In the case of MOF- and COF-derived SACs, where metal atoms are often coordinated with nitrogen or oxygen donors within complex porous frameworks, DFT simulations help clarify how local coordination environments influence adsorption strength and charge transfer. This is crucial for unraveling the mechanisms driving key steps in CO_2 reduction, such as CO_2 activation, proton-electron transfer, and C–C coupling. DFT has become an indispensable computational tool for probing the catalytic mechanisms of SACs, providing atomic-level insights into their structural, electronic, and interaction energy properties. Over the past few decades, numerous quantum chemical software packages such as VASP, Quantum Espresso, CASTEP, SIESTA, and ABINIT have enabled the accurate modeling of diverse catalytic materials.[274–278] These first principles calculations allow researchers to predict stable atomic configurations, elucidate electronic structures, quantify adsorption energies, and map out complete reaction pathways, including the identification of transition states and rate-determining steps.

5.1.1. Computational perspectives on SAC formation and stabilization. DFT calculations have not only been widely applied to study the catalytic mechanisms of MOF-derived SACs and COF-based SACs but have also proven invaluable in elucidating the thermodynamic and kinetic factors governing the formation and stabilization of SAs during synthesis. Particularly, DFT helps to calculate formation energies, energy barriers, and competing pathways, allowing researchers to predict conditions that favour atomic dispersion over agglomeration. For instance, a DFT-based study explored the atomization and sintering competition during the thermal conversion of Pd nanoparticles to Pd SAs in nitrogen-coordinated MOF-derived carbon.[279] The calculations revealed that the transformation of Pd clusters (Pd_{10}) into atomically dispersed Pd–N_4 sites requires overcoming a kinetic barrier of 1.47 eV, with a substantial exothermicity of -3.96 eV. However, the sintering process, driven by the diffusion of Pd clusters, exhibited a much lower energy barrier of only 0.58 eV. These insights explained why

sintering dominates at moderate temperatures (300–900 °C), while atomization and stable Pd–N_4 formation prevail only at elevated temperatures above 900 °C, where sufficient thermal energy is available to surmount the atomization barrier. Such DFT-supported synthesis guidance not only aids in optimizing thermal activation processes for noble metal SACs but also provides generalizable design principles for constructing MOF-derived or COF-based transition metal SACs with stable M–N_4 coordination environments. This example underscores how integrating DFT predictions into synthesis planning offers critical insights into the delicate balance between atomic dispersion and sintering, which is particularly relevant for thermally activated MOF-derived SACs. Future studies could further leverage such predictive modeling to systematically tune precursor selection, pyrolysis temperature profiles, and defect engineering strategies to maximize SAC yield while minimizing particle agglomeration.

5.1.2. DFT insights into CO_2 activation and conversion. In general, to better understand the role of DFT in elucidating the catalytic behavior of SACs, it is important to examine how the modeling strategy adapts to the nature of the activation source. Although the foundational DFT formalism remains consistent, the computational setup, boundary conditions, and interpretation of key descriptors, such as charge redistribution, adsorption energetics, and reaction pathways, can differ significantly depending on the type of activation source involved, including electrochemical potential, photon excitation, or thermal input.[273] For instance, in electrocatalytic CO_2 reduction, DFT simulations generally employ periodic slab models to represent the electrode surface and account for interfacial interactions through solvation models. The solvation effect is usually modelled using implicit continuum solvation schemes, or hybrid approaches that incorporate explicitly added water molecules near the surface to more accurately describe local hydrogen bonding and interfacial structure.[280] To account for the influence of applied potential, the computational hydrogen electrode (CHE) framework is typically employed to calculate potential-dependent free energy landscapes for key intermediates and reaction steps.[281,282] In photocatalytic systems, the focus shifts toward analyzing band structure alignment, band edge positions relative to redox potential, and the spatial separation and migration behavior of photoexcited charge carriers, which strongly influence charge utilization efficiency. A more detailed analysis of exciton dynamics and electronic transitions may require methods beyond standard DFT, such as time-dependent DFT or many-body perturbation theory.[283,284] In contrast, thermocatalytic CO_2 conversion emphasizes reaction kinetics derived from transition state searches, adsorption and desorption energetics, and entropic contributions under finite temperature conditions.[285,286] These distinctions are summarized in Table 4,[287–289] which outlines representative methodological considerations and mechanistic targets across different catalytic regimes. Despite the variations in catalytic systems, most mechanistic investigations on MOF-derived and COF-based SACs continue to utilize standard ground-state DFT protocols to explore coordination geometries, electronic structure (*e.g.*, density of states), charge density distributions,

9688 | *Energy Environ. Sci.*, 2025, **18**, 9632–9712

This journal is © The Royal Society of Chemistry 2025

Table 4 Comparison of DFT modelling strategies for electrocatalytic, photocatalytic, and thermocatalytic CO_2 conversion

Regime	Key methodological considerations	Main mechanistic descriptors	Typical DFT protocols/models	Ref.
Electrocatalysis	Electrode–electrolyte interface (implicit/explicit solvation)	Free energy profiles of intermediates	GGA, VASP/Gaussian/CP2K, VASPsol, CHE, Bader, NEB	281 and 287–289
	Applied potential corrections (CHE model)	Overpotential *COOH, *HCOO, *CO adsorption energies		
	Charge transfer analysis (*e.g.*, Bader charge, charge difference mapping)	Charge redistribution pathways		
Photocatalysis	Band structure & alignment (relative to redox levels)	Band gap, band edge positions	GGA, HSE06 (for better band gaps), periodic DFT, slab models	283,284
	Static charge separation (potential mapping)	Projected DOS		
	Band edge calculations (vacuum alignment)	Charge localization/static separation		
	(Carrier dynamics often beyond ground-state DFT: TDDFT, GW, BSE)	Surface reaction energetics		
Thermocatalysis	Transition state location (climbing NEB, dimer) Adsorption/desorption energy profiles	Reaction energy barriers	GGA, periodic DFT, TS searches, frequency calculations	285,286
	Entropic and zero-point energy corrections (vibrational analysis)	Turnover frequency (TOF, *via* microkinetics)		
	Reaction barriers	Adsorbate binding energies		
		Activation entropy & free energies		

and Gibbs free energy profiles associated with CO_2 activation and transformation.

DFT has become an indispensable computational tool for uncovering the mechanistic intricacies of CO_2RR on SACs, particularly those derived from MOFs and COFs. By simulating the electronic structure, adsorption behavior, and reaction energetics at the atomic scale, DFT complements *in situ* techniques, bridging critical knowledge gaps regarding transition states, binding preferences, and energy barriers along the catalytic pathway. For instance, DFT studies have systematically evaluated the free energy profiles of key intermediates such as *COOH, *CO, and *CHO, offering valuable predictions regarding the preferred reaction pathways and product selectivity.[290] Moreover, DFT helps elucidate the role of heteroatom coordination (*e.g.*, N, B, or S) in tuning the local electronic environment of metal centers, thereby enhancing catalytic efficiency. For example, in the case of boron- and nitrogen-coordinated Sb SACs, DFT calculations have shown that pre-adsorbed hydrogen on boron sites suppresses the competitive hydrogen evolution, improving CO_2 selectivity.[291] Advanced DFT approaches, including *ab initio* molecular dynamics (AIMD), also provide further provide insights into catalyst stability under realistic electrochemical conditions, which is crucial for ensuring long-term performance in CO_2RR. These computational insights help rationalize experimentally observed trends and guide the design of next-generation SACs by predicting optimal metal centers, coordination motifs, and electronic descriptors for enhanced catalytic selectivity and activity.

5.1.2.1. DFT insights into electrocatalytic CO_2 reduction pathways. For electrocatalytic CO_2RR, DFT serves as an efficient framework to mechanistically evaluate SACs derived from MOF and COF precursors under electrochemical conditions. Recent studies have shown that integrating implicit solvation models, applied potential corrections *via* the computational hydrogen electrode (CHE), and charge density enables a more realistic representation of the electrode–electrolyte interface. For instance, a systematic DFT screening of 325 dual-metal-site catalysts supported on nitrogen-doped graphene, modelled using revised Perdew–Burke–Ernzerhof (RPBE) functionals with implicit aqueous solvation, revealed distinct trends in limiting potentials and adsorption energies for CO_2RR intermediates.[292] The inclusion of charge density difference plots and Bader charge analysis provided insight into electron transfer dynamics between metal centers and CO_2-derived adsorbates. In several cases, the formation of key intermediates such as COOH or HCOO was identified as the potential-determining step, with calculated free energy profiles and transition states supporting observed trends in product selectivity. These computational insights, when interpreted based on structural motifs derived from MOF or COF based SACs, highlight the predictive power of DFT in guiding the design of active and selective electrocatalysts for CO_2 conversion. A study modeled CO_2RR to CO over Fe–N–C SACs on graphene, incorporating explicitly applied potentials with GC-DFT. Adsorption and activation energies for key intermediates (*COOH, *CO) were calculated at various potentials (*e.g.*, −0.3, −0.7, −1.2 V *vs.* SHE).[293] The GC-DFT approach enabled direct simulation of the electrode electrolyte interface under working conditions, revealing the crucial role of potential in favouring CO_2 activation and governing the selectivity between CO production and hydrogen evolution.[294] Free energy diagrams showed that at more negative potentials, *COOH formation becomes more favourable, consistent with experimental results.

A compelling example illustrating the power of DFT for COF based SACs come from the investigation comparing CO_2RR pathways on two metal-active centers, Ni and Ti, embedded in the aldehyde-amine COF (TAPT-Tp) framework.[295] Structural models were constructed to simulate the adsorption of CO_2 and the stepwise reduction to CO, with Gibbs free energy changes computed for each elementary reaction step (Fig. 35a and b). The DFT calculations revealed that Ni centers consistently exhibited lower energy barriers for critical intermediates (*COOH and *CO) than
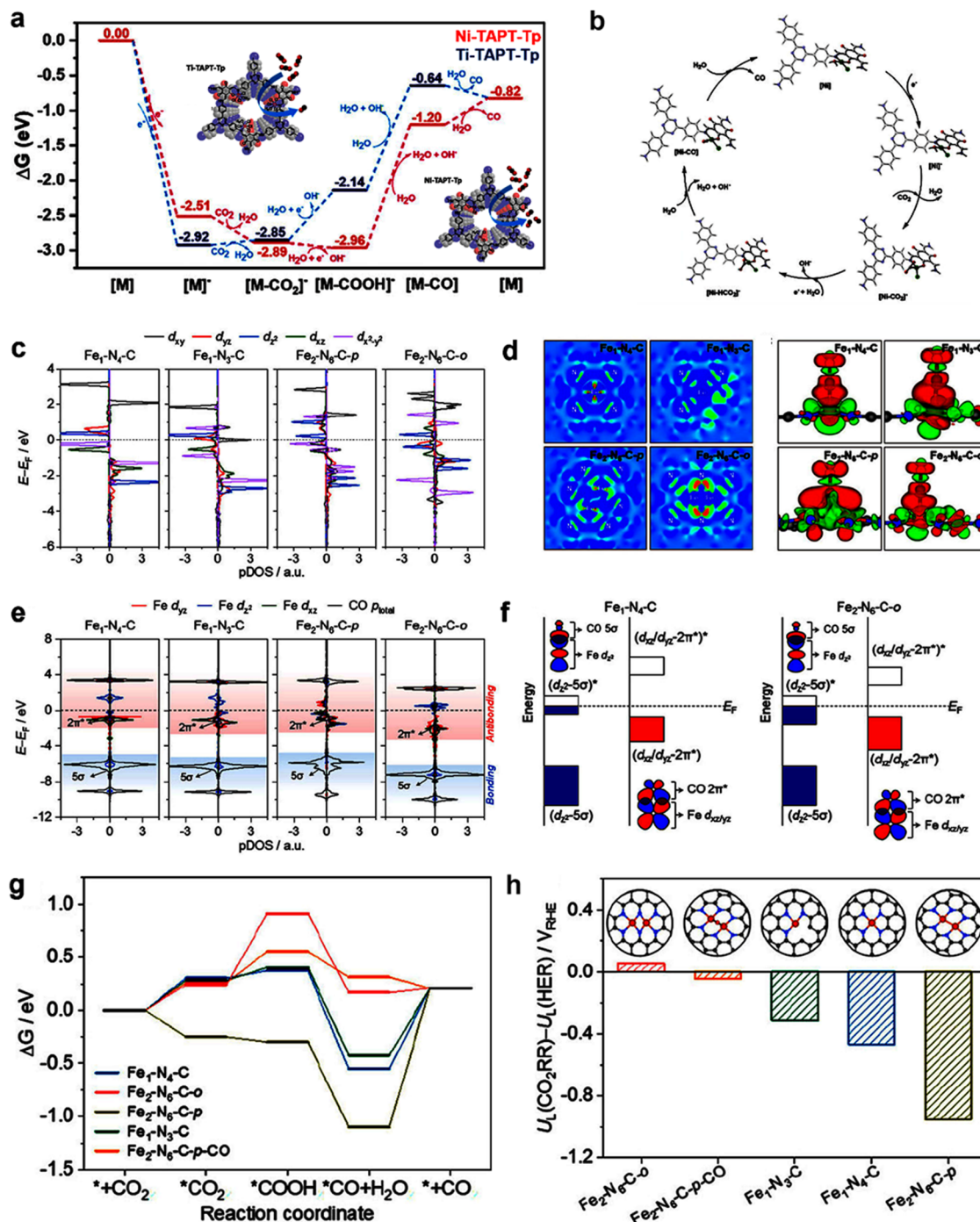
Fig. 35 (a) Free energy diagrams for CO_2RR on Ni-TAPT-Tp and Ti-TAPT-Tp COFs, highlighting key intermediates and energy barriers for each step. (b) Proposed CO_2 reduction mechanism based on DFT insights. Reproduced from ref. 295 with permission from Wiley, copyright 2025. (c) Partial density of states showing Fe 3d orbital contributions in MOF-derived Fe−N−C catalysts. (d) Charge density difference plots illustrating electron redistribution before and after *CO adsorption. (e) pDOS of Fe-3d orbitals and adsorbed CO orbitals, indicating orbital coupling during CO_2 reduction. (f) Schematic representation of Fe−CO orbital interactions comparing single- and dual-Fe sites, emphasizing their effect on *CO binding and desorption. (g) Comparison of free energy profiles highlighting the potential-determining steps for CO_2 reduction at single *versus* dual-Fe atom active sites, (h) Theoretical comparison of limiting potentials for CO_2RR and HER across various Fe−N−C configurations. Reproduced from ref. 296 with permission from American Chemical Society, copyright 2022.

Ti sites (Fig. 35c). Notably, Ni-TAPT-Tp required only −0.07 eV for the *COOH formation step, compared to +0.61 eV for Ti-TAPT-Tp, indicating a more favourable proton–coupled electron transfer process on Ni. The structural coordination environment also played a decisive role. The four-coordinated, planar geometry of Ni-TAPT-Tp resulted in a more delocalized π-conjugated

environment, which enhances light harvesting and charge mobility. The less sterically hindered coordination environment further facilitates CO_2 adsorption and enables faster ligand exchange for CO desorption, thereby reducing the likelihood of active site poisoning. In contrast, the six-coordinated octahedral environment of Ti-TAPT-Tp restricts adsorption flexibility and increases desorption barriers, limiting catalytic efficiency. Such comprehensive modelling, which links geometric, electronic, and thermodynamic factors, provides a complete mechanistic map for designing optimal COF-SACs.

For MOF-derived SACs, DFT calculations have also provided transformative insights into the evolution from single-atom to dual-atom active sites, highlighting synergistic electronic interactions. In a study of Fe–N–C catalysts derived from Fe-doped MOFs, the partial density of states calculations were used to compare the electronic structures of Fe–N_4–C (single-Fe) and Fe_2–N_6–C (dual-Fe) configurations (Fig. 35c).[296] The results showed significant peak splitting and delocalization of Fe-3d orbitals in the dual-atom configuration, indicating strong electronic coupling between adjacent Fe atoms (Fig. 35c and d). This electronic delocalization shifted the d-band center of Fe to a more negative energy relative to the Fermi level (from -2.05 eV in Fe–N_4–C to -3.00 eV in Fe_2–N_6–C–O), making *CO adsorption

less favourable and thereby promoting its desorption, which is a common bottleneck in CO_2RR (Fig. 35e and f). Charge density difference plots in Fig. 33d further illustrate enhanced electron transfer from Fe to adjacent N atoms, stabilizing the catalytic site and modulating intermediate binding. DFT-based crystal orbital Hamilton population analysis confirms that the Fe-CO is less covalent in Fe_2–N_6–C–O, resulting in a lower *CO desorption barrier relative to Fe–N_4–C sites (Fig. 35g and h). The computed free energy diagrams (Fig. 35g) revealed that the potential-limiting step shifted from *CO desorption in Fe–N_4–C (0.70 eV) to *COOH formation in Fe_2–N_6–C–O (0.35 eV), demonstrating how dual-metal synergy optimizes both activity and selectivity. Further, DFT calculations were employed to evaluate the CO_2RR performance of complex COF@MOF-SACs (Fig. 36a), comparing catalytic pathways at dual metal sites (Co and Zn sites).[83] The results showed that the formation of *COOH was the rate-determining step, with Co sites exhibiting a much lower free energy barrier (0.25 eV) than Zn sites (0.58 eV in COF@-MOF800-Co and 1.32 eV in COF@MOF800) (Fig. 36b and d). Additionally, the competing HER reaction was analyzed, demonstrating that Co sites effectively suppressed HER in favour of CO_2RR (UL(CO_2)–UL(H_2) = -0.11 eV), while Zn sites exhibited greater activity toward HER under similar conditions (Fig. 36c).
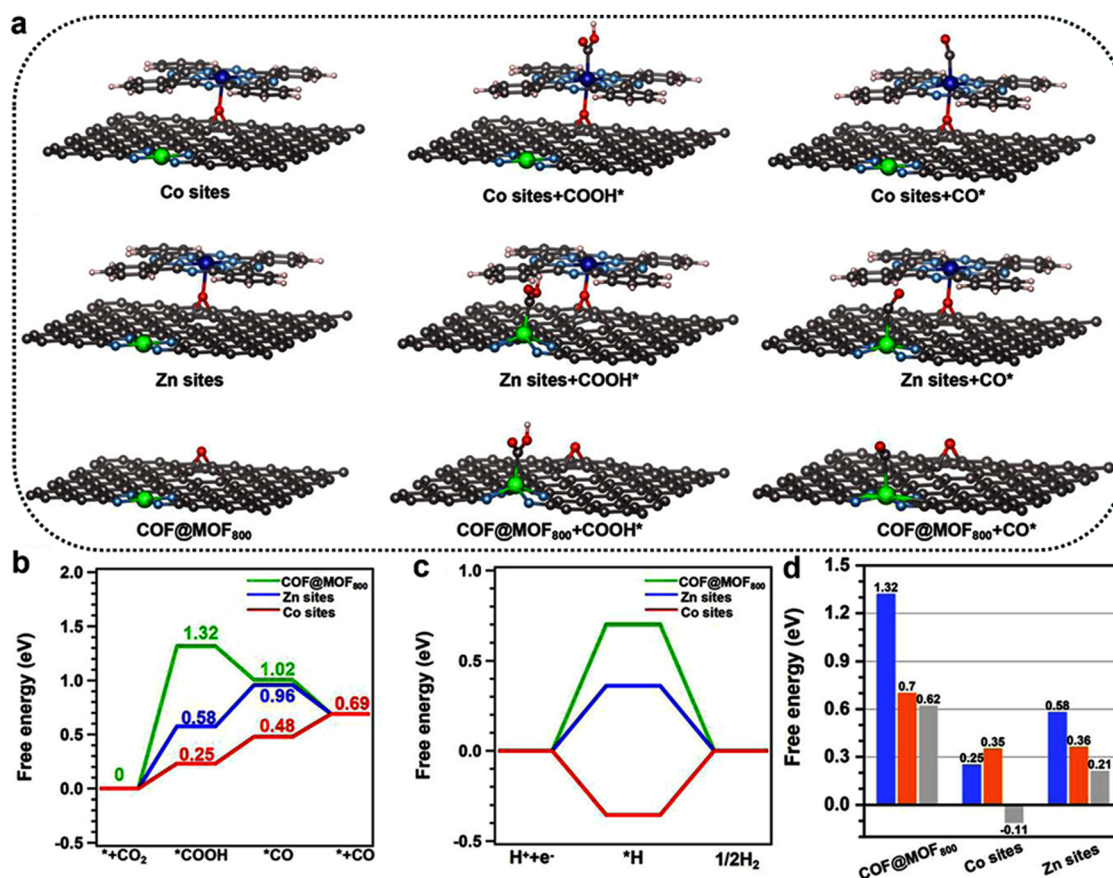
Fig. 36 (a) Geometric optimization of the COF@MOF–Co complex with key CO_2RR intermediates, obtained through DFT simulations. Comparative energy profiles of COF@MOF–Co, Co, and Zn sites for (b) CO_2RR, (c) HER, and (d) overpotentials at the rate-limiting step of CO_2RR catalytic sites. Reproduced from ref. 83 with permission from Wiley (CC-BY 4.0), copyright 2023.

This journal is © The Royal Society of Chemistry 2025

Energy Environ. Sci., 2025, 18, 9632–9712 | 9691

This example highlights the critical role of heterometallic synergy in COF@MOF-SACs for tuning reaction selectivity and optimizing CO_2RR efficiency (Fig. 36d).

5.1.2.2. DFT insights into photocatalytic CO_2 reduction pathways. In the context of photocatalytic CO_2 reduction, DFT serves as a powerful framework for elucidating how light-induced electronic processes govern catalytic performance at the molecular level. Unlike thermally or electrochemically activated systems, photocatalysis involves the generation, separation, and migration of photoexcited charge carriers, as well as their subsequent interaction with surface-bound CO_2 molecules.[297,298] DFT enables quantitative evaluation of key factors that influence photocatalytic activity, including band gap tuning, band edge alignment with CO_2 reduction potentials, charge redistribution at active sites, and the role of heterojunction interfaces in carrier separation. Particularly in MOF- and COF- based systems, where SAC centers are integrated into extended π-conjugated frameworks, DFT provides predictive insights into how orbital hybridization, local coordination environments, and photogenerated carrier dynamics affect both the thermodynamics and kinetics of CO_2 activation. As highlighted in recent mechanistic studies, such as those on S-scheme heterojunctions, doped COFs, and MOF-based hybrids,[299,300] DFT also facilitates analysis of surface potential gradients, work function shifts, and adsorption energy landscapes, which are key metrics that link electronic structure to product selectivity and solar-to-fuel conversion efficiency.[301,302] The following example illustrates how DFT modelling has been applied to unravel these complex interactions in a representative Pt-COF photocatalyst for CO_2-to-CO conversion.

A representative application of DFT in photocatalytic CO_2 reduction is exemplified by the mechanistic investigation of a Pt SACs anchored on a triazine-based COF.[303] In this system, density functional theory provided comprehensive insights into how atomic-level Pt incorporation modulates electronic structure and catalytic behavior under light-driven conditions. Geometry optimizations and binding energy calculations identified the most stable configuration as a Pt atom coordinated to one nitrogen and two carbon atoms within the COF matrix. This N–Pt–C_2 site exhibited a binding energy of −2.42 eV and bond distances consistent with established SA coordination geometries, indicating strong structural anchoring. Bader charge analysis and charge density difference plots revealed that Pt donates approximately 0.46 electrons to adjacent framework atoms, confirming its partial oxidation and effective electronic coupling with the COF lattice. Band structure and DOS calculations further showed that Pt loading reduces the band gap from 2.33 to 1.73 eV, promoting enhanced visible-light absorption. The observed hybridization between Pt d-orbitals and the COF π-system introduces new frontier states, which enhance the redox capacity and facilitate charge separation under illumination. Work function analysis indicated a decrease from 5.88 to 5.56 eV upon Pt incorporation, accompanied by an upward shift in the Fermi level. This electronic modification favours photoinduced electron transfer from the COF backbone toward adsorbed reactants, thus enhancing surface reactivity. From an electronic

perspective, the incorporation of Pt atoms into the COF framework enhances CO_2 adsorption by modulating the local charge distribution at the active site, as revealed by charge density difference analysis (Fig. 37a and b), and by narrowing the band gap, as shown by the calculated band structure and density of states (Fig. 37c and d). This dual modulation of electronic structure and charge localization contributes to improved photocatalytic CO_2 conversion efficiency and product selectivity in the Pt-COF system. DFT-derived reaction energy profiles (Fig. 37e and f) further demonstrate that the initial hydrogenation of CO_2 to the *COOH intermediate proceeds with a significantly lower energy barrier on the Pt-COF surface compared to the SAC-free COF. Subsequent *CO formation and desorption are also thermodynamically favourable, steering the reaction pathway towards selective CO evolution while suppressing deeper hydrogenation to hydrocarbons. These findings demonstrate how DFT elucidates structure–function relationships at the atomic level and guides the rational design of high-performance COF-based SAC photocatalysts for solar-driven CO_2 reduction.

While the discussed Pt-COF study provides valuable mechanistic insights based on conventional Kohn–Sham DFT with generalized gradient approximation (GGA) functionals, further refinement of electronic structure predictions in photocatalysis can benefit from the application of advanced computational approaches. For instance, hybrid functionals such as HSE06 or range-separated methods offer improved accuracy in predicting band gaps and band edge positions, which are critical for evaluating light absorption and redox alignment.[304,305] Time-dependent DFT (TDDFT) and many-body perturbation theories like GW and Bethe–Salpeter equation (BSE) methods can provide deeper insight into photoexcited states and exciton dynamics, while periodic DFT using slab models allows for more realistic simulation of surfaces and interfaces,[306–308] particularly in heterojunction or MOF/COF composite photocatalysts. Incorporating these advanced tools into DFT workflows enhances the reliability of descriptors such as band bending, surface dipoles, and charge carrier mobility, thereby enabling more predictive modelling of photocatalytic CO_2 reduction performance under solar irradiation.

5.1.2.3. DFT insights into thermocatalytic CO_2 reduction pathways. Unlike photocatalytic and electrocatalytic systems, which rely on photon or potential input, thermocatalytic CO_2 hydrogenation proceeds *via* enthalpy-governed surface reactions under elevated temperatures and pressures.[309,310] In this context, DFT provides a quantitative basis for mapping energetic landscapes, reaction kinetics, and structure–activity relationships of SACs. These thermal systems typically involve multi-step hydrogenation mechanism with surface-bound intermediates such as *HCOO, *COOH, or *CO, ultimately converting CO_2 into value added products like CH_3OH, CH_4 or higher oxygenates.[311,312] DFT facilitates a molecular level understanding by enabling precise modeling of adsorption thermodynamics, transition-state structures, and energy barriers, as well as the role of SAC active centers embedded within MOF-or carbon derived supports.

Standard DFT workflows in this domain include transition-state identification *via* the climbing-image nudged elastic band

9692 | *Energy Environ. Sci.*, 2025, **18**, 9632–9712

This journal is © The Royal Society of Chemistry 2025
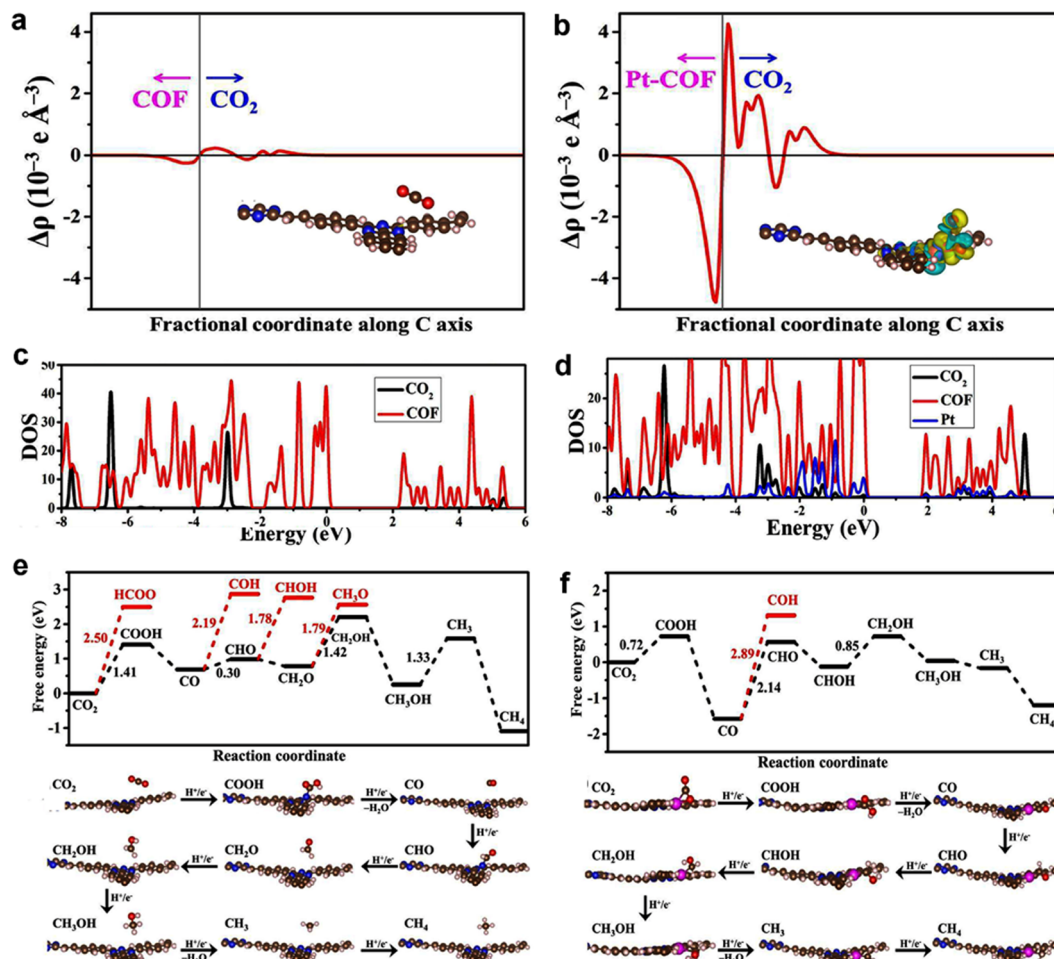
Fig. 37 DFT analysis of the Pt-COF photocatalyst for CO_2 reduction. (a) and (b) Charge density difference and Bader charge results showing electron transfer from Pt to the COF. (c) and (d) Band structure and density of states illustrating band gap narrowing and Pt-COF orbital hybridization. (e) and (f) Free energy diagram and reaction pathway showing reduced energy barrier for *COOH formation and enhanced CO selectivity. Reproduced from ref. 303 with permission from Elsevier, copyright 2023.

(CI-NEB) method, vibrational frequency analysis for entropic and zero-point corrections, and Bader charge analysis to track electron transfer across intermediates.[313,314] Energetic span theory is frequently applied to link computed barriers to turnover frequencies (TOFs), offering predictive insights into catalyst activity trends. Importantly, thermodynamic descriptors derived from DFT calculations are often coupled with microkinetic modeling to resolve complex product networks and competing mechanistic routes.

A representative example by Liu *et al.* evaluated five transition metals (Cu, Fe, Ni, Pd, Pt) anchored on Zr nodes in MOF-808 using periodic DFT.[315] Binding energy analysis revealed that Pt was the most strongly anchored species, whereas Cu exhibited the most favourable catalytic reactivity (Fig. 38a). Two full reaction mechanisms for CO_2 hydrogenation were examined, the *HCOO (formate) and *COOH (carboxyl) pathways. For Cu-MOF-808, the formate route was both thermodynamically and kinetically preferred, with the rate-limiting step, *$H_2COOH \rightarrow$ *H_2CO, exhibiting a barrier of 10.4 kcal mol^{-1} (0.45 eV) (Fig. 38b). Energetic span analysis revealed that Cu

had the highest predicted TOF of 6.63×10^{-15} among the five metals, aligning with experimental findings. Mulliken charge analysis indicated electron-rich Cu sites facilitated stronger *CO_2 activation, while frequency analysis confirmed thermal accessibility of key steps under realistic reaction conditions.

Similarly, DFT-guided mechanistic investigation in thermocatalytic CO_2 hydrogenation involves Cu SACs supported on buckled C_3N_4, where the coordination environment of the Cu site (Cu–N_3 *vs.* Cu–N_4) was shown to govern product selectivity and pathway preference.[316] Geometry optimizations confirmed stable Cu anchoring at both tri and tetra coordinated nitrogen sites, with higher binding energy observed for Cu–N_4 (2.98 eV), indicating stronger thermodynamic stabilization. *Ab initio* molecular dynamics simulations at 450 K affirmed structural integrity of both configurations, while Bader charge and PDOS analyses revealed greater electron transfer and d–p orbital coupling in the Cu–N_3 model, consistent with a higher Cu valence state. Subsequent DFT calculations mapped out distinct reaction pathways: CO_2 hydrogenation over Cu–N_4 favoured the formate route toward CH_3OH, with energetically accessible *HCOO and *H_2COOH
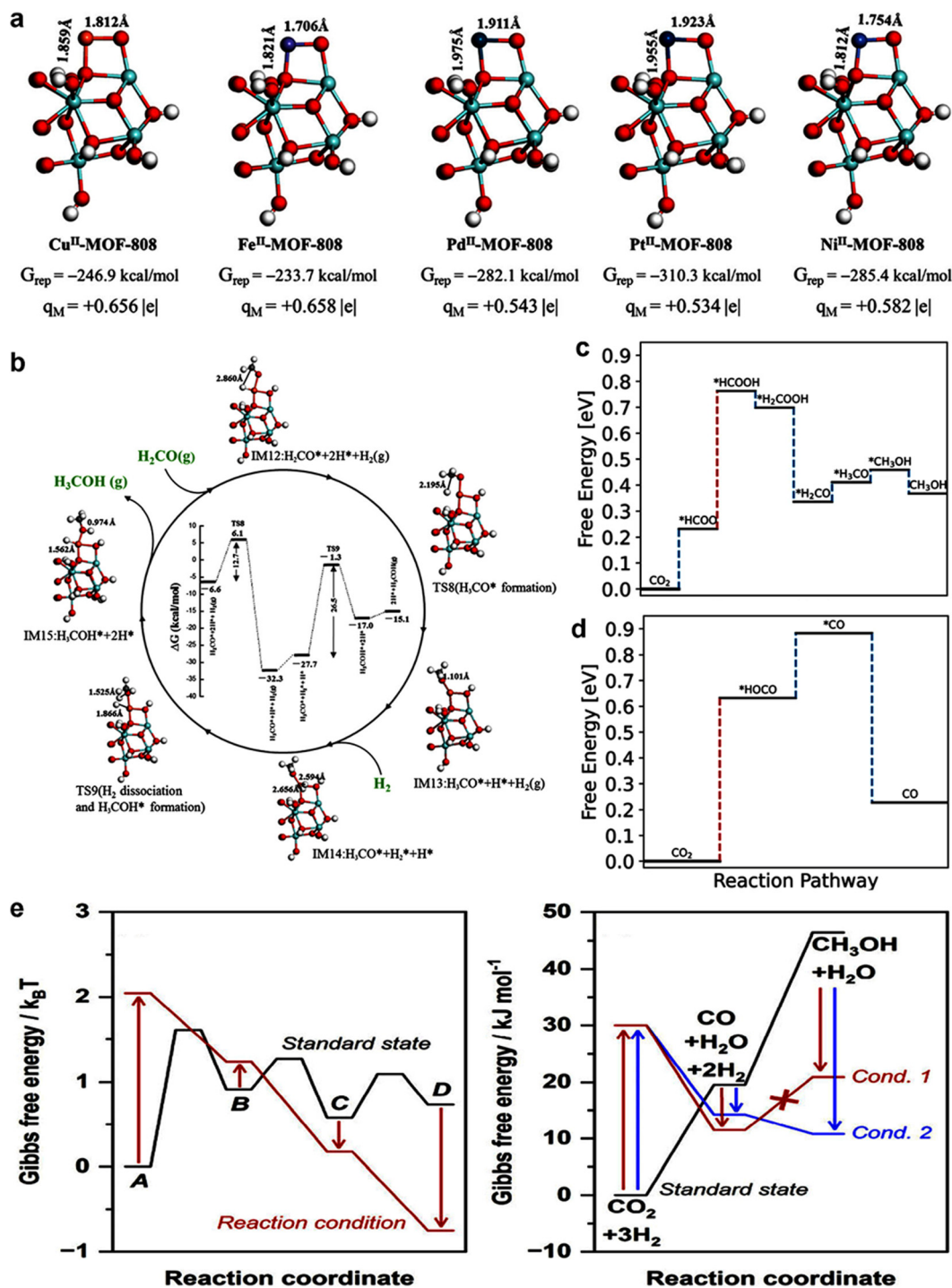
Fig. 38 DFT-based mechanistic insights into thermocatalytic CO_2 hydrogenation; (a) optimized geometries of MOF-808 supported single-metal sites (M = Cu, Ni, Pd, Pt, Fe), showing stable coordination environments. (b) Free energy profile for CO_2 hydrogenation to formic acid (HCOOH) over Cu(II)-MOF-808. Reproduced from ref. 315 with permission from American Chemical Society, copyright 2025. (c) Energy diagram for CO_2 hydrogenation to CH_3OH *via* the formate pathway over Cu–N_4 SAC and (d) Energy diagram for CO_2-to-CO conversion *via* the RWGS pathway over Cu–N_3 single-atom catalyst. Reproduced from ref. 316 with permission from Nature (CC-BY 4.0), copyright 2021. (e) Thermodynamic validation approach from Lin *et al.*, illustrating how reversibility analysis supports or challenges DFT-predicted mechanisms. Reproduced from ref. 286 with permission from American Chemical Society, copyright 2022.

intermediates and a free energy drop of 0.36 eV in the final C–O bond cleavage (Fig. 38c). In contrast, Cu–N_3 supported CO formation *via* the RWGS pathway through a *HOCO intermediate,

with lower CO desorption energy (−0.36 eV), facilitating rapid turnover (Fig. 38d). These results demonstrate how fine-tuning the coordination environment of SACs can selectively direct CO_2

9694 | *Energy Environ. Sci.*, 2025, **18**, 9632–9712

This journal is © The Royal Society of Chemistry 2025

conversion toward CH_3OH or CO under identical thermal conditions, reinforcing DFT power in correlating active site structure with catalytic function in SACs.

While DFT derived energy profiles allow detailed mapping of elementary steps, Lin et al. emphasized that reaction feasibility must also satisfy global thermodynamic and kinetic criteria. To this end, they developed a theoretical framework based on De Donder's inequality and effective reversibility analysis to assess the thermodynamic self-consistency of proposed multi-step pathways, such as $CO_2 \rightarrow CO \rightarrow CH_3OH$. Mechanistic schemes that appear kinetically feasible at the step level may nevertheless exhibit thermodynamic inconsistency when evaluated over the full reaction network, particularly if reversibility constraints are not satisfied (Fig. 38e). To strengthen mechanistic discrimination, Lin et al. further integrated DFT calculations with experimental delplot analysis and time-resolved yield measurements, enabling the distinction between primary product formation and secondary transformation routes. This combined approach establishes a direct link between atomistic-level modelling and macroscopic kinetic observables, providing a more robust foundation for interpreting DFT-derived selectivity trends in thermocatalytic systems.

These DFT case studies exemplify the wide applicability of theoretical modeling in understanding and designing SACs for CO_2RR. For COF-SACs, DFT clarifies how framework topology, metal coordination, and orbital distributions collectively influence catalytic pathways. For MOF-SACs, DFT elucidates how neighboring metal centers create electronic synergy, which fundamentally alters binding energies, electronic structure, and rate-determining steps. Such insights are crucial when interpreting experimental data, designing new catalysts, and guiding machine-learning models for predictive catalyst discovery. The combined theoretical-experimental approach ensures that DFT not only validates existing observations but also uncovers hidden correlations that might be experimentally inaccessible. As shown in these examples, DFT is essential for dissecting how electronic structures evolve within the dynamic microenvironments of MOFs and COFs, paving the way for the rational design of next-generation SACs tailored for efficient and selective CO_2 reduction.

5.2. High-throughput screening and machine learning approaches

The complexity of MOF- and COF-derived catalysts arises from the vast combinations of metal centers, coordination geometries, and organic linkers, making conventional experimental design challenging.[317–319] This complexity is further compounded when optimizing multiple catalytic parameters such as activity, selectivity, stability, and synthetic feasibility.[320] To address these challenges, high-throughput computational screening and ML have emerged as transformative strategies for accelerating catalyst discovery, particularly for CO_2RR.[321]

The identification of efficient catalysts relies on determining optimal active sites, coordination environments, and electronic structures. However, the extensive number of possible SAC configurations in MOF- and COF-derived systems makes traditional theoretical screening resource-intensive. High-throughput

screening leverages DFT-based automated workflows to compute key catalytic descriptors such as adsorption energies, reaction-free energies, and rate-determining steps, across numerous SAC candidates.[322,323] These workflows generate predictive performance maps, ranking materials based on expected catalytic efficiency.[324] However, comprehensive DFT studies demand substantial computational resources, particularly when assessing multimetallic SACs or catalysts embedded in MOF/COF matrices, where periodic boundary conditions and solvent effects must be considered.

To mitigate computational costs, ML techniques have been applied to accelerate materials discovery. By training predictive models on extensive DFT datasets and validated experiments, ML algorithms rapidly estimate key catalytic descriptors for materials that have not been directly computed, maintaining high accuracy while significantly reducing computational time.[325] Additionally, ML models uncover fundamental structure–property relationships,[326] which is particularly advantageous for SACs within MOF/COF frameworks due to their intricate coordination environments. Graph neural networks (GNNs) have demonstrated particular effectiveness in MOF- and COF-derived catalysts, capturing both atomic-level metal coordination and long-range framework interactions, which are crucial for accurate catalytic performance predictions.[327] Beyond simple property prediction, ML-driven inverse design has gained prominence.[328] This approach allows researchers to define target catalytic properties such as optimal binding energies for intermediates while the model recommends suitable metal centers, coordination geometries, and linker environments, streamlining the transition from computational design to experimental realization. Different ML models are selected depending on dataset size. Linear models (e.g., LASSO, ENR) are suitable for small datasets, kernel regression models (e.g., SVR, GPR, KRR) for moderate-sized datasets, decision trees (e.g., KNR, RFR, ETR) and neural networks (e.g., FNN) for larger datasets, etc.[329,330] GNNs have proven particularly effective for various SAC systems by encoding both the local metal site and supported coordination.[327]

For MOF-derived and COF-based SACs, DACs, and MACs, ML-assisted screening approaches remain largely unexplored. However, they represent an adaptable and promising methodology for catalytic applications. For instance, an ML-accelerated workflow analyzed $M–N_4–C$ catalysts based on graphdiyne for CO_2RR, predicting catalytic performance with accuracy comparable to DFT while reducing computational cost.[331,332] Similarly, a multi-objective ML framework integrating DFT adsorption energy data with heuristic stability metrics has been used to identify high-performance active sites in COF-supported SACs.[319] Beyond screening, ML has been instrumental in inverse design, where target CO_2 intermediate binding energies guide the selection of optimal SAC configurations, predicting ideal metal coordination environments and linker modifications for enhanced selectivity and stability. The dependence correlation mechanism establishes a direct relationship between reaction energy barriers, elemental composition, and active site configurations, providing crucial insights for electrocatalyst screening.[331] In particular, the

This journal is © The Royal Society of Chemistry 2025

Energy Environ. Sci., 2025, **18**, 9632–9712 | **9695**

double-dependence correlation model refines this approach by identifying strong preferences for both specific elements and active sites simultaneously, thereby narrowing down promising catalyst candidates to a highly selective range.[333] This methodology enhances the predictive accuracy of electrocatalyst discovery by prioritizing key reaction steps that dictate catalytic performance. As illustrated in Fig. 37, this framework is integrated into machine learning-assisted screening, where high-throughput DFT calculations first establish selectivity trends (Fig. 39a), followed by the mapping of comprehensive reaction pathways for CO_2 valorisation (Fig. 39b). The double-dependence

correlation mechanism (Fig. 39c) is particularly effective in refining catalyst selection by limiting viable candidates to those exhibiting optimal electronic and structural properties. Reported SACs for CO_2 valorisation (Fig. 39d) demonstrate the applicability of this strategy, while the overall workflow of first-principles machine learning models (Fig. 39e) highlights its role in accelerating catalyst design. While SACs have been the primary focus of ML-driven screening, these methods have also been extended to DACs and MACs for improved catalytic synergy.[331,333,334] A comprehensive computational screening study reported the favourability of Fe–Ni dual atoms on defective graphene for

Fig. 39 (a) DFT-based selectivity analysis of SACs for CO_2RR. Reproduced from ref. 290 with permission from Elsevier, copyright 2023. (b) Comprehensive reaction pathways for CO_2 valorisation into value-added products. (c) Schematic representation of the double-dependence correlation model. Reproduced from ref. 332 with permission from American Chemical Society, copyright 2022. (d) Overview of various SACs reported for CO_2 valorisation into different products. Reproduced from ref. 336 with permission from Royal Society of Chemistry (CC-BY 4.0), copyright 2023. (e) Workflow of the first-principles machine learning strategy for catalyst discovery. Reproduced from ref. 337 with permission from Wiley, copyright 2023.

9696 | *Energy Environ. Sci.*, 2025, **18**, 9632–9712

This journal is © The Royal Society of Chemistry 2025

CO_2RR.[287] Additionally, prediction studies on DACs and MACs on metal surfaces have been well-practiced and reported. For instance, Karmodak et al. identified 11 stable Fe–M systems on an Au surface for CO_2RR, demonstrating their potential to suppress the competitive HER.[287] Similarly, a recent high-throughput ML study screened DACs for CO_2RR by analyzing electronic descriptors and coordination-dependent adsorption energies, revealing that Cr-Zr DAC on Cu surface exhibited superior C_2 selectivity compared to monometallic SACs due to enhanced charge redistribution at active sites.[335] Overall, integrating high-throughput screening, ML, and experimental validation is transforming SAC development for CO_2 valorisation. These data-driven strategies complement traditional experimental and mechanistic insights from DFT and in situ studies, establishing a rational and efficient platform for catalyst design. Further advancements in high-quality materials databases, predictive algorithms, and multi-source experimental–computational integration will enhance ML-driven catalyst design, ensuring broader adoption and practical implementation in CO_2 conversion technologies.

6. Assessment of industrial scalability and sustainable performance

6.1. Industrial feasibility and technoeconomic evaluation

Scaling up eCO_2RR from laboratory to industrial levels presents significant challenges, necessitating a thorough techno-economic analysis to assess its viability. Translating the laboratory-scale results in terms of selectivity and efficiency into profitable large-scale production remains challenging due to various issues such as catalyst degradation, mass-transport limitations, reactor design and product selectivity and purification. Particularly, several high-performance CO_2R catalysts fail to show long-term stability under continuous industrial operation conditions, due to issues such as catalyst poisoning, corrosion, or structural changes that reduce efficiency. This necessitates frequent replacement and increases operational costs, thus lowering profitability significantly. Maintaining adequate catalyst lifespans is crucial for large scale high-volume production, which requires substantial efforts in materials science innovation.[338–345]

Likewise, efficient reactant (CO_2) transport towards- and product removal from the catalyst surface is crucial for scaling-up. Lab-scale experiments often employ conditions facilitating excellent mass transport. However, industrial systems face more complex dynamic issues and mass transport limitations, hampering the effectiveness of highly active electrocatalysts. Scaling up to larger sizes requires addressing limitations in transferring material which greatly impacts cost and overall productivity. Integrating innovative material transportation systems for ensuring effective flow, improves the material transport to improve large-scale commercial applications that meet industrial production requirements. Also, electrochemical reactors designed for laboratory setups do not translate readily to industrial scales. Industrial-scale reactors require cost-effective, high-volume manufacturing with reliable materials. The capital expenditure and operation costs can be reduced with significant engineering design changes. Optimizing the flow design along with improving transport of reactant through appropriate materials are significant engineering hurdles needing innovation to achieve efficient and high production processes.

Similarly, achieving high product selectivity at industrial scale is challenging. Laboratory studies frequently report high selectivity towards certain products. However, this often comes from simplified experimental parameters at reduced scales where mass transport, chemical concentration or byproduct contamination effects were not accounted during optimization. Achieving high selectivity and maintaining quality consistently at large scale production remains more challenging due to increased occurrence of cross-contamination from diverse reactants, which increase challenges in efficient and cost-effective purification. The separation of desired products from mixtures becomes an energy intensive process and substantial source that greatly contributes to the increased production cost and requires advanced post processing which adds significantly higher cost for purification that will influence economic viability and make commercial success far more difficult to achieve. Advanced membrane technologies, advanced processing methodologies and exploring novel configurations along with refining processing methods and streamlining and implementing cost-effective procedures would enhance potential toward wider applicability and facilitate large-scale deployment in industrial setting while maintaining higher profits by minimizing processing step cost and maximizing overall energy efficiency in purification processes along with producing consistent and adequate purity requirements demanded. A comprehensive techno-economic analysis needs detailed cost assessment of the multiple stages for effectively capturing and transporting materials for deployment.

The electrochemical reduction of CO_2 (CO_2RR) requires a carefully designed electrolysis system that balances catalytic efficiency, mass transport, energy consumption, and long-term operational stability. Electrolysis setups for CO_2RR can be broadly categorized into three main configurations:

H-type cells, flow cells with gas diffusion electrodes (GDEs), and membrane electrode assembly (MEA) systems. In contrast, flow cells enable higher performance by continuously supplying CO_2 gas to a gas diffusion layer. These systems incorporate anion exchange membranes (AEMs), cation exchange membranes (CEMs), or bipolar membranes (BPMs) to facilitate ion transport and separate the electrode compartments (Fig. 40a). Flow cells are capable of operating at current densities $> 100–500$ mA cm^{-2} and support continuous product removal and electrolyte control. The membrane electrode assembly (MEA) configuration integrates the catalyst layers directly onto the membrane, eliminating the liquid electrolyte in the reaction zone. This design improves system compactness and reduces ohmic resistance, although challenges include water management and gas sealing. As a starting point towards achieving industrial applications the eCO_2RR usually investigated using flow-cell or membrane electrode assembly (Fig. 40b). Although not many MOF based materials were studied for high current density analysis, other CO_2 reduction materials

This journal is © The Royal Society of Chemistry 2025

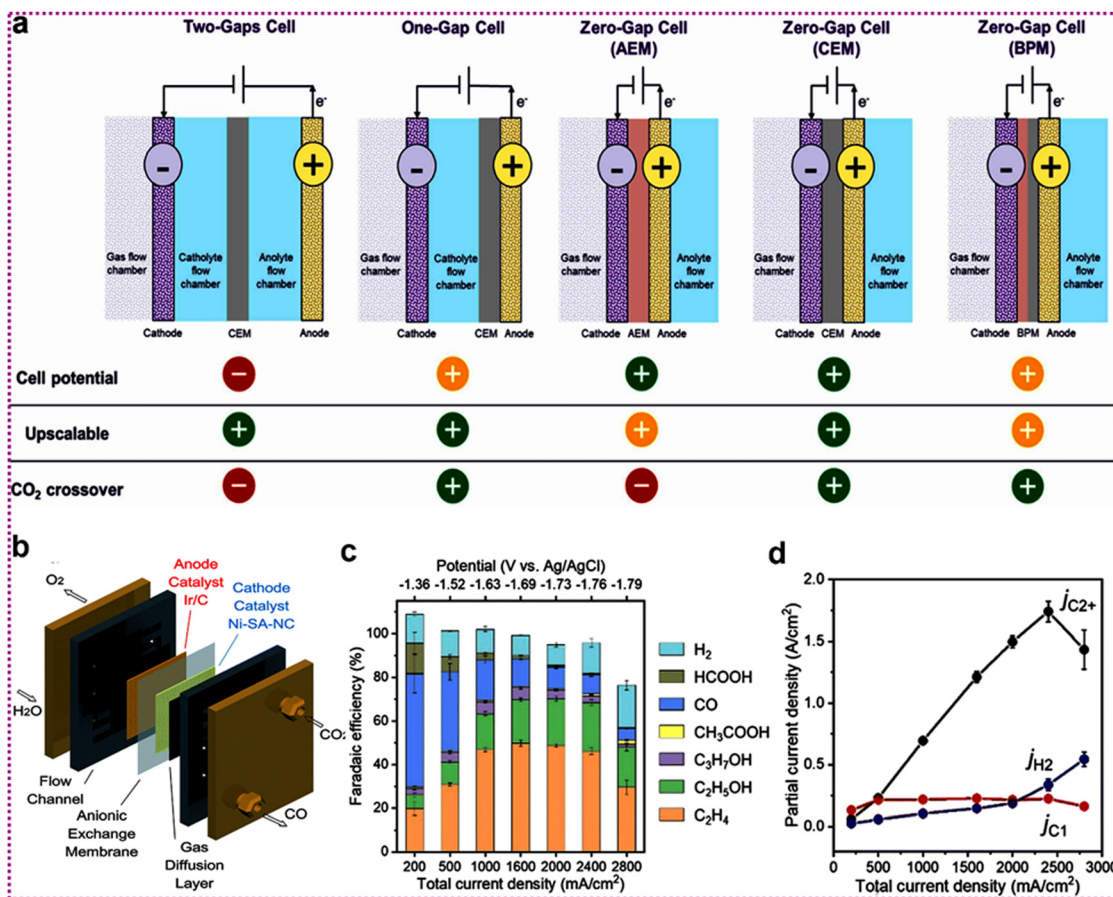Energy Environ. Sci., 2025, 18, 9632–9712 | 9697

Fig. 40 (a) Configuration of various electrochemical cells (AEM, PEM, BPM). Reproduced from ref. 346 with permission from Elsevier (CC–BY 4.0), copyright 2024. (b) Typical membrane electrode assembly. (c) FEs under various applied potentials catalyzed by CuONPs in 1 M KCl. (d) Partial current density of eCO$_2$ reduction products catalyzed by CuONPs in 1 M KCl. Reproduced from ref. 347 with permission from Royal Society of Chemistry (CC–BY 4.0), copyright 2023.

were tested for long-time operation with high current density. For instance, various copper-based materials have been tested for C$_2$ products with very high current density with long-time operational stability (Fig. 40c and d). Operational parameters such as current density, cell voltage, CO$_2$ flow rate, temperature, and electrolyte composition all influence performance. Industrial targets include current densities >200 mA cm^{-2}, faradaic efficiencies above 80%, and cell voltages under 3 V. Challenges such as carbonate formation, product crossover, electrode flooding, and long-term catalyst degradation remain critical bottlenecks. Addressing these issues through membrane innovation, water management strategies, and robust catalyst development is essential for commercial viability.[347]

6.2. Energy consumption and economic feasibility of CO$_2$ electroreduction

The successful industrialization of CO$_2$ electroreduction depends not only on catalytic performance but also on its overall energy efficiency and economic viability. Electrochemical CO$_2$ conversion is inherently electricity-intensive, and even with advanced catalysts, the system often requires significant overpotentials. Typically, CO$_2$ electroreduction operates at cell

voltages ranging from 2.5 to 3.5 V, depending on the catalyst system and reactor design. For instance, converting CO$_2$ to CO (a 2e$^-$ process) ideally requires ~ 260 kJ mol^{-1} based on thermodynamics, but practical systems may consume >600–800 kJ mol^{-1} due to kinetic barriers and energy losses at the electrodes and across the membrane. For the system illustrated in Fig. 41a, the electrolysis cells consume 6.82 kWh per kilogram of CO produced. Considering an overall plug to power efficiency of 80%, this corresponds to a total energy requirement of 8.53 kWh per kilogram of CO. The conventional route for CO production *via* partial combustion of heavy fuel oil demands approximately 2.30 MWh of electricity and 660 kg of fuel oil per tonne of CO, totalling about 34 GJ per tonne. In comparison, electrolysis-based systems consume around 9.36 MWh (33.7 GJ) per tonne of CO, closely matching conventional energy costs, while plasma-based methods require only 5.41 MWh (19.5 GJ), offering a 43% reduction in total energy consumption (Fig. 41b). Multi-carbon (C$_{2+}$) products such as ethylene or ethanol involve more complex reaction pathways and higher energy demands, often exceeding 1000–1500 kJ mol^{-1} due to 12e$^-$ transfers and competing side reactions.[349–352] From an economic perspective, several recent techno-economic assessments (TEAs) have

9698 | *Energy Environ. Sci.*, 2025, **18**, 9632–9712

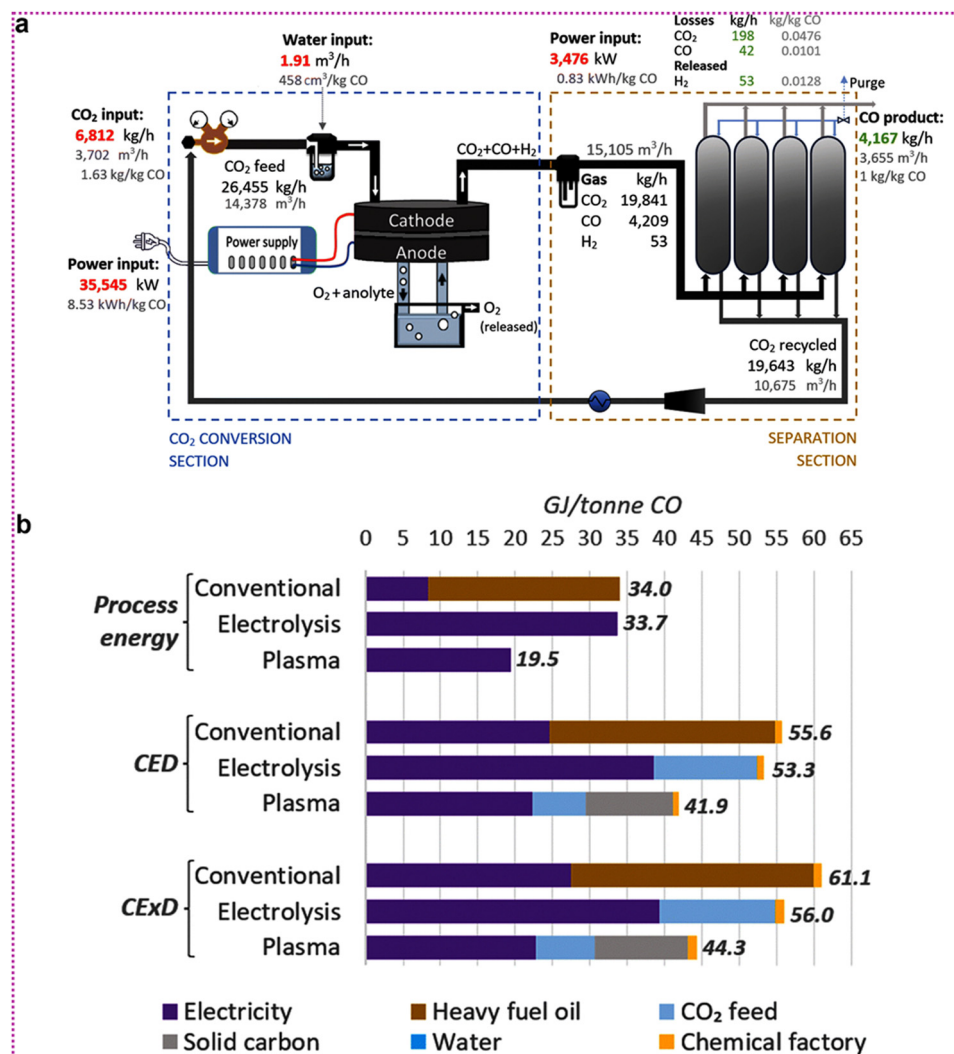This journal is © The Royal Society of Chemistry 2025

Fig. 41 (a) Schematic flow diagram illustrating the operation of an electrolyser-based facility designed to produce 100 tonnes of carbon monoxide. (b) Comparison of energy costs associated with conventional, electrolysis-based, and plasma-based CO production methods, based on their respective baseline scenarios. Reproduced from ref. 350 with permission from Royal Society of Chemistry (CC-BY 4.0), copyright 2024.

provided benchmarks for viability. According to Jouny et al.[344] a CO_2-to-CO system becomes cost-competitive at an electricity cost of <\$0.03–0.04 per kWh, assuming the following conditions such as Current density >200 mA cm^{-2}, faradaic efficiency >90%, Single-pass conversion >60% and Electrolyzer stack lifetime >5 years. Under these conditions, the levelized cost of CO production can approach \$0.60–\$0.80 per kg, making it comparable to syngas derived from fossil fuels when renewable electricity is cheap. However, these thresholds are tighter for C_{2+} products. For example, CO_2 to ethylene and ethanol production may cost \$2–4 per kg, depending on carbon efficiency, energy input, and capital costs for product separation and purification.[348–351] Another critical factor is the energy return on energy invested (EROEI). Systems with low selectivity or high energy input may consume more energy than the calorific value of the product, leading to negative net energy balance. Coupling CO_2 electroreduction with renewable energy sources (e.g., solar, wind) and using waste CO_2 streams (e.g., from fermentation or flue gas) can improve the overall sustainability.

In addition to electricity, balance of plant costs including gas purification, product separation, water management, and stack replacement contribute significantly to the overall cost. Innovations such as Gas diffusion electrodes (GDEs) for better mass transport, zero-gap or membrane electrode assembly (MEA) reactors for reduced ohmic loss, Anodic organic oxidation (replacing OER) to generate co-products and lower energy input and Pressurized operation to improve CO_2 solubility and system compactness are being explored to reduce total energy consumption and improve economic returns. Moreover, policy incentives, carbon pricing, and green premium markets for synthetic fuels and chemicals can further tilt the economic balance in favour of CO_2 electroreduction technologies. For example, with a carbon credit of \$50–100 per ton CO_2, many systems could become economically favourable even at slightly higher electricity prices or lower product yields. Recent TEAs have shown that products like CO and formic acid are closest to commercial viability, while multi-carbon products (C_{2+}) such as

Table 5 Production costs and technological performance

Techno-economics	Products				
	Carbon monoxide	Formate	Methanol	Ethanol	Ethylene
2019 US market prices ($ kg^{-1})	0.15	0.50	0.26	0.48	0.58
Published production costs ($ kg^{-1}) Average ± standard deviation [minimum, maximum]	0.39 ± 0.19 [0.18, 0.64]	0.96 ± 0.78 [0.10, 2.63]	1.40 ± 1.03 [0.54, 2.64]	3.92 ± 3.96 [0.37, 11.27]	2.48 ± 1.83 [0.65, 4.92]
Figures of merit					
Catalysts	Ni SACs[a]	Bi, Sn	Co–Pc	N–C/Cu	Cu
Faradaic efficiency (%)	90–99	80–90	~30	~50	>70
Cell voltage[b] (V)	2.2–2.5	3–4	>2	2.5–3.0	2.4
Current density (mA cm^{-2})	>400	>100	<100	>100	>200

[a] Single-atom catalysts. [b] For half-cell studies, the cell voltage is estimated from the assumption of 1.6–1.8 V *versus* a reversible hydrogen electrode for the oxygen evolution as the counter electrode reaction.[351]

ethanol and ethylene require significant advancements in performance and system integration to reduce production costs Table 5.[351]

6.3. Integrated electrocatalysis for CO$_2$ and biomass conversion: a future opportunity for COF and MOF based SACs

Coupling CO$_2$RR with the oxidation and valorisation of organic compounds offers a compelling approach to enhance both sustainability and economic feasibility by leveraging the energy released during organic oxidation to drive the CO$_2$RR. Although eCO$_2$RR is a promising strategy for transforming captured carbon dioxide into useful chemicals and fuels, its energy efficiency is often limited by the oxygen evolution reaction (OER) at the anode, which is thermodynamically demanding and kinetically sluggish. To minimise the energy input, an alternative strategy involves replacing OER has been suggested. For instance, electro-oxidation of organic compounds that are thermodynamically easier to oxidize and yield value-added products can be considered. Coupling exothermic organic oxidation with endothermic CO$_2$RR improves energy efficiency by reducing the external energy input required. Electrons generated from oxidation directly drive CO$_2$RR, minimizing reliance on external electricity. This approach allows the conversion of organic waste streams, including biomass, into valuable products, thereby reducing waste disposal burdens and utilizing renewable resources. Strategic catalyst design can create synergistic effects between oxidation and reduction, improving reaction kinetics and selectivity. Optimized catalyst systems, possibly utilizing hybrid materials or tailored metal–organic frameworks, could offer enhanced electron transfer, reduced overpotentials, and targeted product formation, reducing the energy barrier of both half-reactions while lowering activation energies for desired product formations. This integrated approach enhances overall energy efficiency while co-producing commercially relevant chemicals from both the cathode and anode. Organic molecules such as glycerol, ethanol, glucose, furfural, and 5-hydroxymethylfurfural (5-HMF) have significantly lower oxidation potentials compared to water. The advantage of co-electrolysis of CO$_2$ with organic/biomass oxidation shown in (Fig. 42a).[341]

For Instance, an efficient CO$_2$ electrolysis system was demonstrated by replacing the oxygen evolution reaction with biomass oxidation using 5 nm nickel oxide (NiO) nanoparticles as anodic catalysts. A two-compartment electrolysis cell was constructed to couple 5-hydroxymethylfurfural (HMF) oxidation using NiO nanoparticles with CO$_2$ reduction to formate on BiO$_x$ electrocatalysts. Operating in CO$_2$-saturated 0.5 M KHCO$_3$, the system achieved a stable 2.5 V cell voltage at 2 mA cm^{-2} over 3 hours, yielding 81% faradaic efficiency (FE) for formate and 36% FE for biomass oxidation (Fig. 42b).[352]

Similarly, a co-electrolysis system combining CO$_2$ reduction to ethylene (C$_2$H$_4$) at a copper cathode with glycerol oxidation to glycolic acid at a gold nano-dendrite anode was developed using a bipolar membrane to prevent carbonate crossover. The system operated at 175–225 mA cm^{-2} with 50% faradaic efficiencies for both C$_2$H$_4$ and GA, reducing cell voltage by 0.8 V compared to conventional setups. Techno-economic analysis showed the process could achieve a competitive ethylene price of ~$1.1 per kg, highlighting its industrial potential over traditional eCO$_2$R routes (Fig. 42c).[353] A paired electrolysis system was developed for economical formate production and biomass valorisation by coupling CO$_2$ reduction (eCO$_2$RR) with 5-hydroxymethylfurfural oxidation (HMFOR). Single-atom Cu-doped Bi (Cu$_1$Bi) served as the cathode, achieving formate current densities >1 A cm^{-2} and long-term stability, while NiCo layered double hydroxides (NiCo LDHs) catalyzed HMF oxidation to 2,5-furandicarboxylic acid with >95% faradaic efficiency. This coupling reduced energy consumption to ~3493 kWh per ton of formate 22.9% lower than conventional systems highlighting a promising strategy for efficient CO$_2$ utilization and biomass upgrading (Fig. 42d).[354] To enhance product value and energy efficiency, Cu foam was modified into CuO nanoflowers (CuO–NF@Cu), enabling dual-function electrocatalysis for CO$_2$ reduction (CO$_2$RR) and 5-hydroxymethylfurfural oxidation (HMFOR). During CO$_2$RR, CuO converted into Cu$_2$O/Cu nanoflowers, delivering 70% faradaic efficiency (FE) for ethylene at 104.5 mA cm^{-2} over 45 h. For HMFOR, CuO–NF@Cu achieved 99.3% FE for FDCA at 1.62 V. In a paired system, using Cu$_2$O/Cu–NF@GDL (cathode) and CuO–NF@Cu (anode), 188.8 mA cm^{-2} was reached at 2.75 V with 74.5%/96.6% FEs for C$_2$H$_4$ and FDCA, respectively. This demonstrates a practical route to co-produce high-value chemicals from CO$_2$ and biomass.[355]

Successful implementation of paired electrolysis relies on the rational design of compatible COF and MOF based SACs, membrane architectures, and operating conditions to ensure
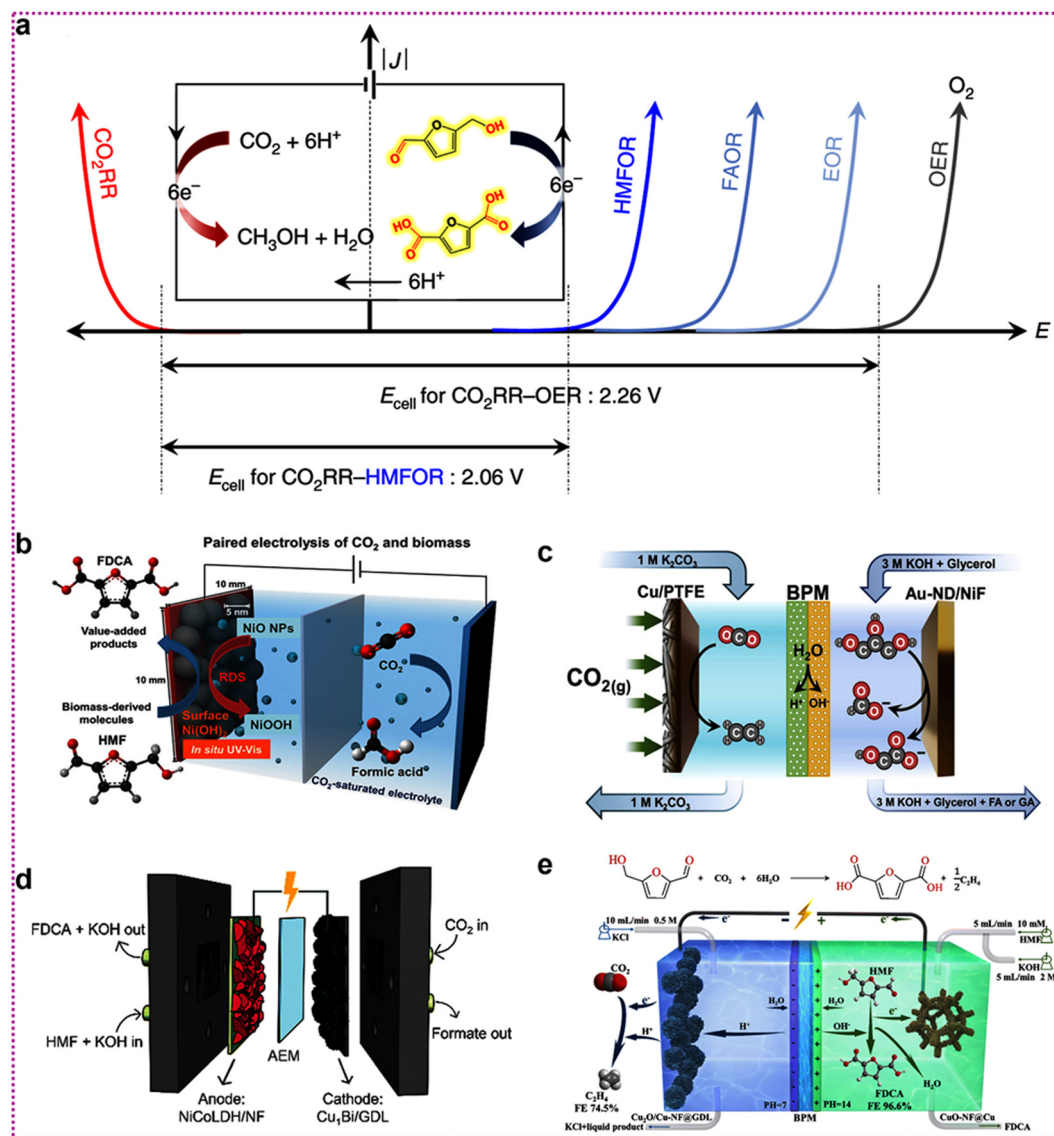
9700 | *Energy Environ. Sci.*, 2025, **18**, 9632–9712

This journal is © The Royal Society of Chemistry 2025

Fig. 42 (a) Pictorial representation of the advantage of co-electrolysis of CO_2 with organic/biomass oxidation. Reproduced from ref. 341 with permission from Nature (CC-BY 4.0), copyright 2019. (b) Paired-electrolysis of CO_2 with hydroxymethylfurfural. Reproduced from ref. 352 with permission from American Chemical Society, copyright 2020. (c) Co-electrolysis of CO_2 and glycerol using bipolar membrane. Reproduced from ref. 353 with permission from Elsevier, copyright 2022. (d) Schematic of the coupled eCO_2RR-HMFOR system in the MEA setup. Reproduced from ref. 354 with permission from Royal Society of Chemistry, copyright 2023. (e) Schematic representation of integrated electrolysis flow cell coupling CO_2RR with HMFOR. Reproduced from ref. 355 with permission from Royal Society of Chemistry (CC-BY 4.0), copyright 2023.

synchronized kinetics and selective conversion at both electrodes. As a sustainable and modular platform, paired electrolysis offers a powerful route for integrating carbon capture with biomass vaporization, enabling circular chemical production powered by renewable electricity. This area of research opens a wide window for the development of COF and MOF based SACs.

7. Prospects, limitations, proposed solutions and conclusions

As the world seeks sustainable technologies to mitigate CO_2 emissions, and alternative resources for chemicals and fuels,

the applications of SACs for the valorisation of CO_2 hold immense significance in paving the way for more sustainable and environmentally beneficial technologies for CO_2 capture and utilization. On this basis, there are significant prospects in this area which must be thoroughly considered.

7.1. Prospects

(1) According to recent literature, global CO_2 emissions have reached approximately 37.4 billion tons per year. Despite this staggering figure, the conversion of CO_2 into valuable products with 100% efficiency remains a goal far from being realized. Achieving this level of efficiency is still in the early stages of development. Therefore, it is crucial not only to advance the

This journal is © The Royal Society of Chemistry 2025

Energy Environ. Sci., 2025, **18**, 9632–9712 | **9701**

development of SACs but also to optimize the conditions under which CO_2 can be effectively converted. Among the most promising materials for this challenge are COF and MOF, which are recognized as some of the best porous materials available. These materials hold exceptional potential for both capturing CO_2 directly from the air and converting it into value-added products. The ability to directly capture CO_2 from the atmosphere and convert it into useful compounds is of paramount importance for making real-world applications of CO_2 conversion a viable and scalable solution to mitigate climate change.

(2) COF and MOF materials offer tunable pore environments that enable precise control over CO_2 diffusion, adsorption, and single-atom catalyst (SAC) exposure crucial factors in enhancing CO_2RR activity and selectivity. Looking forward, the design of functionalized ligands with electron-donating groups can strengthen metal–ligand interactions, stabilize active sites, and modulate local electronic structures for optimal CO_2 activation. Post-synthetic modifications (PSM) further expand the toolbox for tailoring coordination environments and introducing catalytic specificity. These framework-based strategies hold significant promise for advancing SAC-based CO_2RR toward higher efficiency, product selectivity, and long-term operational stability.

(3) Unraveling catalytic mechanisms at the atomic level remains a cornerstone for the rational design and optimization of single-atom catalysts (SACs). Traditional *ex situ* characterization offers only a static snapshot of the catalyst, often missing critical insights into the dynamic behavior of active sites under operating conditions. Therefore, integrating *in situ* and *operando* spectroscopic techniques such as X-ray absorption spectroscopy (XAS), Raman, infrared (IR), and ambient pressure X-ray photoelectron spectroscopy (AP-XPS) is imperative. These tools enable real-time tracking of the coordination environment, electronic structure, and intermediate species during catalysis, thereby shedding light on the true nature of active sites and their evolution.

(4) SACs face challenges in cost-effectiveness and scalability due to expensive precursors, complex synthesis, and material stability, including costly noble metals, precise methods, and stability of catalysts. Therefore, more research must be focused on reducing these drawbacks. Scalable synthesis *via* spray pyrolysis, electrospinning, or self-assembly strategies can reduce fabrication expenses.

(5) MOF/COF-SAC hybrids using carbon-based supports such as graphene, and CNT can improve durability and reduce the required metal content. Bimetallic and alloy-based SACs may improve efficiency, reducing metal consumption.

(6) DFT studies can be utilized to optimize metal–ligand interactions, electronic structures, and reaction pathways, reducing experimental trial-and-error. Molecular dynamics simulations assess catalyst stability under real-world conditions, and multiscale modeling for reaction kinetics, including Kinetic Monte Carlo and microkinetic modeling which can provide accurate predictions of catalytic activity.

(7) Emerging COF and MOF based SACs architectures are revolutionizing tandem synthesis workflows, particularly in the integration of CO_2 reduction reaction (CO_2RR) with the oxidation and valorisation of organic compounds. These organic substrates (ethanol, methanol, glycerol, aldehydes, amino acids, furans, glucose, and fructose *etc.*), which are more easily oxidized than water, provide a promising pathway for coupling CO_2RR with organic transformations, leading to the simultaneous production of valuable chemicals. This approach not only maximizes resource utilization but also enhances process efficiency by harnessing the synergy between CO_2 reduction and organic compound oxidation. Future advancements will focus on optimizing catalyst selectivity, stability, and reaction conditions to enable seamless integration of these processes, thereby advancing the sustainability and economic viability of CO_2 valorisation strategies.

7.2. Limitations and solutions

We have presented the limitations and their corresponding solutions in a graphical model (Fig. 43). Additionally, a detailed description of each point is provided below.

Limitation 1. Selectivity remains a major hurdle in CO_2 valorisation, primarily due to the uncontrollable formation of complex mixtures, including CO, CH_4, HCOOH, CH_3OH, and C_{2+} compounds. Furthermore, achieving 100% conversion efficiency of CO_2 into valuable products I not only a monumental challenge but also one of the primary obstacles preventing the large-scale commercialization of CO_2 conversion technologies.

Solution 1. It is essential to develop single-atom engineered catalysts with multi-metal single atoms sites on a single substrate, which can improve both selectivity and conversion efficiency.

Limitation 2. One of the most significant limitations in developing COF and MOF based SACs is the difficulty in controlling their size, growth, and porosity. These parameters must be finely tuned to optimize performance, but achieving such precise control remains an exceptionally challenging task, limiting the scalability and practical application of these materials.

Solution 2. This may be possible by tuning the synthesis conditions, such as temperature, pressure, and precursor ratio, as well as by functionalizing MOFs and COFs with alternative chemical moieties, such as polymers and gels.

Limitation 3. Solvent chemistry plays a major role in designing various types of MOF and COF-based SACs. However, hazardous solvents used in the preparation of SACs pose a significant issue in terms of environmental impact and green technology.

Solution 3. Selecting sustainable and economically viable green solvents is imperative for the scalable application of single-atom catalysts (SACs), especially in energy and environmental catalysis. Emerging solvent systems such as deep eutectic solvents (DESs) and ionic liquids (ILs) offer unique physicochemical properties including low volatility, high thermal stability, and tunable polarity that are highly beneficial for stabilizing single-atom sites, enhancing reactant solubility, and facilitating selective CO_2 reduction. Moving forward, the integration of these green solvents with SAC systems not only aligns with green chemistry principles but also opens new avenues for designing more efficient and eco-friendly catalytic processes.
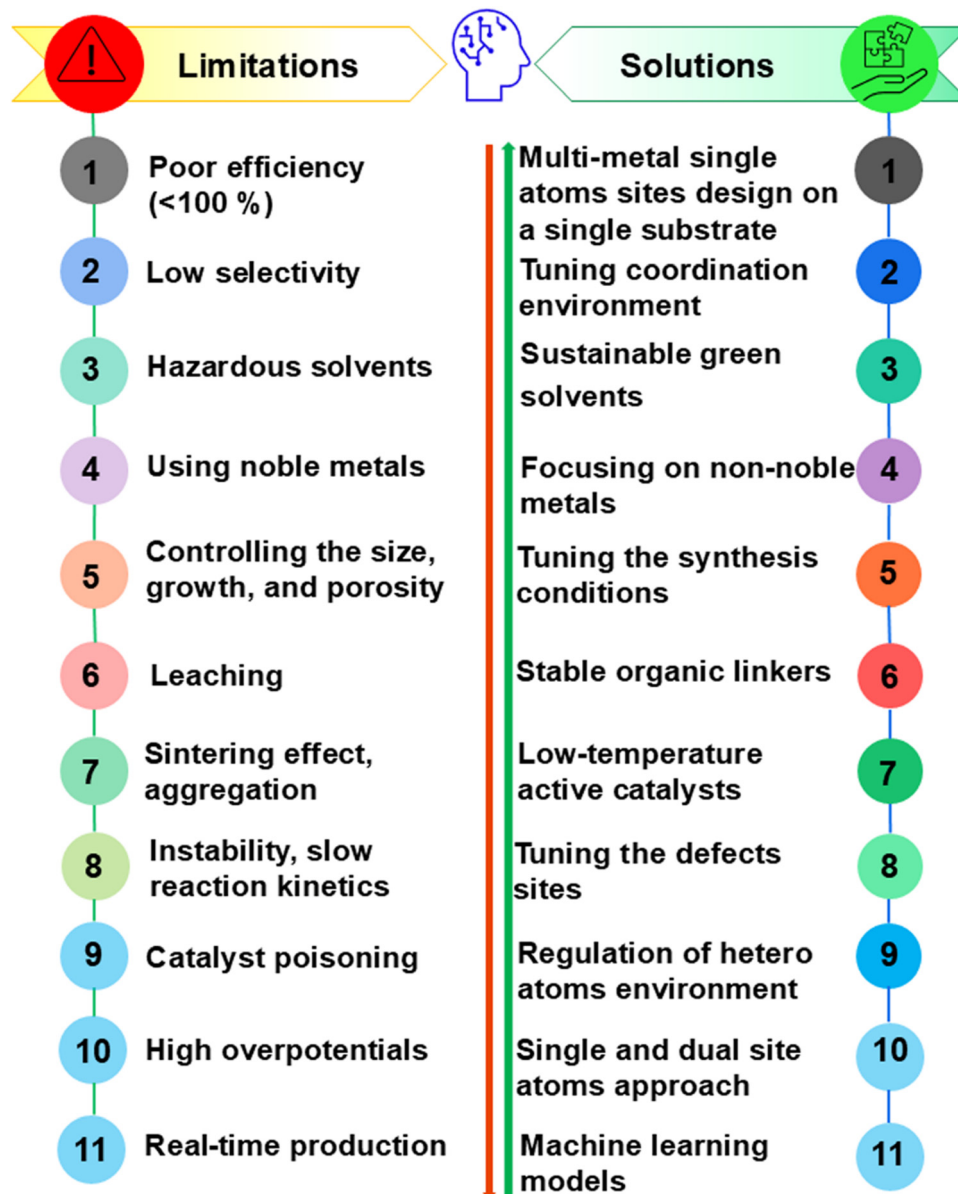
9702 | *Energy Environ. Sci.*, 2025, **18**, 9632–9712

This journal is © The Royal Society of Chemistry 2025

Fig. 43 Brief note on the limitations and solutions of COF and MOF–based SACs for CO_2 valorisation.

Limitation 4. The majority of highly active SACs are based on noble metals, which, despite their exceptional catalytic performance, are both expensive and increasingly scarce over time, posing a significant barrier to their long-term sustainability and widespread application.

Solution 4. Focusing on non-noble metal-based SACs is critical for addressing the challenges associated with the high cost and limited availability of noble metals. Non-noble metals such as Al, Fe, Ni, Zn, and Cu offer several key advantages: they are abundant, inexpensive, and environmentally friendly, making them ideal candidates for large-scale applications. Moreover, recent advances in the design and synthesis of non-noble metal SACs have shown that they can achieve comparable catalytic performance to their noble metal counterparts, especially when engineered at the atomic level for optimal active site

exposure. By developing non-noble metal SACs, it becomes possible to significantly reduce the economic burden of catalytic processes, enhancing their sustainability and making them more accessible for industrial applications. Therefore, focusing on these materials represents not just a solution to the limitations of noble metals but a major step toward more efficient, scalable, and cost-effective catalytic technologies.

Limitation 5. Whether in Thermocatalysis, electrochemical catalysis, or photochemical catalysis, the long-term stability of COF and MOF-based SACs is a critical issue due to metal single atom leaching, pore collapse, and degradation, which limits the efficiency of the catalyst and the products.

Solution 5. Multifunctional heteroatoms offering strong coordination bonds and stable organic linkers may help reduce leaching. Hybridizing MOFs and COFs with stable substrates,

such as boron nitride nanotubes, and incorporating functional groups onto carbon substrates are effective strategies for maintaining the long-term stability of SAC catalysts.

Limitation 6. Thermocatalysis requires high temperatures, leading to high power consumption. Additionally, at elevated temperatures, metal single atoms may aggregate into nanoparticles due to the sintering effect, which limits the efficiency of the catalyst.

Solution 6. Designing low-temperature active catalysts and utilizing thermal sources such as solar thermal energy, waste-generated power, and modular reactor designs are the most feasible approaches to improving thermocatalysis methods for converting CO_2 into value-added C_1 and C_{2+} products.

Limitation 7. Electrochemical CO_2RR is plagued by a range of significant and interrelated challenges such as the necessity for high overpotentials (≥ 0.5 V), slow reaction kinetics, mass transport limitations, catalyst poisoning, the dominance of the hydrogen evolution reaction, low faradaic efficiency, and membrane degradation that severely restrict its efficiency and effectiveness. Moreover, the enormous hurdle of scaling up from lab-scale to industrial applications remains a major bottleneck, hindering its commercial viability.

Solution 7. To achieve low overpotentials, single atoms are the best contenders due to their 100% atom efficiency and selectivity. Controlling the active sites of SACs, as well as the defects and porosity of MOF and COF surfaces, can enhance reaction kinetics. Another approach is designing a modular electrochemical cell reactor.

Limitation 8. Despite extensive research, photochemical CO_2RR continuous to suffer from critical limitations including poor efficiency, low selectivity, instability, and slow reaction kinetics, which fundamentally hinder their path towards commercial applications.

Solution 8. Tuning the band gap of SACs can improve light absorption efficiency, thereby enhancing overall efficiency and reaction kinetics. Additionally, advancements in Z-scheme heterojunctions, plasmonic enhancement, and cocatalyst engineering (including SACs) can drive photochemical catalysis toward a more advanced sector for CO_2 valorisation.

Limitation 9. The reliance on manual and traditional screening processes, coupled with lengthy method validations, severely impede the real-time production of compounds.

Solution 9. Focusing on advanced technologies, such as machine learning models and artificial intelligence (AI) based predictive catalyst design, can save significant time, accelerate economic growth, and promote environmental sustainability.

7.3. Conclusion

This review has comprehensively summarized recent advancements in the design and application of COF and MOF-derived or based SACs for the thermochemical, photochemical, and electrochemical conversion of CO_2 into value added C_1, C_{2+} products. We have outlined key synthesis strategies including pyrolytic (direct, sacrificial template, and confined), non-pyrolytic methods (pre and post synthetic metalation), and other advanced techniques such as ALD, CVD, electrospinning,

alongside a discussion of critical physiochemical parameters influencing catalytic performance. Particularly emphasis was placed on heteroatom (boron, carbon, nitrogen (pyridinic/pyrrolic), phosphorous, oxygen, sulphur, halogens), coordination environments, axillary ligand effects, p-block metal sites, dual atom active sites, morphological, porosity features and electrolyte interactions, all of which play a crucial role in enhancing CO_2 reduction efficiency. Furthermore, we highlighted advanced characterization tools, including HAADF-STEM, XAS, *in situ* FTIR, and Raman spectroscopy, as well as the integration of DFT and ML models to unravel reaction mechanisms and guide catalyst design. We have also underlined how this emerging COF an MOF SACs system is of significant importance from an industrial techno scale perspective. The insights gathered in this review underscore the significant potential of COF and MOF based or derived SACs in addressing pressing global challenges related to carbon management, clear energy conversion, sustainable chemical synthesis. Ultimately, these advancements inspire a broader scientific community aimed at addressing global environmental challenges through cutting-edge scientific approaches. Accordingly, this review serves as a valuable resource for scientists engaged in both academic and industrial research across diverse fields, including chemistry, catalysis, environmental science, materials science, and energy-related technologies.

Author contributions

R. Z., R. V. J., and A. B. supervised the preparation of the review manuscript. S. V., M. B., and S. V. conceptualization, wrote the original draft. M. G. S., EA. L., K. K. wrote the manuscript, review & editing, R. P., V. G., A. G. B., M. U., N. V. V. J., S. R., M. V., D. I. S. formal analysis, review & editing. All authors had approved the final version of the manuscript.

Conflicts of interest

The authors declared no conflict of interest.

Data availability

No Data were generated for the production of this work. Figures and schemes are adapted with permission from research papers accessible *via* DOI which may be requested by the corresponding authors.

Acknowledgements

9704 | *Energy Environ. Sci.*, 2025, **18**, 9632–9712

This journal is © The Royal Society of Chemistry 2025

References

1 J. Rogelj, M. d Elzen, N. Höhne, T. Fransen, H. Fekete, H. Winkler, R. Schaeffer, F. Sha, K. Riahi and M. Meinshausen, *Nature*, 2016, **534**, 631–639.

2 A. A. Fawcett, G. C. Iyer, L. E. Clarke, J. A. Edmonds, N. E. Hultman, H. C. McJeon, J. Rogelj, R. Schuler, J. Alsalam, G. R. Asrar, J. Creason, M. Jeong, J. McFarland, A. Mundra and W. Shi, *Science*, 2015, **350**, 1168–1169.

3 F. Wang, Z. Lu, H. Guo, G. Hao, W. Jiang and G. Liu, *Coord. Chem. Rev.*, 2024, **515**, 215962.

4 UNFCCC. Adoption of the Paris Agreement. Report No. FCCC/CP/2015/L.9/Rev.1, **https://unfccc.int/resource/docs/2015/cop21/eng/l09r01.pdf** (UNFCCC, 2015).

5 CO_2 emission in 2023, International Energy Agency, **https://www.iea.org/reports/co2-emissions-in-2023/the-changing-landscape-of-global-emissions**.

6 Y. Huang, X. Deng, Y. Duan, C. Liu and X. Xu, *DeCarbon*, 2024, **5**, 100054.

7 G. Licht, K. Hofstetter and S. Licht, *DeCarbon*, 2024, **4**, 100044.

8 Y. Guo, T. Li, D. Li and J. Cheng, *Renew. Sust. Energ. Rev.*, 2023, **189**, 114053.

9 G. H. Han, J. Bang, G. Park, S. Choe, Y. J. Jang, H. W. Jang, S. Y. Kim and S. H. Ahn, *Small*, 2023, **19**, 2205765.

10 R. E. Vos, K. E. Kolmeijer, T. S. Jacobs, W. Van Der Stam, B. M. Weckhuysen and M. T. M. Koper, *ACS Catal.*, 2023, **13**, 8080–8091.

11 X. Tan, K. Sun, Z. Zhuang, B. Hu, Y. Zhang, Q. Liu, C. He, Z. Xu, C. Chen, H. Xiao and C. Chen, *J. Am. Chem. Soc.*, 2023, **145**, 8656–8664.

12 T. Xiang, T. Liu, T. Ouyang, S. Zhao and Z. Liu, *Interdiscip. Mater.*, 2024, **3**, 380–388.

13 X. Li, J. Yu, M. Jaroniec and X. Chen, *Chem. Rev.*, 2019, **119**, 3962–4179.

14 S. Garg, Z. Xie, A. X. Lam and J. G. Chen, *ACS Energy Lett.*, 2024, **9**, 2990–2996.

15 W. Ahmad, G. Bhardwaj, R. Lakshman, P. Koley and A. Tanksale, *Energy Fuels*, 2023, **37**, 19377–19399.

16 Y. Y. Birdja, E. P. Gallent, M. C. Figueiredo, A. J. Göttle, F. C. Vallejo and M. T. M. Koper, *Nat. Energy*, 2019, **4**, 732–745.

17 Y. Wang, T. Liu and Y. Li, *Chem. Sci.*, 2022, **13**, 6366–6372.

18 H. Dong, M. Jung, Y. Zhang, S. Wang and S. Ding, *Mol. Catal.*, 2024, **560**, 114133.

19 L. H. Vieira, L. F. Rasteiro, C. S. Santana, G. L. Catuzo, A. H. M. da Silva, J. M. Assaf and E. M. Assaf, *ChemCatChem*, 2023, **15**, e202300493.

20 G. Wang, J. Chen, Y. Ding, Y. Li, C. Tu, Y. Hou, P. Cai, Z. Wen, L. Yi and L. Dai, *Chem. Soc. Rev.*, 2021, **50**, 4993–5061.

21 A. R. Woldu, Z. Huang, P. Zhao, L. Hu and D. Astruc, *Coord. Chem. Rev.*, 2022, **454**, 214340.

22 F. Zhang, Y. Zhu, Q. Lin, L. Zhang, X. Zhang and H. Wang, *Energy Environ. Sci.*, 2021, **14**, 2954.

23 K. Lee, J. H. Jang, M. Balamurugan, J. E. Kim and K. T. Nam, *Nat. Energy*, 2021, **6**, 733–741.

24 Z. Fu, Q. Yang, Z. Liu, F. Chen, F. Yao, T. Xie, Y. Zhong, D. Wang, J. Li, X. Li and G. Zeng, *J. CO_2 Util.*, 2019, **34**, 63–73.

25 S. Man, W. Jiang, X. Guo, O. Ruzimuradov, S. Mamatkulov, J. Low and Y. Xiong, *Chem. Mater.*, 2024, **36**, 1793–1809.

26 X. Pan, X. Zhou, X. Liao, R. Yu, K. Yu, S. Lin, Y. Ding, W. Luo, M. Yan and L. Mai, *ACS Mater. Lett.*, 2022, **4**, 2622–2630.

27 M. Yadav, T. Gyulavari, J. Kiss, K. B. Abrahamne, A. Efremova, A. Szamosvolgyi, Z. Pap, A. Sapi, A. Kukovecz and Z. Konya, *J. CO_2 Util.*, 2023, **78**, 102621.

28 L. Li, Z. Wang, L. Zhao, H. Liu and Y. Li, *Coord. Chem. Rev.*, 2025, **522**, 216223.

29 X. Liu, T. Chen, Y. Xue, J. Fan, S. Shen, Md. S. A. Hossain, M. A. Amin, L. Pan, X. Xu and Y. Yamauchi, *Coord. Chem. Rev.*, 2022, **459**, 214440.

30 C. Li, J. Wang, L. Tong, Y. Wang, P. Zhang, M. Zhu and H. Dong, *Coord. Chem. Rev.*, 2024, **502**, 215623.

31 B. Qiao, A. Wang, X. Yang, L. F. Allard, Z. Jiang, Y. Cui, J. Liu, J. Li and T. Zhang, *Nat. Chem.*, 2011, **3**, 634–641.

32 S. Kment, A. Bakandritsos, I. Tantis, H. Kmentova, Y. Zuo, O. Henrotte, A. Naldoni, M. Otyepka, R. S. Varma and R. Zboril, *Chem. Rev.*, 2024, **124**, 11767–11847.

33 Z. Ma, C. Kuloor, C. Kreyenschulte, S. Bartling, M. Malina, H. Haumann, P. W. Menezes, R. Zboril, M. Beller and R. V. Jagadeesh, *Angew. Chem., Int. Ed.*, 2024, **63**, e202407859.

34 Q. Wang, H. Qi, Y. Ren, Z. Cao, K. Junge, R. V. Jagadeesh and M. Beller, *Chem*, 2024, **10**, 1897–1909.

35 V. G. Chandrashekhar, T. Senthamarai, R. G. Kadam, O. Malina, J. Kaslík, R. Zboril, M. B. Gawande, R. V. Jagadeesh and M. Beller, *Nat. Catal.*, 2021, **5**, 20–29.

36 S. Venkateswarlu, M. Umer, Y. Son, S. Govindaraju, G. Chellasamy, A. Panda, J. Park, S. Umer, J. Kim, S. I. Choi, K. Yun, M. Yoon, G. Lee and M. J. Kim, *Small*, 2023, **20**, 2305289.

37 G. Chellasamy, E. Varathan, K. Sekar, S. Venkateswarlu, S. Govindaraju and K. Yun, *Coord. Chem. Rev.*, 2024, **502**, 215606.

38 E. Murphy, B. Sun, M. Rüscher, Y. Liu, W. Zang, S. Guo, Y. H. Chen, U. Hejral, Y. Huang, A. Ly, I. V. Zenyuk, X. Pan,

This journal is © The Royal Society of Chemistry 2025

Energy Environ. Sci., 2025, **18**, 9632–9712 | **9705**

J. Timoshenko, B. R. Cuenya, E. D. Spoerke and P. Atanassov, *Adv. Mater.*, 2024, **36**, 2401133.

39 Z. Jin, Y. Xu, M. Chhetri, J. Wood, B. Torreon, F. Che and M. Yang, *Chem. Eng. J.*, 2024, **491**, 152072.

40 Y. Sun, X. Liu, M. Zhu, Z. Zhang, Z. Chen, S. Wang, Z. Ji, H. Yang and X. Wang, *DeCarbon*, 2023, **2**, 100018.

41 S. Wang, L. Wang, D. Wang and Y. Li, *Energy Environ. Sci.*, 2023, **16**, 2759–2803.

42 J. Qin, B. Han, X. Lu, J. Nie, C. Xian and Z. Zhang, *JACS Au*, 2023, **3**, 801–812.

43 S. Vallem, S. Venkateswarlu, Y. Li, S. Song, M. Li and J. Bae, *Energy Storage Mater.*, 2024, **65**, 103159.

44 L. Wang, J. Li, S. Ji, Y. Xiong and D. Wang, *Energy Environ. Sci.*, 2024, **17**, 8482–8528.

45 H. Liu, M. Cheng, Y. Liu, J. Wang, G. Zhang, L. Li, L. Du, G. Wang, S. Yang and X. Wang, *Energy Environ. Sci.*, 2022, **15**, 3722–3749.

46 Y. Zhang, H. Li, X. He, A. Wang, G. Bai and X. Lan, *Green Chem.*, 2023, **25**, 5557–5565.

47 X. Yan, N. Liu, W. Liu, J. Zeng, C. Liu, S. Chen, Y. Yang, X. Gui, D. Yu, G. Yang and Z. Zeng, *Chem. Commun.*, 2024, **60**, 12787–12802.

48 H. Zhang, J. Wei, J. Dong, G. Liu, L. Shi, P. An, G. Zhao, J. Kong, X. Wang, X. Meng, J. Zhang and J. Ye, *Angew. Chem., Int. Ed.*, 2016, **55**, 14310–14314.

49 Y. Yao, H. Yin, M. Gao, Y. Hu, H. Hu, M. Yu and S. Wang, *Chem. Eng. Sci.*, 2019, **209**, 115211.

50 S. Wei, Y. Wang, W. Chen, Z. Li, W. C. Cheong, Q. Zhang, Y. Gong, L. Gu, Q. Peng and Y. Li, *Chem. Sci.*, 2020, **11**, 786–790.

51 L. Ran, Z. Li, B. Ran, J. Cao, Y. Zhao, T. Shao, Y. Song, M. K. H. Leung, L. Sun and J. Hou, *J. Am. Chem. Soc.*, 2022, **144**, 17097–17109.

52 W. Ni, X. He, Y. Zhang, H. Chen, M. Dai, W. Zhang, S. Wang and S. Zhang, *Energy Environ. Sci.*, 2024, **17**, 3191–3201.

53 J. W. Lim, D. H. Choo, J. H. Cho, J. Kim, W. S. Cho, O. F. N. Okello, K. Kim, S. Lee, J. Son, S. Y. Choi, J. K. Kim, H. W. Jang, S. Y. Kim and J. L. Lee, *J. Mater. Chem. A*, 2024, **12**, 11090–11100.

54 A. Gao, B. Wan, S. Ren, C. Jia, W. Liu, X. Han, F. Xing and J. Liu, *Small*, 2025, **21**, 2411690.

55 Q. Cao, L. L. Zhanga, C. Zhoua, J. H. Hea, A. Marcominib and J. M. Lu, *Appl. Catal., B*, 2021, **294**, 120238.

56 Y. Hu, G. Liu, T. Song, X. Hub, B. Long and G. J. Deng, *Appl. Catal., B*, 2025, **361**, 124587.

57 J. Xiao, T. Zhang and Q. Wang, *Curr. Opin. Green Sustainable Chem.*, 2022, **37**, 100660.

58 Y. C. Hao, L. W. Chen, J. Li, Y. Guo, X. Su, M. Shu, Q. Zhang, W. Y. Gao, S. Li, Z. L. Yu, L. Gu, X. Feng, A. X. Yin, R. Si, Y. W. Zhang, B. Wang and C. H. Yan, *Nat. Commun.*, 2021, **12**, 2682.

59 L. H. Mou, J. Du, Y. Li, J. Jiang and L. Chen, *ACS Catal.*, 2024, **14**, 12947–12955.

60 R. E. Sikma, R. A. Reyes, D. Richards, P. G. Kotula, M. L. Meyerson, D. P. Schafer, J. K. Romàn-Kustas, S. J. Percival and D. F. S. Gallis, *ACS Appl. Nano Mater.*, 2024, **7**, 26629–26635.

61 X. Chen, J.-Y. Song, J. Zheng, Y.-M. Wang, J. Luo, P. Weng, B.-C. Cai, X.-C. Lin, G.-H. Ning and D. Li, *J. Am. Chem. Soc.*, 2024, **146**, 19271–19278.

62 K. G. Liu, F. Bigdeli, A. Panjehpour, A. Larimi, A. Morsali, A. Dhakshinamoorthy and H. Garcia, *Coord. Chem. Rev.*, 2023, **493**, 215257.

63 W. Chen, B. Ma and R. Zou, *Acc. Mater. Res.*, 2025, **6**, 210–220.

64 P. Singh and P. N. Dave, *Greenhouse Gases:Sci. Technol.*, 2024, **14**, 914–938.

65 Y. Wu, R. Wang and Y. Kim, *ACS Appl. Mater. Interfaces*, 2024, **16**, 66874–66899.

66 X. Han, T. Zhang and J. Arbiol, *Energy Adv.*, 2022, **2**, 252–267.

67 R. Wang, Y. Yuan, K.-T. Bang and Y. Kim, *ACS Mater. Au*, 2022, **3**, 28–36.

68 C. Wang, Z. Lv, W. Yang, X. Feng and B. Wang, *Chem. Soc. Rev.*, 2023, **52**, 1382–1427.

69 Z. Chen, Y. Guo, L. Han, J. Zhang, Y. Liu, J. Baeyens and Y. Lv, *Prog. Energy Combust. Sci.*, 2024, **104**, 101175.

70 G. Cai, P. Yan, L. Zhang, H. C. Zhou and H. L. Jiang, *Chem. Rev.*, 2021, **121**, 12278–12326.

71 Y. Liu, W. Peng, H. Ma, J. Tian, K. Wang, Z. Zheng, L. Xu and Y. Ding, *ACS Appl. Mater. Interfaces*, 2025, **17**, 19806–19817.

72 W. Zhou, W. Deng and X. Lu, *Interdiscip. Mater.*, 2024, **3**, 87–112.

73 H. Li, J. Liu, Y. Wang, C. Guo, Y. Pi, Q. Fang and J. Liu, *Coord. Chem. Rev.*, 2024, **523**, 216240.

74 N. Stock and S. Biswas, *Chem. Rev.*, 2012, **112**, 933–969.

75 M.-M. Millet, G. Algara-Siller, S. Wrabetz, A. Mazheika, F. Girgsdies, D. Teschner, F. Seitz, A. Tarasov, S. V. Levchenko, R. Schlögl and E. Frei, *J. Am. Chem. Soc.*, 2019, **141**, 2451–2461.

76 X. Shang, X. Yang, G. Liu, T. Zhang and X. Su, *Chem. Sci.*, 2024, **15**, 4631–4708.

77 M. Song, Q. Zhang, G. Luo, H. Hu and D. Wang, *Coord. Chem. Rev.*, 2025, **523**, 216281.

78 A. W. Thornton, R. Babarao, A. Jain, F. Trousselet and F. X. Coudert, *Dalton Trans.*, 2016, **45**, 4352–4359.

79 N. A. Rejali, M. Dinari and Y. Wang, *Chem. Commun.*, 2023, **59**, 11631–11647.

80 C. Li, W. Ju, S. Vijay, J. Timoshenko, K. Mou, D. A. Cullen, J. Yang, X. Wang, P. Pachfule, S. Brückner, H. S. Jeon, F. T. Haase, S.-C. Tsang, C. Rettenmaier, K. Chan, B. R. Cuenya, A. Thomas and P. Strasser, *Angew. Chem., Int. Ed.*, 2022, **61**, e202114707.

81 M. Zhang, C. Lai, F. Xu, D. Huang, S. Liu, Y. Fu, L. Li, H. Yi, L. Qin and L. Chen, *Coord. Chem. Rev.*, 2022, **466**, 214592.

82 T. H. Dolla, B. Zhang, T. Matthews, M. P. Chabalala, S. O. Ajayi, L. L. Sikeyi, X. Liu and M. K. Mathe, *Coord. Chem. Rev.*, 2024, **518**, 216061.

83 M. Liu, S. Liu, Q. Xu, Q. Miao, S. Yang, S. Hanson, G. Z. Chen, J. He, Z. Jiang and G. Zeng, *Carbon Energy*, 2023, **5**, e300.

9706 | *Energy Environ. Sci.*, 2025, **18**, 9632–9712

This journal is © The Royal Society of Chemistry 2025

84 B. Shao, D. Huang, R.-K. Huang, X. L. He, Y. Luo, Y. L. Xiang, L. Jiang, M. Dong, S. Li, Z. Zhang and J. Huang, *Angew. Chem., Int. Ed.*, 2024, **63**, e202409270.

85 T. Zhang, X. Han, H. Liu, M. Biset-Peiró, J. Li, X. Zhang, P. Tang, B. Yang, L. Zheng, J. R. Morante and J. Arbiol, *Adv. Funct. Mater.*, 2022, **32**, 2111446.

86 H. Huang, K. Shen, F. Chen and Y. Li, *ACS Catal.*, 2020, **10**, 6579–6586.

87 L. Zou, Y. S. Wei, C.-C. Hou, C. Li and Q. Xu, *Small*, 2021, **17**, 2004809.

88 E. Doustkhah, R. Hassandoost, A. Khataee, R. Luque and M. H. N. Assadi, *Chem. Soc. Rev.*, 2021, **50**, 2927–2953.

89 Y. N. Gong, L. Jiao, Y. Qian, C. Y. Pan, L. Zheng, X. Cai, B. Liu, S. H. Yu and H. L. Jiang, *Angew. Chem., Int. Ed.*, 2020, **59**, 2705–2709.

90 W. Xia, B. Qiu, D. Xia and R. Zou, *Sci. Rep.*, 2013, **3**, 1935.

91 Y. Guo, L. Feng, C. Wu, X. Wang and X. Zhang, *J. Catal.*, 2020, **390**, 213–223.

92 W. Dong, N. Huang, Y. Zhao, Y. Feng, G. Zhao, S. Ran and W. Liu, *J. Electroanal. Chem.*, 2024, **959**, 118184.

93 Q. Pang, X. Fan, K. Sun, K. Xiang, B. Li, S. Zhao, Y. D. Kim, Q. Liu, Z. Liu and Z. Peng, *Energy Environ. Mater.*, 2024, **7**, e12731.

94 Y. Sun, X. Liu, J. Tian, Z. Zhang, Y. Li, Y. Xie, M. Hao, Z. Chen, H. Yang, G. I. N. Waterhouse, S. Ma and X. Wang, *ACS Nano*, 2025, **19**, 4528–4540.

95 J. Li, H. Luo, B. Li, J.-G. Ma and P. Cheng, *Mater. Chem. Front.*, 2023, **7**, 6107–6129.

96 K. Parveen and S. Pakhira, *J. Phys. Chem. C*, 2025, **129**, 2973–2987.

97 A. Shankar, S. Marimuthu and G. Maduraiveeran, *J. Mater. Chem. A*, 2024, **12**, 121–127.

98 Q. Zuo, R. Cui, L. Wang, Y. Wang, C. Yu, L. Wu, Y. Mai and Y. Zhou, *Sci. China Chem.*, 2023, **66**, 570–577.

99 Z. Zhang, Z. Zhang, C. Chen, R. Wang, M. Xie, S. Wan, R. Zhang, L. Cong, H. Lu, Y. Han, W. Xing, Z. Shi and S. Feng, *Nat. Commun.*, 2024, **15**, 2556.

100 X. Liang, S. Ji, Y. Chen and D. Wang, *iScience*, 2022, **25**, 104177.

101 A. M. A. Mageed, B. Rungtaweevoranit, M. P. Wojtan, X. Pei, O. M. Yaghi and R. J. Behm, *J. Am. Chem. Soc.*, 2019, **141**, 5201–5210.

102 Y. Qu, Z. Li, W. Chen, Y. Lin, T. Yuan, Z. Yang, C. Zhao, J. Wang, C. Zhao, X. Wang, F. Zhou, Z. Zhuang, Y. Wu and Y. Li, *Nat. Catal.*, 2018, **1**, 781–786.

103 S. Chen, W.-H. Li, W. Jiang, J. Yang, J. Zhu, L. Wang, H. Ou, Z. Zhuang, M. Chen, X. Sun, D. Wang and Y. Li, *Angew. Chem., Int. Ed.*, 2022, **61**, e202114450.

104 G. Wang, C.-T. He, R. Huang, J. Mao, D. Wang and Y. Li, *J. Am. Chem. Soc.*, 2020, **142**, 19339–19345.

105 J. Fonseca and J. Lu, *ACS Catal.*, 2021, **11**, 7018–7059.

106 S. Liu, M. Wang, X. Yang, Q. Shi, Z. Qiao, M. Lucero, Q. Ma, K. L. More, D. A. Cullen, Z. Feng and G. Wu, *Angew. Chem., Int. Ed.*, 2020, **59**, 21698–21705.

107 R. C. Klet, T. C. Wang, L. E. Fernandez, D. G. Truhlar, J. T. Hupp and O. K. Farha, *Chem. Mater.*, 2016, **28**, 1213–1219.

108 D. Ma, X. Wei, J. Li and Z. Cao, *Inorg. Chem.*, 2024, **63**, 915–922.

109 Z. Li, N. M. Schweitzer, A. B. League, V. Bernales, A. W. Peters, A. B. Getsoian, T. C. Wang, J. T. Miller, A. Vjunov, J. L. Fulton, J. A. Lercher, C. J. Cramer, L. Gagliardi, J. T. Hupp and O. K. Farha, *J. Am. Chem. Soc.*, 2016, **138**, 1977–1982.

110 Y. Qu, Z. Li, W. Chen, Y. Lin, T. Yuan, Z. Yang, C. Zhao, J. Wang, C. Zhao, X. Wang, F. Zhou, Z. Zhuang, Y. Wu and Y. Li, *Nat. Catal.*, 2018, **1**, 781–786.

111 Y. Yang and S. Liu, *J. Phys. Chem. C*, 2024, **128**, 6269–6279.

112 S. Back, J. Lim, N.-Y. Kim, Y.-H. Kim and Y. Jung, *Chem. Sci.*, 2017, **8**, 1090–1096.

113 S. C. Sarma, J. Barrio, A. Bagger, A. Pedersen, M. Gong, H. Luo, M. Wang, S. Favero, C.-X. Zhao, Q. Zhang, A. Kucernak, M. M. Titirici and I. E. L. Stephens, *Adv. Funct. Mater.*, 2023, **33**, 2302468.

114 L. Sun, V. Reddu and X. Wang, *Chem. Soc. Rev.*, 2022, **51**, 8923–8956.

115 Y. Zhou, Q. Zhou, H. Liu, W. Xu, Z. Wang, S. Qiao, H. Ding, D. Chen, J. Zhu, Z. Qi, X. Wu, Q. He and L. Song, *Nat. Commun.*, 2023, **14**, 3776.

116 M. Zhang, D. Zhou, X. Mu, D. Wang, S. Liu and Z. Dai, *Small*, 2024, **20**, 2402050.

117 Y. Sun, L. Tao, M. Wu, D. Dastan, J. Rehman, L. Li and B. An, *Nanoscale*, 2024, **16**, 9791–9801.

118 P. Qi, J. Wang, X. Djitcheu, D. He, H. Liu and Q. Zhang, *RSC Adv.*, 2022, **12**, 1216–1227.

119 X. Li, X. Yang, J. Zhang, Y. Huang and B. Liu, *ACS Catal.*, 2019, **9**, 2521–2531.

120 P. A. Ocana, J. M. Rodriguez, J. A. P. Omil, J. J. Calvino, C. E. Castillo and M. L. Haro, *Commun. Mater.*, 2024, **5**, 1–11.

121 X. Ren, J. Zhao, X. Li, J. Shao, B. Pan, A. Salame, E. Boutin, T. Groizard, S. Wang, J. Ding, X. Zhang, W. Y. Huang, W. J. Zeng, C. Liu, Y. Li, S. F. Hung, Y. Huang, M. Robert and B. Liu, *Nat. Commun.*, 2023, **14**, 1–10.

122 L. Jiao and H. L. Jiang, *Chem*, 2019, **5**, 786–804.

123 S. Mitchell, F. Pares, D. F. Akl, S. M. Collins, D. M. Kepaptsoglou, Q. M. Ramasse, D. G. Gasulla, J. P. Ramlrez and N. Lopez, *J. Am. Chem. Soc.*, 2022, **144**, 8018–8029.

124 Z. Fan, R. Luo, Y. Zhang, B. Zhang, P. Zhai, Y. Zhang, C. Wang, J. Gao, W. Zhou, L. Sun and J. Hou, *Angew. Chem., Int. Ed.*, 2023, **62**, e202216326.

125 D. Deng, X. Chen, L. Yu, X. Wu, Q. Liu, Y. Liu, H. Yang, H. Tian, Y. Hu, P. Du, R. Si, J. Wang, X. Cui, H. Li, J. Xiao, T. Xu, J. Deng, F. Yang, P. N. Duchesne, P. Zhang, J. Zhou, L. Sun, J. Li, X. Pan and X. Bao, *Sci. Adv.*, 2015, **1**, e1500462.

126 M. Kottwitz, Y. Li, H. Wang, A. I. Frenkel and R. G. Nuzzo, *Chem. Methods*, 2021, **1**, 278–294.

127 Y. Liu, X. Su, J. Ding, J. Zhou, Z. Liu, X. Wei, H. B. Yang and B. Liu, *Chem. Soc. Rev.*, 2024, **53**, 11850–11887.

128 M. Kou, W. Liu, Y. Wang, J. Huang, Y. Chen, Y. Zhou, Y. Chen, M. Ma, K. Lei, H. Xie, P. K. Wong and L. Ye, *Appl. Catal., B*, 2021, **291**, 120146.

129 D. Wang and Y. Zhao, *Chem*, 2021, **7**, 2635–2671.

This journal is © The Royal Society of Chemistry 2025

Energy Environ. Sci., 2025, **18**, 9632–9712 | 9707

130 Q. Pana, Y. Chena, S. Jianga, X. Cuia, G. Maa and T. Ma, *EnergyChem*, 2023, **5**, 100114.

131 R. Lang, W. Xi, J. C. Liu, Y. T. Cui, T. Li, A. F. Lee, F. Chen, Y. Chen, L. Li, L. Li, J. Lin, S. Miao, X. Liu, A. Q. Wang, X. Wang, J. Luo, B. Qiao, J. Li and T. Zhang, *Nat. Commun.*, 2019, **10**, 1–10.

132 L. Zhang, Y. Li, L. Zhang, K. Wang, Y. Li, L. Wang, X. Zhang, F. Yang and Z. Zheng, *Adv. Sci.*, 2022, **9**, 2200592.

133 J. Timoshenko and B. R. Cuenya, *Chem. Rev.*, 2021, **121**, 882–961.

134 S.-F. Hung, A. Xu, X. Wang, F. Li, S.-H. Hsu, Y. Li, J. Wicks, E. G. Cervantes, A. S. Rasouli, Y. C. Li, M. Luo, D.-H. Nam, N. Wang, T. Peng, Y. Yan, G. Lee and E. H. Sargent, *Nat. Commun.*, 2022, **13**, 819.

135 D. Zhang, X. Liu, Y. Zhao, H. Zhang, A. V. Rudnev and J. F. Li, *Chem. Sci.*, 2025, **16**, 4916–4936.

136 X. Cao, D. Tan, B. Wulan, K. S. Hui, K. N. Hui and J. Zhang, *Small Methods*, 2021, **5**, 2100700.

137 H. B. Yang, S. F. Hung, S. Liu, K. Yuan, S. Miao, L. Zhang, X. Huang, H. Y. Wang, W. Cai, R. Chen, J. Gao, X. Yang, W. Chen, Y. Huang, H. M. Chen, C. M. Li, T. Zhang and B. Liu, *Nat. Energy*, 2018, **3**, 140–147.

138 B. B. Sarma, F. Maurer, D. E. Doronkin and J. D. Grunwaldt, *Chem. Rev.*, 2023, **123**, 379–444.

139 L. Chen, C. Zhang and X. Jiao, *ChemCatChem*, 2025, **17**, e202401388.

140 H. Y. Jeong, M. Balamurugan, C. H. Choi and K. T. Nam, Bridging homogeneous and heterogeneous systems: atomically dispersed metal atoms in carbon matrices for electrocatalytic CO$_2$ reduction, in *Carbon Dioxide electrochemistry: Homogeneous and heterogeneous catalysis*, ed. M. Robert, C. Costentin and K. Daasbjerg, Royal Society of Chemistry, 2020, pp. 226–286.

141 H. Jeong, M. Balamurugan, V. S. K. Choutipalli, J. Jo, H. Baik, V. Subramanian, M. Kim, U. Sim and K. T. Nam, *Chem. Eur. J.*, 2018, **24**, 18444–18454.

142 H. Y. Jeong, M. Balamurugan, V. S. K. Choutipalli, E. S. Jeong, V. Subramanian, U. Sim and K. T. Nam, *J. Mater. Chem. A*, 2019, **7**, 10651–10661.

143 Š. Kment, A. Bakandritsos, I. Tantis, H. Kmentová, Y. Zuo, O. Henrotte, A. Naldoni, M. Otyepka, R. S. Varma and R. Zbořil, *Chem. Rev.*, 2024, **124**, 11767–11847.

144 L. Jiao, Y. Wang, H. Jiang and Q. Xu, *Adv. Mater.*, 2017, **30**, 1703663.

145 A. Han, B. Wang, A. Kumar, Y. Qin, J. Jin, X. Wang, C. Yang, B. Dong, Y. Jia, J. Liu and X. Sun, *Small Methods*, 2019, **3**, 1800471.

146 J. Ye, J. Yan, Y. Peng, F. Li and J. Sun, *Catal. Today*, 2023, **410**, 68–84.

147 M. Balamurugan, L. Merakeb, K. T. Nam and M. Robert, *Chemical Valorisation of Carbon Dioxide*, The Royal Society of Chemistry, 2022, pp. 362–387.

148 M. Humayuna, S. Alia, A. Khana, P. M. Ismaila, C. Wang, M. Bououdina and M. Israr, *Coord. Chem. Rev.*, 2025, **538**, 216678.

149 W. Ma, X. He, W. Wang, S. Xie, Q. Zhang and Y. Wang, *Chem. Soc. Rev.*, 2021, **50**, 12897–12914.

150 S. Nitopi, E. Bertheussen, S. B. Scott, X. Liu, A. K. Engstfeld, S. Horch, B. Seger, I. E. L. Stephens, K. Chan, C. Hahn, J. K. Nørskov, T. F. Jaramillo and I. Chorkendorff, *Chem. Rev.*, 2019, **119**, 7610–7672.

151 L. Wang, W. Chen, D. Zhang, Y. Du, R. Amal, S. Qiao, J. Wu and Z. Yin, *Chem. Soc. Rev.*, 2019, **48**, 5310–5349.

152 A. J. Garza and A. T. Bell, *ACS Catal.*, 2018, **8**, 1490–1499.

153 R. Kortlever, J. Shen, K. J. P. Schouten, F. Calle-Vallejo and M. T. M. Koper, *J. Phys. Chem. Lett.*, 2015, **6**, 4073–4082.

154 C. Zhao, X. Dai, T. Yao, W. Chen, X. Wang, J. Wang, J. Yang, S. Wei, Y. Wu and Y. Li, *J. Am. Chem. Soc.*, 2017, **139**, 8078–8081.

155 Y. Ye, F. Cai, H. Li, H. Wu, G. Wang, Y. Li, S. Miao, S. Xie, R. Si, J. Wang and X. Bao, *Nano Energy*, 2017, **38**, 281–289.

156 T. N. Huan, N. Ranjbar, G. Rousse, M. Sougrati, A. Zitolo, V. Mougel, F. Jaouen and M. Fontecave, *ACS Catal.*, 2017, **7**, 1520–1525.

157 J. Yang, Z. Qiu, C. Zhao, W. Wei, W. Chen, Z. Li, Y. Qu, J. Dong, J. Luo, Z. Li and Y. Wu, *Angew. Chem., Int. Ed.*, 2018, **57**, 14095–14100.

158 F. Pan, H. Zhang, K. Liu, D. Cullen, K. More, M. Wang, Z. Feng, G. Wang, G. Wu and Y. Li, *ACS Catal.*, 2018, **8**, 3116–3122.

159 K.-J. Noh, B. J. Park, Y. Wang, Y. Choi, S.-H. You, Y.-T. Kim, K.-S. Lee and J. W. Han, *Carbon Energy*, 2024, **6**, e419.

160 Z. Geng, Y. Cao, W. Chen, X. Kong, Y. Liu, T. Yao and Y. Lin, *Appl. Catal., B*, 2019, **240**, 234–240.

161 P. Lu, Y. Yang, J. Yao, M. Wang, S. Dipazir, M. Yuan, J. Zhang, X. Wang, Z. Xie and G. Zhang, *Appl. Catal., B*, 2019, **241**, 113–119.

162 L. Jiao, W. Yang, G. Wan, R. Zhang, X. Zheng, H. Zhou, S.-H. Yu and H.-L. Jiang, *Angew. Chem., Int. Ed.*, 2020, **59**, 20589–20595.

163 C. Wang, X. Hu, X. Hu, X. Liu, Q. Guan, R. Hao, Y. Liu and W. Li, *Appl. Catal., B*, 2021, **296**, 120331.

164 N. Mohd Adli, W. Shan, S. Hwang, W. Samarakoon, S. Karakalos, Y. Li, D. A. Cullen, D. Su, Z. Feng, G. Wang and G. Wu, *Angew. Chem., Int. Ed.*, 2021, **60**, 1022–1032.

165 H. Cheng, X. Wu, X. Li, X. Nie, S. Fan, M. Feng, Z. Fan, M. Tan, Y. Chen and G. He, *J. Chem. Eng.*, 2021, **407**, 126842.

166 Q.-H. Zheng, C. Chen, S.-M. Cao, M.-T. Peng, B.-X. Dong and Y.-L. Teng, *Chin. Chem. Lett.*, 2023, **34**, 107273.

167 M. Xie, J. Wang, X.-L. Du, N. Gao, T. Liu, Z. Li, G. Xiao, T. Li and J.-Q. Wang, *RSC Adv.*, 2022, **12**, 32518–32525.

168 F. Ismail, A. Abdellah, V. Sudheeshkumar, A. Rakhsha, W. Chen, N. Chen and D. C. Higgins, *ACS Appl. Energy Mater.*, 2022, **5**, 9408–9417.

169 Y. Zhang, T. Sun, P. Zhang, K. Liu, F. Li and L. Xu, *J. Colloid Interface Sci.*, 2023, **631**, 96–101.

170 J. W. Lim, D. H. Choo, J. H. Cho, J. Kim, W. S. Cho, O. F. Ngome Okello, K. Kim, S. Lee, J. Son, S.-Y. Choi, J. K. Kim, H. W. Jang, S. Y. Kim and J.-L. Lee, *J. Mater. Chem. A*, 2024, **12**, 11090–11100.

171 K. Zhao, X. Nie, H. Wang, S. Chen, X. Quan, H. Yu, W. Choi, G. Zhang, B. Kim and J. G. Chen, *Nat. Commun.*, 2020, **11**, 2455.

9708 | *Energy Environ. Sci.*, 2025, **18**, 9632–9712

This journal is © The Royal Society of Chemistry 2025

172 J. Gu, C.-S. Hsu, L. Bai, H. M. Chen and X. Hu, *Science*, 2019, **364**, 1091–1094.

173 J. Li, S. Hu, Y. Li, X. Fan, F. Zhang, G. Zhang and W. Peng, *Carbon*, 2023, **206**, 62–71.

174 Q. Song, B. Guo, H. Liu, H. Wang, M. Schmidt, P. A. van Aken, D. Luo and E. Klemm, *Cell Rep. Phys. Sci.*, 2023, **4**, 101737.

175 C. Yan, H. Li, Y. Ye, H. Wu, F. Cai, R. Si, J. Xiao, S. Miao, S. Xie, F. Yang, Y. Li, G. Wang and X. Bao, *Energy Environ. Sci.*, 2018, **11**, 1204–1210.

176 X. Wang, Z. Chen, X. Zhao, T. Yao, W. Chen, R. You, C. Zhao, G. Wu, J. Wang, W. Huang, J. Yang, X. Hong, S. Wei, Y. Wu and Y. Li, *Angew. Chem., Int. Ed.*, 2018, **57**, 1944–1948.

177 A. Guan, Z. Chen, Y. Quan, C. Peng, Z. Wang, T.-K. Sham, C. Yang, Y. Ji, L. Qian, X. Xu and G. Zheng, *ACS Energy Lett.*, 2020, **5**, 1044–1053.

178 Y. Zhang, L. Jiao, W. Yang, C. Xie and H.-L. Jiang, *Angew. Chem., Int. Ed.*, 2021, **60**, 7607–7611.

179 X.-C. Yan, H. Dong, H. Tong, Y. Wang, L.-H. Shao, Y.-J. Du, J.-T. Ge, W.-B. Fang and F.-M. Zhang, *Appl. Surf. Sci.*, 2023, **636**, 157828.

180 H. Tian, Z. Shui, M. A. Raza, L. Zhu and X. Chen, *J. Alloys Compd.*, 2023, **958**, 170544.

181 J. H. Cho, J. Ma, C. Lee, J. W. Lim, Y. Kim, H. Y. Jang, J. Kim, M.-G. Seo, Y. Choi, Y. J. Jang, S. H. Ahn, H. W. Jang, S. Back, J.-L. Lee and S. Y. Kim, *Carbon Energy*, 2024, **6**, e510.

182 W. Zhang, D. Liu, T. Liu, C. Ding, T. Chen, Y. Li, X. Liu, L. Wang, C. Li, J. He, T. Ding and T. Yao, *Nano Res.*, 2023, **16**, 10873–10880.

183 H. Cheng, X. Wu, X. Li, Y. Zhang, M. Feng, Z. Fan and G. He, *J. Catal.*, 2021, **395**, 63–69.

184 X. Wang, Y. Wang, X. Sang, W. Zheng, S. Zhang, L. Shuai, B. Yang, Z. Li, J. Chen, L. Lei, N. M. Adli, M. K. H. Leung, M. Qiu, G. Wu and Y. Hou, *Angew. Chem., Int. Ed.*, 2021, **60**, 4192–4198.

185 H. Cheng, Z. Fan, X. Wu, M. Feng, W. Zheng, G. Lei, X. Li, F. Cui and G. He, *J. Catal.*, 2022, **405**, 634–640.

186 X. Song, H. Zhang, Y. Yang, B. Zhang, M. Zuo, X. Cao, J. Sun, C. Lin, X. Li and Z. Jiang, *Adv. Sci.*, 2018, **5**, 1800177.

187 F. Yang, H. Yu, Y. Su, J. Chen, S. Chen, Z. Zeng, S. Deng and J. Wang, *Nano Res.*, 2023, **16**, 146–154.

188 D. Zhao, K. Yu, P. Song, W. Feng, B. Hu, W.-C. Cheong, Z. Zhuang, S. Liu, K. Sun, J. Zhang and C. Chen, *Energy Environ. Sci.*, 2022, **15**, 3795–3804.

189 T. Yue, H. Sui, J. Jia, Y. Chang, S. Guo, Y. Su and M. Jia, *Appl. Catal., B*, 2025, **361**, 124618.

190 J. Pei, H. Shang, J. Mao, Z. Chen, R. Sui, X. Zhang, D. Zhou, Y. Wang, F. Zhang, W. Zhu, T. Wang, W. Chen and Z. Zhuang, *Nat. Commun.*, 2024, **15**, 416.

191 H.-Y. Tan, S.-C. Lin, J. Wang, C.-J. Chang, S.-C. Haw, K.-H. Lin, L. D. Tsai, H.-C. Chen and H. M. Chen, *ACS Appl. Mater. Interfaces*, 2021, **13**, 52134–52143.

192 L. Kong, M. Wang, Y. Tuo, S. Zhou, J. Wang, G. Liu, X. Cui, J. Wang and L. Jiang, *J. Energy Chem.*, 2024, **88**, 183–193.

193 Z. Zhu, S. Lv, X. Sun, C. Liu, X. Qi, X. Liu, L. Wang and J. Zhang, *Appl. Catal., A*, 2024, **683**, 119824.

194 M. Qu, Z. Chen, Z. Sun, D. Zhou, W. Xu, H. Tang, H. Gu, T. Liang, P. Hu, G. Li, Y. Wang, Z. Chen, T. Wang and B. Jia, *Nano Res.*, 2023, **16**, 2170–2176.

195 Y. Yan, Y. Wang, C. Peng, J. Wang, X. Wang and L. Shi, *ACS Sustainable Chem. Eng.*, 2025, **13**, 1628–1636.

196 J.-X. Peng, W. Yang, Z. Jia, L. Jiao and H.-L. Jiang, *Nano Res.*, 2022, **15**, 10063–10069.

197 Z. Li, X. Qi, J. Wang, Z. Zhu, J. Jiang, X. Niu, A. Cabot, J. S. Chen and R. Wu, *SusMat*, 2023, **3**, 498–509.

198 Y. Lin, C. Xia, Z. Zhu, J. Wang, H. Niu, S. Gong, Z. Li, N. Yang, J. Song Chen, R. Wu and B. Y. Xia, *Angew. Chem., Int. Ed.*, 2025, **64**, e202414569.

199 Z. Li, R. Wu, S. Xiao, Y. Yang, L. Lai, J. S. Chen and Y. Chen, *Chem. Eng. J.*, 2022, **430**, 132882.

200 H. Shang, T. Wang, J. Pei, Z. Jiang, D. Zhou, Y. Wang, H. Li, J. Dong, Z. Zhuang, W. Chen, D. Wang, J. Zhang and Y. Li, *Angew. Chem., Int. Ed.*, 2020, **59**, 22465–22469.

201 P. Lu, X. Tan, H. Zhao, Q. Xiang, K. Liu, X. Zhao, X. Yin, X. Li, X. Hai, S. Xi, A. T. S. Wee, S. J. Pennycook, X. Yu, M. Yuan, J. Wu, G. Zhang, S. C. Smith and Z. Yin, *ACS Nano*, 2021, **15**, 5671–5678.

202 W. Guo, X. Tan, J. Bi, L. Xu, D. Yang, C. Chen, Q. Zhu, J. Ma, A. Tayal, J. Ma, Y. Huang, X. Sun, S. Liu and B. Han, *J. Am. Chem. Soc.*, 2021, **143**, 6877–6885.

203 J. Zhang, G. Zeng, L. Chen, W. Lai, Y. Yuan, Y. Lu, C. Ma, W. Zhang and H. Huang, *Nano Res.*, 2022, **15**, 4014–4022.

204 E. Zhang, T. Wang, K. Yu, J. Liu, W. Chen, A. Li, H. Rong, R. Lin, S. Ji, X. Zheng, Y. Wang, L. Zheng, C. Chen, D. Wang, J. Zhang and Y. Li, *J. Am. Chem. Soc.*, 2019, **141**, 16569–16573.

205 Z. Ma, B. Wang, X. Yang, C. Ma, W. Wang, C. Chen, F. Liang, N. Zhang, H. Zhang, Y. Chu, Z. Zhuang, H. Xu, Y. Wang and J. Liu, *J. Am. Chem. Soc.*, 2024, **146**, 29140–29149.

206 J. Guo, W. Zhang, L.-H. Zhang, D. Chen, J. Zhan, X. Wang, N. R. Shiju and F. Yu, *Adv. Sci.*, 2021, **8**, 2102884.

207 S. A. Chala, K. Lakshmanan, W. H. Huang, A. W. Kahsay, C. Y. Chang, F. T. Angerasa, Y. F. Liao, J. F. Lee, H. Dai, M.-C. Tsai, W.-N. Su and B. J. Hwang, *Appl. Catal., B*, 2024, **358**, 124420.

208 Y. Chen, M. Xia, C. Zhou, Y. Zhang, C. Zhou, F. Xu, B. Feng, X. Wang, L. Yang, Z. Hu and Q. Wu, *ACS Nano*, 2023, **17**, 22095–22105.

209 L. Wang, D. Zhang, S. Luo, Y. Xu and C. Wu, *New J. Chem.*, 2024, **48**, 3423–3430.

210 C. Hu, Y. Wang, J. Chen, H.-F. Wang, K. Shen, K. Tang, L. Chen and Y. Li, *Small*, 2022, **18**, 2201391.

211 W. Ren, X. Tan, W. Yang, C. Jia, S. Xu, K. Wang, S. C. Smith and C. Zhao, *Angew. Chem., Int. Ed.*, 2019, **58**, 6972–6976.

212 Q. Zhang, D. Liu, Y. Zhang, Z. Guo, M. Chen, Y. Chen, B. Jin, Y. Song and H. Pan, *J. Energy Chem.*, 2023, **87**, 509–517.

213 J. Zhu, M. Xiao, D. Ren, R. Gao, X. Liu, Z. Zhang, D. Luo, W. Xing, D. Su, A. Yu and Z. Chen, *J. Am. Chem. Soc.*, 2022, **144**, 9661–9671.

This journal is © The Royal Society of Chemistry 2025

Energy Environ. Sci., 2025, **18**, 9632–9712 | **9709**

214 L. Zhang, J. Feng, S. Liu, X. Tan, L. Wu, S. Jia, L. Xu, X. Ma, X. Song, J. Ma, X. Sun and B. Han, *Adv. Mater.*, 2023, **35**, 2209590.

215 R. Yun, F. Zhan, X. Wang, B. Zhang, T. Sheng, Z. Xin, J. Mao, S. Liu and B. Zheng, *Small*, 2021, **17**, 19417.

216 M. Feng, X. Wu, H. Cheng, Z. Fan, X. Li, F. Cui, S. Fan, Y. Dai, G. Lei and G. He, *J. Mater. Chem. A*, 2021, **9**, 23817–23827.

217 T. Ding, X. Liu, Z. Tao, T. Liu, T. Chen, W. Zhang, X. Shen, D. Liu, S. Wang, B. Pang, D. Wu, L. Cao, L. Wang, T. Liu, Y. Li, H. Sheng, M. Zhu and T. Yao, *J. Am. Chem. Soc.*, 2021, **143**, 11317–11324.

218 Y. Wang, B. J. Park, V. K. Paidi, R. Huang, Y. Lee, K.-J. Noh, K.-S. Lee and J. W. Han, *ACS Energy Lett.*, 2022, **7**, 640–649.

219 X. Zhao, K. Zhao, Y. Liu, Y. Su, S. Chen, H. Yu and X. Quan, *ACS Catal.*, 2022, **12**, 11412–11420.

220 J. Hao, Z. Zhuang, J. Hao, C. Wang, S. Lu, F. Duan, F. Xu, M. Du and H. Zhu, *Adv. Energy Mater.*, 2022, **12**, 2200579.

221 L. Jiao, J. Zhu, Y. Zhang, W. Yang, S. Zhou, A. Li, C. Xie, X. Zheng, W. Zhou, S. H. Yu and H. L. Jiang, *J. Am. Chem. Soc.*, 2021, **143**, 19417–19424.

222 Z. Ma, D. Wu, X. Han, H. Wang, L. Zhang, Z. Gao, F. Xu and K. Jiang, *J. CO$_2$ Util.*, 2019, **32**, 251–258.

223 M. Wen, N. Sun, L. Jiao, S.-Q. Zang and H.-L. Jiang, *Angew. Chem., Int. Ed.*, 2024, **63**, e202318338.

224 J.-H. Guo, X.-Y. Zhang, X.-Y. Dao and W.-Y. Sun, *ACS Appl. Nano Mater.*, 2020, **3**, 2625–2635.

225 C. Liu, N. Liu, X. Chen, Y. Zhao, J. Mi, Z. Yang, P. Wu, J. Chen and J. Li, *J. Mater. Chem. A*, 2025, **13**, 11782–11792.

226 X. Chen, D.-D. Ma, B. Chen, K. Zhang, R. Zou, X.-T. Wu and Q.-L. Zhu, *Appl. Catal., B*, 2020, **267**, 118720.

227 W. Xiong, D. Si, J. Yi, Y. Huang, H. Li and R. Cao, *Appl. Catal., B*, 2022, **314**, 121498.

228 L. Li, Z. Jiang, Y. Li, F. Li, Y. Pan, X. Zhang, Y. Liang and Z. Zheng, *Small Methods*, 2023, **7**, 2201213.

229 H. Wang, G. Liu, C. Chen, W. Tu, Y. Lu, S. Wu, D. O'Hare and R. Xu, *ACS Sustainable Chem. Eng.*, 2021, **9**, 3792–3801.

230 X. Sun, R. Wang, S. O. Chikh, D. Osadchii, G. Li, A. Aguilar, J. L. Hazemann, F. Kapteijn and J. Gascon, *J. Catal.*, 2019, **378**, 320–330.

231 Q. Yang, C. C. Yang, C.-H. Lin and H. L. Jiang, *Angew. Chem., Int. Ed.*, 2019, **58**, 3511–3515.

232 Y. Hou, Y. L. Liang, P. C. Shi, Y. B. Huang and R. Cao, *Appl. Catal., B*, 2020, **271**, 118929.

233 C. P. Liang, J. R. Huang, P. Q. Liao and X.-M. Chen, *Inorg. Chem. Front.*, 2025, **12**, 975–979.

234 X. Hu, J. Li, Z. Zhou and L. Wen, *ACS Mater. Lett.*, 2023, **5**, 85–94.

235 H. Yang, Q. Lin, C. Zhang, X. Yu, Z. Cheng, G. Li, Q. Hu, X. Ren, Q. Zhang, J. Liu and C. He, *Nat. Commun.*, 2020, **11**, 593.

236 H. Yang, Y. Wu, G. Li, Q. Lin, Q. Hu, Q. Zhang, J. Liu and C. He, *J. Am. Chem. Soc.*, 2019, **141**, 12717–12723.

237 H. Wang, H. Chuai, X. Chen, J. Lin, S. Zhang and X. Ma, *ACS Appl. Mater. Interfaces*, 2023, **15**, 1376–1383.

238 S. Wei, J. Zhu, X. Chen, R. Yang, K. Gu, L. Li, C.-Y. Chiang, L. Mai and S. Chen, *Nat. Commun.*, 2025, **16**, 1652.

239 P. Yue, K. Xiong, L. Ma, J. Li, L. Zhang, X. Zhu, Q. Fu and Q. Liao, *ACS Appl. Mater. Interfaces*, 2022, **14**, 54840–54847.

240 N. Yang, L. Yang, X. Zhu, P. Zhao, H. Liu, C. Xia, S. Dai and C. Tian, *ACS Mater. Lett.*, 2022, **4**, 2143–2150.

241 F. Wu, X. Liu, S. Wang, L. Hu, S. Kunze, Z. Xue, Z. Shen, Y. Yang, X. Wang, M. Fan, H. Pan, X. Gao, T. Yao and Y. Wu, *Nat. Commun.*, 2024, **15**, 6972.

242 H. Yun, S. Yoo, J. Son, J. H. Kim, J. Wu, K. Jiang, H. Shin and Y. J. Hwang, *Chem*, 2025, 102461.

243 S. R. Lingampalli, M. M. Ayyub and C. N. R. Rao, *ACS Omega*, 2017, **2**, 2740–2748.

244 X. Chang, T. Wang and J. Gong, *Energy Environ. Sci.*, 2016, **9**, 2177–2196.

245 N. Sun, S. S. A. Shah, Z. Lin, Y.-Z. Zheng, L. Jiao and H.-L. Jiang, *Chem. Rev.*, 2025, **125**, 2703–2792.

246 W. Zhong, R. Sa, L. Li, Y. He, L. Li, J. Bi, Z. Zhuang, Y. Yu and Z. Zou, *J. Am. Chem. Soc.*, 2019, **141**, 7615–7621.

247 P. Fu, C. Chen, C. Wu, B. Meng, Q. Yue, T. Chen, W. Yin, X. Chi, X. Yu, R. Li, Y. Wang, Y. Zhang, W. Luo, X. Liu, Y. Han, J. Wang, S. Xi and Y. Zhou, *Angew. Chem., Int. Ed.*, 2025, **64**, e202415202.

248 J. Wang, J. Ning, Q. Tang, L. Che, Y.-Y. Gu, X. Wang, X. Wang, L. Hao and L. Shi, *J. Catal.*, 2025, **446**, 116078.

249 P. Wang, Y. Dai, Z. Song, Y. Wang, J. Wei, Z. Liu, Y. Ma, F. Yang, J. Qu, S. Liu, Y. Cai, X. Yang, M. Li and J. Hu, *Chem. Eng. J.*, 2025, **511**, 162084.

250 P. Zhang, T. Sun, L. Xu, Q. Xu, D. Wang, W. Liu, T. Zheng, G. Yang and J. Jiang, *ACS Sustainable Chem. Eng.*, 2023, **11**, 343–352.

251 Q. Xu, Y. Jin, T. Sun, T. Zheng, P. Zhang, Y. Han, Y. Wang, T. Li, D. Qi, L. Xu, D. Wang and J. Jiang, *Chem. Eng. J.*, 2024, **479**, 147837.

252 Y. Li, S. Wang, X.-S. Wang, Y. He, Q. Wang, Y. Li, M. Li, G. Yang, J. Yi, H. Lin, D. Huang, L. Li, H. Chen and J. Ye, *J. Am. Chem. Soc.*, 2020, **142**, 19259–19267.

253 Y. Wang, T. Zheng, Y. Jin, T. Sun, X. Ding, X. Wang, Q. Xu, T. Li, S. Zhang and J. Jiang, *Sci. China Mater.*, 2024, **67**, 1292–1300.

254 T. Zhou, Z. Xie, H. Luo, H. Chen, L. Li, M. Chen and W. Shi, *Inorg. Chem.*, 2024, **63**, 24778–24786.

255 Q. Zhang, S. Gao, Y. Guo, H. Wang, J. Wei, X. Su, H. Zhang, Z. Liu and J. Wang, *Nat. Commun.*, 2023, **14**, 1147.

256 G. Huang, Q. Niu, Y. He, J. Tian, M. Gao, C. Li, N. An, J. Bi and J. Zhang, *Nano Res.*, 2022, **15**, 8001–8009.

257 W. Luo, J. Chen, Z. Tang, B. Yang, G. Chen, S. Wang, G. Chen, M. Liu, H. Xu, J. Ye and N. Zhang, *J. Energy Chem.*, 2025, **108**, 400–409.

258 G. Huang, Q. Niu, J. Zhang, H. Huang, Q. Chen, J. Bi and L. Wu, *Chem. Eng. J.*, 2021, **427**, 131018.

259 Y. Che, C. Zhu, X. Liu, M. Li, X. Liu and H. Xing, *Chem. Eng. J.*, 2025, **513**, 162811.

260 A. Zheng, X. Li, P. Chen, W. Li, Y. Zhang, J. Shi, C. Su and L. Guo, *ChemSusChem*, 2025, **18**, e202500330.

261 Y. Lia, Z. Zhao, W. Lu, H. Zhu, F. Sun, B. Mei, Z. Jiang, Y. Lyu, X. Chen, L. Guo, T. Wua, X. Ma, Y. Meng and Y. Ding, *Appl. Catal., B*, 2023, **324**, 122298.

9710 | *Energy Environ. Sci.*, 2025, **18**, 9632–9712

This journal is © The Royal Society of Chemistry 2025

262 L. Liu, J. Liu, G. Li, X. Shi, J. Yin, S. Zheng, K. Yung, H. B. Yang and T. W. B. Lo, *Angew. Chem., Int. Ed.*, 2025, **64**, e202422744.

263 M. G. Sibi, M. K. Khan, D. Verma, W. Yoon and J. Kim, *Appl. Catal., B*, 2022, **301**, 120813.

264 M. G. Sibi, D. Verma, H. C. Setiyadi, M. K. Khan, N. Karanwal, S. K. Kwak, K. Y. Chung, J. Park, D. Han, K. Nam and J. Kim, *ACS Catal.*, 2021, **11**, 8382–8398.

265 J. Wei, Q. Ge, R. Yao, Z. Wen, C. Fang, L. Guo, H. Xu and J. Sun, *Nat. Commun.*, 2017, **8**, 15174.

266 S. Zou, Y. Liang, X. Zhang, Q. Gu, L. Wang, H. Sun, X. Liao, J. Huang and A. R. Masri, *Angew. Chem., Int. Ed.*, 2025, **64**, e202412835.

267 X. Hu, X. Liu, X. Hu, C. Zhao, Q. Guan and W. Li, *Adv. Funct. Mater.*, 2023, **33**, 2214215.

268 X. Hu, C. Zhao, X. Hu, Q. Guan, Y. Wang and W. Li, *ACS Appl. Mater. Interfaces*, 2019, **11**, 25100–25107.

269 X. Ci, D. Zhai, R. Tu, X. Li, S. Jiang, X. Wang, W. Deng and G. Ren, *Chem. Eng. J.*, 2024, **497**, 154951.

270 A. K. Fellenberg, A. Addad, S. A. Chernyak, Y. Zhou, M. Corda, D. O. D. Souza, O. V. Safonova, V. Martin-Diaconescu, V. V. Ordomsky, G. Ji and A. Y. Khodakov, *Cell Rep. Phys. Sci.*, 2024, **5**, 101926.

271 O. Martin, A. J. Martín, C. Mondelli, S. Mitchell, T. F. Segawa, R. Hauert, C. Drouilly, D. Curulla-Ferré and J. Pérez-Ramírez, *Angew. Chem., Int. Ed.*, 2016, **55**, 6261–6265.

272 A. Rosado, I. Popa, A. A. Marke, J. Moral-Vico, E. M. Naughton, H. Eckhardt, J. A. Ayllón, A. M. López-Periago, C. Domingo and L. Negahdar, *J. Mater. Chem. A*, 2024, **12**, 21758–21771.

273 J. K. Nørskov, F. Abild-Pedersen, F. Studt and T. Bligaard, *Proc. Natl. Acad. Sci. U. S. A.*, 2011, **108**, 937–943.

274 G. Kresse and J. Furthmüller, *Phys. Rev. B:Condens. Matter Mater. Phys.*, 1996, **54**, 11169–11186.

275 P. Giannozzi, *et al.*, *J. Phys.: Condens. Matter*, 2009, **21**, 395502.

276 S. J. Clark, M. D. Segall, C. J. Pickard, P. J. Hasnip, M. I. J. Probert, K. Refson and M. C. Payne, First principles methods using CASTEP, *Z. Kristallogr.*, 2005, **220**, 567–570.

277 J. M. Soler, E. Artacho, J. D. Gale, A. García, J. Junquera, P. Ordejón and D. Sánchez-Portal, *J. Phys.: Condens. Matter*, 2022, **14**, 2745–2779.

278 X. Gonze, B. Amadon, P. M. Anglade, J. M. Beuken, F. Bottin, P. Boulanger, F. Bruneval, D. Caliste, R. Caracas, M. Côté, T. Deutsch, L. Genovese, P. Ghosez, M. Giantomassi, S. Goedecker, D. R. Hamann, P. Hermet, F. Jollet, G. Jomard, S. Leroux, M. Mancini, S. Mazevet, M. J. T. Oliveira, G. Onida, Y. Pouillon, T. Rangel, G. M. Rignanese, D. Sangalli, R. Shaltaf, M. Torrent, M. J. Verstraete, G. Zerah and J. W. Zwanziger, *Comput. Phys. Commun.*, 2009, **180**, 2582–2615.

279 S. Wei, A. Li, J. Liu, Z. Li, W. Chen, Y. Gong, Q. Zhang, W. Cheong, Y. Wang, L. Zheng, H. Xiao, C. Chen, D. Wang, Q. Peng, L. Gu, X. Han, J. Li and Y. Li, *Nat. Nanotechnol.*, 2018, **13**, 856–861.

280 A. Panda, Y. Son, M. Umer, G. Lee, M. Balamurugan, J. Lee, W. Kim, R. Umapathi, E. A. Lohith, K. Keerthi, K. T. Nam, R. Zboril, M. J. Kim, S. Venkateswarlu and M. Yoon, *Chem. Eng. J.*, 2025, **509**, 160831.

281 Z. W. Seh, J. Kibsgaard, C. F. Dickens, I. Chorkendorff, J. K. Nørskov and T. F. Jaramillo, *Science*, 2017, **355**, eaad4998.

282 S. Ringe, N. G. Hörmann, H. Oberhofer and K. Reuter, *Chem. Rev.*, 2021, **122**, 10777–10820.

283 T. Li, P. Wang, M. He, T. Zhang, C. Yang and Z. Li, *Coord. Chem. Rev.*, 2024, **521**, 216179.

284 S. Gusarov, *Materials*, 2024, **17**, 2119.

285 F. Abild-Pedersen, J. Greeley, F. Studt, J. Rossmeisl, T. R. Munter, P. G. Moses, E. Skúlason, T. Bligaard and J. K. Nørskov, *Phys. Rev. Lett.*, 2007, **99**, 016105.

286 T. C. Lin, E. E. B. Rogers and A. Bhan, *ACS Catal.*, 2024, **15**, 780–788.

287 N. Karmodak, S. Vijay, G. Kastlunger and K. Chan, *ACS Catal.*, 2022, **12**, 4818–4824.

288 S. Ringe, C. G. Morales-Guio, L. D. Chen, M. Fields, T. F. Jaramillo, C. Hahn and K. Chan, *Nat. Commun.*, 2020, **11**, 33.

289 G. McCarver, T. Yildirim and W. Zhou, *ChemCatChem*, 2024, **16**, e202400960.

290 A. Tripathi and R. Thapa, *Carbon*, 2023, **208**, 330–337.

291 Y. Liu, Y. Jing and Y. Li, *J. Phys. Chem. Lett.*, 2024, **15**, 6216–6221.

292 Z. Bai, Z. Zhi, X. Z. Jiang and K. H. Luo, *Ind. Eng. Chem. Res.*, 2025, **64**, 4378–4387.

293 P. Brimley, H. Almajed, Y. Alsunni, A. W. Alherz, Z. J. L. Bare, W. A. Smith and C. B. Musgrave, *ACS Catal.*, 2022, **12**, 10161–10171.

294 M. A. Ramzan, R. Favre, S. N. Steinmann, T. L. Bahers and P. Raybaud, *J. Phys. Chem. C*, 2024, **128**, 10025–10034.

295 X. Yuan, D. Xiao, C. Zhao and C. Zhang, *Small*, 2025, **21**, 2411316.

296 Y. Wang, B. J. Park, V. K. Paidi, R. Huang, Y. Lee, K. Noh, K. Lee and J. W. Han, *ACS Energy Lett.*, 2022, 7, 640–649.

297 C. Lin, J. Rohilla, H. Kuo, C. Chen, T. M. Chang, M. Sone, P. P. Ingole, Y. Lo and Y. Hsu, *Sol. RRL*, 2024, **8**, 2300948.

298 X. Zhao, S. Xiao, B. Yao, Y. Chen and S. Yu, *J. Chem. Theory Comput.*, 2024, **20**, 9770–9786.

299 Q. Niu, S. Dong, J. Tian, G. Huang, J. Bi and L. Wu, *ACS Appl. Mater. Interfaces*, 2022, **14**, 24299–24308.

300 S. Wang, X. Nie, C. Song and X. Guo, *CCS Chem.*, 2024, **6**, 3018–3029.

301 M. Khan, Z. Akmal, M. Tayyab, S. Mansoor, A. Zeb, Z. Ye, J. Zhang, S. Wu and L. Wang, *Carbon Capture Sci. Technol.*, 2024, **11**, 100191.

302 Y. Zhang, H. Liu, F. Gao, X. Tan, Y. Cai, B. Hu, Q. Huang, M. Fang and X. Wang, *EnergyChem*, 2022, **4**, 100078.

303 F. Xie, C. Bie, J. Sun, Z. Zhang and B. Zhu, *J. Mater. Sci. Technol.*, 2023, **170**, 87–94.

304 K. T. Butler, C. H. Hendon and A. Walsh, *ACS Appl. Mater. Interfaces*, 2014, **6**, 22044–22050.

305 Ž. Kovačič, B. Likozar and M. Huš, *ACS Catal.*, 2020, **10**, 14984–15007.

306 A. C. Tsipis and A. A. Sarantou, *Dalton Trans.*, 2021, **50**, 14797–14809.

This journal is © The Royal Society of Chemistry 2025

Energy Environ. Sci., 2025, **18**, 9632–9712 | 9711

307 Ž. Kovačič, B. Likozar and M. Huš, *Chem. Eng. J.*, 2024, **485**, 149894.

308 X. Leng, F. Jin, M. Wei and Y. Ma, *Wiley Interdiscip. Rev.: Comput. Mol. Sci.*, 2016, **6**, 532–550.

309 J. Xiong, J. Ji, Q. Lei, X. Yang, Y. Bai, X. Zhang and H.-M. Cheng, *eScience*, 2024, **5**, 100306.

310 K. Lorber and P. Djinović, *iScience*, 2022, **25**, 104107.

311 X. Lu, K. B. Tan, J. Zhao and G. Zhan, *Chem Catal.*, 2025, **5**, 101264.

312 R.-P. Ye, J. Ding, W. Gong, M. D. Argyle, Q. Zhong, Y. Wang, C. K. Russell, Z. Xu, A. G. Russell, Q. Li, M. Fan and Y.-G. Yao, *Nat. Commun.*, 2019, **10**, 5698.

313 X. Lu and A. Roldan, *Appl. Catal., A*, 2024, **673**, 119589.

314 C. Li, Y. Ji, Y. Wang, C. Liu, Z. Chen, J. Tang, Y. Hong, X. Li, T. Zheng, Q. Jiang and C. Xia, *Nano-Micro Lett.*, 2023, **15**, 113.

315 J. Liu, W. Xue, W. Zhang and D. Mei, *J. Phys. Chem. C*, 2023, **127**, 4051–4062.

316 T. Yang, X. Mao, Y. Zhang, X. Wu, L. Wang, M. Chu, C.-W. Pao, S. Yang, Y. Xu and X. Huang, *Nat. Commun.*, 2021, **12**, 6022.

317 C. Altintas, O. F. Altundal, S. Keskin and R. Yildirim, *J. Chem. Inf. Model.*, 2021, **61**, 2131–2146.

318 A. Nandy, G. Terrones, N. Arunachalam, C. Duan, D. W. Kastner and H. J. Kulik, *Sci. Data*, 2022, **9**, 1–11.

319 P. Yang, H. Zhang, X. Lai, K. Wang, Q. Yang and D. Yu, *ACS Omega*, 2021, **6**, 17149–17161.

320 J. T. Margraf, H. Jung, C. Scheurer and K. Reuter, *Nat. Catal.*, 2023, **6**, 112–121.

321 D. H. Mok, H. Li, G. Zhang, C. Lee, K. Jiang and S. Back, *Nat. Commun.*, 2023, **14**, 1–12.

322 R. Ramprasad, R. Batra, G. Pilania, A. Mannodi-Kanakkithodi and C. Kim, *Npj Comput. Mater.*, 2017, **3**, 1–13.

323 Z. Lou, W. Li, H. Yuan, Y. Hou, H. Yang and H. Wang, *J. Mater. Chem. A*, 2022, **10**, 3585–3594.

324 Z. Li, S. Wang, W. S. Chin, L. E. Achenie and H. Xin, *J. Mater. Chem. A*, 2017, **5**, 24131–24138.

325 T. Williams, K. McCullough and J. A. Lauterbach, *Chem. Mater.*, 2019, **32**, 157–165.

326 W. Yang, T. T. Fidelis and W. Sun, *ACS Omega*, 2019, **5**, 83–88.

327 C. Li, L. Bao, Y. Ji, Z. Tian, M. Cui, Y. Shi, Z. Zhao and X. Wang, *Coord. Chem. Rev.*, 2024, **514**, 215888.

328 Y. Luo, S. Bag, O. Zaremba, A. Cierpka, J. Andreo, S. Wuttke, P. Friederich and M. Tsotsalas, *Angew. Chem., Int. Ed.*, 2022, **61**, e202200242.

329 X. Wan, Z. Zhang, W. Yu and Y. Guo, *Mater. Rep. Energy*, 2021, **1**, 100046.

330 S. Saxena, T. S. Khan, F. Jalid, M. Ramteke and M. A. Haider, *J. Mater. Chem. A*, 2019, **8**, 107–123.

331 Y. Shi and Z. Liang, *Appl. Catal., A*, 2024, **676**, 119674.

332 J. Wang, M. Zheng, X. Zhao and W. Fan, *ACS Catal.*, 2022, **12**, 5441–5454.

333 M. Sun, H. H. Wong, T. Wu, Q. Lu, L. Lu, C. H. Chan, B. Chen, A. W. Dougherty and B. Huang, *Adv. Energy Mater.*, 2023, **13**, 2203858.

334 C. Deng, Y. Su, F. Li, W. Shen, Z. Chen and Q. Tang, *J. Mater. Chem. A*, 2020, **8**, 24563–24571.

335 A. Das, D. Roy, S. Manna and B. Pathak, *ACS Mater. Lett.*, 2024, **6**, 5316–5324.

336 C. Chen, J. Li, X. Tan, Y. Zhang, Y. Li, C. He, Z. Xu, C. Zhang and C. Chen, *EES Catal.*, 2023, **2**, 71–93.

337 M. Sun and B. Huang, *Adv. Energy Mater.*, 2023, **13**, 2301948.

338 M. H. Barecka, J. W. Ager and A. A. Lapkin, *STAR Protoc.*, 2021, **2**, 100889.

339 A. Somoza-Tornos, O. J. Guerra, A. M. Crow, W. A. Smith and B. M. Hodge, *iScience*, 2021, **24**, 102813.

340 I. Bagemihl, L. Cammann, M. Pérez-Fortes, V. van Steijn and J. R. van Ommen, *ACS Sustainable Chem. Eng.*, 2023, **11**, 10130–10141.

341 J. Na, B. Seo, J. Kim, C. W. Lee, H. Lee, Y. J. Hwang, B. K. Min, D. K. Lee, H. S. Oh and U. Lee, *Nat. Commun.*, 2019, **10**, 5193.

342 B. Kumar, B. Muchharla, M. Dikshit, S. Dongare, K. Kumar, B. Gurkan and J. M. Spurgeon, *Environ. Sci. Technol. Lett.*, 2024, **11**, 1161–1174.

343 H. Shin, K. U. Hansen and F. Jiao, *Nat. Sustainability*, 2021, **4**, 911–919.

344 M. Jouny, W. Luc and F. Jiao, *Ind. Eng. Chem. Res.*, 2018, **57**, 2165–2177.

345 G. Leonzio, A. Hankin and N. Shah, *Chem. Eng. Res. Des.*, 2024, **208**, 934–955.

346 B. Sahin, M. Kraehling, V. Facci Allegrini, J. Leung, K. Wiesner-Fleischer, E. Magori, R. Pastusiak, A. Tawil, T. Hodges, E. Brooke, E. C. Corbos, M. Fleischer, E. Simon and O. Hinrichsen, *J. CO₂ Util.*, 2024, **82**, 102766.

347 A. Inoue, T. Harada, S. Nakanishi and K. Kamiya, *EES Catal.*, 2023, **1**, 9–16.

348 M. H. Barecka, J. W. Ager and A. A. Lapkin, *STAR Protoc.*, 2021, **2**, 100889.

349 J. M. Spurgeon and B. Kumar, *Energy Environ. Sci.*, 2018, **11**, 1536–1551.

350 J. Osorio-Tejada, M. Escriba-Gelonch, R. Vertongen, A. Bogaerts and V. Hessel, *Energy Environ. Sci.*, 2024, **17**, 5833–5853.

351 S. M. Jordaan and C. Wang, *Nat. Catal.*, 2021, **4**, 915–920.

352 S. Choi, M. Balamurugan, K.-G. Lee, K. H. Cho, S. Park, H. Seo and K. T. Nam, *J. Phys. Chem. Lett.*, 2020, **11**, 2941–2948.

353 M. A. Khan, S. K. Nabil, T. Al-Attas, N. G. Yasri, S. Roy, M. M. Rahman, S. Larter, P. M. Ajayan, J. Hu and M. G. Kibria, *Chem. Catal.*, 2022, **2**, 2077–2095.

354 S. Q. Liu, M. R. Gao, S. Wu, R. Feng, Y. Wang, L. Cui, Y. Guo, X. Z. Fu and J. L. Luo, *Energy Environ. Sci.*, 2023, **16**, 5305–5314.

355 Z. Zhang, S. Liu, Z. Wu, X. Chen, J. Wang, Y. Gao, S. Wang, F. Tao and G. Lv, *Green Chem.*, 2023, **25**, 5404–5415.

9712 | *Energy Environ. Sci.*, 2025, **18**, 9632–9712

This journal is © The Royal Society of Chemistry 2025